Control of integrin adhesions by myotubularin and phosphatidylinositol 3-kinase C2β in a myotubular myopathy model

Inaugural-Dissertation

to obtain the academic degree

Doctor rerum naturalium (Dr. rer. nat.)

submitted to the Department of Biology, Chemistry, Pharmacy

of Freie Universität Berlin

by

Paula Samsó Ferré

from Barcelona, Spain

2022

Period of doctorate studies	October 2016 to March 2022
Supervisor	Prof. Dr. Volker Haucke
Institute	Leibniz-Forschungsinstitut für Molekulare Pharmakologie (FMP), Berlin

First reviewer	Prof. Dr. Volker Haucke
Second reviewer	Prof. Dr. Sigmar Stricker

Date of defense	August 11th 2022

Affidavit

I declare that my dissertation has been written independently and with no other sources and aids than quoted.

I declare that my dissertation has not been submitted to other institutions in this or any other form.

Berlin, May 25th 2022

Paula Samsó Ferré

Acknowledgements

I am deeply grateful for the excellent direction, support, and training that Prof. Dr. Volker Haucke has provided me as a supervisor, as well as for his sharing of genuine commitment and passion for science with me.

I would like to thank Dr. York Posor, Dr. Wen-Ting Lo and specially Philipp A. Koch for their support, fruitful discussions, and most importantly their essential contribution to the success of this project. Thank you for your commitment – it has been a privilege to be part of such a talented and skilful team. I am also thankful for the advice and reagents I received from Dr. Alexander Wallroth and Dr. Wonyul Jang, whose input and teachings have been of great value to this project.

Additionally, I thank Dr. Martin Lehmann and Dr. Christopher Schmied for their advice and assistance in microscopy and image analysis, as well as Dr. Linda Sawade and Lennart Hoffmann for their help in troubleshooting the troublesome phosphoinositide immunostainings and adhesion and migration analysis, respectively. I would also like to thank Prof. Dr. Tanja Maritzen, and Prof. Dr. Michael Krauss for their interest and valuable comments about the project, and Prof. Dr. Dorothea Fiedler for her insightful guidance as a dissertation committee member.

I owe deep gratitude to Prof. Dr. Jocelyn Laporte (IGBMC, Strasbourg, France) for our successful collaboration and his excellent contribution to the project, as well as for the reagents and training on cell-based muscle models that he kindly provided during my stay in his lab. I would also like to thank all his group, especially Dr. Vasugi Nattarayan and the Spanish dream-team.

I also thank Prof. Dr. Len Stephens as well as Prof. Dr. Phillip Hawkins (Babraham Institute, Cambridge, UK) for hosting me in their lab and providing valuable input and training on phospholipidomics. I owe a special thanks to Dr. Karen Anderson and the lipidomics facility staff for their kind support.

I am grateful for the funding by Horizon 2020 ITN “PI3K in Health and Disease” (GA 675392) and the enriching experience participating in the consortium’s scientific and training activities together with top-class scientists and talented PhD fellows, with whom I had a wonderful time too.

I want to thank the lab’s technicians for their essential and dedicated work in keeping the science show running: Uwe Fink for the purification of PI(3)P probes, Jenny Eichhorst for much-needed LSM troubleshooting, Delia Löwe for the management of cell culture, Silke Zillmann for the ordering management and experimental troubleshooting, Claudia Schmidt and Maria Mühlbauer for always providing life-saving experimental support, and Sabine Hahn. A special thanks goes to Alexandra Chylla and the Sekretariat team for their warm support and commitment to the group’s well-being.

Thank you to all of my colleagues from AG Haucke, AG Maritzen, AG Krauß and AG Lehmann for being so supportive and contributing to an enriching and positive environment in the lab, as well as for the great times together – I certainly couldn’t have wished for better colleagues: Kerem C. Akkaya, Domenico Azarnia Tehran, Marietta Bergmann, Svenja Bolz, Caroline Bruns, Gabrielle Capin, Gillian Leigh Dornan, Michael Ebner, Marine Gil, Hannes Gonschior, Manuel Hessenberger, Maria Jäpel, Natalie Kaempf, Mudassar Khan, Gaga Kochlamazashvili, Marijn Kuijpers, Guan-Ting Liu, Tania López Hernández, Max Lucht, Fabian Lukas, Albert Mackintosh, Marta Maglione, Charles Malek, Phuong Nguyen, Kristine Oevel, Christoph Ott, Dymtro Puchkov, Julia Riedlberger, Filiz Sila Rizalar, Dorien Roosen, Giulia Russo, Kyungyuen Song, Tolga Soykan, Miaomiao Tian, Rozemarijn van der Veen, Dennis Vollweiter, Haibin Wang, Mirjana Weimershau, Agata Witkowska, Anna Wulf, Su Yanwei, and Klaas Yperman. I would like to extend my gratitude to the colleagues from other groups and facilities of the FMP for their help and availability, and for giving me the opportunity to participate in the institute’s life as a PhD representative.

A special and warm thanks goes to the colleagues whom I now call friends, my other fantastic and supportive friends in Berlin and Barcelona, and my most solid fanbase: my family and my partner – you have been a fundamental part of the journey, gràcies de tot cor.

"*Life did not take over the globe by combat, but by networking.*"

Lynn Margulis

1938 – 2011

Table of content

I. Abstract

X-linked centronuclear myopathy (XLCNM), also known as myotubular myopathy, is a rare and severe skeletal muscle disorder that manifests with congenital hypotonia and leads to early childhood mortality due to its currently limited therapeutic options. XLCNM is caused by loss-of-function mutations in the gene encoding the lipid phosphatase myotubularin (MTM1), which dephosphorylates the phosphoinositide phosphatidylinositol 3-phosphate [PI(3)P] at endosomal membranes. Among XLCNM pathomechanisms is impaired muscle cell adhesion via integrins, the transmembrane components of focal adhesions (FAs). Integrin subunit β1 (β1-integrin) plays key roles in the formation and maintenance of specialized skeletal muscle adhesions essential to muscle function. Importantly, MTM1-mediated PI(3)P turnover plays a role in the exocytosis of integrins from endosomes to the plasma membrane, yet the impact of MTM1on cell adhesions has not been described in detail. A functional association between MTM1 and phosphatidylinositol 3-kinase C2β (PI3KC2β), a lipid kinase that synthesizes PI(3)P and phosphatidylinositol 3,4-bisphosphate [$PI(3,4)P_2$], was uncovered in mammals when skeletal muscle-specific ablation of PI3KC2β rescued the disease phenotype of XLCNM mouse models. Previous studies have proposed a direct rebalancing of PI(3)P levels by PI3KC2β as the mechanism underlying the rescue of XLCNM. However, the precise mechanistic interplay between MTM1 and PI3KC2β, and its relevance in skeletal muscle physiological and pathological conditions remains elusive. Thus, in this project we aimed to mechanistically characterize this functional interaction in a cell-based context relevant to XLCNM. By pursuing this objective, we intended to gain insights into the molecular pathogenesis of XLCNM and the role of PI3KC2β in this context, serving as a basis for the development of XLCNM therapeutic strategies. For this purpose, the murine myoblast cell line C2C12 was used to generate knockout (KO) cell lines lacking MTM1, PI3KC2β, or both enzymes. In this system, we described that loss of MTM1 led to cell adhesion defects evidenced by decreased cell spreading, number of FAs and surface activated β1-integrin, which functionally resulted in enhanced migration and impaired myoblast differentiation. Cell adhesion defects and correlated functional phenotypes were completely rescued by co-depletion of PI3KC2β. Contrary to the prevailing opinion, we showed that the accumulation of the MTM1 substrate PI(3)P observed in *Mtm1*KO myoblasts was not normalized upon co-depletion. Instead, we showed that blockage of endocytosis ameliorated adhesion defects in *Mtm1*KO myoblasts. Data from HeLa cells, included in this dissertation for completeness purposes, showed that PI3KC2β knockdown (KD) leads to impaired active β1-integrin internalization, a phenotype that we mechanistically explained by a role of PI3KC2β in clathrin-mediated endocytosis (CME) of active β1-integrins. Hence, we propose that MTM1 and PI3KC2β play antagonistic roles in the control of active β1-integrin adhesions by respectively mediating recycling to the plasma membrane and internalization via CME. Treatment of MTM1-depleted cells with a newly developed PI3KC2β inhibitor rescued the reported cell adhesion phenotypes, thus establishing proof-of-principle evidence for a PI3KC2β-targeted XLCNM therapy. Altogether, our findings provide insights into cell adhesion defects key to XLCNM pathogenesis in a newly established *in vitro* model system. Moreover, we uncover a novel function of PI3KC2β in the regulation of integrin adhesions, setting a mechanistic background for its rescue of the XLCNM disease phenotype, an essential step towards the development of therapies targeting PI3KC2β.

II. Zusammenfassung

Myotubuläre Myopathie (*X-linked centrouclear myopathy*; XLCNM) ist eine seltene und schwere Skelettmuskelerkrankung, die sich mit angeborener Hypotonie manifestiert und zu frühkindlicher Sterblichkeit führt aufgrund von begrenzten therapeutischen Behandlungsmöglichkeiten. XLCNM wird durch Mutation des für die Phosphatase Myotubularin (MTM1) codierenden *MTM1*-Gens verursacht, wodurch die zelluläre Funktion von MTM1, die Entfernung des Phosphoinositids Phosphatidylinositol-3-phosphat [PI(3)P] an endosomalen Membranen durch Dephosphorylierung, gestört wird. Einer der XLCNM Pathomechanismen ist die beeinträchtigte Muskelzell-Adhäsion mittels Integrine, die Transmembranproteine in fokalen Zelladhäsionen (FA). Die β1-Integrin-Untereinheit ist von besonderer Bedeutung in der Formation und Aufrechterhaltung von speziellen Skelettmuskel-Zelladhäsionen, welche essenziell sind für eine normale Muskelfunktion. Frühere Studien haben gezeigt, dass MTM1 durch die Konversion von PI(3)P eine Rolle bei der Exozytose von Integrinen aus Endosomen spielt. Inwiefern intrazellulärer Transport der Integrine durch MTM1 an der Bildung und Aufrechterhaltung spezialisierter Zelladhäsionen im Muskel beteiligt ist, ist jedoch unzureichend verstanden. Des Weiteren wurde eine funktionelle Assoziation zwischen MTM1 und der Phosphatidylinositol 3-Kinase C2β (PI3KC2β), einer Lipidkinase, die PI(3)P und Phosphatidylinositol-3,4-bisphosphat [PI(3,4)P2] synthetisiert, in Säugetieren beschrieben, da die skelettmuskelspezifische genetische Ausschaltung von PI3KC2β die XLCNM-assoziierten Krankheitsphänotypen in Mausmodellen revidiert. Frühere Studien haben eine Normalisierung der PI(3)P-Level durch PI3KC2β als den Mechanismus vorgeschlagen, der der Rettung von XLCNM zugrunde liegt. Allerdings ist der genaue Mechanismus, der dem inversen Zusammenhang zwischen den zellulären Funktionen von MTM1 und PI3KC2β zugrunde liegt, und dessen Relevanz in physiologischen und pathologischen Zuständen der Skelettmuskulatur, nicht vollständig erforscht. Daher war das Ziel dieser Studie, das Zusammenspiel beider Proteine in einem für XLCNM relevanten zellbasierten Kontext mechanistisch weiter aufzuklären, um so die molekulare Grundlage zur Entwicklung von therapeutischen Strategien für XLCNM durch Manipulation von PI3KC2β zu schaffen. Zu diesem Zweck wurde die murine myoblastische Zelllinie C2C12 verwendet, um Knockout (KO)-Zelllinien zu erzeugen, denen MTM1, PI3KC2β oder beide Enzyme fehlen. In diesem System konnten wir beschreiben, dass der Verlust von MTM1 zu defekter Zelladhäsion führt, da *Mtm1*KO Zellen eine verringerte Zellausbreitung und eine reduzierte Anzahl an FA und oberflächenaktivierten β1-Integrin zeigen, was funktionell mit einer verstärkten Migration und einer beeinträchtigten Muskelzelldifferenzierung verbunden ist. Diese Phänotypen konnten vollständig durch den Co-KO von MTM1 und PI3KC2β umgekehrt werden. Allerdings unterliegt dieser Umkehrung der XLCNM-assoziierten Phänotypen nicht die, wie in der Literatur angenommen, Akkumulation des MTM1-Substrats PI(3)P, da die durch MTM1-Verlust angereicherten PI(3)P Level durch die gleichzeitige Ausschaltung von PI3KC2β nicht reduziert werden konnten. Stattdessen zeigen wir, dass die Inhibition der Endozytose Adhäsionsdefekte in *Mtm1*KO-Myoblasten verbessern kann. In HeLa-Zellen resultiert der Knockdown (KD) von PI3KC2β in einer beeinträchtigten aktiven β1-Integrin Internalisierung. Mechanistisch wird dies durch eine wichtige Rolle von PI3KC2β bei der Clathrin-vermittelte Endozytose (*clathrin-mediated endocytosis*; CME) von aktiven β1-Integrinen erklärt. Unsere Ergebnisse unterstützen ein Modell, in dem MTM1 und PI3KC2β antagonistische Rollen bei der Kontrolle aktiver β1-Integrin-Adhäsionen zugewiesen werden, da MTM1 die Integrin Exozytose zur Plasmamembran und PI3KC2β die rückführende Internalisierung der Integrine

über CME vermittelt. Weiterhin konnten wir zeigen, dass die Behandlung von Zellen, denen MTM1 fehlt, mit einem neu entwickelten PI3KC2β-Inhibitor die Zelladhäsionsphänotypen umkehren kann und liefern damit die molekulare Grundlage für eine PI3KC2β-gerichtete XLCNM-Therapie. Zusammenfassend geben unsere Ergebnisse Einblicke in Zelladhäsionsdefekte, die für die XLCNM-Pathogenese in einem neu etablierten *in vitro*-Modellsystem von entscheidender Bedeutung sind. Wir decken außerdem eine neue Funktion von PI3KC2β bei der Regulation von Integrin-Adhäsionen durch CME auf und schaffen einen mechanistischen Hintergrund für die Umkehrung des XLCNM-Krankheitsphänotyps durch PI3KC2β Inhibition, ein wesentlicher Schritt, der den Weg zur Entwicklung von XLCNM-Therapien ebnet.

1. Introduction

1.1. Centronuclear myopathies

Centronuclear myopathies (CNM) are a group of skeletal muscle disorders named after the histopathological sign of abnormally central nuclei in muscle cells. This finding was first observed in 1966 in a biopsy sample from a teenage patient with a muscle-wasting disorder, which had muscle fibers reminiscent of poorly differentiated fetal myotubes [1]. This observation contributed to coining the term of myotubular myopathy [2], nowadays used to refer to the most common and severe genetic type of CNM, X-linked centronuclear myopathy (XLCNM).

CNM are rare monogenic disorders that clinically manifest with myopathy symptoms of mostly congenital onset. These symptoms are characterized by a generalized muscle weakness and hypotonia that leads to respiratory complications and failure in severely affected patients, accompanied by associated physical disabilities due to motor impairment [3,4]. Consequently, the average life expectancy of CNM patients is 29 months [5]. Clinical manifestations of CNM, including severity and onset are dependent on their genetic etiology, although a significant component of phenotypic variability has been reported [2,3,6].

CNM are caused by mutations in a limited number of genes (**Table 1-1**) involved in the development, maintenance, and function of skeletal muscle, some of whose physiological and pathological functions are poorly understood [2,6]. Moreover, a percentage of patients meeting the CNM diagnostic criteria do not bear any of the genetic mutations described to date, implying that some CNM-associated genetic alterations remain uncharacterized [5].

Table 1-1. Genes and proteins involved in CNM [7,8].

Gene	Inheritance	Protein	CNM-causing mutations
MTM1	XL	Myotubularin (MTM1)	LOF
DNM2	AD	Dynamin 2 (DNM2)	GOF
BIN1	AD, AR	Bridging integrator 1 (BIN1), amphiphysin 2	LOF
RYR1	AR	Ryanodine receptor 1 (RYR1)	LOF
MTMR14	unknown	Myotubularin-related protein 14 (MTMR14), hJUMPY	LOF
SPEG	AR	Striated muscle preferentially expressed protein kinase (SPEG)	LOF
TTN	AR	Titin	LOF
CCDC78	AD	Coiled-coil domain-containing protein 78	LOF

XL, X-linked; AD, autosomal dominant; AR, autosomal recessive; LOF, loss of function; GOF, gain of function.

From an epidemiological perspective, XLCNM patients account for 70% of CNM diagnoses, with an estimated total (male and female) population incidence of 16.7 cases per million. Autosomal CNM estimated incidence is 7.3 cases per million, corresponding to a 2.8% of *BIN1*, 8.3% of *DNM2* and 8.3% of *RYR1*-associated CNM, and an 11.0% to unidentified causal mutations. Collection of precise epidemiological data is challenging due to the rare nature and high mortality of these disorders [55].

1.1.1. X-linked centronuclear myopathy

A study by Laporte *et al* [9] contributed to the first association of XLCNM to loss-of-function mutations in the gene *MTM1*, which encodes for myotubularin (MTM1), a phosphatase that mainly acts on the phospholipid phosphatidylinositol 3-phosphate [PI(3)P], mostly present at intracellular membranes. According to its clinical manifestations, XLCNM is classified into severe or mild forms, with the former accounting for approximately 80% of XLCNM diagnoses and frequently presenting prenatal manifestations [10]. Newborns affected with severe XLCNM suffer from decreased body weight, musculoskeletal deformities and often require respiratory and feeding support during the first year of life, when 25% die due to derived complications [2]. A minor proportion of severe XLCNM patients develop clinical presentations unrelated to skeletal muscle function; whether these are associated to XLCNM-causing *MTM1* mutations or unrelated disorders remains undescribed. These presentations include gastrointestinal, kidney, and cardiac alterations, as well as hepatic peliosis, a rare vascular condition of the liver [2,3]. Only around 20% of XLCNM patients classify into a mild to moderate spectrum, which includes very rare adult-onset cases. These patients require less or no mobility assistance, and only temporary ventilation and feeding support, if any. Mild XLCNM is associated to certain missense mutations, whereas most severe manifestations are due to deletions resulting in protein truncation or changes in amino acids key to MTM1 function [9].

The X-linked inheritance pattern of *MTM1* causes distinct clinical manifestations of myopathy in heterozygous females. Although most heterozygous female carriers are believed to be asymptomatic [11], some mild late-onset cases have been reported, especially in individuals bearing *MTM1* mutations associated to severe XLCNM in males [12]. Heterozygous patients present asymmetrical muscle function impairment, as observed in carriers of other X-linked muscular disorders such as Duchenne dystrophy, due to mosaic X chromosome inactivation [12]. Histopathological and ultrastructural findings are common with those observed in affected males, with presence of typical XLCNM adult-onset hallmarks [13].

1.1.2. Autosomal centronuclear myopathies

A detailed description of all autosomal CNM genetic forms (**Table 1-1**) is beyond the scope of this thesis. This section contains a brief description of the most well-characterized and frequently mutated proteins in CNM.

1.1.2.1. Dynamin 2-associated CNM

Dynamin 2 (DNM2) is a large ubiquitously expressed GTPase involved in membrane fission in endocytic and endosomal transport pathways, which also plays roles in cytoskeletal regulation [14]. Gain-of-function mutations in *DNM2*, concentrated at domains that determine protein assembly, phosphoinositide binding and subcellular localization [15], are associated to mild adult-onset clinical presentations and believed to mainly impact skeletal muscle maintenance [7]. Mutations in *DNM2* are also reported to cause certain types of Charcot-Marie-Tooth neuropathy [16] (see section 1.3.1.2), and some studies have reported nerve alterations and other non-muscle defects in DNM2-associated CNM [7]. An interesting link between DNM2 and MTM1 in CNM pathogenesis was revealed in a study [17] that observed increased expression of DNM2 in XLCNM mouse models and patients, and

demonstrated that its reduction ameliorated XLCNM phenotypes, uncovering a potential therapeutic strategy [17,18].

1.1.2.2. Bridging integrator 1-associated CNM

Bridging integrator 1 (BIN1) is a membrane curvature sensing and remodeling protein containing a Bin/Amphiphysin/Rvs (BAR) domain [19], whose splicing isoform 8 is skeletal-muscle specific and accounts for 99.6% expression of BIN1 in this tissue [20]. In contrast to other isoforms, BIN1 isoform 8, referred as BIN1 in this thesis unless indicated, lacks the clathrin-binding domain of neuronal BIN1 isoforms and has instead a polybasic phosphoinositide-binding domain [21]. BIN1 binds MTM1 in skeletal muscle and plays a role in the formation of a specialized structure involved in muscle contraction, the transverse (T)-tubule (see section 1.3.3.5) [22]. In other tissues, BIN1 isoforms play roles in endocytosis and nuclear positioning [23,24]. Loss-of-function mutations in *BIN1*, some at the BAR domain [25], lead to CNM clinical manifestations of variable severity. Like for DNM2, a link between XLCNM and BIN1-related CNM has been established in a study showing that increasing BIN1 expression rescued XLCNM phenotype in mouse models [26]. Additionally, BIN1 has been shown to interact with DNM2 to suppress its GTPase activity and regulate T-tubule stabilization [27], and mutations in their mutual binding domains have been associated with CNM phenotypes [21,27]. These observations further indicate a common pathway involving MTM1, DNM2 and BIN1 in CNM pathogenesis, a potential target pathway for therapeutic approaches.

1.1.2.3. Ryanodine receptor 1-associated CNM

Ryanodine receptor 1 (RYR1) is the skeletal muscle-specific isoform of an endoplasmic reticulum (ER) calcium ion (Ca^{2+}) channel that is activated upon direct binding to dihydropyridine receptor (DHPR) during muscle contraction, thereby releasing a Ca^{2+} flux into the cytoplasm that activates the contractile machinery [28]. DHPR is a skeletal muscle-specific plasma membrane voltage-gated Ca^{2+} channel that, together with RYR1, constitutes the core machinery of excitation-contraction coupling located at the T-tubule of skeletal muscle cells [29]. Loss-of-function mutations of *RYR1* have been associated to CNM [30,31] and other rare congenital myopathies with common clinical manifestations, as well as with malignant hyperthermia, a severe reaction to anesthetic drugs [29].

1.1.3. Investigational therapies for centronuclear myopathies

Therapeutic options for CNM patients are currently limited, and a curative treatment is not available. Treatment is thus focused on symptomatic and supportive care according to each patient's clinical manifestations [2,32]. In the recent years, insights into CNM molecular pathology have led to the development of investigational therapies, some of which are currently at clinical or pre-clinical trial phases. Most of these approaches are based on gene therapy targeting the three most commonly mutated genes in CNM, and taking advantage of their functional interplay recently uncovered in genetic studies in animal models [6,32]. To date, ongoing phase I/II clinical trials include (i) adenoviral delivery of *MTM1* to XLCNM patients [33], supported by several proof-of-concept studies [34–36], and (ii) treatment with antisense oligonucleotides against *DNM2* in *DNM2*-related or XLCNM patients [37], based on various preclinical studies [17,18,38]. Additionally, other studies on animal models have provided proof-of-principle evidence for therapeutic development based on similar strategies, aiming to normalize the disease

pathways. These include studies by Lionello *et al* [26] and Raess *et al* [39], who demonstrated that exogenous *BIN1* or *MTMR2* delivery ameliorated the XLCNM phenotype in mouse models. Maani *et al* [40] and Gayi *et al* [41] showed that the estrogen receptor antagonist tamoxifen reduced expression levels of *DNM2* in XLCNM models, thereby rescuing their myopathy phenotype. Other inhibitor-based approaches targeting general muscle homeostasis have been tested with limited phenotype improvement outcomes [6,32].

A potential therapeutic strategy of special relevance to this project emerges from a study by Sabha *et al* [42], who showed that skeletal muscle-specific ablation of phosphatidylinositol 3-kinase C2β (PI3KC2β) rescued the disease phenotype of XLCNM mouse models. This observation uncovered an unexpected functional link between PI3KC2β and MTM1, respectively a lipid kinase and phosphatase acting on phosphoinositides, and set a background for the development of a novel XLCNM therapy targeting PI3KC2β inhibition. In the following sections of the introduction, the molecular components of this scenario and their interplay will be described in detail, with special focus on the skeletal muscle context in physiological and pathological conditions.

1.2. Phosphoinositides in membrane identity and dynamics

Cellular membranes, comprising the plasma membrane and endomembranes, control central cellular processes such as cell division, migration, signal transduction and molecular transport via membrane dynamics, the continuous modifications in membrane shape, tension, and transport within the cell's membranous system [43]. Phosphoinositides (PIs) are key minor components of cellular membranes that determine identities of cell compartments and mediate a variety of cellular and organismal functions by controlling membrane dynamics. Structurally, PIs are formed by a diacylglycerol backbone, composed of two fatty acid chains and a glycerol molecule, bound via a phosphodiester linkage to the D1 position of a *myo*-inositol ring, whose hydroxyl groups can be phosphorylated at any combination of the positions D3, D4 and D5, resulting in a total of 7 possible PI species (**Fig. 1-1**) [44,45]. As evidenced by their structure, PIs are amphiphilic molecules that integrate into hydrophobic lipid bilayers of cellular membranes via their fatty acid moieties, whereas their negatively charged head groups protrude from the cytoplasmic layer to interact with effector molecules [45,46]. Phosphatidylinositol-phosphate species, referred here as PIs, constitute up to 1% of the total cellular phospholipids, whereas unphosphorylated PI accounts for a proportion of up to 20%, with wide subcellular compartment, cell-type and organismal-specific variability [46].

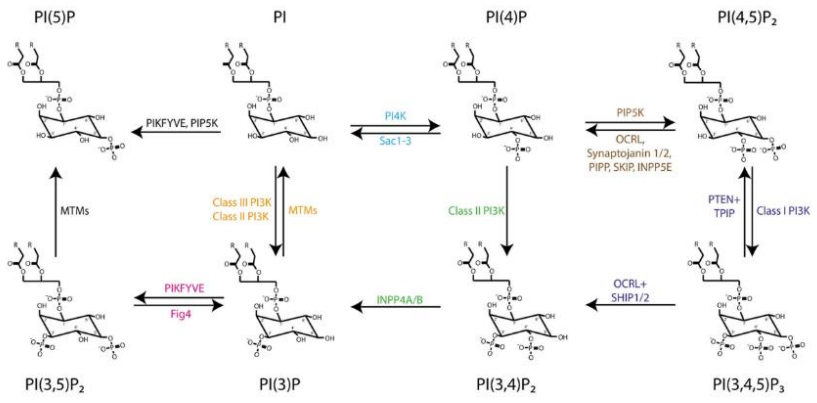

Figure 1-1. Interconversion of PI species by PI-metabolizing enzymes [47].

Biosynthesis of PI occurs at the ER and distribution to other cellular membranes is promoted by PI transfer proteins and vesicular trafficking [46]. Synthesis and turnover of specific PI species is mediated by PI-kinases and phosphatases (**Fig. 1-1**) that respectively transfer or hydrolyze phosphoryl groups from ATP to

the inositol ring in a highly position-selective manner [46]. Enzymes mediating most PI interconversion reactions have been characterized, many of which have common substrates or redundant catalytic functions, thereby exemplifying the highly-regulated compartment- and cell-specific nature of these reactions [47].

Action of different PI kinases and phosphatases at cellular compartments allows a differential compartment-specific PI composition that is essential for determining membrane identities [44,48] (**Fig. 1-2**). Broadly, PI 4-phosphate species play major roles in plasma membrane dynamics and receptor-mediated signal transduction [47,49]. In contrast, 3-phosphate species hallmark the endolysosomal system, where PI(3)P defines early endosomal membranes, mostly synthesized from a PI(3,4)P_2 pool following plasma membrane endocytosis (see section 1.4.2.2.1), and sorting endosomes, where cargo distribution is defined. PI(3,5)P_2 characterizes late endosomes and multivesicular bodies (MVB), acidified intermediate compartments generally *en route* to lysosomal degradation [45, 47,49]. Related to these, a pool of PI(3)P is relevant in the formation of autophagosomes, the organelles that mediate the degradative process of autophagy upon fusion with lysosomes (see sections 1.3.3.2 and 1.5.2). In turn, PI(3,4)P_2 is a short-lived species whose cellular functions remain partially undescribed, yet reported be involved in endocytosis from the plasma membrane and signaling from late endosomal/lysosomal membranes [50,51]. Importantly, compartmental identities are not stationary, as PI interconversion is highly dynamic and spatiotemporally controlled, and specific PI pools frequently define subdomains at certain compartments [48,52]. Ultimately, membrane dynamics is determined by the finely-modulated sequential conversion of PIs throughout the cell membranous system, thus supporting membrane trafficking and evidencing the essential role of PIs in cellular homeostasis.

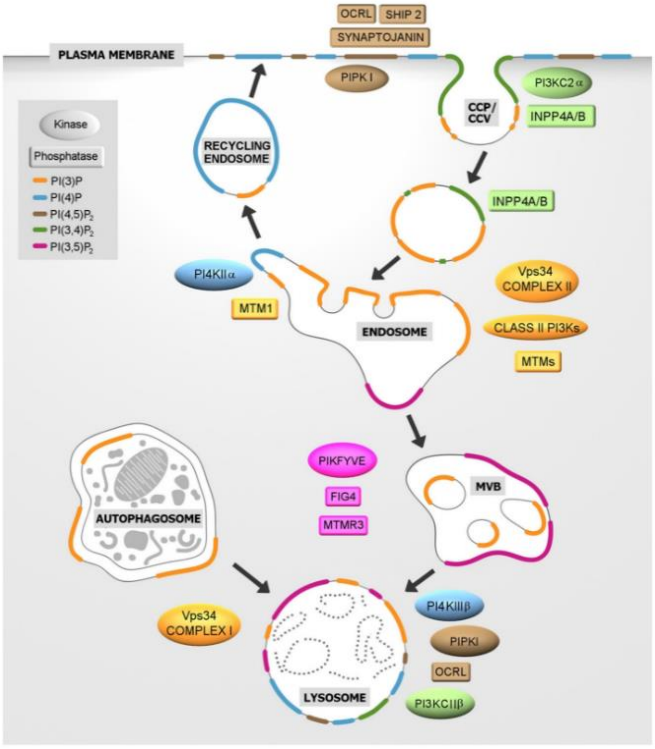

Figure 1-2. Compartmental distribution and conversion of PIs by PI-metabolizing enzymes at the plasma membrane and the endolysosomal system [47].

PIs mediate their actions in membrane trafficking and signaling mostly by reversible recruitment of effector proteins to specific pools, as well as by direct regulation of transmembrane proteins such as ion channels or transporters [44]. PI effector proteins contain PI-binding domains that allow recruitment at certain compartments by a process of coincidence detection [53]. Among the PI-binding domains of interest for this project are FYVE (Fab1, YOTB/ZK632, Vac1p, and EEA1) and PX (Phox homology) domains binding PI(3)P, PDZ (PDS95-Dlg1-Zo1) domain binding PI(4,5)P_2, PH (Pleckstrin homology) domain binding PI 4-phosphate species, and BAR domain with broad specificity. Due to the low affinity of PI-protein interactions, binding is frequently aided by regulatory proteins such as small RAB GTPases, a family of proteins that act as molecular switches in GTP- or GDP-bound states [45,46,54].

1.3. Myotubularin in physiological and pathological conditions

Myotubularin (MTM1) is the founding member of the myotubularin family of proteins, referred as myotubularins in this thesis, a large and evolutionarily conserved group of lipid phosphatases whose roles remain partially uncharacterized, yet known to catalyze PI(3)P and PI(3,5)P_2 turnover at the endosomal system. A distinctive trait of this family of proteins with similar structure and substrate specificity is their classification into catalytically active or inactive phosphatases, as several lack phosphatase activity (**Fig. 1-3**).

1.3.1. Myotubularin family of proteins

Myotubularins are conserved in almost all eukaryotes and evolutionarily believed to appear in yeast, which expresses a single homolog [55,56]. In humans, the myotubularin family is composed of 14 paralogs: MTM1 and 13 myotubularin-related proteins (MTMR1-13) [57,58]. Additionally, MTMR14 is occasionally included in this family independently of its differing phylogenetic origin and structure [59]. Myotubularins are ubiquitously expressed in humans, with tissue-specific enrichments of certain family members. The existence of 14 ubiquitously-expressed human myotubularin paralogs that share a similar structure and substrate specificity would intuitively lead to hypothesize a functional redundancy. However, myotubularins have been reported to play tissue-specific functions determined by enriched expression, splice isoforms and interaction partners. An illustrative example is MTM1, which despite the fact that it is associated to a skeletal muscle disorder, is expressed at low levels in skeletal muscle compared to other tissues [4], suggesting that the disease phenotype is likely linked to muscle-specific MTM1 variants or interactors. This hypothesis is supported by the fact that two mRNA variants of *MTM1* are skeletal muscle-specific and encode for proteins lacking some functional domains [60]. The evolutionary conservation of myotubularin family members, including inactive phosphatases, further argues against a functional redundancy within this family.

1.3.1.1 Structure and regulation of myotubularins

Myotubularins are composed of a core signature domain and several additional functional domains mediating protein and PI interactions. The core domain includes a phosphatase-like domain, sometimes classified as a Protein Tyrosine Phosphatase (PTP) domain due to the presence of a $C(X)_5R$ motif, and a PH-GRAM (PH-Glucosyltransferase, RAB-like GTPase Activator and Myotubularin) domain [60]. The first mediates the catalytic activity of myotubularins, reported to hydrolyze the phosphoryl group at the D3 position of the inositol ring of PI(3)P and PI(3,5)P_2 [61–64]. Whereas substrate specificity *in vitro* is reported or expected from structural data to be non-discriminative for both PI

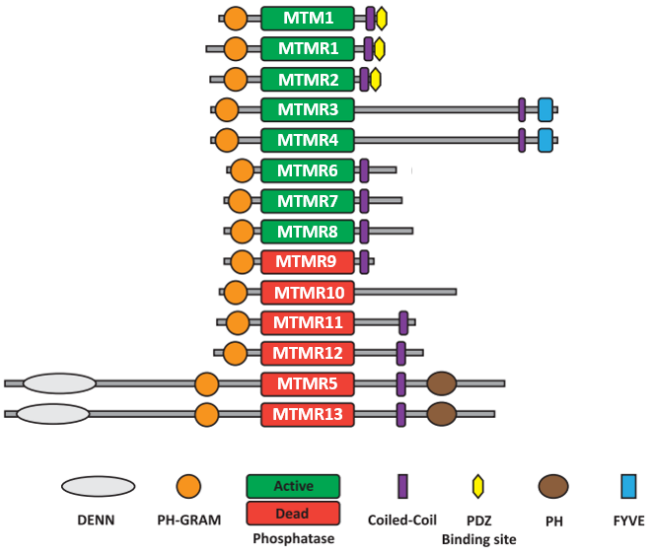

Figure 1-3. Human myotubularin family of proteins: functional domain organization. Scaled representation according to amino acid length of the most described protein isoform. Adapted figure [60].

species, *in vivo* substrate specificity is thought to be modulated by protein interactions or substrate availability at certain cellular membranes. Catalytically inactive myotubularins (MTMR5, MTMR9-13) bear substitutions in essential residues of the $C(X)_5R$ signature motif [65] that disrupt their activity. The PH-GRAM domain plays a regulatory role through its ability to bind PI and effector proteins. Differing amino acid sequences in PH-GRAM domains of myotubularins are suggested to confer different PI binding specificity and potentially compartment targeting [66]. For instance, the MTM1 PH-GRAM domain has highest affinity to $PI(3,5)P_2$ binding compared to other species, potentially necessary to mediate its translocation to late endosomes [67]. Most missense mutations in MTM1 as well as in other disease-causing myotubularins disrupt their signature core structure, clustering at the PH-GRAM or active site of the catalytic domain, and therefore disrupting catalytic activity. Additional mutations have been reported at the surface of MTM1, a globular protein, where they have been hypothesized to affect protein interactions [60]. In addition, myotubularin family members contain other functional domains characteristic to some of them, a PDZ binding site additionally mediating protein interactions, PH and FYVE domains involved in PI binding, a DENN (Differentially Expressed in Normal and Neoplastic Cells) domain to activate small RAB GTPases by acting as guanine-nucleotide exchange factors (GEF) [68], and a CC (coiled-coiled) domain mainly playing a role in homo- and heteromerization within the myotubularin family [60] (**Fig. 1-3**).

Homo- and heteromeric interactions within the myotubularin family are key to their regulation, generally controlling subcellular localization, substrate specificity and catalytic activity. An important regulatory mechanism specific to this family is the interaction between catalytically active and inactive myotubularins, reported in several studies where inactive myotubularins target active myotubularins to certain cellular membranes or enhance their catalytic activity [58, 60,69]. MTM1 has been reported to form heptamers in the presence of its substrate *in vitro*, resulting in an allosteric activation [70]. Moreover, interaction of MTM1 with inactive myotubularins MTMR10 [69] and MTMR12 [65] has been described. Whereas MTM1-MTMR10 complexes are functionally unstudied, MTM1-MTMR12 interaction has been suggested to be of prominent importance in skeletal muscle. Gupta *et al* [71] showed that, in zebrafish (*D. rerio*), depletion of MTMR12 phenocopied muscle function and histological hallmarks of MTM1 loss, and ablation of either MTM1 or MTMR12 resulted in reduced levels of the other complex member. Mutations in the domain that mediates their interaction led to the same phenotype, suggesting reciprocal roles in complex stabilization. Furthermore, myotubularins have been reported to have numerous interactors beyond their own family, mostly playing regulatory roles or acting as effector proteins. An example is the interaction of MTM1 with desmin [72], the main muscle-specific intermediate filament protein (see 1.3.3.3 section). Importantly, MTM1 has also been shown to bind with tissue specificity to proteins associated to other types of CNM: BIN1 [22] and SPEG (Striated Muscle Preferentially Expressed protein kinase) [8].

1.3.1.2. Myotubularin-related proteins in disease

In addition to XLCNM, other proteins from the myotubularin family have been linked to human diseases. Loss-of-function mutations in MTMR2, MTMR13 and MTMR5 lead to Charcot-Marie-Tooth (CMT) neuropathy type 4B1, 4B2 and 4B3, respectively, a group of demyelinating peripheral neuropathies that cause limb muscular atrophy [73–75]. MTMR5 and MTMR13 are catalytically inactive interactors of active phosphatase MTMR2 that modulate its subcellular localization and stabilize its activity. These three myotubularins are highly expressed in the peripheral nervous system, where MTMR2 has been shown to interact with light neurofilament (NFL), a

neuronal intermediate filament protein [60]. CMT 4B2 has been mechanistically linked to mTORC1 activation via interaction of the involved myotubularins with RAB35 [76,77] in Schwann cells, resulting in excessive axonal myelination. In turn, impaired myelination in CMT 4B3 is due to alteration of the process of axonal sorting [78], by which axons dictate which regions need to be myelinated [79]. Besides CMT neuropathies, MTMR2 and MTMR5, both with relatively high expression in testis, have been linked to defective spermatogenesis and infertility potentially via tissue-specific interactors [80]. Altogether, these studies evidence that ubiquitously expressed myotubularins cause tissue-specific diseases and highlight the relevance of heteromeric interactions. Myotubularins have also been associated with multifactorial conditions such as cancer, obesity, and Creutzfeldt-Jakob disease [60].

1.3.2. Myotubularin in membrane trafficking

Membrane trafficking is the fundamental transport mechanism defining membrane dynamics, thus being essential for multiple cellular functions. Finely-regulated membrane trafficking at distinct cellular compartments is key for maintaining cell homeostasis and function. MTM1 is involved in membrane trafficking routes at the PI(3)P-rich endosomal compartment and its depletion has been shown to disrupt endolysosomal homeostasis due to altered of membrane identities and trafficking.

Accumulation of the MTM1 substrate PI(3)P has been reported in multiple *in vivo* models of XLCNM. Dowling *et al* [81] observed 1.6-fold increased PI(3)P in zebrafish muscle in a study that linked the XLCNM phenotype to MTM1 catalytic activity *in vivo* for the first time. Since then, similar PI(3)P accumulations in cell-based and animal models of XLCNM have been described, including a 1.5 to 2-fold increase in MTM1 knockdown (KD) cultured cells [81–84], 1.7-fold increase in Mtm KD *D. melanogaster* cells [85], and 2-fold increase in yeast lacking the MTM1 homolog [66], among other examples. Few techniques provide quantitative and distribution data of PI pools, yet immunocytochemistry with antibodies or probes based on purified PI-binding protein domains offer semi-quantitative information. Overexpression of PI-binding domains in cells has alternatively been used to report quantity and localization of PI pools. However, this method is less optimal due to blockage of membrane trafficking by overexpressed PI-binding domains. Studies using these techniques [83,85,86] reported an endosomal accumulation of PI(3)P that colocalized with early, late and recycling endosomal markers RAB5, RAB7 and RAB11, respectively, with some variable observations between studies. Subsequent to endosomal PI(3)P accumulation, an enlargement of these compartments accompanied by PI(3)P effector protein accumulation is described in several studies [85,86]. Regarding other MTM1 substrates, increases of 1.6-fold in $PI(3,5)P_2$ have been reported in MTM1-depleted myoblasts [72]. The relevance of this PI species in defining XLCNM pathology is poorly investigated, partially due to the absence of reliable quantitative methods. Velichkova *et al* [85] provided evidence that $PI(3,5)P_2$ was unlikely to play a crucial role in XLCNM as depletion of PIKfyve homolog, which phosphorylates the 5' position of PI and PI(3)P, did not phenocopy Mtm loss in *D. melanogaster*-derived cellular models. Similar evidence was observed by Ketel *et al* [83] in MTM1-depleted HeLa cells. Studies that investigated other PI species [82,83,87] did not report changes in PI(4)P, $PI(3,4)P_2$ or $PI(4,5)P_2$.

Mechanistically, the roles of MTM1 in controlling membrane trafficking at endosomes have been described in two distinct contexts (**Fig. 1-2**). At early endosomes, MTM1 counteracts PI(3)P-synthesizing activity of VPS34

complex II (see section 1.5.2) by binding its VPS15 subunit [86]. Although more insights into the regulation of this kinase-phosphatase complex are needed, it is known that its formation inactivates MTM1 and prevents VPS34 complex II from RAB5 GTPase binding, as VPS15 interaction with MTM1 and endosomal RABs is mutually exclusive [82,86]. In this scenario, RAB GTPases are proposed to control PI(3)P synthesis and turnover by regulating activation and localization of these kinase-phosphatase complexes, as shown in some studies [88]. Inactivation of MTM1-VPS34 complex II pathway results in a blockage of early and late endosomal dynamics thus promoting accumulation of signaling receptors such as epidermal growth factor receptor (EGFR) at endosomes [82]. EGFR is well described to be predominantly sorted for lysosomal degradation rather than recycling to the plasma membrane [89]. Further mechanistic insights into MTM1 catalytic activity and its impact on endosomal trafficking were described in detail by Ketel *et al* [83] in a study showing that MTM1-mediated PI(3)P conversion is necessary for cargo exocytosis from endosomes. This occurs upon PI(3)P turnover and PI(4)P synthesis by sequential actions of MTM1 and PI4K2α, respectively, resulting in a conversion from PI(3)P-rich RAB5-positive sorting endosomes to PI(4)P-rich RAB11-positive recycling endosomes. This process is accompanied by release of PI(3)P effectors of the sorting nexin (SNX) family involved in endosomal sorting. PI(4)P-enriched exocytic vesicles then rapidly fuse the with the plasma membrane by recruitment and action of the exocyst, an octameric complex (EXOC1-8) that mediates vesicle tethering at the plasma membrane via direct interaction of its subunits Sec3 (EXOC1) and Exo70 (EXOC7) [90]. Accordingly, MTM1 depletion results in impaired transferrin receptor (TfR) exocytosis, a receptor that is well known to mainly undergo recycling, unlike EGFR [91]. Hence, decreased plasma membrane levels and a sub-plasma membrane accumulation of TfR in early and recycling endosomal compartments is observed in MTM1-depleted cells, similarly than for the adhesion protein β1-integrin. As expected from their roles in this exocytic pathway, depletion of PI4K2α or exocyst components lead to the same TfR and β1-integrin accumulation phenotypes [83].

1.3.3. Myotubularin in XLCNM pathogenesis

Due to its role in XLCNM pathogenesis, studies of MTM1 have been largely conducted in skeletal muscle *in vivo* and *in vitro* models, as well as patient-derived samples. Consequently, the multiple cellular functions of MTM1 have been frequently described in the context of muscle, where it plays important roles in development, maintenance, and function. Several pathomechanisms have been proposed for XLCNM, and the contribution of each of them to the disease phenotype is still under . In fact, it has been proposed that XLCNM may result from combinatorial and synergistic effects of several pathomechanisms, arising from the multiple functions of MTM1 in skeletal muscle. Whereas most of the proposed roles of MTM1 in XLCNM pathogenesis are briefly summarized in this section, the control of cell adhesions by MTM1 and its relevance to the disease phenotype, of special relevance in this thesis, are described in detail in section 1.4.

1.3.3.1. mTORC signaling

Mechanistic target of rapamycin complex 1 (mTORC1) is an heteromeric complex formed by serine/threonine protein kinase mTOR, regulatory-associated protein of mTOR (raptor) and mammalian lethal with SEC thirteen 8 (mLST8). mTORC1 is a key regulator of cell metabolism, proliferation, growth, and survival due to its capacity to integrate extra- and intracellular cues to modulate these essential processes via a variety of downstream

effectors. Primarily, these cues include extracellular inputs linked to growth factor, survival signaling and nutrient availability, and intracellular signals from cellular energy (ATP, oxygen) and stress (DNA damage) sensors, altogether converging in mTORC1 via multiple upstream regulators.

A more detailed description of its complex signaling network would be the following: in response to extracellular stimuli, the activation of plasma membrane receptors triggers downstream signaling cascades that lead to tuberous sclerosis complex (TSC) complex inhibition. In the case of receptor tyrosine kinase (RTK) stimulation, this cascade generally involves class I PI3K-mediated synthesis of $PI(3,4,5)P_3$ (see section 1.5.1) and AKT activation. In turn, intracellular cues directly inhibit TSC complex via sensor proteins and their effectors. TSC inhibition results in mTORC1 activation and localization at the surface of late endosomes/lysosomes which migrate to the cell periphery, a phenomenon shown to be necessary for the activation process [92]. Active mTORC1 complex regulates multiple downstream signaling and transcription factor effectors such as p70S6 kinase (S6K), Unc-51 like autophagy activating kinase (ULK), or transcription factor EB (TFEB) that promote protein synthesis, energy metabolism and lipid biosynthesis, and inhibit lysosome biogenesis and autophagy [93,94]. In agreement with its role in stimulating anabolic metabolism at a cellular level, mTORC1 has been shown to promote hypertrophy and survival in skeletal muscle via PI3K-AKT-S6K and other AKT-dependent pathways [95], as well as being essential to maintain muscle mass [96].

Several studies have reported altered mTORC1 signaling in MTM1-depleted models, and associated it with XLCNM pathogenesis. Hyperactivation of mTORC1 due to increased upstream signaling has been reported in symptomatic (4-week-old) XLCNM mice muscle but not in presymptomatic (2-week-old) mice [97,98]. It has been proposed that mTORC1 hyperactivation is a compensatory mechanism secondary to muscle atrophy rather than an early pathogenic mechanism, which eventually leads to downstream pathway alterations that negatively contribute to the disease phenotype [97]. Conversely, other studies in mouse models have proposed that mTORC1 hyperactivation is independent of upstream regulators such as AKT, suggesting that MTM1 activates mTORC1 via a nutrient-independent mechanism [98]. In both scenarios, enhanced mTORC1 signaling at late disease stages leads to alterations in downstream processes including autophagy and proteasome degradation pathways [72,97–99]. Intriguingly, an opposite effect on mTORC1 signaling has been observed in MTM1-depleted cell-based models. In HeLa cells and differentiated muscle cell lines, MTM1 loss decreased AKT, mTORC1, and downstream effector activation upon growth factor stimulation, whereas MTM1 overexpression had the opposite effect [84]. In this system, mTORC1 hypoactivation led to enhanced pro-apoptotic signaling, postulated as a potential XLCNM pathogenic mechanism. The discrepancy between cell-based studies and animal models regarding the activation status of mTORC1 is proposed to be due to differential compensatory mechanisms affecting this complex signaling network [97], and evidences the need for further research on the potential roles of mTORC1 signaling in XLCNM pathology.

1.3.3.2. Autophagy and degradative pathways

In mammalian cells, protein degradation is mediated by two distinct catabolic processes: autophagy and lysosomal degradation, and the ubiquitin-proteasome system (UPS). Autophagy is the process by which cells degrade cytoplasmic components such as organelles, aggregates of misfolded proteins, or pathogens in order to

avoid cytotoxicity, promote turnover or obtain sources of energy; it is triggered by stimuli but also occurs at basal level [100,101]. Mechanistically, autophagy is initiated upon ULK activation followed by VPS34-mediated PI(3)P synthesis at the phagophore membrane, an ER-derived organelle that engulfs cytoplasmic content and becomes an autophagosome upon maturation, a point in which it fuses with lysosomes containing hydrolytic enzymes to accomplish degradation [102]. This process is sequentially regulated by a cascade of autophagy-related proteins (ATG) [101]. UPS, in turn, mediates specific turnover of defective or misfolded proteins by targeting them to the proteasome, an enzymatic complex that mediates ATP-dependent degradation. Proteasomal targeting occurs by polyubiquitination of defective proteins by action of E3-ubiquitin ligases [103].

These two proteolytic mechanisms have been involved in the maintenance and regeneration of skeletal muscle, one of the most metabolically active tissues that requires balanced catabolic-anabolic homeostasis and efficient turnover of damaged components. Both excessive and defective autophagy and UPS-mediated degradation have been reported to impact muscle by decreasing mass and leading to myopathy-triggering accumulation of abnormal molecules, suggesting that stable basal levels of autophagy and UPS-mediated degradation are necessary to maintain muscle mass and integrity [100,101,103].

Due to its PI(3)P-metabolizing activity, MTM1 has been postulated as a potential autophagy modulator, possibly reducing autophagy initiation due to PI(3)P dephosphorylation. However, most studies have described the link to autophagy in relation to mTORC1: hyperactivation of mTORC1 in symptomatic XLCNM mouse models inhibits autophagy initiation via ULK, as well as progression due to decreased lysosomal biogenesis via the transcription factor TFEB [97,98]. Consequently, a muscle-specific accumulation of autophagosomes and proteins degraded via this pathway is observed in Mtm1 KO mice [97,98]. Some of these phenotypes are also observed at earlier disease stages, suggesting an autophagy alteration could precede mTORC1 dysregulation and be exacerbated at late stages by its hyperactivation [97]. Overall, it is thought that defective autophagy partially contributes to XLCNM pathogenesis, although deletion of key autophagy proteins (ATG5, ATG7) leads to impaired muscle strength and atrophy at a later onset than MTM1 depletion, suggesting other pathogenic mechanisms must be involved [104,105]. As with autophagy impairment, alterations in UPS-mediated degradation have been reported in MTM1-depleted models, with an important impact on the intermediate filament cytoskeleton (see section 1.3.3.3).

1.3.3.3. Intermediate filament cytoskeleton

The intermediate filament cytoskeleton is mainly responsible for maintaining structural and mechanical integrity of cells, as well as being involved in organelle positioning and signaling. Desmin is the most abundant intermediate filament protein in skeletal muscle, where it forms a scaffold for contractile machinery and links it to other cellular compartments, defining their subcellular localization [106].

MTM1 plays a role in the regulation of the intermediate filament cytoskeleton by directly binding desmin [72,98]. This interaction, which is independent of MTM1 phosphatase activity, has been suggested to be relevant for desmin assembly and stability, demonstrated by filament disorganization and aggregation upon MTM1 loss [72]. In a later study, Gavriilidis *et al* [107] showed MTM1 to play a role in misfolded desmin filament degradation via association with UPS proteins. Mutations in MTM1 leading to a destabilization of the interaction with desmin have been reported in XLCNM patients. Furthermore, the association of desmin mutations to human myopathies

with common traits to XLCNM, and the phenotype of desmin KO mouse models evidence its relevance in maintaining muscle architecture and function [106,108].

1.3.3.4. Mitochondrial function

Mitochondria are necessary for oxidative respiration and thus crucial for cellular energy supply. Skeletal muscle is a tissue with a high energetic demand that mainly relies on mitochondrial function, to such an extent that their subcellular localization in muscle fibers is highly specific. In general, direct or indirect mitochondrial alterations affecting their morphology, distribution or function will impact skeletal muscle homeostasis [109].

MTM1 has been reported to influence mitochondrial localization, morphology, and activity in muscle cell lines [99] and muscle sections [34,98]. This has been postulated to lead to decreased ATP levels in muscle and promote hypotonia in XLCNM. Despite the known roles of intermediate filaments in mitochondrial organization [110,111], MTM1 mutations induce perinuclear mitochondrial redistribution independently of their effect on desmin aggregation. Several studies [97,98] report an accumulation of dysfunctional mitochondria linked to autophagy impairment, suggesting a defective autophagy-mediated mitochondrial degradation (mitophagy).

1.3.3.5. Triad organization and excitation-contraction coupling

Skeletal muscle is a highly specialized tissue whose composition and organization reflect the complexity of its main function: muscle contraction. The two key components involved in this process are a highly organized contractile apparatus and the excitation-contraction coupling (ECC) system. Whereas the contractile machinery occupies most of the myotube cytoplasm, forcing a peripheral nuclear and organellar localization, ECC takes place at the triad, a structure composed of a plasma membrane invagination named transverse (T)-tubule in close contact with ER cisternae. Upon depolarization, plasma membrane voltage-gated channels induce opening of ER Ca^{2+} channels that release a flux necessary for the activation of the contractile machinery [28,112].

Profound morphological and functional abnormalities in the triad have been reported in XLCNM patients and recapitulated in animal models, which suggests that MTM1 is essential for its biogenesis and/or remodeling [34,35,81,113]. Among these alterations are a decreased number and disorganized triad pattern accompanied by decreased expression of key ECC channels, functionally leading to altered depolarization and Ca^{2+} dynamics. Such defects offer an explanation to hypotonia in XLCNM, although the presence of triadic morphological abnormalities in presymptomatic mouse models suggests a role of MTM1 in an earlier pathogenic mechanism [113,114]. The fact that loss-of-function mutations in RYR1 lead to autosomal CNM [30,31] further supports the importance of triad organization and function in CNM pathogenesis, although RYR1-related CNM patients and mouse models generally display milder phenotypes [7].

1.4. Cell adhesions and their relevance in XLCNM

Cell adhesions are complex structures at the cell surface that mediate their interaction and attachment to other cells or to their substrate, an extracellular matrix (ECM) of variable composition. Accordingly, cell adhesions are classified as cell-cell adhesions or cell-ECM adhesions, both playing crucial structural and functional roles in the maintenance of cell and tissue homeostasis. Cell adhesions provide structural cohesion and integrity to solid tissues and allow their morphogenesis by mediating cell migration, a process of major importance in fluid tissues

and other migratory cell types. Simultaneously, cell adhesions are actively involved in signaling, thereby acting as important sensors for environmental cues with impact on a variety of pathways [115,116].

The main cell-ECM adhesions by which cells attach to their substrate and sense their environment are focal adhesions (FAs). FAs are the most studied type of integrin adhesion complexes (IACs), which mediate the process of cell spreading and migration and serve as anchoring points to maintain morphology in immobile cells, while being involved in signaling. This defines them as dynamic structural and regulatory mechanosensitive components that connect the ECM to the actin cytoskeleton via a complex assembly of transmembrane and intracellular proteins [115,116].

1.4.1 Focal adhesion architecture

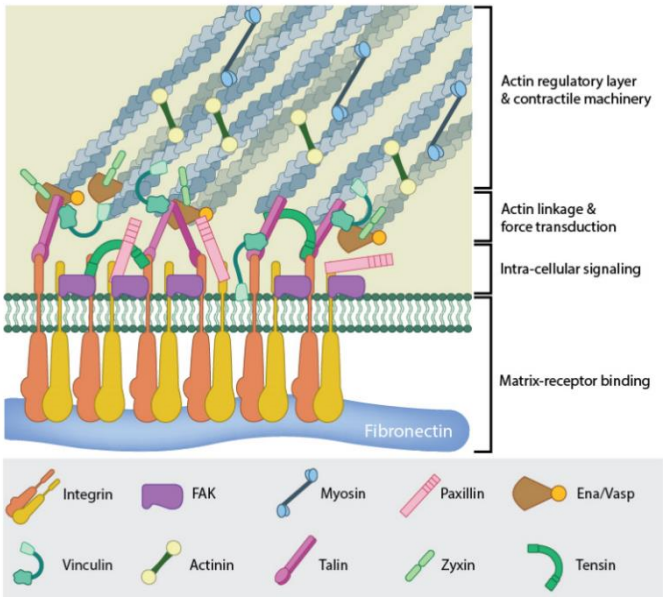

Figure 1-4. Composition and functional structure of mature FAs [266]**.** The theoretical organization and protein-protein interactions as shown are based upon references.

FAs are composed of transmembrane heterodimeric complexes of integrin α- and β-subunits that bind ECM proteins such as collagens, laminins, fibronectins or vitronectins via their extracellular domains. In mammals, 18 α- and 8 β-subunits of integrins have been described, with 24 heterodimeric combinations defined by cell type and ECM composition, each associated to certain signaling cascades or cell functions. The intracellular tail of integrins interacts with an assembly of around 150 proteins organized in functional layers, with variable composition depending on FA maturity [117]. As described by Kanachanawong *et al* [117] and Martino *et al* [118], a first layer of direct integrin interactors is involved in signaling and composed of proteins such as focal adhesion kinase (FAK) and paxillin. During mechanical stimulation, FAK initiates mechanotransduction signaling upon recruitment and activation at early FAs. Paxillin similarly integrates mechanical and growth factor signaling and is regulated by FAK and vinculin. A second functional layer is formed by proteins that mediate actin linkage and force transduction, including talin and kindlin, mechanosensitive proteins that directly activate and link integrins to actin, and vinculin, recruited and activated by talin to bind and modulate the contractile machinery in a force-dependent manner. Proteins involved in actin regulation and the contractile machinery form a third functional layer, where zyxin, actinin and myosin can be found. Zyxin influences actin dynamics by accumulating at and stabilizing adhesions in a tension-dependent manner, thereby becoming a distinctive marker of mature FAs [119]. Actinin and myosin are essential components of the actin filament contractile machinery (**Fig. 1-4**).

1.4.2 Adhesion dynamics and cell migration

FAs are highly dynamic structures exposed to cycles of assembly and disassembly due to their roles in cell spreading, motility, and microenvironment sensing. In general, FA dynamics implies internalization of integrins from the plasma membrane accompanied by intracellular protein complex disassembly, followed by integrin recycling during FA assembly. Together with cytoskeletal reorganization, FA dynamics is core to cell migration, defined as the directed displacement of cells on a matrix upon internal or external cues. In multicellular organisms, migration is essential during development, tissue homeostasis and regeneration, and immune system function [115,116,120]. Additionally, adhesion turnover occurs in non-migrating senescent cells such as those that are part of adult solid tissues, where adhesions maintain tissue integrity [121]. Generally, adhesion turnover rate determines the formation of transient or stable adhesions, respectively typical of migratory or senescent tissue-forming cells.

Despite FA dynamics and integrin cycling being tightly correlated, they are described here separately with a special focus on the latter.

1.4.2.1 Focal adhesions dynamics

FA formation takes place at the lamellipodium, a region where spreading and migrating cells extend their leading edge [115]. Nascent adhesions are small, punctate, and generally short-lived structures already containing integrins and some signaling and actin linkage proteins [120]. Actin polymerization and particularly branched actin is required for FA assembly, yet the mechanism by which this process is mediated is still debated. Some nascent adhesions at the lamellipodium gradually mature to become larger and elongated, leading to the co-existence of various FA sizes in a cell [115]. Besides the enlargement via clustering and FA protein recruitment, maturation is accompanied by changes in FA signaling properties, which in turn modulate their maturation by regulating actin polymerization. Mechanical forces as well contribute to this self-regulatory process [116]. FAs can further mature to form fibrillar adhesions, large long-lived structures associated with actin filament bundles that play an active role in controlling ECM organization while maintaining a similar composition as nascent and mature FAs [120]. FA dynamics and morphology generally vary in a cell type-specific manner due to differences in their composition or actin cytoskeleton. This variation is exemplified by small, short-lived adhesions in highly migratory cells like leukocytes in contrast to stable fibrillar adhesions in senescent cells [116,120].

Several mechanisms have been proposed to mediate FA disassembly, which is generally triggered by a series of phosphorylation events at the signaling layer of FAs accompanied by changes in cytoskeletal tension. FAK and kindlin play a role in disrupting FA maturation and enhancing disassembly by decreasing actomyosin contractility leading to FA destabilization [116]. The same pathway has been proposed to modulate paxillin and RHO GTPases, key actin regulators, to promote disassembly [122,123]. Moreover, the Ca^{2+}-dependent protease calpain has also been involved in FA disassembly due to its proteolytic action on talin, FAK and β3-integrin, affecting FA structural and signaling properties that promote further destabilization [124–126]. Additionally, microtubules are proposed to disassemble FAs via a FAK- and dynamin-mediated pathway, as shown by resumed FA disassembly and microtubule regrowth after nocodazole washout [127], a drug that inhibits microtubule polymerization [128]. The fact that dynamin is a key endocytic protein evidences a link between microtubule-mediated disassembly and integrin

internalization via endocytosis (see section 1.4.2.2.1). Alternatively, it has been suggested that microtubules deliver signaling molecules to destabilize adhesions as well as vesicles such as lysosomes containing hydrolytic enzymes that contribute to integrin degradation [129], in a process known as lysosomal exocytosis [130]. This hypothesis is supported by the fact that blockage of motor protein kinesin promotes growth of existing adhesions [131] and ECM degradation occurs at FA sites.

1.4.2.2. Integrin trafficking

Integrin cycling is a steady process in cells that contributes to continuous environmental sensing for adhesion and migratory cues [132]. Like FA assembly and disassembly, integrin internalization generally takes place at the rear of cells and recycling occurs at the leading edge during cell migration, even though other directed long-distance trafficking routes have been described [133]. In cells, integrin heterodimers co-exist in an equilibrium of three possible conformations modulated by extracellular and intracellular signaling events. These consist of (i) an inactive, bent and closed conformation with low affinity to ECM ligands, (ii) a primed, extended and closed conformation with low ligand affinity and (iii) an active, extended and open conformation with ECM ligand affinity [134]. Although active and inactive integrins share 64% of interactome similarity [135], differences in their trafficking routes have been reported.

1.4.2.2.1. Integrin internalization: clathrin-mediated endocytosis

Internalization of integrins has been described to mainly take place via clathrin-dependent mechanisms, although alternative clathrin-independent routes including micropinocytosis, caveolae, and clathrin-independent carriers (CLICs) have also been reported [132,133]. Clathrin-mediated endocytosis (CME) is the major pathway for transmembrane protein internalization in eukaryotic cells. CME is a sequential process of small vesicle formation from the plasma membrane that involves a spatiotemporally organized recruitment of proteins accompanied by membrane PI composition changes [132,136,137]. CME is initiated by the coincidence of a cargo and a PI(4,5)P_2 accumulation in a PI(4)P-rich plasma membrane [48], which altogether recruit adaptor protein complex 2 (AP-2), an heterotetrameric complex formed by two large (α, β2), a medium (μ2) and a small (σ2) subunit [138]. To confer cargo selectivity, further cargo-specific adaptors and scaffolding proteins that assist nucleation process are recruited, including intersectin 1 (ITSN1) [139] (**Fig. 1-5 A**). These eventually shift the equilibrium of AP-2 towards its open conformation, thereby promoting clathrin coat assembly. AP-2 and cargo-specific adaptors contribute to the recruitment of clathrin triskelia, structures formed by three clathrin heavy and three clathrin light chains. Then, membrane curvature is induced by membrane remodeling proteins leading to the formation of a clathrin-coated pit (CCP) (**Fig. 1-5 B)**. These include BAR-domain proteins, membrane curvature-sensitive and actin-binding proteins that act at earlier low-curvature stages of CCP formation, or at late high-curvature

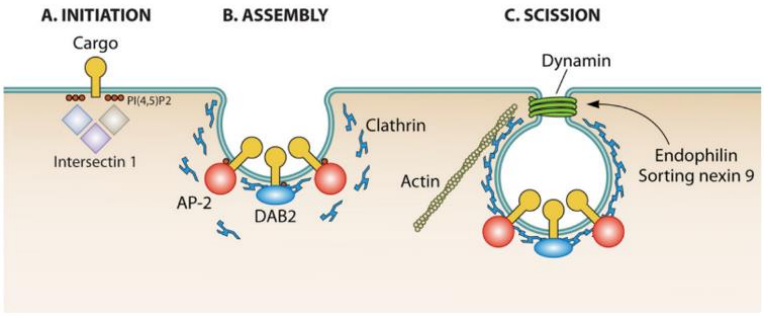

Figure 1-5. Schematic representation of CME initiation, assembly, and scission steps. Adapted figure [267]

stages, such as BIN1 or endophilin [140]. Membrane remodeling during CME is additionally induced by epsins, which bind PI(4,5)P_2-rich regions at early curvature stages, and by clathrin lattices. Prior to scission, mature CCPs undergo constriction via the mentioned BAR-domain proteins including SNX9, which facilitates recruitment of dynamin. Dynamin associates with the constricted CCP neck to mediate membrane scission resulting in clathrin-coated vesicle (CCV) formation [14] (**Fig. 1-5 C**).

A sequential conversion of PIs has been shown to be essential to orchestrate CME [136,137]. Whereas PI(4,5)P_2 is necessary for initiation, it is believed to decrease at CCP during maturation via action of 5-phosphatases such as synaptojanin [141]. Resulting PI(4)P, or plasma membrane PI(4)P, is the substrate of class II phosphatidylinositol 3-kinase C2α (PI3KC2α) which synthesizes a pool of PI(3,4)P_2 at CCPs, reaching its peak prior to scission [50] (see section 1.5.3.3.1). This pool mediates recruitment of key constriction proteins SNX9 and SNX18, BAR-domain proteins that promote CCP maturation, and potentially clathrin uncoating proteins after CCV formation [50,142]. 4-phosphatases INPP4A and INPP4B later act on this PI(3,4)P_2 pool to confer an endosomal PI(3)P identity to vesicles [143] (**Fig. 1-2**).

Cargo-specific adaptors for integrin endocytosis have been described, among which are NUMB and DAB2, which bind the intracellular tail of β1-integrin via a conserved motif [144–146]. DAB2 also binds clathrin, PI(4,5)P_2 and CME scaffolding protein ITSN1 and its depletion leads to surface β1-integrin accumulation and impaired migration, without affecting internalization of other cargoes such as TfR [144,147,148]. Additionally, microtubules have been shown to promote recruitment of some adaptors like DAB2 at CCPs in a FAK-dependent signaling pathway [145]. Conversely, some α-integrin subunits have recognition motifs for AP-2 [149]. In addition to adaptors, small RAB GTPases such as RAB21, RAB25, RAB34 and RAB35 are involved in CME of integrins, in some cases with subunit specificity. Other factors such as mechanical force and ECM composition, as well as certain plasma membrane signaling pathways, further contribute to selective integrin internalization [132]. Regarding integrin conformational status, both active and inactive integrins have been described to share CME as a main internalization pathway, yet active β1-integrin is reported to be more efficiently endocytosed [150].

1.4.2.2.2. Endosomal trafficking of integrins

Upon internalization, integrins localize at RAB5- and EEA1-positive early endosomal compartment, where they can be maintained in active conformation by bound signaling FA components such as FAK or talin [132,150]. At sorting endosomes, most integrins are trafficked into a RAB11-positive perinuclear recycling compartment for slow recycling, or directly to the plasma membrane via a fast-recycling route. A minor proportion is sorted into RAB7-positive late endosomes for lysosomal degradation, implying that integrins are long-lived proteins with a half-life of 12-24h [151] (**Fig. 1-6**). Integrin fate is regulated at endosomes by diverse intracellular mechanisms and modulated by their ECM ligands in a context-specific manner. SNX17 is one of the main mediators of this process by promoting recycling [152] in co-operation with other protein complexes [132].

1.4.2.2.3. Integrin recycling

After endocytic sorting, most integrins are targeted back to the plasma membrane in a process known as recycling. Integrins undergo recycling via several pathways, which are mostly defined by specific integrin subunits

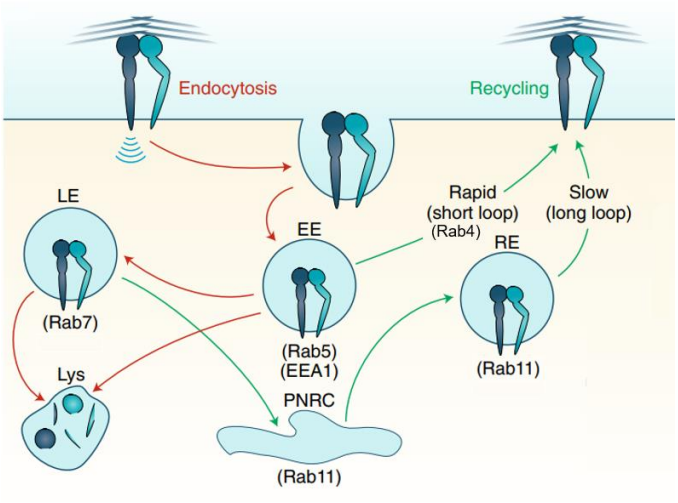

Figure 1-6. Integrin trafficking pathways. LE, late endosome; Lys, lysosome; EE, early endosome; PNRC, perinuclear recycling compartment; RE, recycling endosome. Adapted figure [132].

and different RAB GTPases and adaptors. The best characterized integrin recycling routes are a short-loop pathway and a long-loop pathway (**Fig. 1-6**). The first is especially relevant in growth factor-stimulated cells and has mainly been studied in integrin recycling at lamellipodia of migrating cells. It implies direct recycling of integrins from RAB5-positive endosomes immediately after their endocytosis, via recruitment of RAB4 by growth factor-initiated pathways [133,153]. Conversely, the long-loop pathway implies trafficking of integrins from RAB5-positive endosomes to the RAB11-positive perinuclear recycling compartment, and then to the plasma membrane. Both RAB11 activity and MTM1-mediated PI conversion (see section 1.3.2) are involved in this route. Although long-loop recycling is common to other cargoes such as TfR [154], RAB21 and RAB11 interactors selectively promote integrin trafficking to the plasma membrane while having no effects on other receptors [133,153]. Besides the two described pathways, other less-characterized integrin recycling routes include RAB25-, RAB13- and RAB1A-mediated recycling via various mechanisms in several migrating cell types [133].

The activation status of integrins influences their preferential recycling routes, as it has been reported for β1-integrin in a study by Arjornen *et al* [150]. Whereas inactive integrins tend to undergo fast recycling, integrins in active conformation are targeted into the slow-recycling pathway [134,150]. This might induce ligand dissociation or degradation by later trafficking to acidic RAB7-positive late endosomal and lysosomal compartments [134,150], from which a direct recycling route has also been reported in cancer cells [155]. Conversely, a rapid inactive integrin turnover might facilitate adhesion formation by providing readily available receptors for ECM binding. Differential trafficking of active and inactive integrins results in predominant localization of inactive integrins at the cell surface due to their rapid turnover, and higher abundance of activated integrins at intracellular compartments [150].

1.4.3. Integrin adhesions in skeletal muscle

In skeletal muscle, the structural function of cell adhesions acquires special relevance due to the mechanical stress that this organ is exposed to. However, adhesions do not only preserve structural integrity of myofibers, but additionally play important roles in muscle development and regeneration. α7β1-integrin is the most abundant integrin dimer in skeletal muscle [156].

Studies on skeletal muscle-specific β1-integrin KO mice models, which die perinatally with decreased muscle mass, evidenced that integrin adhesions are necessary for myoblast fusion during development [157]. Interestingly, integrin adhesions play a role in peripheral positioning of myotube nuclei, which occurs during development and

is essential for muscle function. This occurs by promoting extracellular fibronectin accumulation and activating a FAK-dependent signaling pathway that controls nuclei position downstream of α5-integrin [158]. In adult muscle, integrin adhesions are essential at two highly specialized skeletal muscle-specific adhesions: costameres and myotendinous junctions (MTJs). Costameres are specific focal adhesions that anchor the intracellular contractile machinery to the ECM, thereby determining the architecture of sarcomeres [159], the smallest contractile units of skeletal muscle. Accordingly, β1-integrin is necessary for sarcomere assembly [157] and maintenance, as shown by a progressive loss of muscle function due to defective sarcomere architecture in *D. melanogaster* [160] and vertebrate models [161]. MTJs are attachments between muscle fibers and tendons, where intense mechanical forces are transmitted [159]. Vertebrate and invertebrate models lacking integrin adhesions show defective MTJ formation and consequent muscle detachment [157]. Besides β1-integrin, muscle-specific depletion of other adhesion proteins such as talin [162]t, integrin-linked kinase (ILK) [163,164], and α7-integrin [165] leads to myopathy phenotypes mainly linked to defects in costameres and MTJs formation and/or maintenance. Additionally, the role of integrins as signaling molecules is also relevant in skeletal muscle, as shown by Wang *et al* [164] in a study that uncovered an interaction and metabolic modulation of insulin receptor by β1-integrin. Furthermore, β1-integrin plays a role in skeletal muscle regeneration by maintaining homeostasis and promoting expansion and self-renewal of skeletal muscle stem cells [166]. In this study, increasing β1-integrin activity enhanced regeneration after muscle injury as well as in mouse models of dystrophy. Similarly, β2-integrin has been involved in muscle hypertrophy by enhancing stem cell proliferation and muscle differentiation [167].

Despite the importance of integrin-mediated adhesions in skeletal muscle, their trafficking pathways *in vivo* remain poorly understood, partially due to the technical challenges of studying these processes in animal models. Some studies have shown a similar localization of the recycling compartment at the perinuclear region in myotubes than in non-muscular cells [168]. A study in *D. melanogaster* muscle revealed that CME-mediated turnover of adhesion components is necessary for maintenance of MTJs, and that RAB5 is involved in the regulation of this process [121]. In general, it is agreed that alterations in trafficking pathways leading to abnormal adhesion protein localization have an impact on muscle development and maintenance. Few studies that shed light on adhesion protein trafficking in muscle *in vivo* evidenced a relevant role of MTM1 in this process.

1.4.3.1 Integrin adhesions in XLCNM pathogenesis

Cell adhesion defects have been reported in several animal and cell-based models of XLCNM, and mechanistically linked to a role of MTM1 in endosomal exocytosis. The involvement of MTM1 in cell adhesions was initially described in *D. melanogaster* models [169] and recently characterized in XLCNM mouse models [26]. However, the histological observation of hypotrophic and round muscle fibers as well as increased ECM in muscle from XLCNM patients [4] already suggested an adhesion defect upon MTM1 loss. These findings have been recapitulated in MTM1 KO mouse muscle tissue [26], which as well displays abnormally internalized and aggregated β1-integrin at the endosomal compartment, a similar distribution as observed in XLCNM patient-derived myofibers [169169]. Decreased FAK activation accompanied by decreased β1-integrin protein levels with unaffected transcription uncover alterations in FAs in these models [26]. A study by Ribeiro *et al* [169] evidenced a key role of MTM1 in muscle maintenance and remodeling in XLCNM muscle-specific *D. melanogaster* models. Interestingly, complete abrogation or phosphatase inactivation of *mtm*, the fly homolog of human MTM1/MTMR2, leads to lethality. In

these models, muscle detachment due to mislocalized βPS-integrin, the fly homolog of β-integrins, is observed at a developmental stage when its localization at MTJs and costameres is indispensable. Additionally, βPS-integrin but not other adhesion proteins such as α-integrin and talin is intracellularly accumulated at early and late endosomal compartments, suggesting a specific role of MTM1 in β1-integrin trafficking. These adhesion defects were independent of alterations in T-tubule organization. The same study reported normal myogenesis and βPS-integrin localization at earlier developmental stages as shown for XLCNM mouse models [170], suggestive of a differential regulation throughout development. Despite autophagy having been reported to play a role in cell adhesion remodeling, muscle-specific autophagy abrogation by depletion of one of its main regulators (ATG1) did not rescue the adhesion phenotypes in *D. melanogaster* models [169].

Studies on cell-based systems have further elucidated adhesion defects in XLCNM. Intracellular β1-integrin accumulations have been reported in XLCNM patient-derived fibroblasts and MTM1-depleted HeLa cells, where they colocalized with TfR, RAB7 and partially RAB5, as similarly observed in primary MTM1 KO mouse-derived myoblasts [26,83].The latter display impaired adhesion and migration on a laminin matrix associated with decreased myotube differentiation [26]. Likewise, immune cells derived from *mtm*-depleted *D. melanogaster* display impaired migration to wounds, potentially secondary to defective plasma membrane remodeling [85]. Altogether, these studies evidence the importance of MTM1 in the regulation of integrin adhesions in skeletal muscle, thereby postulating defective adhesions upon MTM1 loss as a relevant XLCNM pathogenic mechanism.

1.5 Phosphatidylinositol 3-kinases

Phosphatidylinositol 3-kinases (PI3K) are a family of lipid kinases that phosphorylate the 3' position of the inositol ring of PI (**Fig. 1-1**), therefore synthesizing PI-3-phosphates, and play important roles in signal transduction and membrane trafficking. The PI3K family is subdivided in three classes according to their structural features, regulation, and functions. All PI3K isoforms share a PI3K core domain composed of kinase, helical and C2 domains, and sensitivity to pan-inhibitor wortmannin [171,172], although class II PI3Ks are reportedly less sensitive to it [173]. Due to the link between PI3KC2β and XLCNM [42], revealed by the rescue of the disease phenotype upon genetic ablation of PI3KC2β, this section will focus on class II PI3K and only briefly present class I and class III PI3Ks.

1.5.1 Class I PI3K

Class I PI3Ks are the most widely characterized group of PI3K. They act as heterodimers of a catalytic subunit (p110) and a regulatory subunit, which defines a sub-classification into class IA (p110α, β, δ) and class I B (p110γ) [171]. Class I PI3Ks act at the plasma membrane as signal transductors by phosphorylating $PI(4,5)P_2$ upon RTKs, G protein-coupled receptors or small GTPase stimulation, thereby producing $PI(3,4,5)P_3$. $PI(3,4,5)P_3$ or $PI(3,4)P_2$, which results from action of 5-phosphatases. These PI products can be bound by PH-domain-containing protein effectors triggering cascades that regulate a variety of cellular functions such as cell migration, nutrient sensing or metabolism [174,175]. The 3-phosphatase PTEN in turn regulates cellular levels of $PI(3,4,5)P_3$ and $PI(3,4)P_2$ by turnover into $PI(4,5)P_2$ or PI(4)P, respectively [176] (**Fig. 1-1**).

Substrate specificity of PI3Ks is mainly determined by specific residues at an activation loop of the kinase domain, which mediates affinity to certain inositol head groups. There, class I PI3Ks contain two basic regions that contact the two phosphate groups of $PI(4,5)P_2$, implying a preferential synthesis of $PI(3,4,5)P_3$ [177]. Independently of their catalytic activity, class I PI3Ks also act as scaffolding proteins for complex formation [178].

Class I PI3Ks have been broadly studied in the field of cancer research due to their oncogenic activity upon gain-of-function mutations, especially in the p110α subunit [179]. Together with downstream pathway alterations such as in AKT or mTORC1, class I PI3K mutations have been reported in numerous cancer types and consequently been targeted by anti-cancer therapies [180]. In the recent years, other diseases linked to class I PI3Ks have been described, such as overgrowth and immunodeficiency syndromes [171].

1.5.2 Class III PI3K

The class III PI3K sub-family is only comprised of vacuolar protein sorting 34 (VPS34), which catalyzes PI(3)P synthesis and complexes with beclin 1, VPS15 and either ATG14 to form VPS34 complex I or UVRAG to form complex II [171]. Specificity for PI(3)P synthesis is defined by absence of basic residue stretches at the activation loop of the kinase domain, allowing contacts only with the non-phosphorylated PI head group [177]. Complex I is involved in the production of a PI(3)P pool at the ER that triggers phagophore initiation, eventually leading to the formation of autophagosomes, the organelles mediating autophagy. In turn, complex II produces endosomal PI(3)P (see section 1.3.2) and promotes autophagosome-lysosome fusion in late autophagy (**Fig. 1-2**). In many tissues, VPS34 is the main source of endosomal PI(3)P, accounting for up to 65% of total levels in mouse embryonic fibroblasts [181]. Both VPS34 complexes are highly regulated by upstream growth factor, nutrient-sensing and proliferative pathways such as AKT, mTORC1 and cyclin-dependent kinases [182,183].

Unlike class I PI3K, VPS34 has not been linked to human disease, potentially due to embryonic lethality, as observed in mouse models [184]. Specific VPS34 inhibitors have been developed and used as a tool to decipher its cellular functions and chemically modulate processes such as autophagy [185].

1.5.3 Class II PI3K

Class II PI3K are the least characterized PI3K sub-family and new insights into their structure, regulation and functions have been described in recent years. In vertebrates, class II PI3Ks comprise the ubiquitous isoforms PI3KC2α and PI3KC2β as well as the liver-specific PI3KC2γ, whereas invertebrates such as *D. melanogaster* only express one isoform (Pi3k68d). Specific class II PI3K inhibitors have not been developed to date [186].

1.5.3.1 Structure and regulation

Structurally, class II PI3K share a C-terminal PX domain, an additional C2 domain, and a mostly unstructured N-terminal region containing a RAS-binding domain (RBD) (**Fig. 1-7**). These domains mediate interaction with other proteins and lipids to regulate their activation and localization. The C-terminal PX and C2 domains play an important self-regulatory role by blocking the catalytic domain in solution and releasing it upon membrane binding, inducing a large-scale conformational rearrangement that results in increased kinase activity [187,188]. This mechanism was described in PI3KC2α and likely occurring in the β and γ isoforms. The relevance of this auto-

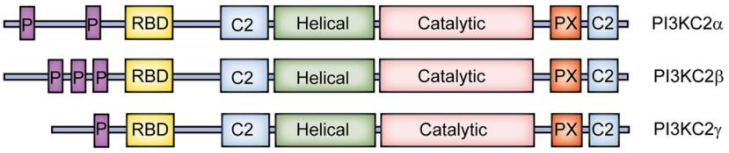

Figure 1-7. Human class II PI3Ks: protein domain organization [268]**.** Scaled representation according to amino acid length.

inhibitory mechanism partly lies in the fact that, unlike class I and III, no regulatory subunits of class II PI3K have been described, suggesting the relevance of their protein and PI interactions for their modulation. Membrane binding in this self-regulatory mechanism is possible due to the capacity of C2 and PX domains to bind $PI(4,5)P_2$ [189]. PI binding also contributes to class II PI3Ks localization at certain compartments and potentially to define their lipid substrates, although detailed description of these interactions requires further study [172]. The regulatory relevance of the unstructured N-terminal region is exemplified in isoforms α and β by increased enzymatic activity upon direct interaction with clathrin [190,191], thereby establishing a link to the role of PI3KC2α in CME [50]. In PI3KC2β, the same region further associates with ITSN1 via a proline-rich (PxxP) stretch [192,193] as well as with the mTORC1 subunit raptor [51]. Post-translational modifications at the unstructured N-terminal region of PI3KC2β further control its function by inducing cytoplasmic sequestration by 14-3-3 proteins [51,194]. Few interactions with small GTPases via the RBD domain have been described to date for class II PI3Ks: the RBD of PI3KC2β has been shown to interact with the small GTPase RAB7, required for PI3KC2β localization to late endosomes/lysosomes upon serum-starved conditions, where it regulates mTORC1 signaling [194]. Similarly, RAB5 binding to the RBD domain of PI3KC2γ promotes recruitment to early endosomes, where it controls insulin signaling [195].

1.5.3.2 Substrate specificity

Substrate specificity of class II PI3Ks has been a recent subject of study and debate, partially due to the difficulties in the detection of short-lived $PI(3,4)P_2$ *in cellulo* [176]. Despite being structurally defined as $PI(3,4)P_2$-synthesizing enzymes due to the presence of a 4-phosphate-binding basic residue stretch at the activation loop of their kinase domain [196], *in cellulo* data suggests that at least PI3KC2α also phosphorylates PI depending on its availability at different cellular compartments [197,198]. Consequently, both PI(3)P and $PI(3,4)P_2$ are currently accepted products of class II PI3Ks, despite further *in vitro* and *in vivo* data is needed to determine the precise conditions that modulate their specificity.

1.5.3.3 Isoform-specific functions

1.5.3.3.1 PI3KC2α

PI3KC2α is the most studied isoform of class II PI3K, with well-described roles in plasma membrane internalization and trafficking at the early endosomal compartment. PI3KC2α-mediated $PI(3,4)P_2$ synthesis plays an essential role in CME (see section 1.4.2.2.1). In this process, it is recruited and activated at CCP via its N-terminal clathrin-binding domain and $PI(4,5)P_2$-binding PX-C2 domain, where it produces a pool of $PI(3,4)P_2$ [50] necessary for the recruitment of downstream effector proteins. This, and the relevance of $PI(3,4)P_2$ in CME, are supported by the finding of stalled CCP upon PI3KC2α depletion [50] or acute plasma membrane $PI(3,4)P_2$ depletion [143]. Tissue-specific effects related to the role of PI3KC2α in CME have been reported in endothelial cells, where its loss impairs growth factor receptor internalization resulting in lethal vascular damage and defective angiogenesis [199].

In addition to CME, PI3KC2α has been shown to mediate internalization via alternative routes such as a dynamin-independent pathway [200] and clathrin-mediated pinocytosis in endothelial cells [201].

In contrast to its function in endocytosis, PI3KC2α has also been linked to plasma membrane delivery. In this context, PI3KC2α synthesizes an endosomal pool of PI(3)P that is independent from complex II VPS34 and facilitates activation of RAB11, a regulator of endosomal recycling. Later turnover of PI(3)P completes the sequential PI conversion required for plasma membrane delivery [198]. PI3KC2α-mediated RAB11 activation is also necessary to trigger a RAB pathway involved in primary cilium elongation, an essential structure in embryonic signaling and kidney homeostasis [202]. In metabolic tissues, PI3KC2α can be activated by insulin to promote plasma membrane translocation of glucose transporter GLUT4, thereby enhancing glucose uptake [203]. This process revealed a link between PI3KC2α and type II diabetes phenotypes, observed in human and mice [171].

Independently of its catalytic activity, PI3KC2α is involved in mitotic spindle stabilization during metaphase, liking PI3KC2α loss of function to enhanced tumor growth in breast cancer mouse models due to genomic instability [204]. This finding uncovers a previously undescribed scaffolding function of class II PI3Ks. Additionally, a role of PI3KC2α during later stages of cell division has been reported, as PI3KC2α-mediated synthesis of $PI(3,4)P_2$ has been shown to be necessary for cytokinetic abscission relevant in the eye lens [205].

Homozygous deletion of PI3KC2α-encoding gene *Pik3c2a* is embryonically lethal in mouse models [199], yet *PIK3C2A* mutations have been reported in humans, suggesting either inter-species variations in PI3KC2α functions or PI3KC2β-mediated compensatory mechanisms, whose expression was reported to be increased in these patients [206].

1.5.3.3.2 PI3KC2β

PI3KC2β functions have been mostly described in the context of cellular metabolism, both linked to the plasma membrane and endolysosomal system, as well as some cell type-specific functions in physiological and pathological conditions.

At endolysosomal compartments, PI3KC2β has recently emerged as an important regulator of cellular signaling via its nutrient-dependent repression of mTORC1 activity. Mechanistically, upon growth factor availability, PI3KC2β remains inactive under cytoplasmatic sequestration by 14-3-3 proteins, which associate to PI3KC2β after protein kinase N 2 (PKN2)-mediated phosphorylation at the N-terminal residue T279. In contrast, in growth factor-depleted conditions, PI3KC2β is dephosphorylated, released from 14-3-3 binding and translocated to late endosomal/lysosomal compartment via interaction with resident activated RAB7. There, it synthesizes a $PI(3,4)P_2$ pool that triggers 14-3-3 association with mTORC1 subunit raptor, leading to its inactivation [51,194]. Additionally, the same $PI(3,4)P_2$ pool enhances late endosomal cholesterol removal [207], thereby further repressing mTORC1 activity via a mechanism described by Castellano *et al* [208]. Thus, PI3KC2β loss results in increased mTORC1 signaling and consequent induction of anabolic pathways such as protein synthesis and lipid biogenesis, and repression of catabolic pathways such as autophagy. This mechanism reveals opposing roles of class I and class II PI3Ks in cellular metabolic regulation.

PI3KC2β, like PI3KC2α, has been involved in some prominently cell- or tissue-specific signaling and trafficking roles at the plasma membrane. Despite sharing a clathrin-binding and other functional domains with PI3KC2α, a general role in CME has been hypothesized yet not reported for PI3KC2β. However, involvement in internalization from the plasma membrane is reported in clathrin-mediated pinocytosis, a mode of fluid-phase endocytosis, in endothelial cells [201]. In this context, ITSN1 was shown to recruit PI3KC2β at clathrin structures associated with actin, where it synthesized a $PI(3,4)P_2$ pool that promoted recruitment of actin-remodeling effectors, thereby allowing completion of clathrin-mediated pinocytosis. In plasma membrane signaling, PI3KC2β association to active EGFR was reported to increase its kinase [192], yet a functional association has not been reported since. In immune cells, PI3KC2β has been linked to Ca^{2+} signaling by promoting KCa3.1 channel gating upon immune receptor activation, inducing T-cell activation and mast cell degranulation [209,210]. These findings led to uncover resistance to anaphylaxis in PI3KC2β KO mice and have positioned PI3KC2β as a potential therapeutic target for immune disorders [211]. In the context of insulin signaling in metabolic tissues, studies in PI3KC2β kinase inactive mutant mice revealed increased insulin sensitivity and glucose tolerance. This has been mechanistically associated with a role in trafficking insulin receptors to EEA1 endosomes in hepatocytes [212], thereby limiting receptor activation and generally playing the opposite role of PI3KC2α in insulin signaling. In neurons, PI3KC2β has been reported to promote AKT pathway activation upon growth factor receptor stimulation and ITSN1 association [193].

A strong link between PI3KC2β and cell migration has been established, mainly from studies in the cancer field. Enhanced migration and epithelial-to-mesenchymal transition are hallmarks of cancer cells that directly determine metastatic capacity [213]. Two studies [214,215] observed a first association when PI3KC2β overexpression decreased integrin adhesions and proliferation and enhanced lamellipodial formation and migration. These phenotypes were proposed to be PI(3)P-dependent and mechanistically mediated by RHO GTPase CDC42, involved in actin reorganization [214], or by EGFR and small GTPase RAC pathway [215]. In prostate and gynecological cancers, PI3KC2β has been involved in activation of mitogenic or lipid-dependent pathways promoting motility [216,217], and shown to localize and promote migration at lamellipodia [218]. Other studies have described PI3KC2β status in cancer models, reporting increased expression in neuroblastoma [219] and breast cancer [220], where its downregulation inhibited invasion and metastasis. Despite the described roles of PI3KC2β, homozygous KO mice models are viable, fertile and reach adulthood without prominent phenotypes [171]. Interestingly, an involvement of PI3KC2α in cell migration has recently been uncovered [221] upon the observation of increased expression in metastatic breast cancer. Mechanistically, it has been shown that PI3KC2α-mediated synthesis of $PI(3,4)P_2$ at FAs promotes the recruitment of a RAS GTPase activator that induces FA turnover and migration. This finding suggests that PI3KC2α plays a similar role than PI3KC2β in promoting cell migration.

Interestingly, PI3KC2β KO mouse models with specific smooth muscle PI3KC2α ablation revealed a role of the two class II isoforms in vascular contraction and blood pressure regulation. This was linked to defective contractility and RHO pathway activation [222]. As blood pressure alterations were not reported in single KO models, these data suggests that PI3KC2α and β might play redundant roles in smooth muscle, and potentially in other tissues.

1.5.3.3.3 PI3KC2γ

PI3KC2γ remains the least studied isoform of class II PI3Ks and its cellular functions have been mainly described in the context of metabolic regulation. Contrary to the ubiquitous expression of class II PI3K isoforms α and β, PI3KC2γ is predominantly present in exocrine glands, especially liver and pancreas, and to a lesser extent breast, prostate and small intestine tissues [223]. Interestingly, PI3KC2γ plays the opposed metabolic role of PI3KC2β by enhancing insulin signaling downstream of its receptor. Mechanistically, PI3KC2γ synthesizes an endosomal pool of $PI(3,4)P_2$ upon recruitment by endosomal GTPase RAB5 which maintains insulin signaling via AKT2 activation. Consequently, PI3KC2γ KO mice suffer from increased tendency to insulin resistance and decreased hepatic glycogen storage due to a reduction of glycogen synthase activity, as well modulated by PI3KC2γ. Besides these alterations, homozygous PI3KC2γ KO mice are viable until adulthood [195]. In line with mouse phenotypes, polymorphisms in *PIK3C2G* gene have been linked to an increased type 2 diabetes risk as well as other metabolic disorders. Additionally, mutations and altered expression have been reported in certain cancer types [224].

1.6 Functional interplay between MTM1 and class II PI3K

Although the mechanistic link between PI(3)P and XLCNM pathogenesis is still debated, many studies hypothesized that the normalization of PI(3)P levels in skeletal muscle may contribute to an improvement or rescue of the XLCNM phenotype. Under this assumption, PI(3)P-synthesizing enzymes have been postulated as potential therapeutic targets for XLCNM. In the last decade, several studies have addressed this question and attempted to decipher the molecular mechanisms underlying PI 3-phosphates homeostasis in the pathological context.

As PI 3-phosphate species metabolizing enzymes, class II PI3Ks and VPS34 complex II have been postulated to co-regulate the same endosomal PI(3)P pool as MTM1, a hypothesis tested in several *in vitro* and *in vivo* studies. A first link between these enzymes was established by Velichkova *et al* [85] in cells derived from a *D. melanogaster* model of XLCNM displaying defective membrane protrusion formation. In these cells, depletion of Pi3k68d or *vps34* restored PI(3)P accumulation and endolysosomal vesicle enlargement observed upon Mtm loss. A similar effect was observed in MTM1-depleted mammalian cells upon VPS34 co-depletion or inhibition, which restored defective endosomal exocytosis and concomitant TfR and β1-integrin mislocalization [83]. Pi3k68d or Vps34 depletion alone decreased PI(3)P levels yet had no effect on membrane remodeling. Whereas Mtm localized at endosomes, Pi3k68d was present at the plasma membrane and acidified compartments [85], consistent with distinct roles of class II PI3Ks in internalization from the plasma membrane [201] and signaling from lysosomes [51]. In a follow-up mechanistic study in *D. melanogaster*, Jean *et al* [88] identified the inactive phosphatase MTMR5/MTMR13 orthologue Sbf to form a complex with Mtm, Pi3k68d and the small GTPase RAB21 at endosomes, where it controlled PI(3)P pools by acting as a GEF for RAB21. Endosomal PI(3)P synthesis and turnover by this kinase-phosphatase module scaffolded by an inactive phosphatase and regulated by a small RAB GTPase determined endosomal sorting and recycling, with an effect on cell protrusion formation. An additional follow-up study at the organismal level in *D. melanogaster* revealed a role of class II PI3K in restoring muscle adhesion defects observed in MTM1-depleted models [169]. Co-depletion of Pi3k68d rescued muscle detachment and βPS-integrin mislocalization, present at intracellular inclusions and not costameres, and associated with

increased lethality and delayed development of MTM1-depleted models. Conversely, *Vps34* co-depletion partially phenocopied Mtm loss regarding lethality, muscle detachment, and lack of βPS-integrin at costameres without forming inclusions. T-tubule disorganization in these models was not reverted by either loss of class II or class III PI3K orthologues.

Altogether, these studies provided a mechanistic and functional basis for MTM1- and class II PI3K-mediated regulation of PI(3)P pools important for endosomal homeostasis and trafficking, with an impact on cell adhesion. Some complementary mechanistic explanations for PI3KC2β-mediated rescue of XLCNM have been proposed. In MTM1-depleted mouse muscle, reported to have Ca^{2+} dynamics and ECC defects, pan-PI3K but not class III PI3K inhibition acutely restored homeostasis [114] via PI(3)P-mediated modulation of DHPR. Another study linked the normalization of PI(3)P in double MTM1- and PI3KC2β-depleted cells to restoration of AKT phosphorylation status, which is abnormally decreased in MTM1-depleted cells triggering pro-apoptotic pathways [84].

Solid evidence on the functional link between MTM1 and class II PI3KC2β in mammalian models was provided by Sabha *et al* [42] in a study showing that KO of PI3KC2β rescued the survival and disease phenotype of XLCNM mice models. In double *Mtm1* KO and skeletal muscle-specific *Pik3c2b* KO models, body weight and muscle function parameters, as well as histological hallmarks such as myofiber size, nuclei positioning and triad organization of *Mtm1* KO mice were restored to normality. Similar results were observed upon *Pik3c2b* KO induction after disease onset, setting proof-of-concept evidence for PI3KC2β-targeting therapies in XLCNM patients with congenital onset. Likewise, treatment of *Mtm1* KO models with pan-PI3K inhibitor wortmannin moderately improved survival and histopathological hallmarks of myopathy, as observed in zebrafish XLCNM models treated with other pan-PI3K inhibitors [114]. Interestingly, and similar to some previous observations [169], skeletal muscle-specific VPS34 ablation exacerbated functional and histological phenotypes upon co-depletion with *Mtm1*. This is a surprising observation considering that PI3KC2β-mediated rescue was attributed to normalization of PI(3)P levels in *Mtm1* and *Pik3c2b* KO muscle in this study [42], as also suggested by previous research. Thus, these data are indicative of a potentially more complex mechanistic explanation to rescue of XLCNM by PI3KC2β loss.

1.7 Aims of the study

Collectively, many studies have evidenced a strong functional association between MTM1 and PI3KC2β, yet their precise mechanistic interaction in mammalian systems, and particularly in a skeletal muscle context, remains elusive. Deciphering the molecular role of PI3KC2β in the rescue of XLCNM is key for the development of targeted therapies as well as gaining insights into its thus far partially undescribed cellular functions.

In this study, we aimed to mechanistically characterize the functional interaction between MTM1 and PI3KC2β underlying XLCNM rescue by co-depletion with PI3KC2β. By pursuing this objective, we intended to gain insights into XLCNM molecular pathogenesis and potentially uncover previously undescribed cellular roles of PI3KC2β. For this purpose, we generated cell-based models of XLCNM in order to identify and characterize cellular phenotypes of MTM1 loss linked to XLCNM pathology, as well as establishing a systematic *in vitro* tool for proof-of-principle studies on XLCNM inhibitor-based therapeutic strategies.

2. Materials and Methods

2.1 Materials

2.1.1. Buffers, solutions, and media

Solutions and buffers were prepared using water ultra-purified at 18.2 MOhm resistivity using Arium pro VF (Sartorius) (UP H_2O) unless indicated, and pH-adjusted with HCl or NaOH.

Table 2-1. Solutions and buffers for molecular biology methods

Solution or buffer	Composition	Solvent
50x Tris-Acetate-EDTA (TAE)	100 mM glacial acetic acid 50 mM EDTA adjusted to pH 8.2 – 8.4	200 mM Tris
10x OrangeG loading dye	2 mg/mL OrangeG	70% (v/v) glycerin
Antibiotic stock solutions	100 mg/mL ampicillin 50 mg/mL kanamycin	UP H_2O
Lysogeny broth (LB) medium	1.0 % (w/v) yeast extract 0.5 % (w/v) tryptone 0.5 % (w/v) NaCl adjusted to pH 7.4	UP H_2O
LB plates	15 g/L LB agar powder	LB medium

Table 2-2. Solutions and buffers for biochemical methods

Solution or buffer	Composition	Solvent
1x Lysis buffer	0.1% (v/v) Triton X-100 20 mM HEPES pH 7.4 150 mM NaCl 10 mM NaF 2 mM $MgCl_2$ 0.03% (v/v) Protease Inhibitor Cocktail (Sigma) 1 mM phenylmethylsulphonyl fluoride (PMSF) Phosphatase Inhibitor Cocktail 2 and 3 (PIC; 1:100 dilution, Sigma)	UP H_2O
2x Bradford solution	150 µM Brilliant Blue G 17% (v/v) phosphoric acid 10% (v/v) ethanol	UP H_2O
1x Washing buffer for immunoprecipitation	0.1% (v/v) Triton X-100 20 mM HEPES pH 7.4 150 mM NaCl 10 mM NaF 2 mM $MgCl_2$	UP H_2O

	0.03% (v/v) PIC 1 mM PMSF	
6x SDS-PAGE sample buffer	6 mM dithiothreitol (DTT) 10% (w/v) SDS 60% (v/v) glycerin 0.3% (w/v) bromophenol blue adjusted to pH 6.8	375 mM Tris
4x Separating gel buffer	0.4% (w/v) SDS adjusted to pH 8.8	1.5 M Tris
4x Stacking gel buffer	0.4% (w/v) SDS adjusted to pH 6.8	0.5 M Tris
1x SDS running buffer	192 mM glycine 0.1% (w/v) SDS adjusted to pH 8.3	25 mM Tris
1x Transfer buffer	192 mM glycine 10-20% (v/v) methanol	25 mM Tris
Ponceau S staining solution	0.3% (w/v) Ponceau S 3% (v/v) glacial acetic acid	UP H_2O
Ponceau S destaining solution	1% (v/v) glacial acetic acid	UP H_2O
10x Tris buffered saline (TBS)	0.2 M Tris 1.4 M NaCl adjusted to pH 7.6	UP H_2O
		UP H_2O
PBS-Tween (PBS-T)	0.05% (v/v) Tween-20	1x PBS
PBS-based WB blocking and primary antibody solution	3% (w/v) bovine serum albumin (BSA) 0.02% (w/v) NaN_3	1x PBS-T
TBS-Tween (PBS-T)	0.05% (v/v) Tween-20	1x TBS
TBS-based WB blocking and primary antibody solution	3% (w/v) bovine serum albumin (BSA) 0.02% (w/v) NaN_3	1x TBS-T

Table 2-3. Media for culturing of mammalian cells

Media	Composition	Solvent
HEK293T cell culture medium	10% (v/v) heat-inactivated fetal bovine serum (FBS; Biochrom, S-0115) 100 U/mL penicillin (Thermo Fisher, 15140122) 100 µg/mL streptomycin (Thermo Fisher, 15140122)	Dulbecco's modified Eagle medium (DMEM) with high D-glucose (25 nM), L-glutamine (4 mM) and phenol red (Thermo Fisher, 11965062)
C2C12 growth media (GM)	20% (v/v) FBS 100 U/mL penicillin 100 µg/mL streptomycin	DMEM with high D-glucose (25 nM), L-glutamine (4 mM) and phenol red

C2C12 differentiation media (DM)	2% (v/v) horse serum (HS; Thermo Fisher, 16050122) 100 U/mL penicillin 100 µg/mL streptomycin	DMEM with high D-glucose (25 nM), L-glutamine (4 mM) and phenol red
C2C12 freezing media	10% (v/v) DMSO (Roth)	C2C12 growth media
Live cell imaging media	4 mM L-glutamine (Thermo Fisher, 25030081) 10% (v/v) FBS 100 U/mL penicillin 100 µg/mL streptomycin	FluoroBrite DMEM (Thermo Fisher, A1896701)
Matrigel coating solution	5% (v/v) Matrigel (Corning, 356231)	Opti-MEM (Thermo Fisher, 51985-042)
Gelatin coating solution	0.1% (w/v) porcine skin gelatin (300 strength, type A; Sigma G2500)	UP H_2O

Table 2-4. Solutions and buffers for immunocytochemistry methods

Solution or buffer	Composition	Solvent
PFA fixative (4%)	4 % (w/v) paraformaldehyde (PFA) 4 % (w/v) sucrose adjusted to pH 7.4	1x PBS
PFA fixative (2%)	2 % (w/v) PFA 2 % (w/v) sucrose adjusted to pH 7.4	1x PBS
PFA fixative (1%)	1 % (w/v) PFA 1 % (w/v) sucrose adjusted to pH 7.4	1x PBS
Immunocytochemistry (ICC) blocking and antibody solution	0.02 % (v/v) Triton X-100 10 % (v/v) normal goat serum (NGS) 1% (w/v) BSA	1x PBS
Surface immunocytochemistry (S-ICC) blocking and antibody solution	10 % (v/v) normal goat serum (NGS) 1% (w/v) BSA	1x PBS
PBB (PIPES-based buffer)	137 mM NaCl 2.7 mM KCl adjusted to pH 6.8	20 mM PIPES
ICC PBB-based blocking solution	5% (v/v) NGS 50 mM NH_4Cl	PBB
ICC PBB-based antibody Solution	5% (v/v) NGS	PBB

2.1.2. Kits

Commercial kits were stored and used according to the manufacturer's protocol.

Table 2-5. Molecular biology kits

Kit	Source	Application
NucleoSpin Tissue	Marcherey-Nagel	gDNA extraction
NucleoSpin Gel and PCR Clean-up		DNA purification from agarose gels and ligation product clean-up
NucleoBond Xtra Mini or Midi kits		Plasmid DNA extraction
RNAeasy	Qiagen	Total RNA extraction

2.1.3. DNA oligonucleotides

DNA oligonucleotides used as primers for polymerase chain reactions (PCR) with diverse applications were obtained from BioTeZ Berlin-Buch GmbH as lyophilized powder, dissolved in DEPC water (Roth) to a stock concentration of 50 µM, and stored at -20 °C.

Table 2-6. Primers

Primer	Sequence (5'-3')	Application
***Mtm1*-targeting sgRNA forward**	CACCGTAAGTATAATTCACACTCCT	CRSPR KO cell line generation
***Mtm1*-targeting sgRNA reverse**	AAACAGGAGTGTGAATTATACTTAC	
***Pik3c2b*-targeting sgRNA forward**	CACCGTCTTCCACTCAGGGCAATG	
***Pik3c2b*-targeting sgRNA reverse**	AAACCATTGCCCTGAGTGGAAGAC	
***Pik3c2b* forward**	ATTTTCACCTGTTGCCTCCA	CRISPR-Cas9 vector screening
***Pik3c2b* reverse**	CGGGAAAGAGCGTCATACTC	KO cell line genotyping
***Mtm1* forward**	ACGCCTTTCTTCTTTGGACA	
***Mtm1* reverse**	GAACAAGGTGGGACGGTAAA	
***Mtm1* forward**	CAAGATGGAGTCAGTCAGGATGT	qPCR
***Mtm1* reverse**	AGCAGAATCCGTTTCCAAACTT	
***Pik3c2b* forward**	GGCTCTGATCCCACCCTAAAT	
***Pik3c2b* reverse**	GCATCCCAGATAGAGACACGAG	
***Pik3cg* forward**	CGAGAGTGTCGTCACAGTGTC	
***Pik3cg* reverse**	TGTTCGCTTCCACAAACACAG	
***Desmin* forward**	CGACACCAGATCCAGTCCTAC	
***Desmin* reverse**	GCAATGTTGTCCTGATAGCCAT	
***Csnk2a2* forward**	CCACATAGACCTAGATCCACACT	
***Csnk2a2* reverse**	CGCAGGAGCTTGTCAAGAAGA	
***Gapdh* forward**	AGGTCGGTGTGAACGGATTTG	
***Gapdh* reverse**	TGTAGACCATGTAGTTGAGGTCA	

Target species of all primers is *Mus musculus.*

2.1.4. RNA oligonucleotides: short hairpin RNA

Generation of shRNA-encoding plasmid vectors and plasmids for lentiviral production, and well as the process of virus production and purification were performed at the Viral Core Facility of the Charité-Universitätsmedizin Berlin.

The indicated shRNA sequences (**Table 2-7**) were cloned into a f(U6)unrw plasmid using 5'-BamHI and 3'-PacI restriction sites, resulting in shRNA expression under U6 promoter, and nuclear localization signal (NLS) andred fluorescence protein (RFP) expression under the ubiquitin promoter.

Table 2-7. Short hairpin RNA oligonucleotides

shRNA	Target species	Sequence (5'-3')
shSCR	Non-targeting	TTCGCACCCTACTTCGTGG
shPI3KC2β #1	mouse	GCCTAATGACATCAACAGTTT
shPI3KC2β #2	mouse	GTCCACCTACGACTCAGAGAT

2.1.4. DNA plasmids

DNA plasmids for recombinant protein expression were obtained as indicated in **Table 2-8**. The Cas9 (*S. pyogenes*) green fluorescent protein (GFP) plasmid px458-pSpCas9(BB)-2A-GFP was used for the generation of CRISPR-engineered KO cell lines by inserting sgRNA sequences. PI3KC2β and myotubularins had been cloned under the control of cytomegalovirus (CMV) promoter into pcDNA3.1-based (Invitrogen) pEGFP, pcFLAG, pcHA, pcmCherry, pcEGFP or pc6xMYC backbone vectors, resulting in constitutive expression of N-terminally tagged proteins. These backbone vectors had been generated by M. Krauss (MK), FMP, Berlin. Plasmid DNA was stored in DEPC water (Roth) at -20 °C.

Table 2-8. Constructs for recombinant protein expression

Construct	Backbone vector	Source
Cas9-GFP	px458-pSpCas9(BB)-2A-GFP	Addgene, #48138
***Mtm1*-targeting sgRNA Cas9-GFP**	px458-pSpCas9(BB)-2A-GFP	this project
***Pik3c2b*-targeting sgRNA Cas9-GFP**	px458-pSpCas9(BB)-2A-GFP	this project
eGFP-PI3KC2β	pEGFP-C1	cloned by Marat *et al* [51]
eGFP-PI3KC2β KI	pEGFP-C1	cloned by Marat *et al* [51]
FLAG-PI3KC2β	pcFLAG-MK *	cloned by A. Marat
HA-PI3KC2β	pcHA-MK	cloned by Marat *et al* [51]
HA-MTM1	pcHA-MK	cloned by Ketel *et al* [83]
mCherry-MTM1	pcmCherry-MK	cloned by Ketel *et al* [83]
mCherry-MTM1 C375S	pcmCherry-MK	cloned by Ketel *et al* [83]
eGFP-MTMR1	pcEGFP-MK	cloned by Ketel *et al* [83]
MYC6x-MTMR2	pc6xMYC-MK	cloned by K. Ketel
eGFP-MTMR3	pcEGFP-MK	cloned by K. Ketel

eGFP-MTMR5	pEGFP-C2	gift from M. Clague
eGFP-MTMR6	pEGFP-C2	gift from M. Clague
eGFP-MTMR7	pcEGFP-MK	cloned by Ketel *et al* [83]
eGFP-MTMR8	pEGFP-C2	gift from M. Clague
eGFP-MTMR9	pEGFP-C2	gift from M. Clague
eGFP-MTMR10	pEGFP-C1	gift from M. Clague
eGFP-MTMR12	pEGFP-C2	gift from M. Clague
FLAG-MTMR13	pcDNA3-FLAG	gift from Gilbert Di Paolo

Insert species of all myotubularins and PI3KC2β constructs is human.

2.1.5. Antibodies

Antibody stock solutions were routinely stored at -20°C and diluted 1:1 (v/v) in 90% (v/v) glycerol in 1x PBS for avoiding repetitive freezing and thawing, unless indicated by the manufacturer. Dilutions indicated in **Table 2-9** and **Table 2-10** correspond to glycerol-diluted stocks.

2.1.5.1 Primary antibodies

Table 2-9. Primary antibodies

Antigen	Clone	Species	WB* dilution	ICC* dilution	Source	Reference
Active β1-integrin	9EG7	rat		1:250	BD Biosciences	550531
AP-2 µ2	31	mouse	1:1000		BD Biosciences	611351
β1-integrin	MB1.2	rat		1:500	Merck Millipore	MAB1997
β-actin	AC-15	mouse	1:1000		Sigma	A5441
β-tubulin	polyclonal	rabbit	1:1000		Cell Signaling	2146
Calnexin	polyclonal	rabbit		1:100	Abcam	ab75801
CHC	polyclonal	rabbit	1:1000		Abcam	ab21679
Cytochrom C (CytC)	6H2.B4	mouse		1:100	BD Biosciences	556432
Desmin	polyclonal	rabbit		1:200	Proteintech	16520-1-AP
EEA1	14	mouse		1:100	BD Biosciences	610456
FLAG	M2	mouse	1:1000		Sigma	F3165
GFP	polyclonal	rabbit	1:1000	1:500	Abcam	ab6556
GM130	35	mouse		1:200	BD Biosciences	610822
HA	polyclonal	rabbit	1:400		Cayman	cay162200-1
LAMP1	CD107a	rat		1:200	BD Biosciences	553792
MYC	9E10	mouse	1:200		Sigma	M5546

Myosin heavy chain (MHC)	MF20	mouse	1:1000	1:50	R&D	MAB4470
Myotubularin 1	polyclonal	rabbit	1:700		from J. Laporte (in-house, IGBMC)	
Paxillin	Y113	rabbit		1:250	Abcam	ab32084
Phospho-(Y397) focal adhesion kinase (pFAK)	polyclonal	rabbit		1:50	Abcam	discontinued
PI3KC2α	17	mouse	1:400		BD Biosciences	611046
PI3KC2β	22	mouse	1:300		BD Biosciences	611342
PI(3,4)P_2	monoclonal, n.s.	mouse		1:150	Echelon	Z-P034b-EC
PI(4)P	monoclonal, n.s.	mouse IgM		1:200	Echelon	Z-p004
RAB5	polyclonal	rabbit		1:500	Abcam	ab18211
RAB7	D95F2	rabbit		1:50	Cell Signaling,	9367
Transferrin receptor (TfR)	H68.4	mouse		1:300	Zymed	13-6800
Vinculin	polyclonal	rabbit		1:200	Abcam	ab73412
VPS34	D9A5	rabbit	1:1000		Cell Signaling	4263S
Zyxin	CL2502	mouse		1:300	Novus Biologicals	NBP2-36768

All antibodies are IgG unless indicated; n.s., not specified

2.1.5.2 Secondary antibodies

Secondary antibodies for ICC were Alexa Fluor (AF)-conjugated, whereas horse radish peroxidase (HRP)-conjugated, or LI-COR fluorescent dye-conjugated secondary antibodies were used for immunoblotting.

Table 2-10. Secondary antibodies

Raised in	IgG species recognized	Conjugate	WB* dilution	ICC* dilution	Source	Reference
Donkey	rat	Alexa Fluor 647		1:400	Jackson Immuno Research Labs	712-605-153
Donkey	rat	Alexa Fluor 488		1:400	Thermo Fisher	A21208
Goat	rabbit	Alexa Fluor 488		1:400		A11034

Goat	rabbit	Alexa Fluor 568		1:400		A11011
Goat	mouse	Alexa Fluor 488		1:400		A11001
Goat	mouse	Alexa Fluor 568		1:400		A11031
Goat	mouse	Alexa Fluor 647		1:400		A21235
Goat	mouse IgM	Alexa Fluor 568		1:400		A21043
Goat	mouse	IRDye 680RD	1:10000		LI-COR Biosciences	926-68070
Goat	rabbit	IRDye 680RD	1:10000			926-68071
Goat	mouse	IRDye 800CW	1:10000			926-32210
Goat	rabbit	IRDye 800CW	1:10000			926-32211
Goat	mouse	HRP-conjugated	1:5000		Jackson Immuno Research Labs	115-035-003
Goat	rabbit	HRP-conjugated	1:5000			111-035-003

All antibodies are IgG unless indicated.

2.1.5.3 Probes

A eGFP-tagged tandem version of the PI(3)P binding domain of Hrs (eGFP-2xFYVE (Hrs) [225] was recombinantly expressed in *E. coli*, purified and stored in 50% glycerol at -80 °C (performed by Uwe Fink, FMP, Berlin).

Table 2-11. Probes for immunofluorescent detection

Probe	Conjugate	Target	WB* dilution	ICC* dilution	Source	Reference
Phalloidin	AF647	F-actin		1:50	Thermo Fisher	A22287
DAPI		DNA		1:5000		D9542
eGFP-2xFYVE (Hrs)		PI(3)P	0.25 µg/mL		Gillooly *et al* [225]	

2.1.6. Inhibitors

Inhibitors were dissolved in DMSO to the indicated stock solutions and stored at -20°C, or room temperature (RT) in the case of VPS34-IN1.

Table 2-12. Compounds for enzyme inhibition

Inhibitor	Target protein	Stock solution	Treatment	Source	Reference
Dynasore	Dynamin 1/2	25 mM	50 µM for 6 h in FBS-free GM	Sigma	D7893
PITCOIN3	PI3KC2α/β	50 mM	10 µM for 16 h in GM	in-house, FMP	

Rapamycin	mTOR	2 mM	0.1 or 0.5 µM for 16 h in GM	Santa Cruz	sc3504
Vps34-IN1	Vps34	10 mM	1 µM for 4 h in GM	from James Hastie, MRC PPU Reagents	

2.1.7. Bacterial strains

TOP10 chemically competent *E. coli* bacterial strain (Invitrogen) was used for replication and storage in glycerol stocks of plasmid DNA.

2.1.8. Eukaryotic cell lines

C2C12 cell line was obtained from ATCC (CRL-1772) and genetically engineered by CRISPR-Cas9 technique as part of this project to obtain knockout (KO) clonal cell lines *Mtm1*KO #1, *Mtm1*KO #2, *Mtm1*KO #3, *Pik3c2b*KO, double KO (*Mtm1*KO/*Pik3c2b*KO), and double hypomorphic/KO (*Mtm1*^{hypo}/*Pik3c2b*KO). Cells were not used for experiments beyond passage 12 and routinely tested from mycoplasma.

Human embryonic kidney 293T (HEK293T) cell line was obtained from ATCC (CRL-3216) and used for biochemical experiments due to their high replication rate and transfection efficiency. HEK293T cells expressing endogenous eGFP-PI3KC2β were created as described [51,194]. Cells were not used for experiments beyond passage 30 and routinely tested from mycoplasma.

NIH-3T3 cell line was obtained from ATCC (CRL-1658) and used as a control for testing mRNA expression of PI3Kγ in C2C12 myoblasts.

2.1.9. Software

Table 2-13. Software, databases and webtools

Software	Source	Application
Adobe Illustrator CS6	Adobe	Figure preparation
BD FACSDiva	BD Biosciences	Control of BD FACSAria
FIJI Image J	Online - https://fiji.sc/	Image analysis, figure preparation
FlowJo	BD Biosciences	Flow cytometry analysis
GeneSys	Syngene	DNA electrophoresis gel documentation
GraphPad Prism 5.0	GraphPad Software	Statistical analysis, graph preparation
Image Lab	BioRad	WB documentation
Image Studio Lite	LI-COR	WB documentation and analysis
Inkscape	Online - https://inkscape.org/	Figure preparation
MARS Data Analysis Software	BMG LABTECH	Control of microplate reader
Mendeley Desktop	Mendeley	Bibliography managing

Micromanager v1.4.14		Online - https://micro-manager.org/	Control of Nikon epifluorescence microscope
NCBI		https://pubmed.ncbi.nlm.nih.gov/	sgRNA design, bibliography
Office 365	Excel	Microsoft	Data analysis, including statistical
	OneNote		Lab notebook documentation
	PowePoint		Figure preparation
PrimerBank database		Online - https://pga.mgh.harvard.edu/primerbank/	qPCR primer design
SnapGene		SnapGene	Primer and cloning design
StepOne v2.3		Thermo Fisher	Control and analysis of qPCR
Synthego ICE CRISPR Analysis Tool		Online - https://ice.synthego.com/	KO cell line genotyping
Volocity v6.21		Perkin Elmer	Control of SDC microscope
Zeiss ZEN		Zeiss	Control of Zeiss LSM

2.2. Methods

2.2.1. Molecular biology methods

2.2.1.1. Genomic DNA extraction

Genomic DNA (gDNA) was obtained from confluent C2C12 myoblasts cultured in 6 cm or 10 cm plates. The commercial kit NucleoSpin Tissue kit (Macherey-Nagel) was used following manufacturer's protocol. gDNA was stored at 4°C.

2.2.1.2 Total RNA extraction

Total RNA was obtained from C2C12 or NIH-3T3 cells cultured in 6 cm plates using the RNA extraction commercial kit RNAeasy (Qiagen). To minimize the presence of RNAases, material and surfaces were cleaned with RNAase-free solution RNAase AWAY (Thermo Fisher) prior to extraction and sterile RNAase-free filtered tips were used. Plates were washed once with sterile 1x PBS and extraction was performed according to manufacturer's protocol "Purification of Total RNA from Animal Cells Using Spin Technology". When possible, RNA was reverse-transcribed to complementary DNA (cDNA) immediately after extraction (see section 2.2.1.4). Alternatively, it was stored at 4°C.

RNA concentration and purity were measured as described in section 2.2.1.14. Moreover, purity was further assessed by electrophoresis of 100 ng of RNA on a 1.5% agarose gel (see section 2.2.1.6) and analysis of several parameters. Ribosomal RNA (rRNA) accounts for over 80% of total RNA and it is assumed that rRNA quality reflects messenger RNA (mRNA) quality. Firstly, an approximate quantity ratio of 2 between 28S and 18S rRNA, which respectively correspond to 5 kb and 2 kb in size, was monitored. Secondly, the absence of smear below 18S indicated low sample degradation. Additionally, the presence of signal in agarose gel wells, which usually indicates genomic DNA contamination, was also considered.

2.2.1.3 Polymerase chain reaction (PCR)

Polymerase chain reaction (PCR) is a technique that takes advantage of thermostable DNA polymerases to amplify specific DNA sequences from a DNA template via repetitive temperature- and time-controlled cycles [226]. In this project, PCR was performed in the context of CRISPR-Cas9-engineered cell line generation to amplify regions of newly generated DNA plasmid constructs for later sequencing, as well as genotyping genetically engineered C2C12 cell lines. Phusion high fidelity DNA Polymerase (Thermo Fisher), which contains proofreading activity, and the corresponding GC buffer for GC-rich templates common in gDNA were used to guarantee low error rate. All materials and reagents are kept on ice during PCR preparation (**Table 2-14**), and a peqSTAR 2X (VWR) thermocycler was used to perform the reaction as indicated (**Table 2-15**).

Table 2-14. PCR reaction mix

Reagent	Final concentration
DNA	2-4 ng/µL
Forward primer	0.5 µM
Reverse primer	0.5 µM
GC buffer	1x
dNTPs	0.2 mM
DMSO	6% (*Mtm1*) or 3% (*Pik3c2b*)
Phusion DNA polymerase	0.02 U/µL
DEPC water	up to 25 µL

Table 2-15. PCR thermocycler protocol

Process		Temperature (°C)	Duration
Start		98	1 min
Amplification 40 (*Mtm1*) or 35 (*Pik3c2b*) cycles	Denaturation	98	10 s
	Annealing	58 (*Mtm1*) or 56 (*Pik3c2b*)	30 s
	Extension	72	15 s
End		72	10 in

2.2.1.4 Reverse transcription polymerase chain reaction (RT-PCR)

Analysis of mRNA transcripts by quantitative PCR (qPCR) requires a previous step of reverse transcription of mRNA into cDNA. For this process, all reagents and solutions were kept on ice. Firstly, random primers (random hexamer primers and oligo $d(T)_{20}$) (Thermo Fisher) were annealed to RNA template by mixing these components in diethyl pyrocarbonate (DEPC)- treated water (Roth) to a total volume of 10 µL and incubating them at 75°C for 5 min using a peqSTAR 2X (VWR) thermocycler. Afterwards, the mix was immediately transferred to ice and incubated for at least 1 min. In parallel, a solution mix of 10 µL containing SuperScript IV Reverse Transcriptase and buffer (Thermo Fisher), dNTPs (Thermo Fisher) and DTT (Thermo Fisher) in DEPC water was prepared. A final RT-PCR reaction mix was prepared by mixing the two solutions (**Table 2-16**), and RT-PCR reaction was performed in a thermocycler as indicated on **Table 2-17**. Concentration and purity of cDNA product was measured as described in section 2.2.1.14. cDNA was stored at 4°C.

Table 2-16. RT-PCR reaction mix

Reagent	Final concentration
RNA	2.5 - 25 ng/ µL
Oligo d(T) primer	10 µM
Random hexamer primer mix	10 µM
SuperScript IV Reverse Transcriptase buffer	1x
dNTPs	1 mM
DTT	5 mM
SuperScript IV Reverse Transcriptase	50 U/µL
DEPC water	up to 20 µL

Table 2-17. RT-PCR thermocycler protocol

Process	Temperature (°C)	Duration
Annealing	23	10 min
Annealing, extension	55	20 min
Reaction inactivation	80	10 min

2.2.1.5. Quantitative polymerase chain reaction (qPCR)

Quantitative PCR (qPCR), sometimes referred as real-time PCR, is a PCR-based technique used to obtain real-time semi-quantitative data of gene expression during amplification of cDNA libraries via fluorescence reporters. To perform qPCR, primers were selected from PrimerBank database [227] and tested for off-target amplification and dimerization prior to experiments. This was done by performing qPCR reactions using each pair of primers with and without cDNA template, respectively. PCR product was loaded in a 1% agarose gel (see section 2.2.1.6), where number of amplification products or presence of dimers was observed.

During the experimental process, all reagents and materials were kept on ice. Template cDNA, primers and SsoAdvanced Universal SYBR Green Supermix (BioRad) were loaded following this order in a MicroAmp Optical 96-well plate (Applied Biosystems), to final concentration indicated on **Table 2-18** and a total volume of 20 µL per well. Triplicates of each condition were done. Plates were sealed to avoid evaporation, spinned down and loaded into a Real-Time PCR System StepOne Plus (Applied Biosystems) thermocycler operated by StepOne v2.3 software, where qPCR was performed as indicated (**Table 2-19**). After data collection, cycle threshold (CT) values, indicative of the number of cycles needed for product detection, were automatically determined by the software. Raw data was further processed with Microsoft Excel, where average of triplicate CT values was calculated for each condition, normalized to the corresponding housekeeping gene expression values (*Csnk2a2*) and finally compared to control conditions, from which a relative expression and corresponding error values were obtained.

Table 2-18. qPCR reaction mix

Reagent	Final concentration
cDNA	5 ng/µL
Forward primer	0.5 µM
Reverse primer	0.5 µM
SsoAdvanced Universal SYBR Green Supermix	1x
DEPC water	up to 20 µL

Table 2-19. qPCR thermocycler protocol

Process		Temperature (°C)	Duration
Start		50	2 min
Polymerase activation, DNA denaturation		95	30 s
Amplification 40 cycles	Denaturation	95	15 s
	Annealing, extension	60	1 min
Melting curve, default settings	Step 1	95	15 s
	Step 2	60	1 min
	Step 3	0.3 increment until 95	15

2.2.1.6. Agarose gel electrophoresis

Electrophoresis on agarose gels was performed to separate DNA or RNA samples according to size with the aim of analyzing and/or isolating them. For this purpose, 1% or 1.5% (w/v) agarose (Bio&Sell) was dissolved in 1x TAE buffer by heating in a microwave, and supplemented with 0.3 µg/mL of UV-absorbing DNA-intercalating agent ethidium bromide (Roth). Gels were casted on Compact gel trays (Biometra) and cooled to RT under a fume hood. 1x OrangeG (Sigma) loading dye was added to DNA or RNA samples prior to loading to allow visualization. Samples were loaded to solidified gels together with 5 µL of 1 kb DNALadders (Thermo Fisher) as a standard of fragment sizes. Electrophoresis was performed using Compact chambers (Biometra) in 1x TAE buffer during 20 to 30 min, until the OrangeG signal reached the lower part of the gel. DNA or RNA was visualized on gels due to ethidium bromide incorporation by exposing them to 302 nm UV light on the Gel Documentation GBOX/F3 system (Syngene), operated by GeneSys software (Syngene). When necessary, extraction of DNA fragments from gels was aided by UV transilluminator table UVT-28 (Herolab) using sterile material.

2.2.1.7. DNA purification from agarose gels

Fragments of agarose gels containing DNA were treated with NucleoSpin Gel and PCR Clean-up kit (Marcherey-Nagel) according to manufacturer's protocol in order to extract and purify DNA samples.

2.2.1.8 Oligonucleotide annealing

For the generation of CRISPR-Cas9-engineered cell lines, plasmid DNA vectors containing single guide RNA (sgRNA) sequences were created. For this, the indicated sgRNA sequences (see section 2.2.3.5) were annealed

by incubating them for 5 min at 95°C in a peqSTAR 2X (VWR) thermocycler and cooling down at RT for 1 h prior to ligation.

2.2.1.9 DNA digestion

Plasmid DNA vector px458-pSpCas9(BB)-2A-GFP (Addgene) was digested with endonucleases prior to sgRNA oligonucleotide insertion. In a 20 µL reaction volume, 2 µg of plasmid were treated with 1 µL BbsI FastDigest endonuclease and 1x FastDigest buffer (Fermentas) for 20 min at 37°C. 5' ends of linearized DNA vector were dephosphorylated by further treatment with 1 U of FastAP alkaline phosphatase (Thermo Fisher) to prevent re-ligation. Afterwards, all enzymes were inactivated by a 5 min incubation at 80°C and linearized plasmid DNA was cleaned up prior to ligation as indicated in section 2.2.1.7.

Annealed oligonucleotides containing sgRNA sequences were not restricted as 5' and 3' restriction enzyme target sites were included during primer design.

2.2.1.10 DNA ligation

Oligonucleotides containing sgRNA sequences were inserted into DNA plasmids via DNA ligation. For this, 50 ng of linearized plasmid and 3- or 6-fold molar excess of annealed oligonucleotides were incubated with 1 U of T4-DNA ligase and 1x T4 ligase buffer (Thermo Fisher) to a total volume of 20 µL for 1 h at RT. A control ligation without annealed oligonucleotides was performed in parallel. Ligation products were stored at -20°C.

2.2.1.11. Transformation of chemically competent *E. coli*

To obtain an amount of plasmid DNA sufficient for mammalian cell transfection, we take advantage of bacterial DNA replication. For this process, bacterial strains sensitized to DNA transformation are used, in this case chemically competent *E. coli* TOP10 (Invitrogen). For this, chemically competent bacteria are thawed and incubated with 10 µL of ligation product for 30 min on ice after mixing gently. Ligation product from control reaction was equally transformed. Transformation by heat-shock is performed by 30 sec incubation at 42°C, which forms membrane pores that allow DNA uptake. After a final 5 min incubation on ice, transformed bacteria were plated into LB-agar plates supplemented with 100 µg/mL ampicillin and incubated overnight at 37°C.

2.2.1.12. Culture of transformed bacteria and preparation of glycerol stocks

After bacterial DNA transformation and overnight culture, 5 to 10 colonies were picked from LB-agar plates with sterile tips to screen for the desired DNA constructs. Clones were inoculated into 5 mL of LB medium supplemented with 100 µg/mL ampicillin and cultured overnight at 37°C in an incubator shaking at 180 rpm. On the following day, bacteria were pelleted by centrifugation at 1000 rpm for 5 min for plasmid DNA extraction. The same culture protocol was applied to prepare glycerol stocks of selected clonal transformed bacteria. Glycerol acts as a cryopreserving agent that allows long-term storage of bacterial stocks. For this, pelleted cultures were resuspended in a 50% (v/v) glycerol/LB media solution and stored in cryotubes at -80°C. For obtaining plasmid DNA amounts sufficient for mammalian cell transfection, 200 mL of LB media supplemented with 100 µg/mL ampicillin were cultured overnight and sedimented by centrifugation at 5000 rpm for 30 min at 4°C. Pellets were stored at -20°C or immediately resuspended for plasmid DNA extraction.

2.2.1.13 Plasmid DNA extraction

Plasmid DNA was isolated from pelleted *E. coli* overnight 5 mL or 200 mL cultures using NucleoBond Xtra Mini or Midi kits (Macherey-Nagel), respectively. The protocol indicated by manufacturer was followed and DNA concentration and purity was assessed as indicated in section 2.2.1.14.

2.2.1.14 Determination of DNA and RNA concentration and quality

DNA and RNA concentrations were routinely determined using a SPECTROstar Nano microplate reader and MARS Data Analysis Software (BMG LABTECH). For this, 2 µL of DNA or RNA samples were placed on an LVis plate (BMG LABTECH) in duplicates together with a DEPC water control used to establish a blank value. DNA and RNA samples were analyzed by the default DNA or RNA concentration analysis protocols from the Multi-user Reader Control software. These included analysis at 260 nm, corresponding to maximum absorbance wavelength for these nucleic acids, as well as 230 and 280 nm, absorbances for contaminants such as proteins, salts, phenol and other products derived from the purification process. Regarding DNA purity, ratios of 260 nm to 280 nm corresponding to value of approximately 1.8 for DNA and 2 for RNA, and ratios of 260 nm to 230 nm corresponding to values of 2.0 to 2.2 were used as indicative of absence of contaminants. Additionally, further tests were performed to guarantee RNA quality (see section 2.2.1.2).

2.2.1.15 Sequencing of DNA

DNA samples were sequenced externally by LGC Genomics GmbH using Sanger sequencing method upon provision of primers indicated in **Table 2-6**.

2.2.2. Biochemistry methods

2.2.2.1. Preparation of cell extracts

Cell extracts from C2C12 myoblasts were routinely prepared with a Triton X-100-based 1x lysis buffer (**Table 2-2**). Throughout the protein extraction protocol, buffers and samples were processed and incubated on ice. Cells were washed twice with pre-cooled 1x PBS by aspirating the media and carefully adding 1x PBS to cover the plate surface, which was immediately aspirated. Volumes of 0.3 mL or 1 mL of pre-cooled lysis buffer were added to 6 cm or 10 cm plates, respectively. Cells were harvested from plates by scrapping, transferred to tubes and incubated for 10 to 15 min on ice, mixing by vortexing several times during the incubation. Insoluble phase of cell homogenates was then separated by centrifugation at 13300 rpm at 4°C and aqueous phase was collected into new tubes for protein concentration quantification.

2.2.2.2 Determination of protein concentration from cell extracts

Bradford protein quantification method was routinely used for samples processed with Triton X-100 based lysis buffer. Triplicates of samples and duplicates of a known protein concentration standard were added to 96-well plates and analyzed with SPECTROstar Nano Plate Reader (BMG LABTECH) via the MARS Data Analysis Software (BMG LABTECH) software. Protein concentration standard ranged from 0 mg/mL to 2 mg/mL and was prepared with serial 1:1 (v/v) dilutions of lysis buffer and a 2 mg/mL BSA stock solution in 1x PBS. A 1x Bradford solution was prepared by mixing 1:1 (v/v) 2x Bradford solution (**Table 2-2**) in UP H_2O. On each well, samples and standard were diluted 1:100 (v/v) in Bradford solution to a final volume of 150 µL per well. Plate was incubated at RT and

protected from light for 5 min. Absorbance at 595nm wavelength was measured using the plate reader mentioned above, with a previous step of 5 s mixing by shaking.

Protein concentration of samples was calculated by interpolation from the protein concentration standard. Absorbance mean values and corresponding known concentration values from the BSA protein standard were plotted into a linear regression fit with $R > 0.97$, whose equation was used to interpolate sample concentration from the corresponding mean absorbance values. For each experiment, protein concentrations were equaled for all samples by adding the corresponding volumes of lysis buffer to a known volume of sample. Disulfide bond-reducing agent dithiothreitol (DTT)-based SDS-PAGE sample buffer (**Table 2-2**) was added in a 1:6 dilution to samples, which were mixed by vortexing and incubated at 95°C for 10 min, resulting in a solution of denatured and negatively-charged proteins. Samples were stored at -20°C until analyzed.

2.2.2.3 Immunoprecipitation

Immunoprecipitation (IP) of endogenous or overexpressed protein from cell extracts was performed using commercial antibody-coupled magnetic agarose beads (ChromoTek) for tagged proteins, or protein A/G-coupled magnetic agarose beads (Thermo Fisher) for untagged proteins. Protein A/G is a recombinant fusion protein with binding domains for all human immunoglobulins, thereby allowing to couple any antibody of interest to the beads. Samples, buffers, and materials were kept on ice or at 4°C throughout the IP process.

For IP with antibody-coupled magnetic agarose beads, HEK293T cells were cultured in 10 cm plates. Protein extraction protocol was performed as described before (see section 2.2.2.1) using 1 mL of Triton X-100-based 1x lysis buffer per plate. Protein concentration was measured by Bradford method as described (see section 2.2.2.2), without the last step of DTT treatment. A volume of 10-12 µL of GFP-, FLAG-, or HA-Trap magnetic agarose beads (ChromoTek) per plate was washed once with 1 mL of washing buffer (**Table 2-2**) by placing the tube on a magnetic support and aspirating the buffer. Equal quantities of protein from each sample were added to tubes containing magnetic agarose beads for IP, and a volume corresponding to 5% (w/v) of the protein quantity for IP was transferred to a new tube (starting material, SM). Tubes containing cell lysates and beads were incubated on a rotation wheel at 4°C for 1-3 h. SM samples were kept at 4°C during the same amount of time. After incubation, unspecific interactions were eliminated by washing beads three times with 1 mL of washing buffer as described earlier. Proteins bound to beads were eluted by adding 25 µL of 1x SDS-PAGE sample buffer, spinning down for 30 s, and incubating at 95°C for 10 min. Beads were removed from samples before SDS-PAGE analysis. For SM samples, DTT was added in a 1:6 dilution, mixed by vortexing, and incubated at 95°C for 10 min. Samples were stored at -20°C until analyzed.

For IP with Pierce protein A/G magnetic agarose beads (Thermo Fisher), C2C12 myotubes (4 days of differentiation) were cultured in 15 cm plates. Protein extraction protocol was performed as described before (see section 2.2.2.1) using 1.5 mL of Triton X-100-based lysis buffer per plate. Protein concentration was measured by Bradford method as described (see section 2.2.2.2), without the last step of DTT treatment. A volume of 50 µL of A/G magnetic agarose beads per plate was washed once with 1 mL of 1x PBS. To couple PI3KC2β antibody to beads, mouse anti-PI3KC2β (**Table 2-9**) was diluted 1:100 PBS-T (**Table 2-2**), and a volume of 500 µL of this antibody solution were added to beads. Coupling was performed by incubation on a rotation

wheel at 4°C for 2 h. A control condition without antibody was also processed in parallel. After antibody coupling, beads were blocked on a rotation wheel at 4°C for 30 min with 500 µL of a blocking solution containing 3% BSA in PBS-T, and washed twice with washing buffer (**Table 2-2**) after blocking. Equal quantities of protein from each sample were added to beads for IP, and a volume corresponding to 1% of the protein quantity for IP was transferred to a new tube (starting material, SM). Tubes containing cell lysates and beads were incubated on a rotation wheel at 4°C for 4-6 h. SM samples were kept at 4°C during the same amount of time. After incubation, unspecific interactions were eliminated by washing beads three times with 1 mL of washing buffer as described earlier. Proteins bound to beads were eluted by adding 30 µL of 1x DTT, spinning down for 30 s, and incubating at 95°C for 10 min. Beads were removed from samples before SDS-PAGE analysis. For SM samples, 6x SDS-PAGE sample buffer was added in a 1:6 dilution, mixed by vortexing, and incubated at 95°C for 10 min. Samples were stored at -20°C until analyzed.

2.2.2.4. Sodium dodecyl sulfate polyacrylamide gel electrophoresis (SDS-PAGE)

SDS-PAGE allows the analysis of protein levels from cell lysates based on molecular weight separation. SDS-PAGE protocol and the corresponding buffers and reagents were used and prepared according to the Laemmli system [228]. Mini Protean Tetra Cell System (BioRad) was used to prepare 1.5 mm thickness gels by mixing the indicated components (**Table 2-20**) and perform the electrophoresis. Samples prepared for SDS-PAGE analysis were loaded into gel wells, with a maximal volume of 25 µL for 15-well pockets and 45 µL for 10-well pockets. As a molecular weight reference, 2-5 µL of PageRuler Plus Protein standard (Thermo Fisher) were loaded in preferably two wells of each gel. Electrophoresis was performed in the corresponding tanks (BioRad) containing 1x SDS running buffer (**Table 2-2**). The protocol consisted of two phases: firstly, a voltage of 90 V was applied to allow the migration of proteins though the stacking gel. When proteins, visualized by the blue color of SDS-PAGE sample buffer, accumulated at the interphase between the stacking and separating buffer, voltage was increased to 110 V. Electrophoresis was stopped at different points depending on the molecular weight of the proteins of interest, the earlier being when the SDS-PAGE sample buffer line reached the bottom of the gel.

Table 2-20. SDS-PAGE gel preparation

Components	Separating gel	Stacking gel
1x buffer	Separating gel buffer *	Stacking gel buffer *
Acrylamide/Methylene bisacrylamide 37.5:1 (v/v)	9%	3%
TEMED (v/v)	0.1%	
APS (v/v)	0.1%	

* See **Table 2-2**.

2.2.2.5. Immunoblotting

To selectively detect proteins already separated by mass through electrophoresis, protein immunoblotting, also referred as Western blotting (WB), was performed. For this, negatively charged proteins were transferred from polyacrylamide gels to nitrocellulose membranes (Amersham Protran 0.2; GE Healthcare) by applying an electrical current in an electroblotting Mini Trans-Blot Cell (BioRad). The transfer setup was done on a tray containing 1x transfer buffer (**Table 2-2**) where all material was soaked. Methanol content in 1x transfer buffer

generally varied from 10% for high molecular weight protein analysis (> 150 kDa) to 20% for low molecular weight protein analysis (< 150kDa). On the anodic side of the transfer support (BioRad), a sponge, three Whatman papers (Grade GB003; Sigma) and a nitrocellulose membrane, all equally sized, were stacked in this order. The polyacrylamide gel was carefully removed from its glass support and placed on the membrane avoiding air bubbles. Three more Whatman papers, and a sponge were placed on top, and the support was closed and fitted in the Mini Trans-Blot tank (BioRad) together with an ice block. The tank was filled with 1x transfer buffer. A voltage of 110 V was applied at 4°C for 90 min for protein transfer or, alternatively, 30 V were applied for overnight (16h) transfer at 4°C.

To assess protein transfer efficiency and equal protein loading, nitrocellulose membranes were stained with Ponceau S staining solution (**Table 2-2**) by gentle shaking for 10 min at RT. Before imaging at ChemiDoc-System (BioRad), excess of Ponceau S was eliminated by washing membranes with Ponceau S destaining solution (**Table 2-2**) for 5 min on a shaker, exchanging the solution at least once. Ponceau S staining was then eliminated by washing membranes for 15-45 min, depending on the protein content, at RT on a shaker, exchanging the destaining solution every 10 min.

In immunodetection-based protocols, samples are treated with blocking solutions, high in protein content, with the aim of blocking epitopes and minimizing unspecific antibody binding. For WB, membranes were incubated with blocking solution (**Table 2-2**) at RT and gentle shaking for 1 h. PBS-based blocking and washing solutions were routinely used, except for analysis of phosphorylated proteins, where TBS-based solutions were used. Blocked membranes were cut if necessary and incubated with primary antibodies (**Table 2-9**) diluted in blocking solution overnight at 4°C upon gentle shaking. On the following day, membranes were washed twice with PBS-T or TBS-T for 5 min at RT while shaking. This was followed by incubation with secondary antibodies diluted in PBS-T or TBS-T for 1 h at RT upon gentle shaking. Fluorophore-conjugated IRDye (LI-COR Biosciences) secondary antibodies (**Table 2-10**) were routinely used for WB. After secondary antibody labelling, membranes were washed twice with PBS-T or TBS-T for 10 min at RT while shaking, and a last washing step with 1x PBS or 1x TBS was done. Membranes were then imaged using LI-COR Odyssey Fc Imaging system (LI-COR Biosciences) on 700 nm or 800 nm LI-COR channels with 10 min or 2 min exposure and visualized with Image Studio Lite software (LI-COR Biosciences). Alternatively, HRP-conjugated secondary antibodies were used following the same incubation and washing protocol. For visualization, an enhanced chemiluminescent (ECL) reagent (Amersham ECL; GE Healthcare) was used following the manufacturer's protocol: ECL reagents A and B were mixed in a 1:1 dilution and membranes were covered with a thin layer of solution and protected from light. They were then placed on a ChemiDoc-System imager (BioRad) and imaged via Image Lab software (BioRad) with a chemiluminescence-optimized protocol. Different exposure times depending on primary antibody affinity and antigen concentration were selected. An image with white light exposure protocol was also captured in order to visualize the molecular weight marker. Re-incubation of already analyzed membranes was generally avoided but done if required. For this, membranes were washed twice with PBS-T or TBS-T upon shaking for 10 min, and incubated with primary and secondary antibodies as described above. The species in which the second primary antibody was raised was always different than the species of the first primary antibody, unless there was a significant difference in the molecular weight of the proteins of interest that allowed a clear differentiation.

Immunoblotting for MTM1 detection was done using an in-house antibody kindly provided by J. Laporte. Instead of the blocking solution mentioned above, blocking and primary antibody solutions were supplemented with 5% (w/v) milk (Roth) in PBS-T. HRP-conjugated goat anti-rabbit secondary antibody was diluted in PBS-T and imaged using ECL reagents (GE Healthcare) and ChemiDoc-System imager (BioRad).

2.2.3. Cell biology methods

2.2.3.1. Culture methods of mammalian cell lines

Cells were cultured at 37°C, 5% CO_2 and humidified atmosphere in CO_2 incubators (New Brunswick Scientific, Galaxy 170S). Manipulation of cell cultures was done at RT under sterile conditions in tissue culture biological safety cabinets (Thermo Fisher). A phase contrast microscope Olympus CKX-31 was used to monitor cell confluency and viability, count cells, and assess fluorescent protein transfection. All media, buffers, reagents and material used in cell culture were commercially sterile or manually sterilized by filtering and/or autoclaving before use. Media was stored at 4°C and pre-warmed in a water bath at 37°C before use.

Maintenance of cell cultures implies regular passaging of cells in order to guarantee optimal culture confluency and viability, as well as to expand the cultures prior to certain experiments or generation of cell stocks. For passaging, media was aspirated from plates and cells were washed once with D-PBS (Thermo Fisher), which was added carefully and avoiding a direct stream on the cells. D-PBS was then aspirated, and TrypLE Express Enzyme (Thermo Fisher) dissociation reagent was added, ensuring a thin layer was covering the entire surface of the plate. Plates were incubated at 37°C for 3-5 min and cell detachment was examined under the phase-contrast microscope. Media was added to plates and the remaining adhered cells were detached by pipetting. For routine cell passaging, cell confluency was initially estimated and seeding volumes were calculated according to it. For experimental cell seeding, the cell suspension was transferred to a tube, mixed by inversion, and 10 µL of it were introduced in a Neubauer chamber for counting under the mentioned microscope. Cell suspension was mixed by inversion before a volume of cells was added to a new plate already containing the corresponding final volume (**Table 2-21**). Plates were thoroughly shaken to homogeneously spread cells on the plate or well surface before placing them in the incubator.

In this project, human embryonic kidney 293T cells (HEK293T) were used for biochemical experiments (immunoprecipitation) due to their high replication rate and transfection efficiency. They were cultured in HEK293T cell culture media (**Table 2-3**) and seeded for experiments at the indicated confluency (**Table 2-21**) in 10 cm plates as explained above. HEK293T expressing endogenously-tagged GFP-PI3KC2β and NIH-3T3, used as a control for testing C2C12 mRNA expression, were cultured equally.

Murine cell line C2C12, used in this project to generate genetically-modified *in vitro* models, is a muscle precursor (myoblast) cell line with the capacity to differentiate into mature muscle cells (myotubes) in a process known as myogenesis. Due to the differential signaling requirements of myoblasts and myotubes, these were respectively cultured in growth media (GM) or differentiation media (DM) of the indicated compositions (**Table 2-3**). Importantly, C2C12 myoblasts were always cultured at low confluency (< 70%) in order to avoid differentiation, which is naturally induced in highly confluent cultures. This was achieved by passaging 10-20% of myoblasts from

70% confluent cultures into new plates every 2-3 days. For experimental seeding, C2C12 myoblasts were processed as described above.

C2C12 myoblasts were used for the majority of experiments in this project. For nucleic acid or protein extraction and flow cytometry analysis, C2C12 myoblasts were seeded on 6 cm or 10 cm plates without further surface treatment. ICC and cell migration assays were performed on myoblasts seeded on a Matrigel-coated surface. For ICC, 18 mm diameter glass coverslips were placed in 12-well plates and coated by covering and incubating the surface with Matrigel solution (**Table 2-3**) for 2 min at RT. The solution was then aspirated, and plates were incubated for 30 min at 37°C before cell seeding. Cell seeding and chamber coating for myoblast migration assays was performed as indicated in section 2.2.3.7.

C2C12 myoblasts were differentiated into myotubes for certain experiments, comprising RNA and protein extraction and ICC. For differentiation, cell culture supports (plates or chambers) were coated with 0.1% (w/v) gelatin solution (**Table 2-3**) by covering and incubating the surface for 2 min at RT. The solution was then aspirated, and supports were incubated for approximately 30 min at RT until the surface was dry to then proceed with experimental cell seeding. Cultures were confluent (> 90%) on the following day (differentiation day 0), when GM was replaced by DM. To eliminate traces of FBS that would interfere with differentiation, cells were washed once with D-PBD prior to adding fresh DM. On the two following days (differentiation days 1-2), DM was replaced every 24h, and from differentiation day 3 onwards, this process was repeated three times a day due to the high metabolic rate of the cultures. Myotubes were processed on differentiation day 7 at latest.

Cell stocks were stored in cryotubes at -80°C a maximum of 2 weeks after freezing and transferred into liquid nitrogen for long-term storage. For C2C12, cell stocks of low-passaged knockout (KO) cell lines were generated after KO screening by culture in cell culture supports of progressively increasing surface until obtaining 2-3 15 cm plated of 70% confluent C2C12 myoblasts. Those were dissociated as explained above, pelleted in 15 mL tubes via 5 min centrifugation at 500 rpm, and resuspended in freezing media (**Table 2-3**). Resuspended cells were immediately aliquoted in 500 µL cryotubes and transferred to ice prior to freezing at -80°C. Cell stocks were thaw by adding 0.5 mL of 37 °C pre-warmed GM in cryotubes, mixing by pipetting and immediately transferring cells into a 15 mL tube containing pre-warmed GM. To eliminate traces of DMSO, which could interfere with culturing due to its cytotoxicity, cells were pelleted as indicated above, resuspended in fresh media, and seeded in 6 cm or 10 cm plates. C2C12 were cultured for at least 2 days prior to experimental seeding.

Table 2-21. Experimental cell seeding numbers and media volumes

Support	Cell line, experiment	Cell number (* 10^3)	Media (mL)
15 cm	C2C12	5000 #	20
10 cm plate	HEK293T	1500	10
	C2C12	1000	
6 cm plate	C2C12	350	5
6-well plate	C2C12, DNA plasmid OE	60	2
	C2C12, shRNA-transduced	5	
12-well plate, 18 mm coverslip	C2C12, ICC	50	1

	C2C12, ICC + PITCOIN3 treatment	12	
ibiTreat 8-well chamber	C2C12, ICC	20 #	0.3
	C2C12, Migration assay	1	

seeding number for differentiation. ICC, immunocytochemistry; OE, overexpression

2.2.3.2 Transfection of mammalian cell lines

2.2.3.2.1 Calcium phosphate transfection

DNA plasmid vectors encoding for tagged constructs of our proteins of interest were transfected into HEK293T cells using calcium phosphate method, based in the calcium phosphate assay (Graham and van der Eb, 1973). For this, the indicated amounts of plasmid DNA, 0.1x TE and 2 M $CaCl_2$ buffers were mixed and incubated at RT for 5 min (**Table 2-22**). Afterwards, this mix was added to the indicated volume of 2x HBS drop-wise while vortexing at low speed in order to allow the formation of DNA-calcium-phosphate precipitates, and incubated for 20 min at RT. A volume of 1 mL of transfection mix was carefully added to HEK293T cells cultured in 10 cm plates, ensuring a homogeneous distribution throughout the plate. Cells were harvested 48 h after transfection. All buffers were sterile-filtered prior to use.

Table 2-22. Calcium phosphate transfection volumes

Component	Quantity per 10 cm plate
Plasmid DNA	7 µg in total
2 M $CaCl_2$	60 µl
0.1x TE	440 µl
2x HBS, pH 7.1	500 µl

2.2.3.2.2 JetPrime transfection

DNA plasmid vectors encoding for tagged constructs of MTM1 and PI3KC2β (rescue experiments on C2C12 KOs) or sgRNA-containing Cas9 (CRISPR cell line generation) were transfected into C2C12 myoblasts using JetPrime reagent (VWR), and according to the instructions of the manufacturer. These consist in mixing the indicated amounts of DNA and 1x JetPrime buffer and adding a ratio of 2:1 (v/w) volume of JetPrime reagent at RT per quantity of DNA (**Table 2-23**). The mixture was incubated for 10 min at RT and applied to cells, which were processed for ICC or fluorescence-activated cell sorting (FACS) 48 h after transfection. For ICC, transfected cells were seeded on Matrigel-coated 18 mm coverslips in 12-well plates 24h prior to immunostaining.

Table 2-23. JetPrime transfection volumes

Support	10 cm cell culture plate	6-well
Plasmid DNA	7	2
JetPrime buffer	500	100
JetPrime reagent	14	4

2.2.3.3. Lentiviral transduction of mammalian cell lines

Knockdown (KD) of *Pik3c2b* expression was performed via lentiviral-mediated delivery of shRNA oligonucleotide constructs (**Table 2-7**). A volume of 200 µL of virus preparation was added to cells seeded on 6-well plates and, after 3 days, when cultures were reaching 70% confluency, transduced cells were re-seeded at 5000 cells per well on a 6-well plate. After 2 days, cells were seeded on Matrigel-coated 18 mm coverslips in 12-well plates to perform surface ICC on the following day, implying processing 7 days after lentiviral transduction.

2.2.3.4. Inhibitor treatments

C2C12 myoblasts cultured on Matrigel-coated 18 mm coverslips in 12-well plates were treated with the corresponding inhibitors as indicated in **Table 2-12**. Treatments were applied 24 h after cell seeding.

2.2.3.5. Generation of CRISPR-Cas-engineered cell lines

Clonal C2C12 cell lines lacking MTM1, PI3KC2β or both proteins were generated in order to obtain a cell-based model system for our study. This was achieved using the gene-engineering technique Clustered Regularly Interspaced Short Palindromic Repeats (CRISPR)-Cas9, which allows to modify genome sequences with great specificity. Broadly, CRISPR-Cas9 takes advantage on the *S. pyogenes*-derived endonuclease Cas9 capacity to be targeted to specific DNA sequences by a complementary single-stranded guide RNA (sgRNA). At double-strand DNA break sites produced by Cas9, non-homologous end joining (NHEJ) DNA repair mechanism results in random insertions or deletions, frequently leading to disrupted gene expression and/or function [229].

For generation of MTM1, PI3KC2β and double KO C2C12 cell lines, sgRNA targeting exon 1 of *Mus musculus Mtm1* (NM_001164190.1) and *Pik3c2b* (NM_001099276.2), which respectively encode for MTM1 and PI3KC2β, were designed. *Mtm1*-targeting sgRNA (5'-TAAGTATAATTCACACTCCT-3') and *Pik3c2b*-targeting sgRNA (5'-GTCTTCCACTCAGGGCAATG-3') were cloned into the Cas9-GFP plasmid px458-pSpCas9(BB)-2A-GFP (**Table 2-8**) by annealing the corresponding DNA oligonucleotides (**Table 2-6**) (see section 2.2.1.8), digesting the plasmid using BbsI (5' and 3') restriction sites (see section 2.2.1.9), and ligating the annealed oligonucleotides and plasmid (see section 2.2.1.10). Ligation product was transformed into chemically-competent *E. coli* (see section 2.2.1.11) and bacteria were cultured, seeded on LB-Agar plates for selection, and cultured for DNA plasmid extraction (see section 2.2.1.12). DNA was purified from transformed bacteria (see section 2.2.1.13) and sequenced (see section 2.2.1.15) in order to select clones that incorporated sgRNA sequences without errors. DNA concentration and purity was assessed as indicated (see section 2.2.1.14) prior to transfection.

C2C12 cells at passage 3 cultured in 10 cm plates were transfected using JetPrime reagent (see section 2.2.3.2.2) with px458 plasmid containing *Mtm1*- or *Pik3c2b*-targeting sgRNA inserts. For double KO cell line generation, both plasmids were transfected with the same total DNA quantity. 48h after transfection, GFP-expressing cells were sorted into 96-well plates containing GM at a density of 1 cell per well via fluorescence-activated single cell sorting (see section 2.2.3.9). GM media in these plates consisted on a 1:1 mix of fresh GM media (**Table 2-3**) and conditioned GM media, obtained by sterile-filtering media used for cultures of C2C12 over 24 h. Colonies were progressively expanded by culturing in plates of increasing diameter up to 6 cm, from which cell stocks of the selected clones were made (see section 2.2.3.1). A total of 20 potentially KO clonal cell lines per genotype were

screened for MTM1 and PI3KC2β loss via immunoblotting and sequencing (genotyping). For immunoblotting, C2C12 cultured in 6 cm plates were processed and analyzed as indicated in sections 2.2.2.1-2 and 2.2.2.4-5. Genotyping implied the detection of genetic alterations at sgRNA target site via sequencing and insertion-deletion (InDel) estimation. For this, gDNA was extracted from C2C12 cultured in 6 cm plates (see section 2.2.1.1) and regions containing *Mtm1* or *Pik3c2b*-sgRNA target sites were amplified by PCR (see section 2.2.1.3) using the indicated primers (**Table 2-6**). PCR products were then analyzed in a 1% agarose gel electrophoresis (see section 2.2.1.6), purified (see section 2.2.1.7), and sequenced using the same primers (see section 2.2.1.15). Considering C2C12 polyploidy, sequencing results were further analyzed using Synthego ICE CRISPR Analysis Tool (**Table 2-13**), revealing the following InDel scores: 93%, 19% and 47% at *Mtm1* target site of *Mtm1*KO #1, #2 and #3, respectively; 95% at *Pik3c2b* target site of *Pik3c2b*KO; 91% at *Mtm1* target site and 99% at *Pik3c2b* target site of double KO; and 77% at *Mtm1* target site and 78% at *Pik3c2b* target site of $Mtm1^{hypo}$/*Pik3c2b*KO.

2.2.3.6 Immunocytochemistry

Volumes of solutions used in all ICC protocols are indicated in **Table 2-24**. For total cell ICC, cells seeded on coverslips or ibiTreat chambers were washed once by aspirating the media and adding the indicated volumes of 1x PBS. After aspirating the 1x PBS, cells were fixed during 15 min at RT with 4% PFA fixative. For immunolabelling focal adhesion proteins, fixation was performed for 10 min with pre-cooled 4% fixative. Afterwards, fixed cells were washed 3 times with 1x PBS as described before and cellular membranes were permeabilized during 5 min at RT with 0.2% Triton X-100 diluted in 1x PBS. Cells were washed once with 1x PBS and an ICC blocking solution was added and incubated for 1 h at RT. Afterwards, coverslips were removed from the wells and carefully placed upside-down on a drop of primary antibodies diluted in ICC antibody solution inside a dark humidity chamber and incubated for 1 h. Coverslips were then carefully lifted and transferred to the cell culture plate, where they were washed twice with 1x PBS for 5 min. Incubation with secondary antibodies diluted in ICC antibody solution was performed as described for primary antibodies. Afterwards, coverslips were removed from the humidity chamber, placed in the plate and washed three times with 1x PBS for 10 min. Finally, cells were incubated for 10 min with 1 µg/mL DAPI diluted in 1x PBS, dipped three times in UP H_2O and mounted on an approximately 40 µL drop of Immu-mount (Thermo Fisher) on a labelled glass slide. Mounted slides were dried at RT for 2-4 h and stored at 4°C protected from light until imaging. For ibiTreat chambers, the same protocol was followed except for the fact that primary and secondary antibody solution was added directly to wells and mounting was not performed. Instead, wells were filled with 300 µLof 1x PBS and stored at 4°C until imaging.

For cell surface ICC, immunodetection of extracellular epitopes was performed on living cells incubated on ice in order to arrest membrane trafficking. This protocol was optimized and selected for surface ICC to avoid a fixation step prior to antibody incubation, as PFA induces membrane pore formation [230]. In preliminary tests (data not shown), we observed ICC signal of intracellular proteins in cells treated with fixative solution without cell permeabilization, and therefore decided to perform fixation after primary antibody incubation on ice. Therefore, cells were cooled for 10 min on ice and washed twice with ice-cold 1x PBS. Then, coverslips were removed from the cell culture plate and placed upside-down on a 60 µL drop of ice-cold S-ICC blocking and antibody solution containing primary antibodies and incubated for 30 min on ice. Coverslips were then placed in the plate, where they were washed once with 1x PBS at RT and immediately fixed for 10 min at RT with 4% fixative solution. Fixed

cells were washed three times with 1x PBS and incubated with secondary antibodies as described for blocking and primary antibodies, except on a 45 µL drop of solution. After this step, coverslips were processed as indicated for total cell ICC protocol.

For total PI(3)P, PI(4)P and PI(3,4)P_2 immunofluorescence staining, a protocol from Hammond *et al* [231] was followed. Cells seeded on coverslips were washed once with 1x PBS and fixed during 15 min at RT with 2% PFA fixative. Fixed cells were washed three times with 50 mM NH_4Cl diluted in 1x PBS and then cellular membranes were mildly permeabilized during 5 min at RT with 20 µM digitonin diluted in pipes-based buffer (PBB). Cells were washed three times with PBB and an ICC PBB-based blocking solution containing 0.25 µg/mL GFP-2xFYVE (Hrs) probe was added and incubated for 1 h at RT. Afterwards, cells were washed twice with PBB and coverslips were removed from the wells and carefully placed upside-down on a drop of primary ICC PBB-based antibody solution inside a dark humidity chamber, and incubated for 1 h. Coverslips were then carefully lifted from the humidity chamber and transferred to the cell culture plate, where they were washed twice with PBB for 5 min. Incubation with secondary antibody solution was performed as described for primary antibodies. Afterwards, coverslips were removed from the humidity chamber, placed back to the plate and washed four times with PBB during 5 min. Cells were then post-fixed at RT with 2% PFA fixative for 5 min, and then washed three times for 5 min with 50 mM NH_4Cl diluted in 1x PBS. Finally, cells were incubated for 10 min with 1 µg/mL DAPI diluted in 1x PBS, dipped three times in miQ H_2O and mounted on an approximately 40 µl drop of Immu-mount (Thermo Fisher) on a labelled glass slide. Mounted slides were dried at RT for 2-4h and stored at 4ºC protected from light until imaging.

Table 2-24. ICC solution volumes

Buffer or solution	Volume per coverslip or well (µL)		
	12-well, 18 mm coverslip		**ibiTreat 8-well chamber**
PFA, permeabilization solution, ICC blocking solution	500		300
ICC antibody solution	45		150 - 200
S-ICC blocking and antibody solution	Blocking and primary antibody	60	
	Secondary antibody	45	

2.2.3.7 Random migration assays

The migratory capacity of C2C12 myoblasts was measured in a random migration assay on a Matrigel-coated substrate. For this, ibiTreat 8-well chambers (ibidi) were coated with Matrigel (see section 2.2.3.1) for 1 h and myoblasts were seeded in GM at a density of 1000 cells per well (**Table 2-21**). After 4 h, GM was replaced with live cell imaging media (**Table 2-3**) supplemented with 0.5 µM SiR-DNA dye (Spirochrome). After 2 h, cells were imaged at 37°C and 5% CO_2 (Okolab) on a Nikon Ti Eclipse epifluorescence microscope using a 20x air (0.75 NA) objective for 10 h. Bright-field and epi-fluorescence (Cy5 filter) images were acquired in 10 min intervals at three

pre-set positions per well, with an average of 20 cells per position. Image stacks were processed and analyzed using TrackMate plug-in [232] in Fiji Image J software (**Table 2-13**).

2.2.3.8. Confocal fluorescence microscopy

ICC slides were routinely imaged on a Zeiss Laser Scanning confocal microscope (LSM) 710 or 780, controlled by Zeiss ZEN software, using a 40x or 60x immersion oil (1.3 NA) objective; a 10x air (0.3 NA) objective with maximum pinhole diameter was used for imaging of myotubes. Images of surface-immunolabelled cells were occasionally acquired on a Zeiss spinning disk confocal microscope controlled by Volocity v6.21 using a 40x immersion oil (1.3 NA) objective. A minimum of 12 images per condition and experiment were acquired. Generally, a single z-plane image was acquired except for cell surface ICC and lipid labelling experiments, in which a stack of several z-plane images with 0.7 µm spacing were acquired. These images were pre-processed by generating a maximum intensity projection of the stack, which was then quantified.

2.2.3.9 Flow cytometry

In this project, flow cytometry was performed in the context of cell volume measurements and generation of genetically-engineered cell lines. For the first application, C2C12 myoblasts cultured in 10 cm plates were rinsed with D-PBS and detached with a 5-min incubation at 37°C with TrypLE Express Enzyme. Cells were collected in tubes and washed by adding D-PBS and spinning down for 3 min at 500 rpm. Pelleted cells were resuspended in 1% fixative solution (**Table 2-4**) and incubated for 20 min at RT upon rotation for fixation. Three cycles of washes were repeated after fixation. Cells were filtered with cell strainer tubes before analysis using BD LSR Fortessa flow cytometer controlled by BD FACSDiva software (BD Biosciences) (**Table 2-13**). Forward scatter area (FCS-A) values after cell debris and aggregates filtration were used to calculate mean cell volume of each C2C12 cell line.

In the context of CRISPR-Cas-engineered cell line generation, C2C12 myoblasts transfected with sgRNA-Cas9-GFP DNA plasmid (**Table 2-8**) were sorted to obtain clonal cell lines. As the mentioned vector encodes for a GFP reporter, GFP-positive cells were single-sorted into 96-well plates using BD FACSAria flow cytometer controlled by BD FACSDiva software (BD Biosciences) (**Table 2-13**). Via application of gating filters, a population of cells with intermediate GFP expression and average cell morphology parameters, identified by forward scatter (FCS) and side scatter (SSC) values, was selected for sorting. Cells with very low or high GFP expression were excluded from the sorting, as well as cells with aberrant morphology and cell debris.

2.2.4. Image and statistical analysis

Fiji Image J software (**Table 2-13**) was used for image processing and analysis, mostly semi-automatically via application of self-designed macros (available upon request). Mean intensity values per cell were quantified, expressed as fluorescence intensity (integrated density) within a cell divided by cell area values. Cell area was calculated using cytoskeletal protein F-actin labelled with Alexa Fluor-conjugated Phalloidin (**Table 2-11**) to define the cell outline; these images are not shown in figures. Surface immunolabelling was not normalized to cell area and was therefore expressed as fluorescence intensity (integrated density) per cell. Number of focal adhesions per cell was calculated dividing the number of focal adhesions to the number of DAPI-positive nuclei

per image. PI(3)P, PI(4)P and PI(3,4)P_2 were quantified as total intensity (integrated density) per image divided by the average cell area in a condition. A threshold was applied to subtract unspecific fluorescent signals

GraphPad Prism 5.0 software or Microsoft Excel were used for statistical analysis (**Table 2-13**). Values are depicted as mean ± SD for each condition in comparison to a control group, whose mean was set to 1 for normalization purposes. One-sample two-sided t-tests were used to compare two groups, as controls normalized to 1 do not fulfill the requirement of two-sample t-tests. One-way analysis of variance (ANOVA) with Dunnet's or Tukey's multiple-comparison tests were used to compare three or more groups after the same normalization. The level of significance is indicated in the figures by asterisks (* $p < 0.05$; ** $p < 0.01$; *** $p < 0.001$; **** $p < 0.0001$) and provided in the figure legends as the exact p-value obtained by the indicated statistical test. No statistical method was used to pre-determine sample size as sample sizes were not chosen based on pre-specified effect size. Instead, multiple independent experiments were carried out using several sample replicates as detailed in the figure legends.

Additional methods: This thesis does not include Materials and Methods corresponding to experimental data obtained by Philipp A. Koch and Wen-Ting Lo (Fig. 3-1 A; 3-2 D; 3-11 E; 3-24; 3-25 A-C.).

3. Results

The main goal of this study was to elucidate the molecular mechanism underlying the functional interplay between MTM1 and PI3KC2β in the context of XLCNM. A genetic interaction between the two PI-metabolizing enzymes was reported in animal models [42,85], yet remained elusive at the cellular level. Consequently, we aimed to identify and characterize phenotypes associated to MTM1 loss in cells and investigate whether these were restored by co-depletion of PI3KC2β, as reported in organismal models.

3.1. Myoblastic cell line C2C12 and CRISPR-engineered cellular models

3.1.1 Murine myoblastic cell line C2C12 as a model

The murine myoblastic cell line C2C12 was selected in this project as a model to study the cellular functions of MTM1 and PI3KC2β, with the goal of mimicking the context in which XLCNM rescue by PI3KC2β depletion was described in mouse models (see section 1.6). C2C12 were established by Blau *et al* [233] as a subclone of the C2 cell line generated by Yaffe *et al* [234]. Yaffe *et al* originally isolated satellite cells from a thigh muscle of a 2-month-old female mouse and subjected them to selective serial passages to obtain homogeneous and proliferative cultures. Subclonal selection by Blau *et al* aimed to isolate a line which behaved as a myoblast progenitor, with the ability to spontaneously differentiate into myotubes upon serum removal. This feature of C2C12 turns them into suitable *in vitro* models to study physiological processes such as myogenic differentiation, as well as the cellular insights of skeletal muscle pathology. C2C12 is a hypo-tetraploid cell line that harbors four copies of nearly all chromosomes, including the X chromosome [235], an attribute that may hinder the efficiency of genetic modifications.

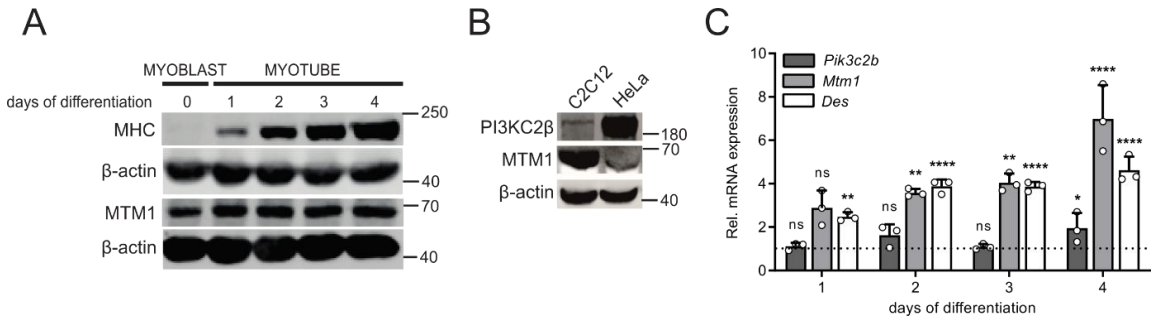

Figure 3-1. Mouse myoblastic cell line C2C12 as a model to study MTM1 and PI3KC2β biology: expression levels during myogenesis. (A) MHC and MTM1 protein levels in C2C12 myoblasts and differentiating myotubes detected by immunoblotting. β-actin was used as a loading control. **(B)** PI3KC2β and MTM1 protein levels in C2C12 myoblasts and HeLa cells detected by immunoblotting. β-actin was used as a loading control. **(C)** Relative mRNA expression levels of *Pik3c2b*, *Mtm1* and *Desmin* (*Des*) in differentiating myotubes detected by qPCR. *Csnk2a2* expression was used for normalization. Mean ± SD from 3 independent experiments represented as fold change compared to control (differentiation day 0 – myoblasts, not shown) with a mean of 1. One-way analysis of variance (ANOVA; F = 3.281) and Dunnett's multiple-comparison test for *Pik3c2b*; day 0 vs day 1 n.s. p = 0.9871, day 0 vs day 2 n.s. p = 0.2216, day 0 vs day 3 n.s. p = 0.9946, day 0 vs day 4 *p = 0.0451. One-way analysis of variance (ANOVA; F = 21.75) and Dunnett's multiple-comparison test for *Mtm1*; day 0 vs day 1 n.s. p = 0.0525, day 0 vs day 2 **p = 0.0095, day 0 vs day 3 **p = 0.0032, day 0 vs day 4 ****p < 0.0001. One-way analysis of variance (ANOVA; F = 54.35) and Dunnett's multiple-comparison test for *Desmin*; day 0 vs day 1 **p = 0.0011, day 0 vs day 2 ****p < 0.0001, day 0 vs day 3 ****p < 0.0001, day 0 vs day 4 ****p < 0.0001. **(A)** Data obtained by P.A.K.

To initially characterize the suitability of C2C12 for this project, the mRNA and protein expression of MTM1 and PI3KC2β were analyzed in myoblasts and during early myogenic differentiation (days 0 to 4). Immunoblotting for MTM1 and myosin heavy chain (MHC), a subunit of the myotube-specific myosin II used as a differentiation marker [236], revealed an increase of MTM1 protein expression upon differentiation, visible on day 1 and stable until day 4 (**Fig. 3-1 A**), as reported in other studies [237]. Due to low PI3KC2β protein expression in C2C12, as shown in comparison to HeLa cells (**Fig. 3-1 B**), expression of *Pik3c2b* mRNA was evaluated. Quantitative PCR (qPCR) analysis showed that, upon differentiation, indicated by increasing expression of differentiation marker desmin (*Des*), *Mtm1* expression increased significantly from day 1, as observed by immunoblotting. In contrast, *Pik3c2b* expression remained unchanged until day 4, when a minor increase was observed (**Fig. 3-1 C**). The observation of increasing *Mtm1* and unchanged *Pik3c2b* expression in early differentiation favored the hypothesis that the two enzymes may act on distinct molecular pathways, rather than as a protein complex. Altogether, these results provided initial information on the abundance of our proteins of interest, and anticipated potential limitations associated to the low expression levels of PI3KC2β. C2C12 were selected as a suitable model for the generation of genetically-engineered clonal cell lines, and measures to overcome the model's potential limitations were taken throughout the project.

3.1.2 Generation of CRISPR-engineered *Mtm1*KO, *Pik3c2b*KO and double KO C2C12 cell lines

Clonal C2C12 cell lines lacking MTM1, PI3KC2β or both proteins were generated with the aim of studying their roles in the context of XLCNM pathogenesis and its rescue. This was achieved by applying the gene-engineering technique CRISPR-Cas9, which allows the modification of specific genome sequences with high precision using a simple technology. For this, each of the indicated (**Fig. 3-2 A**) synthetic sgRNA sequences were cloned into plasmid vectors encoding for Cas9 and GFP as an expression reporter. The selected sgRNA sequences targeted the second exon of the corresponding genes. As indicated schematically, C2C12 myoblasts were transfected, GFP-positive cells were single-sorted into 96-well plates and cultures were expanded. Double KO cell lines were generated by transfecting both *Mtm1*- and *Pik3c2b*-targeting plasmids. Screening of KO clones was performed via immunoblotting and genotyping. A detailed technical description can be found in Materials & Methods (section 2.2.3.5).

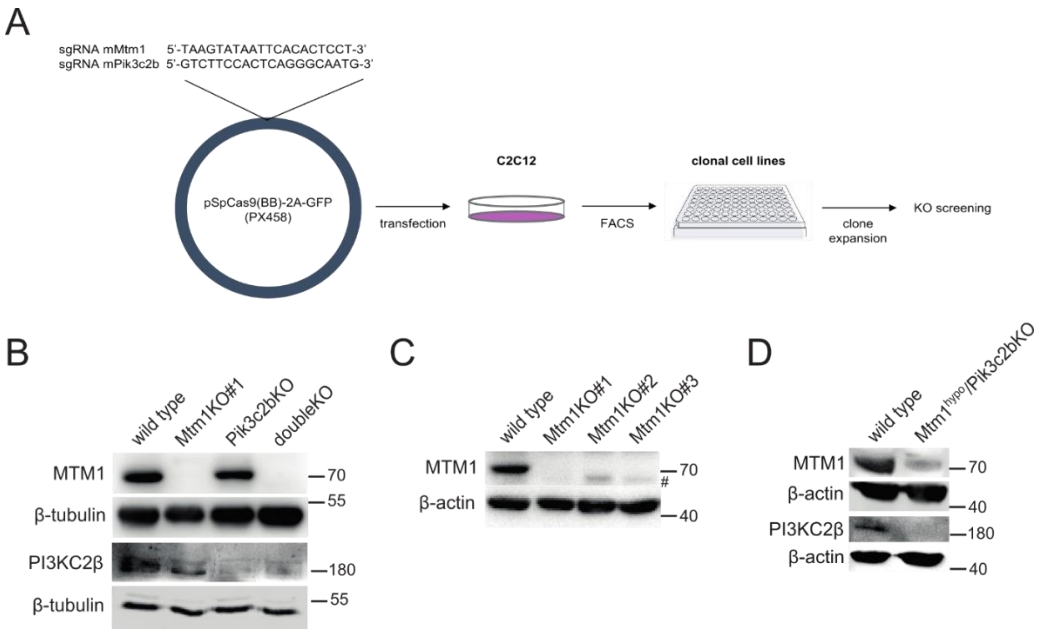

Figure 3-2. Generation of CRISPR-engineered *Mtm1*KO, *Pik3c2b*KO, double KO, and double hypomorphic/KO C2C12 cell lines. (A) Schematic representation of CRISPR cell line generation workflow. See section 2.2.3.5 for detailed methodology. **(B)** MTM1 and PI3KC2β protein levels in wild type (WT) and CRISPR-Cas9-engineered knockout C2C12 clones lacking MTM1 (Mtm1KO#1), PI3KC2β (Pik3c2bKO) or both enzymes (doubleKO) detected by immunoblotting. β-tubulin was used as a loading control. **(C)** MTM1 protein levels in wild type (WT) and CRISPR-Cas9-engineered Mtm1 knockout C2C12 clones #1, #2 and #3 (Mtm1KO#1-3) detected by immunoblotting. β-actin was used as a loading control. **(D)** MTM1 and PI3KC2β protein levels in wild type (WT) and CRISPR-Cas9-engineered C2C12 clones with partial MTM1 and depleted PI3KC2β expression ($Mtm1^{hypo}$/Pik3c2bKO) detected by immunoblotting. β-actin was used as a loading control. **(D)** Data obtained by P.A.K.

After the screening process, clonal cell lines lacking expression of MTM1 (*Mtm1*KO #1), PI3KC2β (*Pik3c2b*KO) or both proteins (double KO) were selected and used throughout the project (**Fig. 3-2 B**) together with wild type (WT) cells. Two additional *Mtm1*KO clones (*Mtm1*KO #2 and *Mtm1*KO #3) (**Fig. 3-2 C**) and one additional clone with partial MTM1 expression and depleted PI3KC2β (*Mtm1*^{hypo}/*Pik3c2b*KO), referred as double hypomorphic/KO clone (**Fig. 3-2 D**) were selected to strengthen reproducibility and detect potential clonal cell line effects.

3.2 Characterization of cell-based models of XLCNM

3.2.1 Loss of MTM1 leads to cell spreading defects in C2C12 myoblasts

A phenotype of *Mtm1*KO myoblasts in culture, initially observed during the screening process, was a reduced cell area compared to WT. Cell area of WT and *Mtm1*KO C2C12 myoblasts seeded on Matrigel-coated coverslips was measured by immunostaining of F-actin using Alexa-conjugated Phalloidin. Confocal microscopy images were taken, scaled, and analyzed by outlining the cell's perimeter using F-actin as a mask, thereby allowing the calculation of cell areas. A significant decrease in cell area was observed in *Mtm1*KO #1-3 in comparison to WT (**Fig. 3-3 A**). As represented in the scheme (**Fig. 3-3 B**), reduced cell area can be indicative of either a decreased cell volume or a defective cell spreading, defined as the capacity of cells to attach to their culture substrate. Correspondingly, two cells with equal volumes (a, b), could have smaller (a) or larger (b) cell area depending on their decreased or increased spreading capacity, respectively. To elucidate which of these factors was affected in *Mtm1*KO myoblasts, flow cytometric analysis was used to measure relative cell volumes, which revealed no differences between WT and *Mtm1*KO (**Fig. 3-3 C**), suggesting the spreading capacity of *Mtm1*KO cells to be

altered. Additionally, the recurrent observation of fewer *Mtm1*KO than WT cells retained after routine culture passaging as well as during immunocytochemistry experiments further suggested that cells lacking MTM1 display decreased adhesion capacity and are more prone to detach from their substrate upon washing. To provide quantitative evidence of the hypothesized spreading defect, the cell area to volume ratio was calculated, showing *Mtm1*KO myoblasts to have significantly lower ratios than WT myoblasts (**Fig. 3-3 D**), thereby confirming that *Mtm1*KO myoblasts have a decreased capacity to spread on a Matrigel substrate in comparison to WT myoblasts.

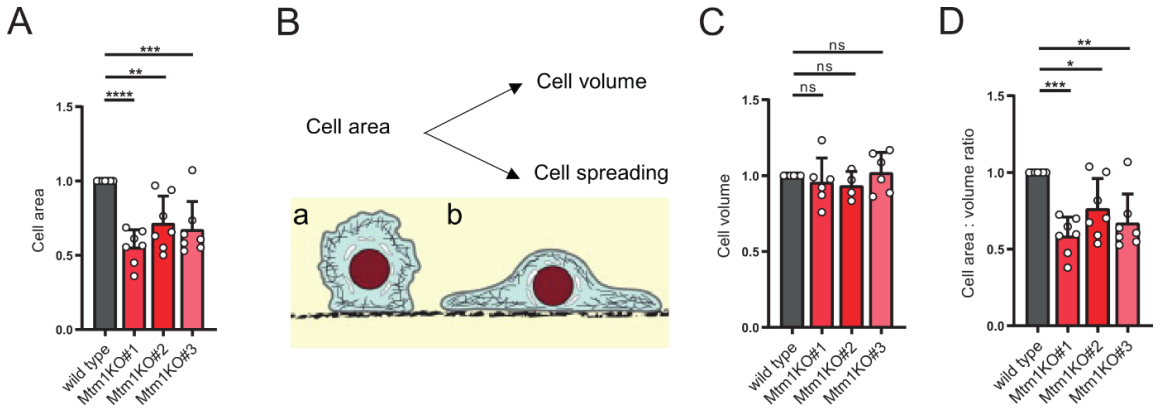

Figure 3-3. MTM1 loss decreases cell spreading capacity in C2C12 myoblasts. (A) Cell area of WT and Mtm1KO C2C12 myoblasts measured using F-actin immunostaining as a mask (not shown). Mean ± SD from 7 independent experiments represented as fold change compared to control (wild type) with a hypothetical mean of 1. One-way analysis of variance (ANOVA; F = 12.09) and Dunnett's multiple-comparison test; WT vs Mtm1KO#1 ****p < 0.0001, WT vs Mtm1KO#2 **p = 0.0031, WT vs Mtm1KO#3 ***p = 0.0008. **(B)** Illustration of the correlation between cell area, cell volume and cell spreading, representing two cells of equal volume with (a) decreased cell spreading and (b) increased cell spreading. **(C)** Cell volume of WT and Mtm1KO C2C12 myoblasts measured as forward scatter values obtained by flow cytometry. Mean ± SD from 4 independent experiments represented as fold change compared to control (wild type) with a hypothetical mean of 1. One-way analysis of variance (ANOVA; F = 0.588) and Dunnett's multiple-comparison test; WT vs Mtm1KO#1 n.s. p = 0.8695, WT vs Mtm1KO#2 n.s. p = 0.7194, WT vs Mtm1KO#3 n.s. p = 0.9796. **(D)** Relative cell area to volume ratio of WT and Mtm1KO C2C12 myoblasts measured normalizing cell area values to mean forward scatter values obtained by flow cytometric analysis. Mean ± SD from 7 independent experiments represented as fold change compared to control (wild type) with a hypothetical mean of 1. One-way analysis of variance (ANOVA; F = 9.795) and Dunnett's multiple-comparison test; WT vs Mtm1KO#1 ***p = 0.0001, WT vs Mtm1KO#2 n.s. p = 0.1342, WT vs Mtm1KO#3 **p = 0.0016.

3.2.2 Loss of MTM1 causes defective cell adhesion in C2C12 myoblasts

The main mechanism that mediates cell to ECM adhesion, and thereby cell spreading in culture, are focal adhesions (FA) (see section 1.4). To investigate whether *Mtm1*KO C2C12 cells presented alterations in FA, myoblasts seeded on a Matrigel matrix were immunostained for FA components paxillin, vinculin, phosphorylated FAK (pFAK) and zyxin, and the number of FA per cell as well as FA area were quantified. As shown in representative images, both the number and morphology of FA in MTM1-depleted myoblasts was altered compared to WT, with similar observations using different markers. Morphological changes included decreased size and intensity, generally indicative of a lack of FA maturity associated to either decreased delivery or increased turnover of FA components. Of note, cell area was decreased as previously shown quantitatively (**Fig. 3-4 A, D-F**). The number of focal adhesions per cell in *Mtm1*KO #1 was significantly reduced compared to WT, a phenotype that was consistent in immunostainings for FA markers paxillin, vinculin, pFAK and zyxin (**Fig. 3-4 B, G, I, K**). *Mtm1*KO #2 and #3 cell lines showed a similar decrease in FA number with paxillin immunostaining (**Fig. 3-4 B**), indicating consistency among clonal cell lines. Having already described a cell spreading defect in MTM1-

depleted myoblasts, a reduced number of FA per cell associated impaired spreading to abnormal cell adhesion via FAs. Data on FA area were more variable, as quantification using FA markers paxillin and zyxin evidenced no changes in MTM1-depleted myoblasts compared to WT (**Fig. 3-4 C, L**), whereas pFAK labelling revealed a decrease in FA size in *Mtm1*KO #1 myoblasts (**Fig. 3-4 J**). Quantification with vinculin as well showed a tendency to decrease despite lack of statistical significance (**Fig. 3-4 H**). Altogether, these data indicated that myoblasts lacking MTM1 adhere to their culture substrate via immature FAs, as shown by reduced size and poor accumulation of FA components. A reduced number of FA per cell associates to either decreased FA formation or rapid turnover, thus suggesting impaired trafficking of FA proteins and potential effects in migratory capacity in these cells.

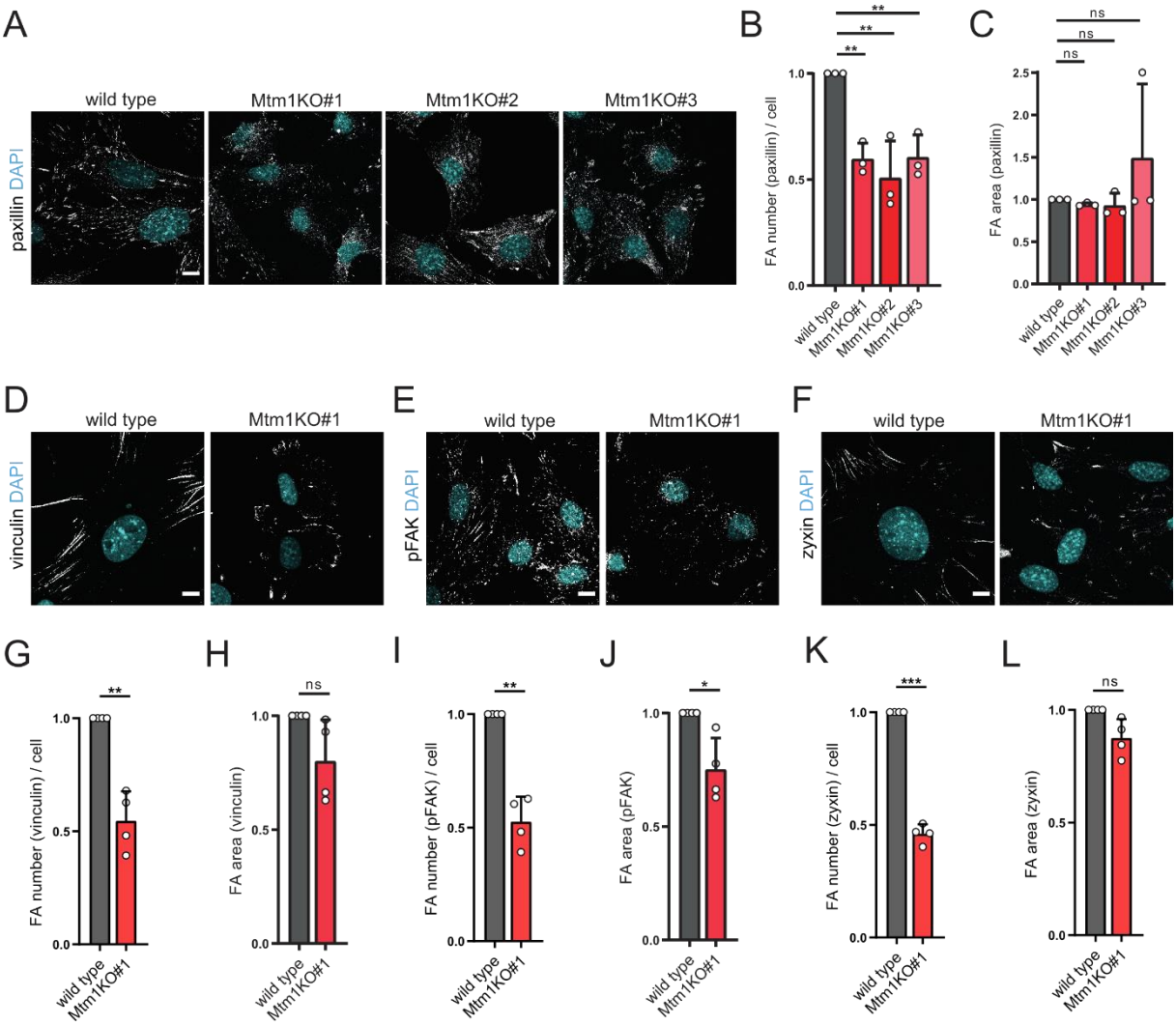

Figure 3-4. MTM1 loss reduces number of focal adhesions in C2C12 myoblasts. (A) Representative images of WT and Mtm1KO C2C12 myoblasts immunostained for paxillin as a focal adhesion (FA) marker and DAPI for nuclear staining. Scale bar 10µm. **(B)** Number of FA per cell in WT and Mtm1KO C2C12 myoblasts measured using paxillin as FA marker. Mean ± SD from 3 independent experiments represented as fold change compared to control (wild type) with a hypothetical mean of 1. One-way analysis of variance (ANOVA; F = 12.33) and Dunnett's multiple-comparison test; WT vs Mtm1KO#1 **p = 0.0048, WT vs Mtm1KO#2 **p = 0.0014, WT vs Mtm1KO#3 **p = 0.0054. **(C)** FA area in WT and Mtm1KO C2C12 myoblasts measured using paxillin as FA marker. Mean ± SD from 3 independent experiments represented as fold change compared to control (wild type) with a hypothetical mean of 1. One-way analysis of variance (ANOVA; F = 1.098) and Dunnett's multiple-comparison test; WT vs Mtm1KO#1 n.s. p = 0.9965, WT vs Mtm1KO#2 n.s. p = 0.9940, WT vs Mtm1KO#3 n.s. p = 0.4380. **(D)** Representative images of WT and Mtm1KO#1 C2C12 myoblasts immunostained for vinculin as a focal adhesion (FA) marker

and DAPI for nuclear staining. Scale bar 10µm. **(E)** Representative images of WT and Mtm1KO#1 C2C12 myoblasts immunostained for phosphorylated (Y397) focal adhesion kinase (pFAK) as a focal adhesion (FA) marker and DAPI for nuclear staining. Scale bar 10µm. **(F)** Representative images of WT and Mtm1KO#1 C2C12 myoblasts immunostained for zyxin as a focal adhesion (FA) marker and DAPI for nuclear staining. Scale bar 10µm. **(G)** Number of FA per cell in WT and Mtm1KO#1 C2C12 myoblasts measured using vinculin as FA marker. Mean ± SD from 4 independent experiments represented as fold change compared to control (wild type) with a hypothetical mean of 1. Unpaired two-tailed t test; **p = 0.0062. **(H)** FA area in WT and Mtm1KO#1 C2C12 myoblasts measured using vinculin as FA marker. Mean ± SD from 4 independent experiments represented as fold change compared to control (wild type) with a hypothetical mean of 1. One-sample two-tailed t test; n.s. p = 0.1162. **(I)** Number of FA per cell in WT and Mtm1KO#1 C2C12 myoblasts measured using pFAK as FA marker. Mean ± SD from 4 independent experiments represented as fold change compared to control (wild type) with a hypothetical mean of 1. One-sample two-tailed t test; **p = 0.0033. **(J)** FA area in WT and Mtm1KO#1 C2C12 myoblasts measured using pFAK as FA marker. Mean ± SD from 4 independent experiments represented as fold change compared to control (wild type) with a hypothetical mean of 1. Unpaired two-tailed t test; *p = 0.0373. **(K)** Number of FA per cell in WT and Mtm1KO#1 C2C12 myoblasts measured using zyxin as FA marker. Mean ± SD from 4 independent experiments represented as fold change compared to control (wild type) with a hypothetical mean of 1. One-sample two-tailed t test; ***p = 0.0001. **(L)** FA area in WT and Mtm1KO#1 C2C12 myoblasts measured using zyxin as FA marker. Mean ± SD from 4 independent experiments represented as fold change compared to control (wild type) with a hypothetical mean of 1. One-sample two-tailed t test; n.s. p = 0.0585.

β1-integrin, the most abundant subunit of the fundamental transmembrane component of FAs [156], was also analyzed by immunostaining. To distinctively quantify integrin at functional, ECM-engaged adhesions, a surface immunostaining of activated β1-integrin was performed using an antibody recognizing an extracellular epitope. It revealed changes in size, intensity, and distribution of activated β1-integrin in *Mtm1*KO compared to WT myoblasts: whereas WT cells displayed an intense and directional filamentous staining along all the cell surface and perimeter, MTM1-depleted cells displayed fewer and fainter adhesions lacking a distribution pattern, and only localized at cell edges (**Fig. 3-5 A**). Quantitatively and in accordance with the data on FA, surface activated β1-integrin was significantly reduced in *Mtm1*KO myoblasts compared to WT (**Fig. 3-5 B**). In contrast, no quantitative differences were observed in total levels of β1-integrin (**Fig. 3-5 C**), evaluated with a total cell immunostaining of β1-integrin that resulted in detection of active and inactive β1-integrin at the cell surface as well as intracellularly. Nevertheless, qualitative observation of total β1-integrin revealed prominent differences in its distribution: WT myoblasts displayed a pattern of directional filaments along the plasma membrane, highly similar to those observed in surface active β1-integrin staining and likely corresponding to integrin adhesions. In contrast, a mainly perinuclear accumulation of total β1-integrin was observed in *Mtm1*KO cells, rarely following the expected adhesion distribution pattern described before (**Fig. 3-5 A**). FA and β1-integrin data altogether indicated that the cell spreading defect observed upon MTM1 depletion (**Fig. 3-3**) are due to cell adhesion defects. Considering surface active β1-integrin data, we hypothesized cell adhesion defects to derive either from impaired plasma membrane delivery or from increased turnover of β1-integrins, processes that would subsequently lead to abnormal FA dynamics. Strong evidence supporting a role of MTM1 in cargo exocytosis from endosomes [83], which also affected integrins, indicated that cell adhesion defects in *Mtm1*KO myoblasts were likely due to impaired β1-integrin recycling.

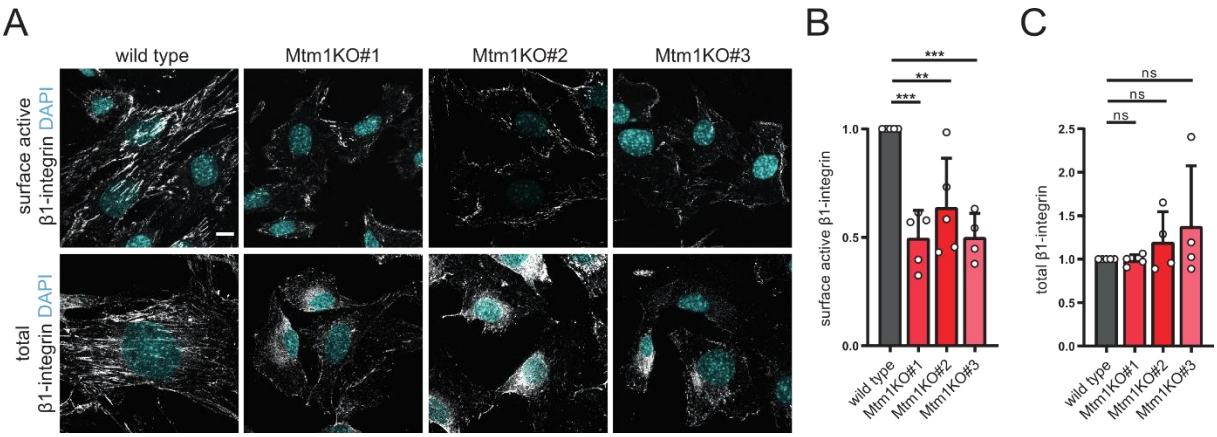

Figure 3-5. MTM1 loss decreases β1-integrin adhesions. (A) Representative images of WT and Mtm1KO C2C12 myoblasts immunostained under non-permeabilizing conditions for active β1-integrin (upper panel), permeabilizing conditions for β1-integrin (lower panel), and DAPI for nuclear staining (both). Scale bar 10µm. **(B)** Surface active β1-integrin intensity per cell in WT and Mtm1KO C2C12 myoblasts. Mean ± SD from 5 independent experiments represented as fold change compared to control (wild type) with a hypothetical mean of 1. One-way analysis of variance (ANOVA; F = 13.12) and Dunnett's multiple-comparison test; WT vs Mtm1KO#1 ***p = 0.0002, WT vs Mtm1KO#2 **p = 0.0033, WT vs Mtm1KO#3 ***p = 0.0003. **(C)** β1-integrin intensity in WT and Mtm1KO C2C12 myoblasts. Mean ± SD from 4 independent experiments represented as fold change compared to control (wild type) with a hypothetical mean of 1. One-way analysis of variance (ANOVA; F = 1.014) and Dunnett's multiple-comparison test; WT vs Mtm1KO#1 ***p > 0.9999, WT vs Mtm1KO#2 n.s. p = 0.7896, WT vs Mtm1KO#3 n.s. p = 0.3526.

In the model proposed by Ketel *et al* [83], phosphatase activity of MTM1 is necessary for its function in exocyst-dependent exocytosis. Therefore, we aimed to determine the relevance of MTM1 catalytic activity on the described adhesion phenotype. For this purpose, mCherry-tagged human MTM1, mCherry-tagged phosphatase inactive mutant (C375S), or an mCherry vector used as a control were overexpressed in *Mtm1*KO #1 myoblasts, and a surface immunostaining for activated β1-integrin was performed. Overexpression of wild type, but not phosphatase-inactive MTM1 nor mCherry was able to rescue the decreased surface active β1-integrin observed upon MTM1 loss, as shown in immunostaining images (**Fig. 3-6 A**) as well as quantitatively (**Fig. 3-6 B**). These results suggested that restoring of MTM1 catalytic activity is necessary and sufficient for the rescue of integrin adhesion defects of *Mtm1*KO myoblasts, thus evidencing a key role of MTM1-mediated PI(3)P turnover in determining adhesion defects in these cells.

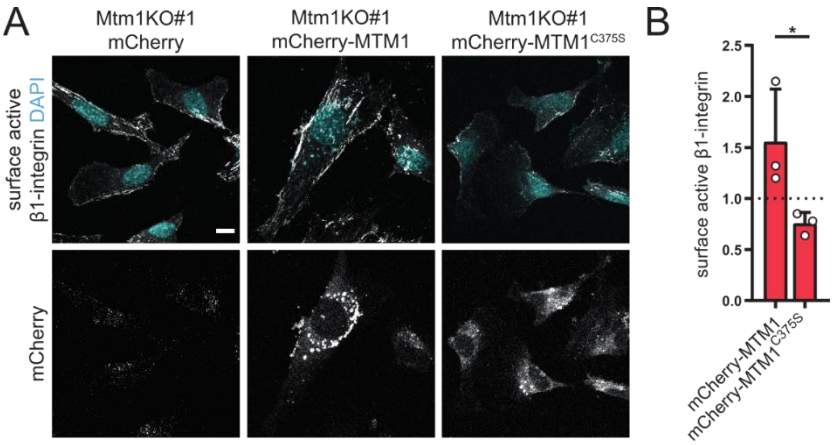

Figure 3-6. Decreased β1-integrin adhesion upon MTM1 loss is phosphatase activity-dependent. (A) Representative images of Mtm1KO#1 C2C12 myoblasts overexpressing mCherry, mCherry-MTM1 or phosphatase inactive (C375S) mCherry-MTM1, immunostained under non-permeabilizing conditions for active β1-integrin and DAPI for nuclear staining. Scale bar 10µm. **(B)** Surface active β1-integrin intensity per cell in Mtm1KO#1 C2C12 myoblasts overexpressing mCherry, mCherry-MTM1 or phosphatase inactive (C375S) mCherry-MTM1. Mean ± SD from 3 independent experiments represented as fold change compared to control (mCherry) with a hypothetical mean of 1. One-way analysis of variance (ANOVA; F = 5.422) and Tukey's multiple-comparison test; mCherry-MTM1 vs mCherry-MTM1^{C375S} *p = 0.0419.

3.2.3 Defective cell adhesion upon MTM1 loss enhances migration of C2C12 myoblasts

Cell adhesions are fundamental components mediating the process of cell migration (see section 1.4). Detection of a β1-integrin adhesion defect in *Mtm1*KO myoblasts led us to hypothesize an altered migratory capacity in these cells. Thus, a random cell migration assay, in which cells are allowed to freely migrate on their culture substrate, was performed to identify differences in migration on a Matrigel matrix. The migrated distance over 10 h was used to calculate an average cell migration speed. This analysis revealed that *Mtm1*KO #1 myoblasts migrated longer distances compared to WT (**Fig. 3-7 A**), corresponding to an increase in their migration speed (**Fig. 3-7 B**). These results suggested that MTM1-depleted myoblasts were either unable to form stable and mature adhesions, or displayed increased adhesion turnover, in both cases leading to an enhancement of their migratory capacity. Although our previous assessment of cell adhesion in *Mtm1*KO did not determine the scenario leading to altered migration, evidence supporting a role of MTM1 in β1-integrin exocytosis suggested that *Mtm1*KO cells suffer from impaired plasma membrane delivery of FA components, thus altering FA dynamics and migration.

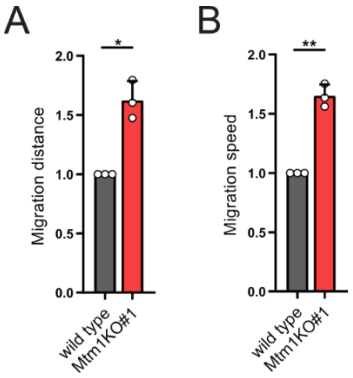

Figure 3-7. MTM1 loss enhances cell migration in C2C12 myoblasts. (A) Migration distance of WT and Mtm1KO#1 C2C12 myoblasts on a Matrigel matrix. Mean ± SD from 3 independent experiments represented as fold change compared to control (wild type) with a hypothetical mean of 1. One-sample two-tailed t test; *p = 0.0216. **(B)** Random migration speed of WT and Mtm1KO#1 C2C12 myoblasts on a Matrigel matrix. Mean ± SD from 3 independent experiments represented as fold change compared to control (wild type) with a hypothetical mean of 1. One-sample two-tailed t test; **p = 0.0074.

3.2.4 Loss of MTM1 leads to impaired myogenesis in C2C12

Considering the important role of cell adhesions and migration in myotube differentiation [157], we hypothesized that *Mtm1*KO cells could present differentiation defects. To investigate this, WT and *Mtm1*KO C2C12 were differentiated for 7 days and immunostained with MHC as an indicator of late differentiation. Important morphological differences between WT and *Mtm1*KO myotubes were observed: whereas WT cells were elongated and multinucleated, following an expected morphological pattern according to the literature, *Mtm1*KO myotubes mostly presented an ovoid and irregular morphology with one or few nuclei (**Fig. 3-8 A**). As polynucleation is characteristic of differentiation, it was quantified as differentiation index (number of nuclei per MHC-positive cell), a common method for quantifying *in vitro* muscle cell differentiation. Whereas WT myotubes had an average of 3.2 nuclei, *Mtm1*KO myotubes were mostly uni- or bi-nucleated, with an average of 1.5-1.6 nuclei per cell, implying a significant decrease of differentiation index in comparison to WT (**Fig. 3-8 B**). In conclusion, these data indicated that loss of MTM1 leads to a myoblast to myotube differentiation impairment, thus reproducing a hallmark of XLCNM observed in *in vivo* disease models, which display profound tissue maintenance defects associated to impaired migration and differentiation of progenitor cells [170].

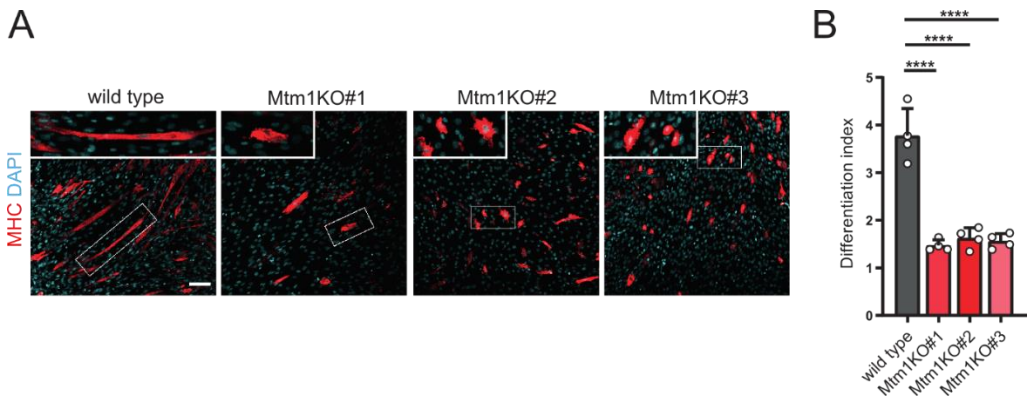

Figure 3-8. MTM1 loss impairs myoblast to myotube differentiation in C2C12. (A) Representative images of WT and Mtm1KO C2C12 myotubes differentiated for 7 days and immunostained for myosin heavy chain (MHC) as a differentiation marker and DAPI for nuclear staining. Scale bar 100µm. Selections correspond to 400µm x 100µm (wild type) or 200µm x 100µm (Mtm1KO) images. **(B)** Myotube differentiation index of WT and Mtm1KO C2C12 expressed as number of nuclei per MHC-positive cell. Mean ± SD from 4 independent experiments compared to control (wild type). One-way analysis of variance (ANOVA; F = 48.53) and Dunnett's multiple-comparison test; ****p < 0.0001.

3.2.5 Loss of MTM1 leads to accumulation of its substrate PI(3)P in C2C12 myoblasts

MTM1 is a phosphatidylinositol 3-phosphatase mainly acting on PI(3)P. An accumulation of MTM1 substrate has been observed in numerous *in vitro* and *in vivo* models of XLCNM (see section 1.3.2). With the aim of determining whether an accumulation of PI(3)P was present in our models, the purified PI(3)P-binding protein GFP-2xFYVE was used for its immunodetection on intracellular membranes. Although a similar and predominantly perinuclear PI(3)P distribution was observed in WT and *Mtm1*KO myoblasts (**Fig. 3-9 A**), quantitative analysis revealed a significant increase of GFP-2xFYVE signal in the latter compared to WT (**Fig. 3-9 D**). To control for specificity of the GFP-2xFYVE labelling, WT C2C12 myoblasts were treated with DMSO or VPS34-IN1, an inhibitor of the main PI(3)P-synthesizing enzyme on endosomes and phagophores, VPS34 [238] (see section 1.5.2), and immunostained with the probe. An absence of GFP-2xFYVE signal in VPS34-IN1-treated cells confirmed its specificity (**Fig. 3-9 H**). Moreover, a range of GFP-2xFYVE protein concentrations was tested to guarantee an optimal 0.25 µl/mL experimental concentration for immunostaining, corresponding to a signal within a dynamic range (**Fig. 3-9 G**).

To assess the effect of MTM1 depletion on other phosphatidylinositol 3-phosphates, an antibody against PI(3,4)P_2 was used to assess its quantity and localization pattern via an intracellular immunostaining. Homogeneously distributed cytoplasmic puncta were equally observed in WT and *Mtm1*KO myoblasts, visibly more intense in *Mtm1*KO #1 (**Fig. 3-9 B**). Quantitatively, a significantly increased signal was observed in *Mtm1*KO #1 compared to WT, but not in #2 or #3, where mild increases were non-significant (**Fig. 3-9 E**). To explore whether this unexpected PI(3,4)P_2 accumulation in *Mtm1*KO #1 was a phenotype associated to MTM1 loss or to other causes, we focused on class I PI3Ks, the main source of PI(3,4)P_2 after turnover of PI(3,4,5)P_3 by 5-phosphatases (**Fig. 1-1;** see section 1.5.1). The fact that the expression of PI3KC2α and PI3KC2β, the other potential sources of PI(3,4)P_2, was mildly decreased in *Mtm1*KO #1 myoblasts (**Fig. 3-2 B**; **3-11 D**) indicated that class II PI3Ks were unlikely related to the observed phenotype. Interestingly, class I PI3Kγ has been reported to promote β1-integrin activation in myeloid cells [239,240]. Since *Mtm1*KO cells displayed adhesion defects associated to decreased active β1-integrin, we hypothesized that they could harbor PI3Kγ gain-of-function alterations as a compensatory mechanism, thus promoting integrin activation and adhesion formation via a PI(3,4)P_2 increase.

To test this hypothesis, we analyzed mRNA expression of *Pik3cg*, the gene encoding for PI3Kγ, in WT and *Mtm1*KO #1 myoblasts in comparison to NIH-3T3, used as a positive control for expression as this murine embryonic fibroblast cell line has been reported to express PI3Kγ at low levels [241]. qPCR analysis (N=2) evidenced a 5-fold increased expression in MTM1-depleted myoblasts compared to WT (**Fig. 3-10**), suggesting that the PI(3,4)P_2 increase in *Mtm1*KO clone #1 is likely due to enhanced class I PI3Kγ signaling. We therefore concluded that MTM1 loss was not associated to PI(3,4)P_2 accumulation in this cell line. A control for PI(3,4)P_2 antibody specificity was performed by treating WT C2C12 myoblasts with DMSO or pan-PI3K inhibitor wortmannin, and immunostaining for PI(3,4)P_2, which resulted in an almost complete absence of signal (**Fig. 3-9 I**). PI(3,5)P_2 abundance was not analyzed due to the unavailability of suitable probes or antibodies for immunostaining.

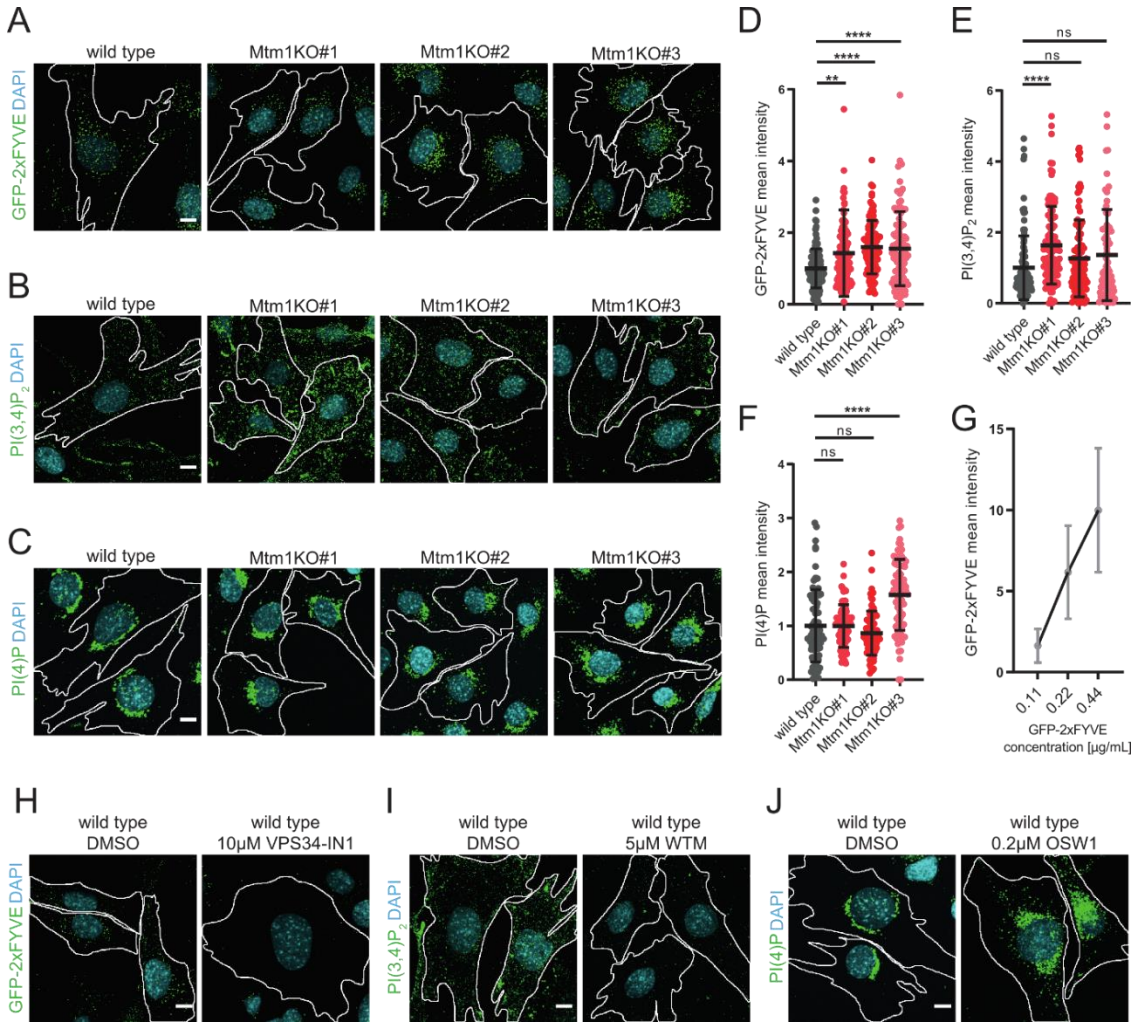

Figure 3-9. MTM1 loss leads to PI(3)P accumulation in C2C12 myoblasts. (A) Representative images of WT and Mtm1KO C2C12 myoblasts immunostained with PI(3)P-binding domain GFP-2xFYVE and DAPI for nuclear staining. Scale bar 10µm. **(B)** Representative images of WT and Mtm1KO C2C12 myoblasts immunostained for PI(3,4)P_2 and DAPI for nuclear staining. Scale bar 10µm. **(C)** Representative images of WT and Mtm1KO C2C12 myoblasts immunostained for PI(4)P and DAPI for nuclear staining. Scale bar 10µm. **(D)** PI(3)P-binding domain GFP-2xFYVE intensity in WT and Mtm1KO C2C12 myoblasts. Mean ± SD from ≥ 600 cells from 5 independent experiments, represented as fold change compared to wild type. Each data point represents mean intensity per image. One-way analysis of variance (ANOVA; F =9.682) and Dunnett's multiple comparison test; WT vs Mtm1KO#1 **p = 0.0013, WT vs Mtm1KO#2 ****p < 0.0001, WT vs Mtm1KO#3 ****p < 0.0001. **(E)** PI(3,4)P_2 intensity in WT and Mtm1KO C2C12 myoblasts. Mean ± SD from ≥ 600 cells from 8 independent experiments, represented as fold change compared to wild type. Each data point represents mean intensity per image. One-way analysis of variance (ANOVA; F =9.682) and Dunnett's multiple comparison test; WT vs Mtm1KO#1 **p = 0.0013, WT vs Mtm1KO#2 ****p <

0.0001, WT vs Mtm1KO#3 ****p < 0.0001. **(F)** PI(4)P intensity in WT and Mtm1KO C2C12 myoblasts. Mean ± SD from ≥ 700 cells from 4 independent experiments, represented as fold change compared to wild type. Each data point represents mean intensity per image. One-way analysis of variance (ANOVA; F = 9.682) and Dunnett's multiple comparison test; WT vs Mtm1KO#1 **p = 0.0013, WT vs Mtm1KO#2 ****p < 0.0001, WT vs Mtm1KO#3 ****p < 0.0001. **(G)** Intensity of PI(3)P-binding domain GFP-2xFYVE used at increasing concentrations in HeLa cells. Mean ± SD from ≥ 60 cells from 1 experiment, normalized to the lowest concentration. **(H)** Representative images of WT C2C12 myoblasts treated for 1h with 10µM VPS34-IN1 or 0.1% DMSO and immunostained with PI(3)P-binding domain GFP-2xFYVE and DAPI for nuclear staining. Scale bar 10µm. **(I)** Representative images of WT C2C12 myoblasts treated for 1h with 5µM wortmannin (WTM) or 0.1% DMSO and immunostained for PI(3,4)P_2 and DAPI for nuclear staining. Scale bar 10µm. **(J)** Representative images of WT C2C12 myoblasts treated for 3h with 0.2µM OSW1 or 0.1% DMSO and immunostained for PI(4)P and DAPI for nuclear staining. Scale bar 10µm.

Complementarily, abundance of PI(4)P on intracellular membranes was assessed using a PI(4)P-specific antibody, which displayed an expected perinuclear immunostaining in WT and *Mtm1*KO myoblasts (**Fig. 3-9 C**) corresponding to the Golgi apparatus, formed by PI(4)P-rich endomembranes [46]. Quantitative analysis revealed no differences in *Mtm1*KO #1 and #2 compared to WT, whereas *Mtm1*KO #3 was statistically significantly increased (**Fig. 3-9 F**). These results led us to conclude that MTM1 depletion does not affect PI(4)P levels and a clonal effect might be resulting in the increase observed in *Mtm1*KO #3, similarly than described for *Mtm1*KO #1 and PI(3,4)P_2, yet in this case the underlying cause was not investigated. PI(4)P antibody specificity was controlled by treating WT C2C12 myoblasts with DMSO or OSW1, an OSBP inhibitor that blocks cholesterol to PI(4)P exchange triggering a PI(4)P accumulation at the Golgi apparatus [242,243], as shown in inhibitor-treated cells (**Fig. 3-9 J**).

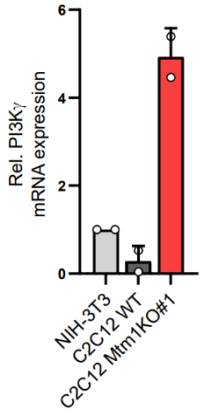

Figure 3-10. Mtm1KO clone #1 overexpresses PI3Kγ. Relative mRNA expression levels of *Pik3cg* in NIH-3T3 cells and WT and Mtm1KO#1 C2C12 myoblasts. *Gapdh* expression was used for normalization. Mean ± SD from 2 independent experiments represented as fold change compared to control (NIH-3T3) with a mean of 1.

In summary, the assessment of the PI 3-phosphate species of interest for this project revealed that our XLCNM cell-based models reproduce the phenotype reported in numerous *in vitro* and *in vivo* models (see section 1.3.2), thereby strengthening the suitability of these models to gain cell biological insights into the disease.

3.2.6 Further characterization of *Mtm1*KO C2C12 myoblasts

Besides the described adhesion impairment in MTM1-depleted cells, changes in the distribution or expression of proteins related to other cellular functions and compartments were monitored in WT and *Mtm1*KO #1 myoblasts. Immunostaining of early endosomal proteins EEA1 and RAB5, as well as late endosomal/lysosomal LAMP1 and RAB7 revealed a compact perinuclear distribution and more intense signal in *Mtm1*KO #1 compared to WT. Conversely, immunostaining of TfR, commonly used to label the recycling compartment, displayed a typically perinuclear localization in WT but a dispersed distribution upon MTM1 loss (**Fig. 3-11 A**), similar to the data reported by Ketel *et al* [83]. Importantly, the effect of decreased spreading of MTM1-depleted cells in signal distribution needs to be taken into consideration, as these cells will tend to display more compact and intense immunostaining signals. Consequently, application of specific methods quantifying relative position within the cell would be necessary to obtain conclusive data on the effect of MTM1 loss in organelle distribution. Immunostaining of *cis*-Golgi-specific GM130, ER-specific calnexin and mitochondrial cytochrome C (CytC)

evidenced no major changes in their distribution upon MTM1 loss compared to WT (**Fig. 3-11 B**), aside from those caused by differential cell spreading in the compared cell lines.

Impairment of cell adhesion in *Mtm1*KO myoblasts prompted us to hypothesize the presence of cytoskeletal alterations in these cells. To investigate this, immunostainings of the muscle-specific intermediate filament component desmin and the actin cytoskeleton component F-actin were performed. Qualitatively, desmin filament directionality was absent in *Mtm1*KO #1, where a disorganized distribution was predominant. On the other hand, F-actin filaments, clearly defined in WT, were rarely present and defined upon MTM1 loss (**Fig. 3-11 C**), indicating cytoskeletal defects upon MTM1 loss, potentially secondary to adhesion impairment.

Expression of certain proteins of interest was assessed in WT and *Mtm1*KO #1 myoblasts, including PI 3-phosphate-metabolizing enzymes, endocytosis-related proteins and signaling markers. Immunoblotting analysis revealed decreased VPS34 and PI3KC2α in *Mtm1*KO #1 compared to WT, and no differences in CHC and adaptor AP-2, the latter determined by its subunit μ2 (**Fig. 3-11 D**). Phosphorylated (T389) S6K (pS6K) was used as a readout to assess mTORC1 activation status, and absence of differences between WT and *Mtm1*KO #1 led us to conclude that lack of MTM1 did not affect mTORC1 signaling in C2C12 myoblasts (**Fig. 3-11 E**).

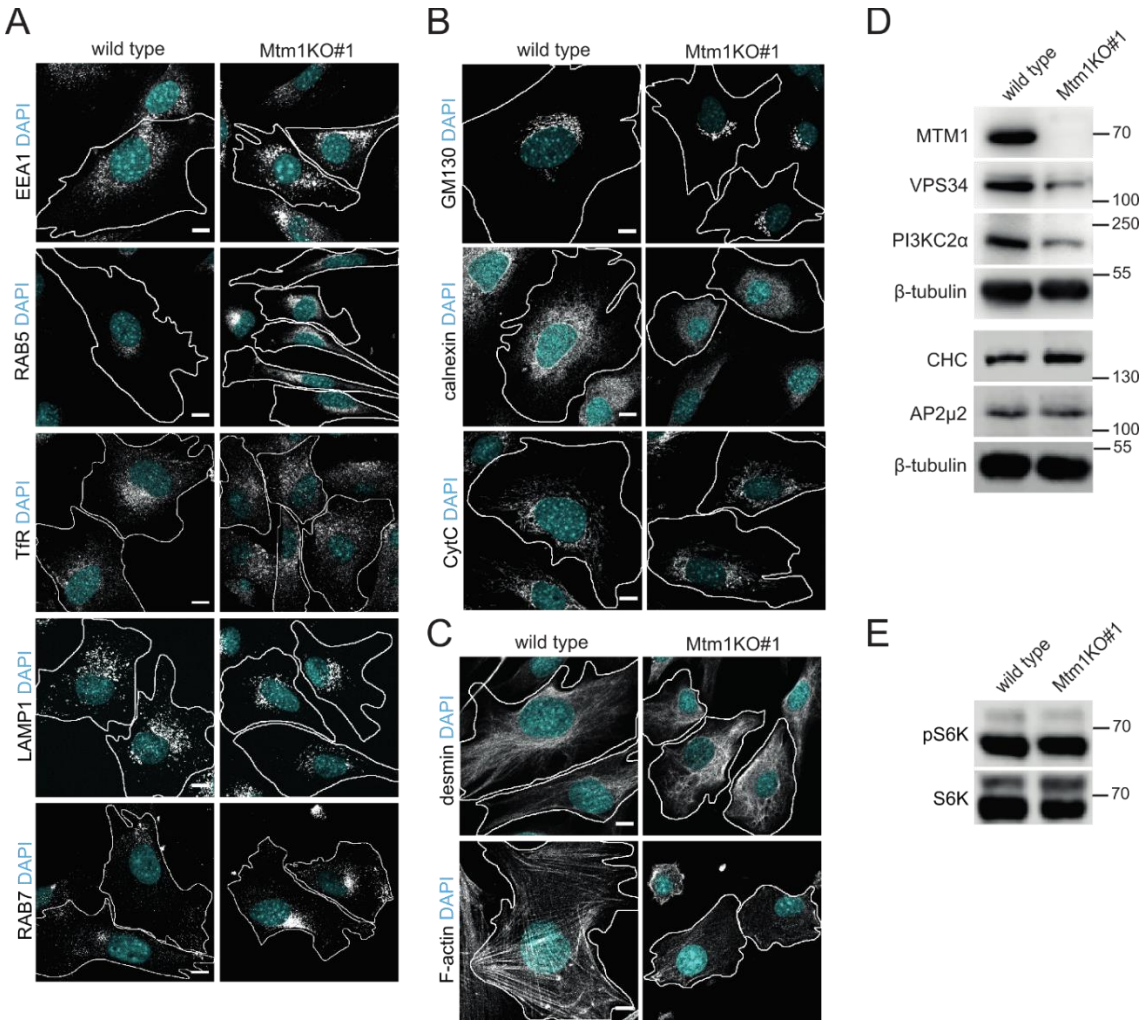

Figure 3-11. Effects of MTM1 loss in endolysosomal compartments, organelles, cytoskeleton and proteins of interest expression in C2C12 myoblasts. [see description in the next page]

[from previous page] **(A)** Representative images of WT and Mtm1KO#1 C2C12 myoblasts immunostained for endolysosomal compartment markers, and DAPI for nuclear staining. Scale bar 10µm. **(B)** Representative images of WT and Mtm1KO#1 C2C12 myoblasts immunostained for organelle markers, and DAPI for nuclear staining. Scale bar 10µm. **(C)** Representative images of WT and Mtm1KO#1 C2C12 myoblasts immunostained for cytoskeletal markers, and DAPI for nuclear staining. Scale bar 10µm. **(D)** Protein levels of PI 3-phosphates-metabolizing enzymes and CME-related proteins in wild type (WT) and Mtm1KO#1 C2C12 myoblasts detected by immunoblotting. **(E)** Phosphorylated (T389) S6K (pS6K) and total S6K protein levels in wild type (WT) and Mtm1KO#1 C2C12 myoblasts detected by immunoblotting. **(E)** Data obtained by P.A.K.

3.3 Genetic ablation of PI3KC2β rescues XLCNM cellular phenotypes

At this point of the study, we had successfully generated and characterized a cell-based model of XLCNM that recapitulated disease phenotypes of our interest, providing specific insights into cell adhesion defects. In order to pursue our main goal of characterizing the molecular interplay of MTM1 and PI3KC2β in the context of XLCNM rescue, we investigated whether the defects observed in XLCNM models were rescued in MTM1- and PI3KC2β-depleted myoblasts, and whether the lack of PI3KC2β led to significant phenotypes potentially compelling mechanistic information on the rescue.

3.3.1 Defective cell spreading in MTM1-depleted C2C12 myoblasts is rescued by loss of PI3KC2β

We previously showed that *Mtm1*KO myoblasts present a cell spreading defect, evidenced by their decreased cell area to volume ratio (**Fig. 3-3**). To test whether loss of PI3KC2β rescued this phenotype, cell area and volume of *Pik3c2b*KO and double KO cells lines were analyzed as previously indicated. Upon PI3KC2β loss, these parameters remained unchanged compared to WT (**Fig. 3-12 A, B**), leading to unaltered cell area to volume ratio (**Fig. 3-12 C**), and providing initial indication that PI3KC2β is not involved in cell spreading in these cells, opposite to our hypothesized rescue. However, loss of PI3KC2β on a XLCNM genetic background, in double KO myoblasts, resulted in increased cell area and absent changes in cell volume (**Fig. 3-12 A, B**), values from which cell area to volume ratio was calculated. A similar area to volume ratio in WT and double KO cells indicated that cell spreading defects of *Mtm1*KO myoblasts were restored in double KO myoblasts (**Fig. 3-12 C**), leading to the conclusion that PI3KC2β plays a role in spreading and is potentially involved in cell adhesion. Additionally, these results provided the first evidence of a genetic interaction between the two enzymes in our cell-based models.

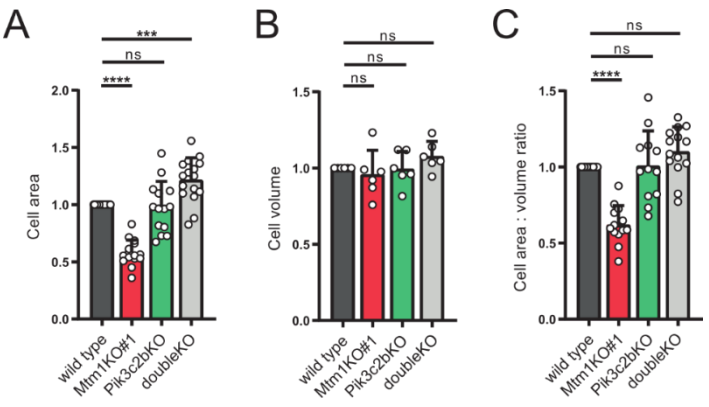

Figure 3-12. PI3KC2β loss rescues decreased cell spreading capacity of C2C12 lacking MTM1. (A) Cell area of WT and C2C12 KO myoblasts measured using F-actin immunostaining as a mask (not shown). Mean ± SD from 16 independent experiments represented as fold change compared to control (wild type) with a hypothetical mean of 1. One-way analysis of variance (ANOVA; F = 44.72) and Dunnett's multiple-comparison test; WT vs Mtm1KO#1 ****p < 0.0001, WT vs Pik3c2bKO n.s. p = 0.9712, WT vs doubleKO ***p = 0.0007. **(B)** Cell volume of WT and C2C12 KO myoblasts measured as forward scatter values obtained by flow cytometry. Mean ± SD from 6 independent experiments represented as fold change compared to control (wild type) with a hypothetical mean of 1. One-way analysis of variance (ANOVA; F = 0.588) and Dunnett's multiple-comparison test; WT vs Mtm1KO#1 n.s. p = 0.8473, WT vs Pik3c2bKO n.s. p = 0.9994, WT vs doubleKO n.s. p = 0.4812. **(C)** Relative cell area to volume ratio of WT and C2C12 KO myoblasts measured normalizing cell area values to mean forward scatter values obtained by flow cytometric analysis (not shown). Mean ± SD from 14 independent experiments represented as fold change compared to control (wild type) with a hypothetical mean of 1. One-way analysis of variance (ANOVA;

F = 26.15) and Dunnett's multiple-comparison test; WT vs Mtm1KO#1 ****p < 0.0001, WT vs Pik3c2bKO n.s. p = 0.9989, WT vs doubleKO n.s. p = 0.2014. **(A-C)** Same Mtm1KO#1 data as shown in Fig. 3-3.

3.3.2 Defective cell adhesion in MTM1-depleted C2C12 myoblasts is rescued by loss of PI3KC2β

We suggested that the decreased cell spreading of myoblasts lacking MTM1 is due to defective adhesion via focal adhesions (FAs) (**Fig. 3-4**). To investigate whether PI3KC2β loss potentiates cell spreading by modulating FA, *Pik3c2b*KO and double KO myoblasts cultured on a Matrigel matrix were immunostained for FA components pFAK, zyxin and paxillin. Loss of PI3KC2β did not lead to prominent morphology or distribution changes (**Fig. 3-13 A, D, G**), nor significant differences in the number of FA compared to WT using any of the mentioned proteins as FA markers (**Fig. 3-13 B, E, H**). Regarding FA area, PI3KC2β loss led to no differences compared to WT in pFAK and zyxin immunostaining (**Fig. 3-13 C, F**), though a mild but statistically significant increase in FA area was observed using paxillin as an FA marker (**Fig. 3-13 I**). In double KO myoblasts, the number of FA was identical to WT in pFAK and zyxin immunostainings, and increased in paxillin (**Fig. 3-13 B, E, H**), whereas FA area was unchanged compared to WT (**Fig. 3-13 C, F, I**). Overall, these data indicated that PI3KC2β depletion does not modulate FAs, contrasting with the fact that its depletion in an *Mtm1*KO genetic background is able to rescue the decreased FA number of these cells.

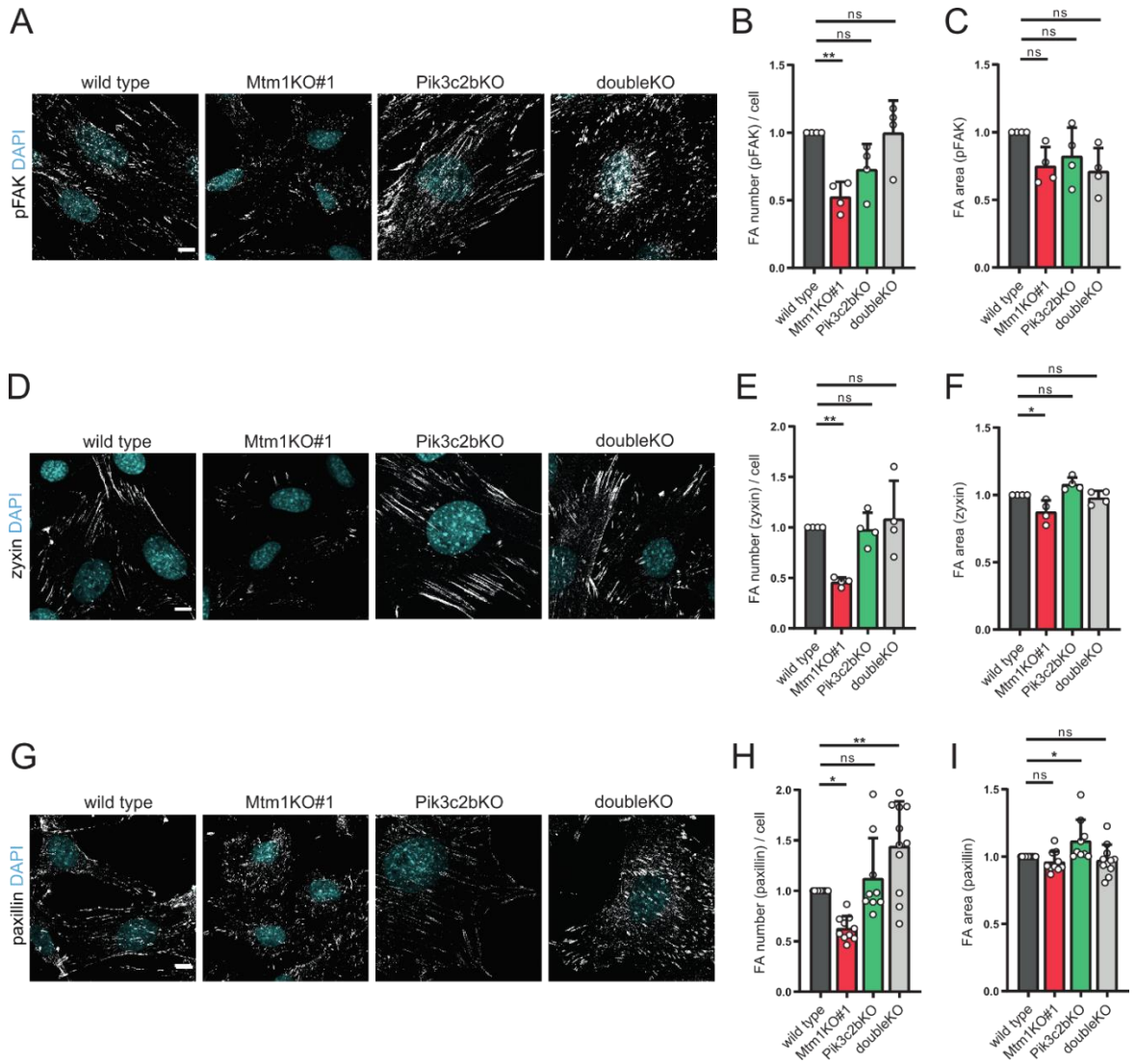

[from previous page] **Figure 3-13. PI3KC2β loss rescues reduced number of focal adhesions of C2C12 lacking MTM1. (A)** Representative images of WT and C2C12 KO myoblasts immunostained for phosphorylated (Y397) focal adhesion kinase (pFAK) as a focal adhesion (FA) marker and DAPI for nuclear staining. 100µm x 100µm images are shown. Scale bar 10µm. **(B)** Number of FA per cell in WT and C2C12 KO myoblasts measured using pFAK as FA marker. Mean ± SD from 4 independent experiments represented as fold change compared to control (wild type) with a hypothetical mean of 1. One-way analysis of variance (ANOVA; F = 8.229) and Dunnett's multiple-comparison test; WT vs Mtm1KO#1 **p = 0.0035, WT vs Pik3c2bKO n.s. p = 0.0848, WT vs doubleKO n.s. p > 0.9999. **(C)** FA area in WT and C2C12 KO myoblasts measured using pFAK as FA marker. Mean ± SD from 9 independent experiments represented as fold change compared to control (wild type) with a hypothetical mean of 1. One-way analysis of variance (ANOVA; F = 2.816) and Dunnett's multiple-comparison test; WT vs Mtm1KO#1 n.s. p = 0.0948, WT vs Pik3c2bKO n.s. p = 0.2841, WT vs doubleKO n.s. p = 0.0504. **(D)** Representative images of WT and C2C12 KO myoblasts immunostained for zyxin as a focal adhesion (FA) marker and DAPI for nuclear staining. Scale bar 10µm. **(E)** Number of FA per cell in WT and C2C12 KO myoblasts measured using zyxin as FA marker. Mean ± SD from 4 independent experiments represented as fold change compared to control (wild type) with a hypothetical mean of 1. One-way analysis of variance (ANOVA; F = 7.655) and Dunnett's multiple-comparison test; WT vs Mtm1KO#1 **p = 0.0079, WT vs Pik3c2bKO n.s. p = 0.9980, WT vs doubleKO n.s. p = 0.8806. **(F)** FA area in WT and C2C12 KO myoblasts measured using zyxin as FA marker. Mean ± SD from 9 independent experiments represented as fold change compared to control (wild type) with a hypothetical mean of 1. One-way analysis of variance (ANOVA; F = 9.691) and Dunnett's multiple-comparison test; WT vs Mtm1KO#1 * p = 0.0185, WT vs Pik3c2bKO n.s. p = 0.1341, WT vs doubleKO n.s. p = 0.9093. **(G)** Representative images of WT and C2C12 KO myoblasts immunostained for paxillin as a focal adhesion (FA) marker and DAPI for nuclear staining. Scale bar 10µm. **(H)** Number of FA per cell in WT and C2C12 KO myoblasts measured using paxillin as FA marker. Mean ± SD from 9 independent experiments represented as fold change compared to control (wild type) with a hypothetical mean of 1. One-way analysis of variance (ANOVA; F = 13.05) and Dunnett's multiple-comparison test; WT vs Mtm1KO#1 *p = 0.0210, WT vs Pik3c2bKO n.s. p = 0.6908, WT vs doubleKO **p = 0.0040. **(I)** FA area in WT and C2C12 KO myoblasts measured using paxillin as FA marker. Mean ± SD from 9 independent experiments represented as fold change compared to control (wild type) with a hypothetical mean of 1. One-way analysis of variance (ANOVA; F = 4.709) and Dunnett's multiple-comparison test; WT vs Mtm1KO#1 n.s. p = 0.7190, WT vs Pik3c2bKO *p = 0.0355, WT vs doubleKO n.s. p = 0.8821. **(B, C, E, F, H, I)** Same Mtm1KO#1 data as shown in Fig. 3-4.

In accordance with alterations in FA, surface activated β1-integrin was shown to be reduced in cells lacking MTM1 (**Fig. 3-5**). To assess whether PI3KC2β loss rescued this phenotype, as shown for FA (**Fig. 3-13**), an immunostaining of surface activated β1-integrin was performed in *Pik3c2b*KO and double KO myoblasts as indicated previously. Qualitative analysis revealed a similar distribution pattern to WT in both cell lines, with generally shorter filamentous adhesions in double KO (**Fig. 3-14 A**). Quantitatively, *Pik3c2b*KO and double KO showed no changes in surface activated β1-integrin compared to WT (**Fig. 3-14 B**), thus evidencing that depletion of PI3KC2β rescues integrin adhesion defects of *Mtm1*KO myoblasts, whilst surprisingly having no impact upon single KO.

To obtain further data on β1-integrin distribution, total β1-integrin, comprising active and inactive fractions in a whole-cell immunostaining, was analyzed. It revealed a highly abundant and intense signal upon PI3KC2β loss, distributed similarly than in WT. MTM1- and PI3KC2β-depleted myoblasts, in contrast, displayed less abundant and less intense total β1-integrin signal with a similar distribution than in WT cells (**Fig. 3-14 A**). The quantification matched these observations by showing increased levels in *Pik3c2b*KO and decreased levels in double KO in comparison to WT (**Fig. 3-14 C**). Altogether, FA and active integrin data indicated that the cell adhesion impairment observed upon MTM1 loss is rescued by co-depletion of PI3KC2β, evidencing roles of the two enzymes in the co-regulation of integrin adhesions. The relevance of this observation concentrates on the fact that a co-modulation of adhesions by MTM1 and PI3KC2β could be the underlying mechanism explaining the rescue of the disease phenotype in XLCNM models with muscle-specific PI3KC2β depletion [42].

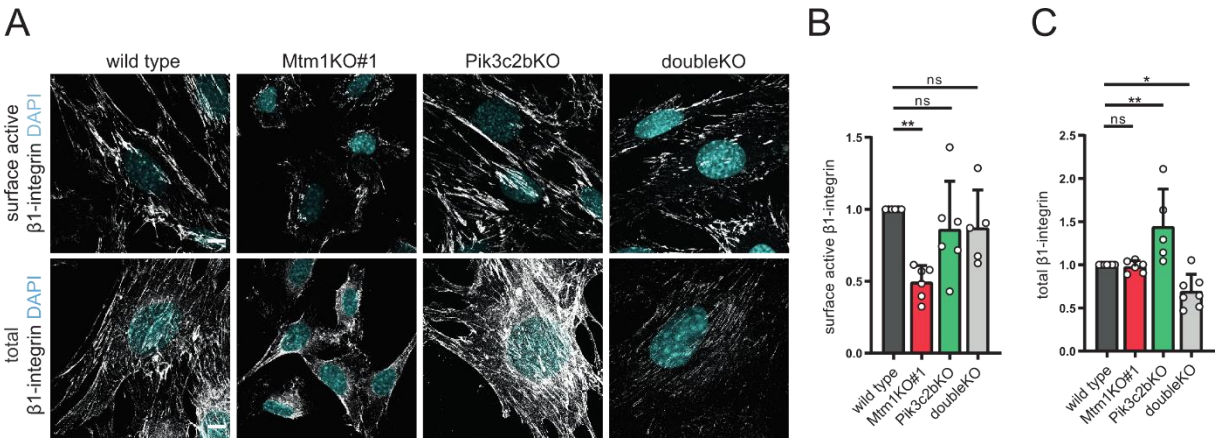

Figure 3-14. PI3KC2β loss rescues decreased β1-integrin adhesions of C2C12 lacking MTM1. **(A)** Representative images of WT and C2C12 KO myoblasts immunostained under non-permeabilizing conditions for active β1-integrin (upper panel), permeabilizing conditions for β1-integrin (lower panel), and DAPI for nuclear staining (both). Scale bar 10µm. **(B)** Surface active β1-integrin intensity per cell in WT and C2C12 KO myoblasts. Mean ± SD from 5 independent experiments represented as fold change compared to control (wild type) with a hypothetical mean of 1. One-way analysis of variance (ANOVA; F = 6.00) and Dunnett's multiple-comparison test; WT vs Mtm1KO#1 **p = 0.0020, WT vs Pik3c2bKO n.s. p = 0.5683, WT vs doubleKO n.s. p = 0.6538. **(C)** β1-integrin intensity in WT and C2C12 KO myoblasts. Mean ± SD from 5 independent experiments represented as fold change compared to control (wild type) with a hypothetical mean of 1. One-way analysis of variance (ANOVA; F = 11.35) and Dunnett's multiple-comparison test; WT vs Mtm1KO#1 n.s. p = 0.9966, WT vs Pik3c2bKO **p = 0.0067, WT vs doubleKO *p = 0.0434. **(B, C)** Same Mtm1KO#1 data as shown in Fig. 3-5.

3.3.3 Rescue of cell adhesion defects in a hypomorphic clonal cell line and by PI3KC2β shRNA-mediated depletion

To further consolidate the data supporting the rescue of cell spreading and adhesion defects of *Mtm1*KO myoblasts in double KO cells (**Fig. 3-12 to 3-14**), as well as excluding potential clonal cell line effects, we used an additional cell line with partial MTM1 expression and depleted PI3KC2β, *Mtm1*^{hypo}/*Pik3c2b*KO, in which the mentioned phenotypes were assessed.

Compared to WT, differences in cell area (**Fig. 3-15 A**) and volume (**Fig. 3-15 B**) of *Mtm1*^{hypo}/*Pik3c2b*KO myoblasts were not observed, resulting in a rescued cell area to volume ratio (**Fig. 3-15 C**), which suggested the absence of a spreading defect in this cell line. Cell adhesion was evaluated via immunostaining of zyxin as a FA marker, which revealed a similar pattern in WT and *Mtm1*^{hypo}/*Pik3c2b*KO myoblasts (**Fig. 3-15 D**), and a restored number of FA per cell (**Fig. 3-15 E**). Accordingly, neither morphological nor distribution differences between WT and *Mtm1*^{hypo}/*Pik3c2b*KO myoblasts were observed in a surface immunostaining of activated β1-integrin (**Fig. 3-15 F**), and quantitative analysis showed no significant differences (**Fig. 3-15 H**), supporting the complete rescue of adhesion defects in *Mtm1*^{hypo}/*Pik3c2b*KO as observed in double KO cells. In a whole-cell immunostaining of total β1-integirn, a similarly distributed yet less intense signal was shown (**Fig. 3-15 G**), quantitatively resulting in decreased β1-integrin in *Mtm1*^{hypo}/*Pik3c2b*KO in comparison to WT (**Fig. 3-15 I**), to a similar extent than reported in double KO (**Fig. 3-14 C**).

To further support the rescue of MTM1 KO adhesion defects upon PI3KC2β loss, shRNA-mediated depletion of PI3KC2β was induced in *Mtm1*KO or double KO myoblasts, and surface activated β1-integrin was assessed by immunostaining. A qualitative observation evidenced that in PI3KC2β-targeting shRNA-transduced cells (shPI3KC2β #1 and #2), indicated by expression of a nuclear RFP (nRFP) reporter, surface active β1-integrin levels

were similar to those in shSCR-treated double KO myoblasts, and increased compared to shSCR-treated *Mtm1*KO myoblasts (**Fig. 3-15 J**). Together with the observations from *Mtm1*^{hypo}/*Pik3c2b*KO myoblasts, these data supported the rescue of cell spreading and adhesion defects of MTM1-depleted myoblasts by co-depletion of PI3KC2β, strongly arguing against random clonal variation as the underlying cause for the observed rescue in double KO.

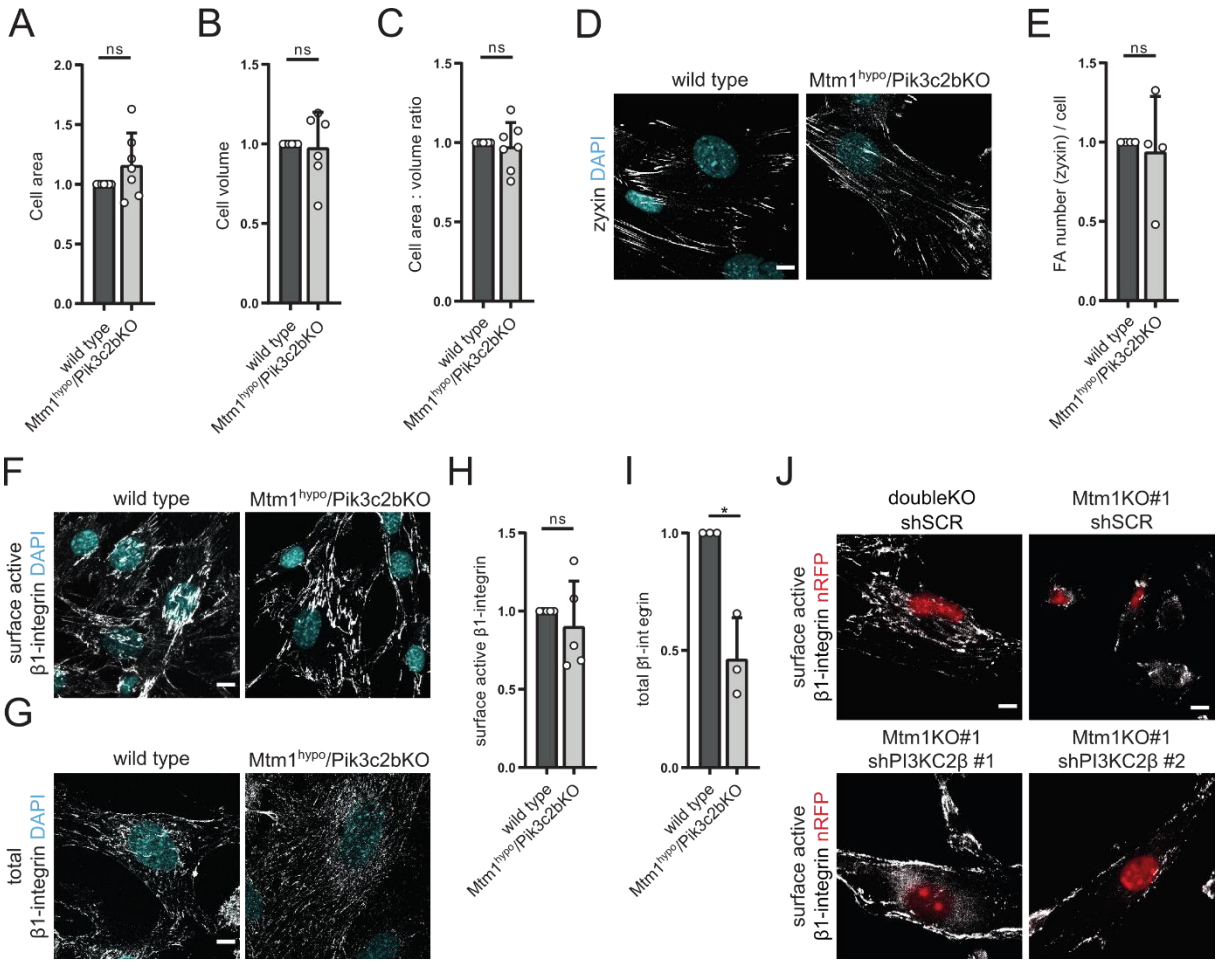

Figure 3-15. PI3KC2β loss rescues the phenotypes of C2C12 lacking MTM1 in a double hypomorphic/KO cell line and by shRNA-mediated depletion. (A) Cell area of WT and Mtm1^{hypo}/Pik3c2bKO C2C12 myoblasts measured using F-actin immunostaining as a mask (not shown). Mean ± SD from 7 independent experiments represented as fold change compared to control (wild type) with a hypothetical mean of 1. One-sample two-tailed t test; n.s. p = 0.1701. **(B)** Cell volume of WT and Mtm1^{hypo}/Pik3c2bKO C2C12 myoblasts measured as forward scatter values obtained by flow cytometry. Mean ± SD from 6 independent experiments represented as fold change compared to control (wild type) with a hypothetical mean of 1. One-sample two-tailed t test; n.s. p = 0.8128. **(C)** Relative cell area to volume ratio of WT and Mtm1^{hypo}/Pik3c2bKO C2C12 myoblasts measured normalizing cell area values to mean forward scatter values obtained by flow cytometric analysis (not shown). Mean ± SD from 7 independent experiments represented as fold change compared to control (wild type) with a hypothetical mean of 1. One-sample two-tailed t test; n.s. p = 0.6783. **(D)** Representative images of WT and Mtm1^{hypo}/Pik3c2bKO C2C12 myoblasts immunostained for zyxin as a focal adhesion (FA) marker and DAPI for nuclear staining. Scale bar 10µm. **(E)** Number of FA per cell in WT and Mtm1^{hypo}/Pik3c2bKO C2C12 myoblasts measured using zyxin as FA marker. Mean ± SD from 4 independent experiments represented as fold change compared to control (wild type) with a hypothetical mean of 1. One-sample two-tailed t test; n.s. p = 0.7527. **(F)** Representative images of WT and Mtm1^{hypo}/Pik3c2bKO C2C12 myoblasts immunostained under non-permeabilizing conditions for active β1-integrin and DAPI for nuclear staining. Scale bar 10µm. **(G)** Representative images of WT and Mtm1^{hypo}/Pik3c2bKO C2C12 myoblasts immunostained under permeabilizing conditions for β1-integrin and DAPI for nuclear staining. Scale bar 10µm. **(H)** Surface active β1-integrin intensity per cell in WT and Mtm1^{hypo}/Pik3c2bKO C2C12 myoblasts. Mean ± SD from 5 independent experiments represented as fold change compared to control (wild type) with a hypothetical mean of 1. One-sample two-tailed t test; n.s. p = 0.4934. **(I)** β1-integrin intensity in WT and Mtm1^{hypo}/Pik3c2bKO myoblasts. Mean ± SD from 3

independent experiments represented as fold change compared to control (wild type) with a hypothetical mean of 1. One-sample two-tailed t test; **p = 0.0340. **(J)** Representative images of doubleKOand Mtm1KO#1 C2C12 myoblasts transduced with control (shSCR) or PI3KC2β-targeting (shPI3KC2β #1-2) shRNA lentivirus expressing a nuclear RFP (nRFP) reporter and immunostained under non-permeabilizing conditions for active β1-integrin. shSCR-transduced cells display 0.68 ± 0.07 and PI3KC2β-depleted cells display 1.11 ± 0.50 (shPI3KC2β #1) and 1.28 ± 0.75 (shPI3KC2β #2) fold change of surface active β1-integrin levels compared to doubleKO+shSCR. Scale bar 10µm. Mean ± SD from 4 independent experiments. One-way analysis of variance (ANOVA; F = 1.1242) and Dunnett's multiple-comparison test; doubleKO+shSCR vs Mtm1KO#1+shSCR n.s. p = 0.6416, doubleKO vs Mtm1KO#1+shPI3KC2β#1 n.s. p = 0.9719, doubleKO vs Mtm1KO#1+shPI3KC2β#2 n.s. p = 0.7179.

3.3.4 Rescue of adhesion defects in double KO C2C12 myoblasts is dependent on the loss of PI3KC2β kinase activity

Most of the cellular functions of PI3KC2β described in the literature have been shown to be kinase activity-dependent (see section 5.3.3.2). The involvement of PI3KC2β catalytic activity in the rescue of *Mtm1*KO cell adhesion defects was tested by overexpressing GFP-tagged wild type or kinase inactive PI3KC2β in double KO myoblasts, and performing a surface immunostaining for activated β1-integrin. Compared to a GFP-overexpressed control, equally distributed but decreased active β1-integrin signal was observed in double KO cells overexpressing wild type GFP-PI3KC2β, whereas kinase inactive GFP-PI3KC2β overexpression did not alter intensities compared to control conditions (**Fig. 3-16 A**). Accordingly, a minor yet significant decrease in surface activated β1-integrin was quantified upon wild type GFP-PI3KC2β overexpression, and no change was quantified upon kinase-inactive GFP-PI3KC2β overexpression when compared to GFP-overexpressed control (**Fig. 3-16 B**). Even though through an indirect approach, these results suggested that abrogation of PI3KC2β kinase activity is sufficient to rescue the loss of integrin adhesions in MTM1-depleted cells. Hence, we hypothesized that PI3KC2β-mediated synthesis of PI 3-phosphate species is involved in the regulation of integrin adhesions.

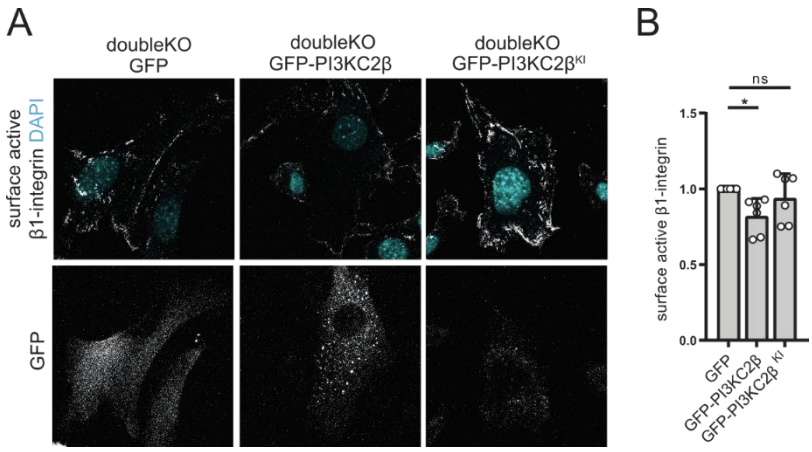

Figure 3-16. Rescue of decreased β1-integrin adhesions of C2C12 lacking MTM1 by PI3KC2β loss is dependent on its kinase activity. (A) Representative images of doubleKO C2C12 myoblasts overexpressing GFP, GFP-PI3KC2β or kinase inactive (KI) GFP-PI3KC2β, immunostained under non-permeabilizing conditions for active β1-integrin and DAPI for nuclear staining. Scale bar 10µm. **(B)** Surface active β1-integrin intensity per cell in doubleKO C2C12 myoblasts overexpressing GFP, GFP-PI3KC2β or kinase inactive (KI) GFP-PI3KC2β. Mean ± SD from 6 independent experiments represented as fold change compared to control (GFP) with a hypothetical mean of 1. One-way analysis of variance (ANOVA; F = 3.818) and Dunnett's multiple-comparison test; GFP vs GFP-PI3KC2β *p = 0.0291, GFP vs GFP-PI3KC2β^{KI} n.s. p = 0.5655.

3.3.5 Enhanced cell migration in MTM1-depleted C2C12 myoblasts is rescued by loss of PI3KC2β

Finding a complete rescue of cell adhesion defects of XLCNM cell-based models by loss of PI3KC2β suggested that enhanced migration of *Mtm1*KO myoblasts (**Fig. 3-7**) could potentially be reverted in double KO cells. In a random cell migration assay, myoblasts lacking PI3KC2β migrated shorter distances at slower speed compared to WT, whereas migration distance and speed in double KO myoblasts was identical to WT (**Fig. 3-17 A, B**). These data confirmed the above hypothesis and uncovered a functional phenotype of *Pik3c2b*KO cells with interestingly

the opposite effect to MTM1 loss, contrasting with the lack of *Pik3c2b*KO phenotypes in focal and integrin adhesions and cell spreading.

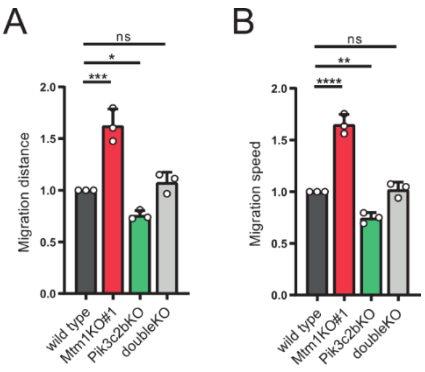

Figure 3-17. PI3KC2β loss rescues increased migration of C2C12 lacking MTM1. (A) Migration speed of WT and C2C12 KO myoblasts on a Matrigel matrix. Mean ± SD from 3 independent experiments represented as fold change compared to control (wild type) with a hypothetical mean of 1. One-way analysis of variance (ANOVA; F = 42.51) and Dunnett's multiple-comparison test; WT vs Mtm1KO#1 ***p = 0.0001, WT vs Pik3c2bKO *p = 0.0392, WT vs doubleKO n.s. p = 0.6667. **(B)** Random migration speed of WT and C2C12 KO myoblasts on a Matrigel matrix. Mean ± SD from 3 independent experiments represented as fold change compared to control (wild type) with a hypothetical mean of 1. One-way analysis of variance (ANOVA; F = 102.6) and Dunnett's multiple-comparison test; WT vs Mtm1KO#1 ****p < 0.0001, WT vs Pik3c2bKO **p = 0.0039, WT vs doubleKO n.s. p = 0.9640. **(A, B)** Same Mtm1KO#1 data as shown in Fig. 3-7.

3.3.6 Impaired myogenesis in MTM1-depleted C2C12 myoblasts is rescued by loss of PI3KC2β

A further functional consequence of defective adhesion and migration in cellular models of XLCNM is an aberrant myotube morphology and decreased differentiation index (**Fig. 3-8**). *Pik3c2b*KO and double KO cells were differentiated for 7 days to evaluate whether loss of PI3KC2β rescued differentiation defects. Observation of differentiated MHC-positive cells, indicative of late differentiation stages, revealed that myotubes lacking PI3KC2β displayed a similar morphology to WT myotubes, and that double KO myotubes were on average longer, thinner, and more abundant than WT myotubes (**Fig. 3-18 A**). Quantitative analysis of differentiation index, expressed as number of nuclei per MHC-positive cell, showed no significant changes in *Pik3c2b*KO cells, with an average of 2.7 nuclei per cell, and double KO, with an average of 3.3, compared to WT (**Fig. 3-18 B**), thus indicating a rescue of myotube differentiation impairment by PI3KC2β ablation in an *Mtm1*KO genetic background.

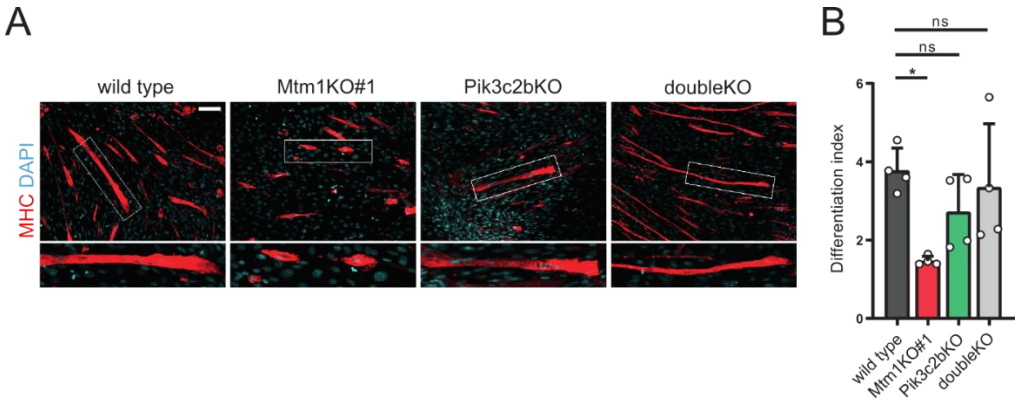

Figure 3-18. PI3KC2β loss rescues impaired myoblast to myotube differentiation of C2C12 lacking MTM1. (A) Representative images of WT and C2C12 KO myotubes differentiated for 7 days and immunostained for myosin heavy chain (MHC) as a differentiation marker and DAPI for nuclear staining. Scale bar 100µm. Selections correspond to 400µm x 100µm images. **(B)** Myotube differentiation index of WT and C2C12 KO expressed as number of nuclei per MHC-positive cell. Mean ± SD from 4 independent experiments compared to control (wild type). One-way analysis of variance (ANOVA; F = 4.185) and Dunnett's multiple-comparison test; WT vs Mtm1KO#1 *p = 0.159, WT vs Pik3c2bKO n.s. p = 0.3377, WT vs doubleKO n.s. p = 0.8710. Same Mtm1KO#1 data as shown in Fig. 3-8.

Altogether, our data at this point of the study indicated that the cell spreading impairment of XLCNM cellular models associated to adhesion defects via FAs, evaluated using different intracellular FA proteins as well as the transmembrane component active β1-integrin, is restored to normality upon co-loss of PI3KC2β. These

observations confirmed a functional link between MTM1 and PI3KC2β in C2C12 myoblasts, suggesting that the two enzymes might co-regulate integrin-mediated adhesions, a mechanism potentially underlying the reported rescue in double KO mouse models [42] and cells (this study). The functional impact of such interaction was shown by restored migratory and differentiation capacity in double KO myoblasts, processes tightly associated to cell adhesion (see section 1.4.2). To confirm and characterize the hypothesized co-regulation of adhesions by MTM1 and PI3KC2β, we explored several mechanistic hypotheses, taking as initial evidence the fact that impaired and restored adhesion in *Mtm1*KO and double KO myoblasts, respectively, is due to the loss of MTM1 and PI3KC2β catalytic activity (**Fig. 3-6, 3-16**), pointing at an involvement of PI 3-phosphate species.

3.3.7 Rescue of adhesion defects in double KO C2C12 myoblasts is independent of PI(3)P normalization

3.3.7.1 Increased PI(3)P in MTM1-depleted C2C12 myoblasts is not rescued by loss of PI3KC2β

After a detailed description of XLCNM cell adhesion-related phenotypes and their rescue by PI3KC2β loss, we aimed to characterize the underlying molecular process in our genetically-engineered C2C12 models. Initially, PI levels were assessed in order to obtain evidence to elaborate a mechanistic hypothesis. As previously shown, loss of MTM1 leads to an accumulation of its substrate PI(3)P in C2C12 myoblasts (**Fig. 3-9 A, D**) as shown for other *in vitro* and *in vivo* models (see section 1.3.2). Since PI 3-phosphates are products of the PI3K family, we hypothesized PI3KC2β to catalyze the reverse reaction to MTM1, therefore promoting PI(3)P synthesis. Under the assumption that MTM1 and PI3KC2β co-regulate the same PI(3)P pool, likely in the same cellular compartment, loss of PI3KC2β in a context of PI(3)P accumulation due to absence of MTM1 would normalize PI(3)P levels.

To test this hypothesis, total PI(3)P was immunostained in *Pik3c2b*KO and double KO myoblasts using the purified PI(3)P-binding protein GFP-2xFYVE. This revealed no prominent changes of PI(3)P distribution in *Pik3c2b*KO or double KO cells (**Fig. 3-19 A**). However, quantitative analysis evidenced decreased PI(3)P upon PI3KC2β loss and increased PI(3)P in double KO myoblasts (**Fig. 3-19 B**), the latter to a higher extent than WT. This observation importantly revealed that the accumulation of MTM1 substrate in *Mtm1*KO cells is not normalized by co-depletion of PI3KC2β, an unforeseen finding that conflicted with previous reports [42, 85,88]. The rescue of cell adhesion-related phenotypes with absence of PI(3)P normalization in double KO myoblasts suggested that both phenotypes were likely independent, implying that the PI3KC2β-mediated rescue occurred via an alternative mechanism.

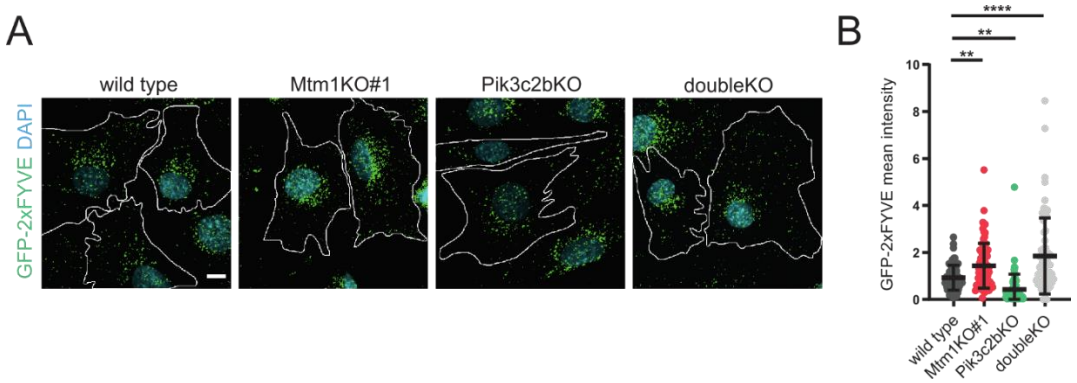

[from previous page] **Figure 3-19. PI3KC2β loss does not rescue PI(3)P accumulation of C2C12 lacking MTM1. (A)** Representative images of WT and C2C12 KO myoblasts immunostained with PI(3)P-binding domain GFP-2xFYVE and DAPI for nuclear staining. Scale bar 10µm. **(B)** PI(3)P-binding domain GFP-2xFYVE intensity in WT and C2C12 KO myoblasts. Mean ± SD from ≥ 300 cells from 5 independent experiments, represented as fold change compared to wild type. Each data point represents mean intensity per image. One-way analysis of variance (ANOVA; F = 26.32) and Dunnett's multiple comparison test; WT vs Mtm1KO#1 **p = 0.0053, WT vs Pik3c2bKO **p = 0.0090, WT vs doubleKO ****p < 0.0001. Same Mtm1KO#1 data as shown in Fig. 3-9.

3.3.7.2 Defective cell adhesion in MTM1-depleted C2C12 myoblasts is not rescued by PI(3)P depletion

Upon the unexpected finding of an absence of PI(3)P normalization in double KO myoblasts, we aimed to decipher whether its accumulation was independent of cell adhesion defects of *Mtm1*KO myoblasts. To specifically investigate whether PI(3)P depletion rescued adhesion defects caused by MTM1 loss, VPS34 was inhibited in WT or *Mtm1*KO myoblasts using VPS34-IN1, and integrin adhesions were labelled with a surface active β1-integrin immunostaining. Inhibitor treatment, shown by us (**Fig. 3-9 H**) and others [238] to deplete PI(3)P, did not induce changes in WT nor *Mtm1*KO myoblasts compared to the corresponding DMSO-treated controls (**Fig. 3-20 A, B**), implying that PI(3)P depletion is not sufficient to rescue the cell adhesion impairment of *Mtm1*KO cells. Altogether, these data indicated that normalization of PI(3)P in double KO myoblasts is unlikely the mechanism mediating the rescue of adhesion defects in these cells.

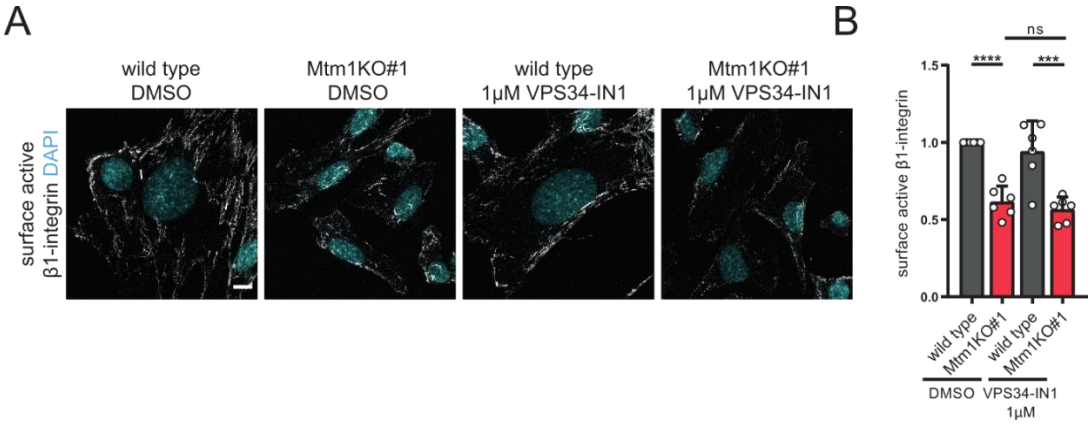

Figure 3-20. Inhibition of endosomal PI(3)P-synthesizing enzyme VPS34 does not rescue decreased integrin adhesions of C2C12 lacking MTM1. (A) Representative images of WT and Mtm1KO#1 C2C12 myoblasts treated for 4h with 1µM VPS34-IN1 or 0.01% DMSO, and immunostained under non-permeabilizing conditions for active β1-integrin and DAPI for nuclear staining. Scale bar 10µm. **(B)** Surface active β1-integrin intensity per cell in WT and Mtm1KO#1 C2C12 myoblasts treated for 4h with 1µM VPS34-IN1 or 0.01% DMSO. Mean ± SD from 6 independent experiments represented as fold change compared to control (wild type+DMSO) with a hypothetical mean of 1. One-way analysis of variance (ANOVA; F = 21.00) and Tukey's multiple-comparison test; WT+DMSO vs Mtm1KO#1+DMSO ****p < 0.0001, WT+VPS34-IN1 vs Mtm1KO#1+VPS34-IN1 ***p = 0.0001, Mtm1KO#1+DMSO vs Mtm1KO#1+VPS34-IN1 n.s. p = 0.8808.

3.4 Potential PI3KC2β-mediated rescue mechanisms of cell adhesion defects in XLCNM cellular models

The finding of a complete rescue of cell adhesion defects in MTM1- and PI3KC2β-depleted myoblasts independently of PI(3)P normalization urged us to develop alternative hypotheses to explain this observation. These were based on previous studies on the function and regulation of MTM1 and PI3KC2β, and essentially focused on elucidating potential opposed roles of the two PI-metabolizing enzymes in the control of cell adhesions.

3.4.1 MTM1 and PI3KC2β do not co-immunoprecipitate in C2C12 myoblasts nor HEK293T cells

Aiming to elucidate the PI3KC2β-mediated rescue mechanism of *Mtm1*KO phenotypes, we initially hypothesized that both proteins could directly or indirectly interact in modules and/or at a certain compartment to co-ordinate opposing functions. Furthermore, interactions of PI3KC2β with myotubularin-related proteins other than MTM1 were explored in order to identify potential binding partners that could provide insights into its cellular functions.

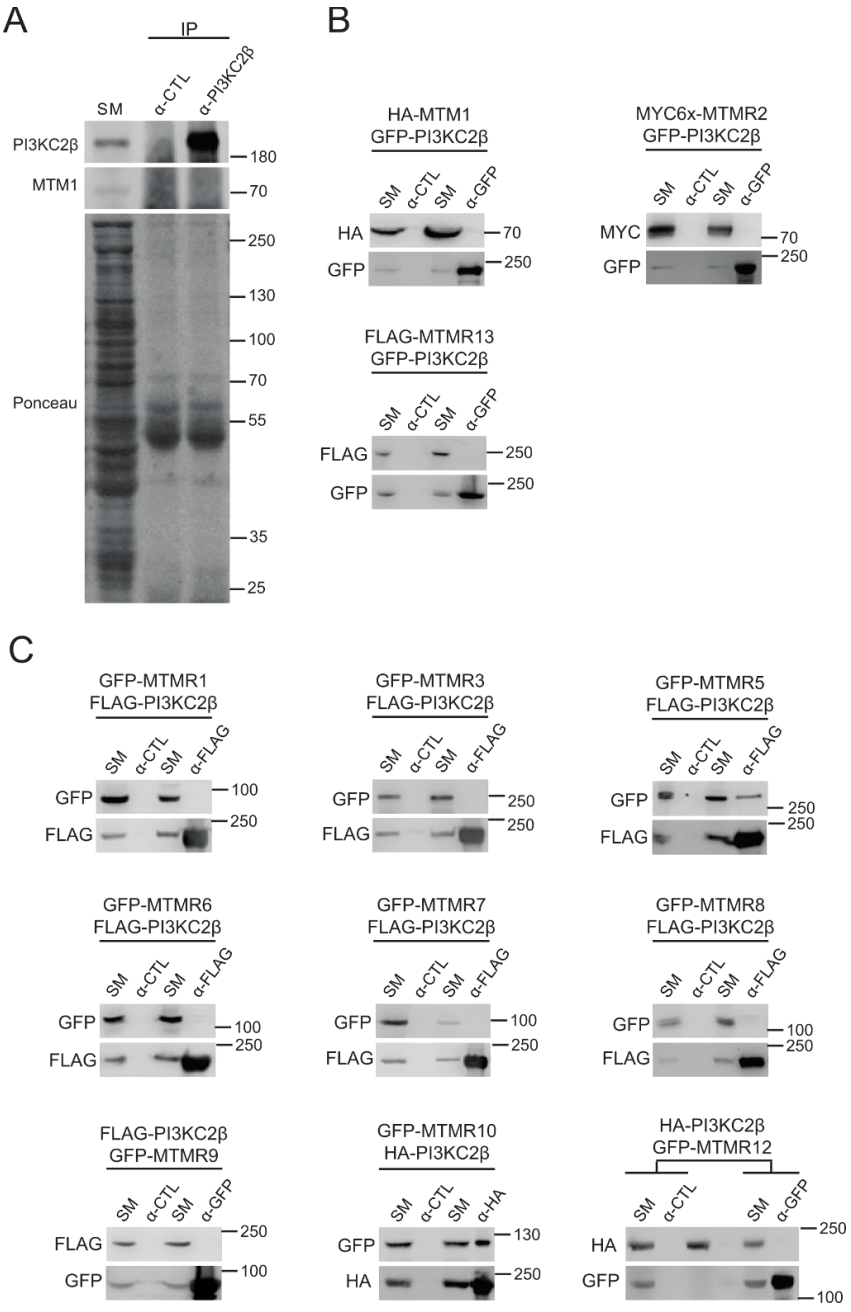

Figure 3-21. MTM1 does not co-immunoprecipitate with PI3KC2β in C2C12 or HeLa cells. (A) Protein levels of WT C2C12 myotubes (4 days of differentiation) detected by immunoblotting from starting material (SM) or bound by affinity capture using uncoupled (α-CTL) or antibody-coupled (α-PI3KC2β) protein A/G magnetic agarose beads. SM corresponds to 1% of total lysate. **(B)** Protein levels of HEK293T cells transfected with plasmids encoding for GFP-tagged myotubularin-related proteins (MTMR1, 3, 5-10, 12) and FLAG- or HA- tagged PI3KC2β, detected by immunoblotting from starting material (SM) or bound by affinity capture using control (α-CTL) or GFP (α-GFP)-Trap magnetic agarose beads. SM corresponds to 5% of total lysate. **(C)** Protein levels of HEK293T endogenously expressing eGFP-PI3KC2β and transfected with plasmids encoding for HA-MTM1, MYC6x-MTMR2 or FLAG-MTMR13, detected by immunoblotting from starting material (SM) or bound by affinity capture using control (α-CTL) or GFP (α-GFP)-Trap magnetic agarose beads. SM corresponds to 5% of total lysate.

Firstly, we evaluated whether MTM1 and PI3KC2β co-exist in modules or compartments in C2C12, as it has been shown for *D. melanogaster* homologs [88] and other kinase-phosphatase complexes (see section 1.6). For testing this, endogenous PI3KC2β was immunoprecipitated from 4-days differentiated WT myotube lysates, and co-immunoprecipitated proteins were analyzed by immunoblotting. Endogenous MTM1 did not co-immunoprecipitate with PI3KC2β, thus suggesting a direct or indirect kinase-phosphatase interaction to be unlikely occurring (**Fig. 3-21 A**). To further investigate this hypothesis in a complementary experimental setup, human GFP-tagged PI3KC2β and HA-tagged MTM1 constructs were co-overexpressed in HEK293T cells, and magnetic agarose control (CTL)- or GFP-Trap magnetic agarose beads were used to immunoprecipitate proteins from cell lysates. Immunoblotting analysis of co-immunoprecipitated proteins revealed the absence of HA-MTM1 (**Fig. 3-21 B**), further arguing against an MTM1-PI3KC2β interaction and suggesting a mechanism involving different cellular localizations or pathways for MTM1 and PI3KC2β.

We took advantage of the same experimental approach to investigate interactions of PI3KC2β with human MYC-tagged MTMR2 and FLAG-tagged MTMR13, which revealed an absence of co-immunoprecipitation (**Fig. 3-21 B**). Due to reagent availability, PI3KC2β interaction with most, but not all, MTMR family members (MTMR1, 3, 5, 6, 7, 8, 9, 10 and 12) was tested by co-overexpression of human FLAG-tagged PI3KC2β and GFP-tagged MTMRs immunoprecipitated with FLAG-Trap magnetic agarose beads. Immunoblotting analysis showed MTMR5 and MTMR10 to co-immunoprecipitate with PI3KC2β, whereas none of the other tested MTMRs did (**Fig. 3-21 C**).

3.4.2 Defective cell adhesion in MTM1-depleted C2C12 myoblasts is not rescued by mTORC1 suppression

Considering the role of PI3KC2β in the regulation of mTORC1 (see section 1.3.3.1), we hypothesized an involvement of mTORC1 in the rescue of cell adhesions in double KO myoblasts. To test this, mTORC1 was inhibited in WT and *Mtm1*KO myoblasts with its specific inhibitor rapamycin [244], and an immunostaining of surface activated β1-integrin was performed. Neither quantitative nor qualitative differences in surface active β1-integrin were observed upon 16 h treatment of *Mtm1*KO myoblasts with either 0.1 µM or 0.5 µM rapamycin (**Fig. 3-22 A, B**). Likewise, 2 h of 1 µM rapamycin treatment did not induce any changes in surface β1-integrin (**Fig. 3-22 C**). These data led us to conclude that the PI3KC2β-mediated regulation of cell adhesions is likely independent of mTORC1 modulation.

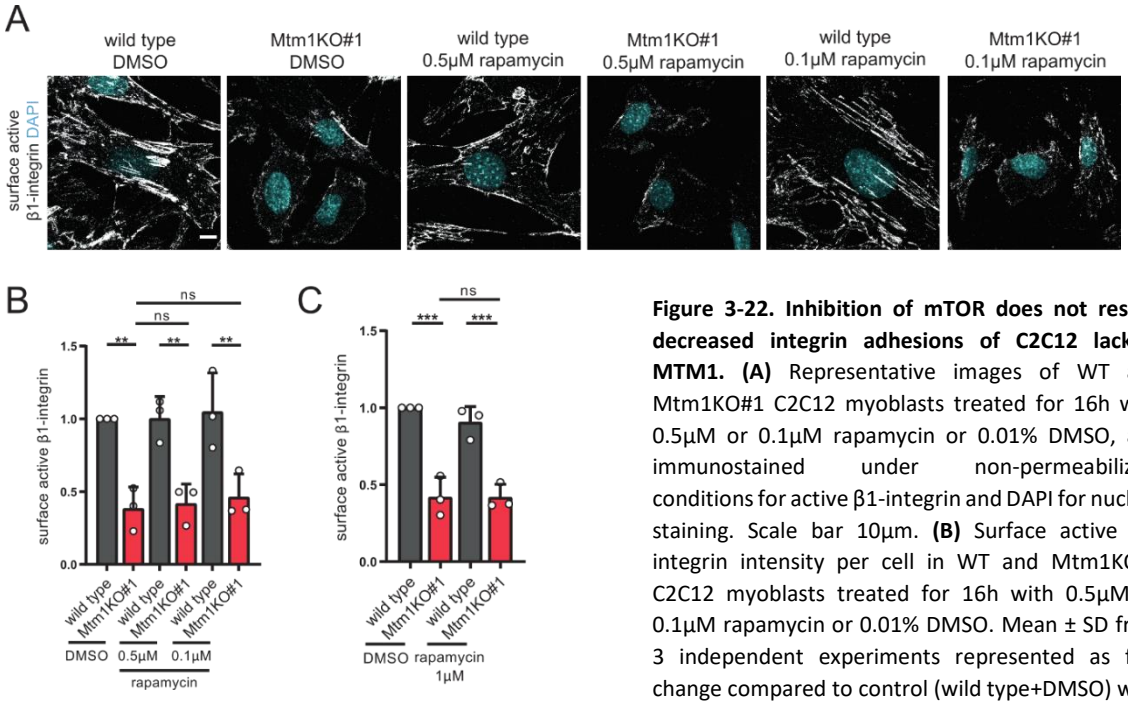

Figure 3-22. Inhibition of mTOR does not rescue decreased integrin adhesions of C2C12 lacking MTM1. (A) Representative images of WT and Mtm1KO#1 C2C12 myoblasts treated for 16h with 0.5µM or 0.1µM rapamycin or 0.01% DMSO, and immunostained under non-permeabilizing conditions for active β1-integrin and DAPI for nuclear staining. Scale bar 10µm. **(B)** Surface active β1-integrin intensity per cell in WT and Mtm1KO#1 C2C12 myoblasts treated for 16h with 0.5µM or 0.1µM rapamycin or 0.01% DMSO. Mean ± SD from 3 independent experiments represented as fold change compared to control (wild type+DMSO) with a hypothetical mean of 1. One-way analysis of variance (ANOVA; F = 12.224) and Tukey's multiple-comparison test; WT+DMSO vs Mtm1KO#1+DMSO **p = 0.0057, WT+0.5µM vs Mtm1KO#1+0.5µM **p = 0.0085, WT+0.1µM vs Mtm1KO#1+0.1µM **p = 0.0083, Mtm1KO#1+DMSO vs Mtm1KO#1+0.5µM n.s. p = 0.9998, Mtm1KO#1+DMSO vs Mtm1KO#1+0.1µM n.s. p = 0.9890. **(C)** Surface active β1-integrin intensity per cell in WT and Mtm1KO#1 C2C12 myoblasts treated for 2h with 1µM rapamycin or 0.05% DMSO. Mean ± SD from 3 independent experiments represented as fold change compared to control (wild type+DMSO) with a hypothetical mean of 1. One-way analysis of variance (ANOVA; F = 12.224) and Tukey's multiple-comparison test; WT+DMSO vs Mtm1KO#1+DMSO ***p = 0.0003, WT+1µM vs Mtm1KO#1+1µM ***p = 0.0008, Mtm1KO#1+DMSO vs Mtm1KO#1+1µM n.s. p > 0.9999.

3.4.3 Inhibition of CME enhances cell adhesion in MTM1-depleted C2C12 myoblasts

Recent studies have suggested a potential role of PI3KC2β in the internalization of adhesion proteins (see section 1.5.3.3.2), a hypothesis that is further strengthened by the reported role of CME in β1-integrin internalization (see section 1.4.2.2.1) and the importance of PI3KC2α, the related class II PI3K family member, in CME (see section 1.5.3.3.1). These observations motivated the hypothesis of a PI3KC2β-mediated endocytosis of adhesion proteins as the underlying mechanism of rescue in double KO myoblasts. To test this, CME was blocked in *Mtm1*KO using dynasore [245], an inhibitor that targets the GTPase dynamin, which is involved in endocytic vesicle fission (see section 1.4.2.2.1). Qualitative observation of surface activated β1-integrin immunostaining in dynasore-treated *Mtm1*KO myoblasts revealed a heterogeneous patch-like distribution (**Fig. 3-23 A**), which quantitatively corresponded to a non-statistically significant increase compared to DMSO-treated *Mtm1*KO myoblasts (**Fig. 3-23 B**). No differences were observed between dynasore-treated *Mtm1*KO and DMSO-treated double KO myoblasts (**Fig. 3-23 B**), altogether suggesting that inhibition of CME contributes to restoring active β1-integrin adhesions in MTM1-depleted cells.

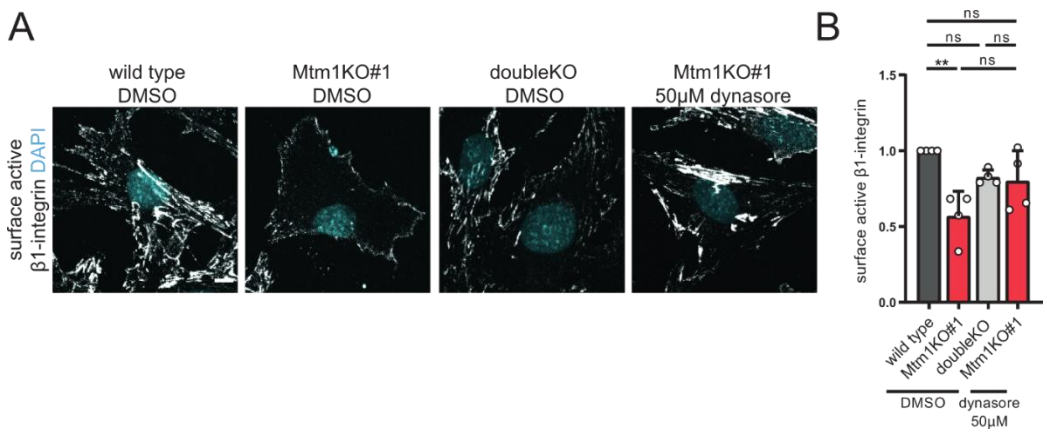

Figure 3-23. Inhibition of dynamin partially rescues decreased integrin adhesions of C2C12 lacking MTM1. (A) Representative images of WT and Mtm1KO#1 C2C12 myoblasts treated for 6h with 50µM dynasore or 0.2% DMSO, and immunostained under non-permeabilizing conditions for active β1-integrin and DAPI for nuclear staining. Scale bar 10µm. **(B)** Surface active β1-integrin intensity per cell in WT and Mtm1KO#1 C2C12 myoblasts treated for 6h with 50µM dynasore or 0.2% DMSO. Mean ± SD from 4 independent experiments represented as fold change compared to control (wild type+DMSO) with a hypothetical mean of 1. One-way analysis of variance (ANOVA; F = 7.306) and Tukey's multiple-comparison test; WT+DMSO vs Mtm1KO#1+DMSO **p = 0.0027, WT+DMSO vs doubleKO+DMSO n.s. p = 0.2856, WT+DMSO vs Mtm1KO#1+dynasore n.s. p = 0.1912, Mtm1KO#1+DMSO vs Mtm1KO#1+dynasore n.s. p = 0.0702.

3.5 PI3KC2β mediates CME of active β1-integrin

Following the evidence of a substantial improvement of integrin-mediated adhesions of *Mtm1*KO cells upon CME inhibition (**Fig. 3-23**), we explored the hypothesis of a co-regulation of integrin trafficking at the plasma membrane by MTM1 and PI3KC2β, a scenario in which PI3KC2β would potentially be involved in its internalization. Experiments in this section (3.5) have been conducted by Philipp A. Koch and included in this dissertation for completeness purposes.

3.5.1 Loss of PI3KC2β increases surface active β1-integrin and decreases internalization in HeLa cells

Investigating the role of PI3KC2β in cell adhesion regulation in C2C12 presented a major challenge, as PI3KC2β-depleted C2C12 myoblasts lack an adhesion phenotype (**Fig. 3-12 to 3-14**). This could be explained by the fact that C2C12 express low PI3KC2β protein levels, nearly undetectable in WT myoblasts compared to HeLa cells (**Fig. 3-1 B**). Consequently, HeLa cells were selected to characterize the role of PI3KC2β in the regulation of cell adhesions, taking advantage of already-available tools and reagents to study the human protein.

To study the effect of PI3KC2β depletion in HeLa cells, a siRNA-mediated knockdown (KD) approach was taken, and its efficiency validated via immunoblotting (data not shown). The impact of PI3KC2β KD in cell adhesions was assessed by surface activated β1-integrin immunostaining with a primary Alexa-conjugated antibody and total internal reflection fluorescence (TIRF) imaging, a microscopy technique that allows visualization of thin sections at the cell surface [246]. PI3KC2β depletion (siPI3KC2β + GFP) led to higher abundance of similarly distributed surface activated β1-integrin (**Fig. 3-24 A**), which was significantly increased (**Fig. 3-24 B**) compared to control conditions (siSCR + GFP). For evaluating the role of PI3KC2β catalytic activity, GFP-tagged kinase-inactive or wild type PI3KC2β constructs were overexpressed in PI3KC2β-depleted HeLa cells. This revealed that re-expression of wild type but not kinase-inactive PI3KC2β significantly rescued the surface active β1-integrin accumulation of PI3KC2β KD cells (**Fig. 3-24 A, B**). These results indicated that, in HeLa cells, PI3KC2β depletion leads to the

opposite integrin adhesion effect as MTM1 loss did in C2C12 cells, supporting the hypothesis of an involvement of PI3KC2β in active β1-integrin internalization.

To test this hypothesis, an active β1-integrin internalization assay was performed on PI3KC2β-depleted HeLa cells, and the ratio of internalized to surface integrin was calculated. A significantly decreased ratio in PI3KC2β KD cells (siPI3KC2β + GFP) compared to control (siSCR + GFP) indicated an internalization defect, which was rescued upon re-expression of wild-type GFP-tagged PI3KC2β, but not kinase-inactive GFP-PI3KC2β (**Fig. 3-24 C**). These data indicated that PI3KC2β plays a role in active β1-integrin internalization, and that its kinase activity is necessary for the process.

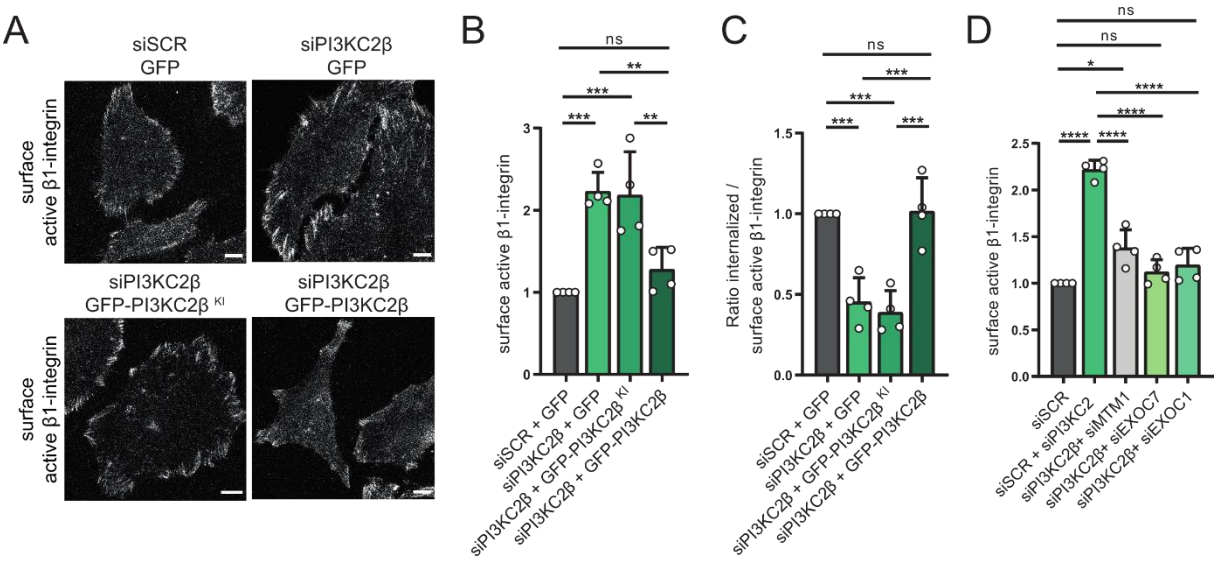

Figure 3-24. Loss of PI3KC2β kinase activity increases β1-integrin adhesions and decreases internalization in HeLa cells. (A) Representative images of HeLa cells treated with control (siSCR) or PI3KC2β-targeting (siPI3KC2β) siRNA and transfected with plasmids encoding for eGFP, eGFP-PI3KC2β or kinase inactive eGFP-PI3KC2β (eGFP-PI3KC2β KI) prior to immunostaining for active β1-integrin under non-permeabilizing conditions. Scale bar 10µm. **(B)** Surface active β1-integrin intensity per cell in HeLa cells treated with control (siSCR) or PI3KC2β-targeting (siPI3KC2β) siRNA and transfected with plasmids encoding for eGFP, eGFP-PI3KC2β or kinase inactive eGFP-PI3KC2β (eGFP-PI3KC2β KI) prior to immunostaining. Mean ± SD from 4 independent experiments represented as fold change compared to control (siSCR+GFP) with a hypothetical mean of 1. One-way analysis of variance (ANOVA; F = 15.83) and Tukey's multiple-comparison test; siSCR+GFP vs siPI3KC2β+GFP ***p = 0.0007, siSCR+GFP vs siPI3KC2β+GFP-PI3KC2β KI ***p = 0.0009, siSCR+GFP vs siPI3KC2β+GFP-PI3KC2β n.s. p = 0.6, siPI3KC2β+GFP vs siPI3KC2β+GFP-PI3KC2β **p = 0.0053, siPI3KC2β+GFP-PI3KC2β KI vs siPI3KC2β+GFP-PI3KC2β **p = 0.0075. **(C)** Relative internalized to surface active β1-integrin ratio in HeLa cells treated with control (siSCR) or PI3KC2β-targeting (siPI3KC2β) siRNA and transfected with plasmids encoding for eGFP, eGFP-PI3KC2β or kinase inactive eGFP-PI3KC2β (eGFP-PI3KC2β KI) prior to immunostaining. Surface immunostaining for active β1-integrin was performed at 4°C under non-permeabilizing conditions in starved cells, and internalization was induced by incubation in serum-containing media at 37°C. Mean ± SD from 4 independent experiments represented as fold change compared to control (siSCR+GFP) with a hypothetical mean of 1. One-way analysis of variance (ANOVA; F = 22.52) and Tukey's multiple-comparison test; siSCR+GFP vs siPI3KC2β+GFP ***p = 0.0008, siSCR+GFP vs siPI3KC2β+GFP-PI3KC2β KI ***p = 0.0003, siSCR+GFP vs siPI3KC2β+GFP-PI3KC2β n.s. p = 0.9981, siPI3KC2β+GFP vs siPI3KC2β+GFP-PI3KC2β ***p = 0.0006, siPI3KC2β+GFP-PI3KC2β KI vs siPI3KC2β+GFP-PI3KC2β ***p = 0.0002. **(D)** Surface active β1-integrin intensity per cell in HeLa cells treated with control (siSCR), PI3KC2β- (siPI3KC2β), MTM1- (siMTM1), EXOC7- (siEXOC7) or EXOC1-targeting (sEXOC1) siRNA in the indicated combinations. Mean ± SEM from 4 independent experiments represented as fold change compared to control (siSCR) with a hypothetical mean of 1. One-way analysis of variance (ANOVA; F = 49.88) and Tukey's multiple-comparison test; siSCR vs siSCR+siPI3KC2β ****p < 0.0001, siSCR vs siPI3KC2β+siMTM1 *p = 0.0107, siSCR vs siPI3KC2β+siExo70 n.s. p = 0.7205, siSCR vs siPI3KC2β+siSec3 n.s. p = 0.3015, siSCR+siPI3KC2β vs siPI3KC2β+siMTM1 ****p < 0.0001, siSCR+siPI3KC2β vs siPI3KC2β+siExo70 ****p < 0.0001, siSCR+siPI3KC2β vs siPI3KC2β+siSec3 ****p < 0.0001. **(A-D)** Data obtained by P.A.K.

As CME is reportedly the most common mechanism of β1-integrin internalization [132], we hypothesized that PI3KC2β was involved in CME of active β1-integrin, similarly to the role PI3KC2α in this process. Our mechanistic hypothesis was confirmed upon observation that PI3KC2β localized at clathrin coated pits (CCP) and immunoprecipitated with CME proteins clathrin and AP-2, as well as scaffolding protein ITSN1 and integrin-specific endocytic adaptor DAB2 (data not shown), indicating that PI3KC2β can localize at CCP with specific cargo adaptors. The functional relevance of the newly-identified integrin adaptors was evidenced when loss of ITSN1 or DAB2 phenocopied the surface active β1-integrin accumulation and reduced internalization of PI3KC2β KD (data not shown). Altogether, these findings contributed to concluding that PI3KC2β mediates CME of activated β1-integrin via the specific cargo adaptors ITSN1 and DAB2, and that this process is dependent on its catalytic activity. Taken together with the role of MTM1 in exocytosis of β1-integrin (see section 1.3.2), these data revealed that PI3KC2β and MTM1 regulate opposite functions in β1-integrin trafficking in HeLa cells, respectively controlling its removal and delivery to cell adhesions at the plasma membrane.

To corroborate these conclusions, we evaluated whether loss of key exocyst subunits rescued the accumulation of integrin adhesions in PI3KC2β-depleted cells. For this, siRNA-mediated KD of PI3KC2β and co-KD with MTM1, EXOC7 or EXOC1 was performed in HeLa cells, and surface activated β1-integrin was quantified as indicated before. Whereas a previously-described increase was observed upon PI3KC2β KD (siSCR + siPI3KC2β) compared to control (siSCR), co-KD with MTM1, EXOC7 or EXOC1 led to a significant decrease compared to PI3KC2β KD and similar levels than in control conditions, with non-significant differences for EXOC7 and EXOC1 co-KD and a slight increase upon MTM1 co-KD (**Fig. 3-24 D**). In summary, these data supported the involvement of PI3KC2β and MTM1 in functionally opposite pathways by revealing a rescue of PI3KC2β KD phenotype upon withdrawal of MTM1-mediated exocytosis.

3.6 PI3KC2β as a novel therapeutic target for XLCNM

3.6.1 Inhibition of PI3KC2α/β enhances cell adhesion in HeLa cells and MTM1-depleted C2C12 myoblasts

Highlighting the relevance of cell adhesions in defining XLCNM pathogenesis and demonstrating that genetic ablation of PI3KC2β rescued adhesion defects of MTM1-depleted myoblasts evidenced that PI3KC2β is a potential therapeutic target for XLCNM. Due to a lack of PI3KC2β-specific chemical inhibitors, we took advantage of the class II PI3KC2α/β inhibitor PITCOIN3 produced by our group (**Fig. 3-25 A**) [247] and the cellular models established in this project to perform proof-of-principle experiments for a novel therapeutic approach for XLCNM.

To evaluate the effect of PI3KC2α/β inhibition on integrin adhesions, HeLa cells were treated for 24 h with 10 µM PITCOIN3 inhibitor, and a surface β1-integrin immunostaining was performed and analyzed using an Alexa fluorophore directly-labelled antibody and TIRF imaging. It revealed a similarly distributed (**Fig. 3-25 B**) and increased signal in inhibitor-treated cells compared to DMSO-treated control (**Fig. 3-25 C**), indicating that PI3KC2α/β inhibition phenocopies PI3KC2β loss in HeLa cells. Following this observation, we hypothesized that PITCOIN3 treatment could rescue adhesion defects caused by MTM1 depletion in C2C12 myoblasts, similarly as observed in double KO cells (**Fig. 3-13; 3-14**). Hence, WT, *Mtm1*KO and double KO myoblasts were treated for 16

h with 10 µM PITCOIN3 or DMSO, and surface active β1-integrin was immunostained following the described protocol for C2C12. PI3KC2α/β inhibition qualitatively led to more abundant and mildly disorganized adhesions in WT and *Mtm1*KO myoblasts compared to the corresponding DMSO-treated controls (**Fig. 3-25 D**). Quantitatively, these corresponded to an increase of surface active β1-integrin in inhibitor-treated WT and *Mtm1*KO cells in comparison to DMSO-treated controls. This increase was significant for WT myoblasts (p-value = 0.016) but non-significant for *Mtm1*KO cells (p-value = 0.070) yet with a clear tendency in the latter (**Fig. 3-25 E**). The lack of differences between inhibitor-treated *Mtm1*KO and DMSO-treated WT or double KO myoblasts further supported a rescue of surface active β1-integrin defects in *Mtm1*KO cells upon PI3KC2α/β inhibition. The improvement of integrin adhesion defects of MTM1-depleted cells upon PITCOIN3 treatment sets initial proof-of-concept evidence for a potential new XLCNM therapeutic approach based on chemical inhibition of PI3KC2β, strongly supported by genetic studies in mouse [42] and cell-based models (this study).

A

Compound	Target	IC_{50} (µ
PITCOIN3	PI3KC2α	0.1
	PI3KC2β	1.5

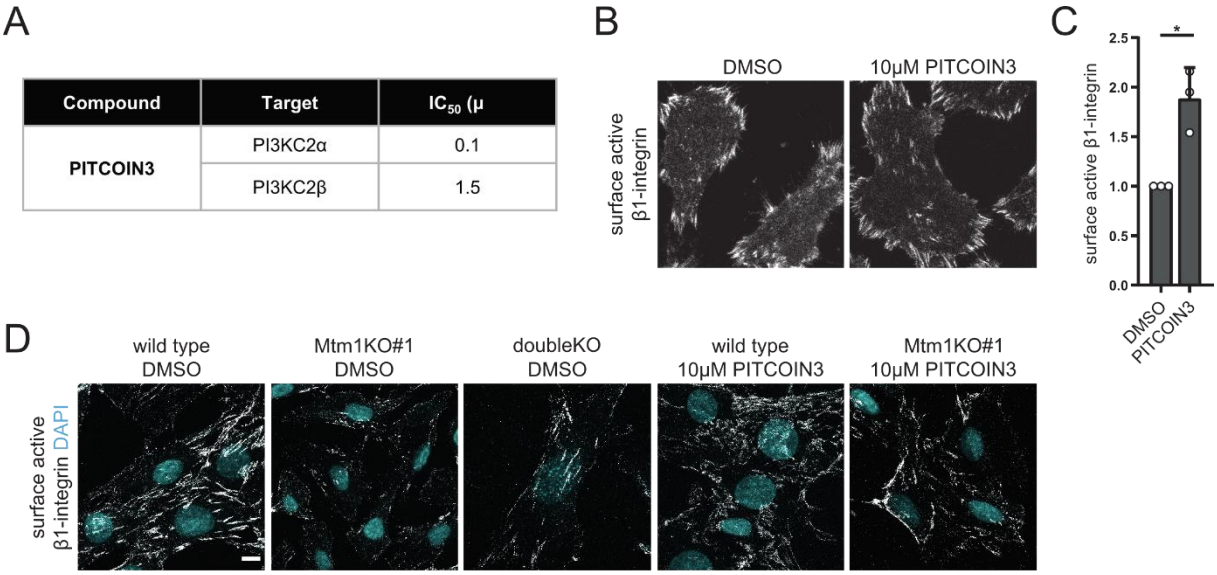

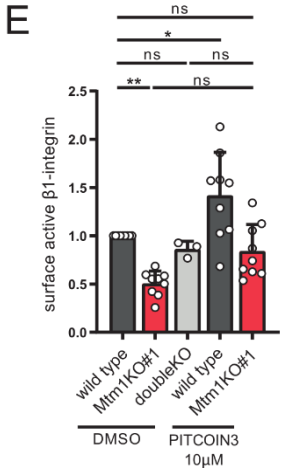

Figure 3-25. PI3KC2β inhibition rescues decreased β1-integrin adhesions of C2C12 lacking MTM1. (A) IC_{50} values of PITCOIN3 inhibitor targeting PI3KC2α and PI3KC2β. **(B)** Representative images of HeLa cells treated for 24h with 10µM PITCOIN3 inhibitor or 0.1% DMSO, and immunostained under non-permeabilizing conditions for active β1-integrin. Scale bar 10µm. **(C)** Surface active β1-integrin intensity per cell in HeLa cells treated for 24h with 10µM PITCOIN3 inhibitor or 0.1% DMSO. Mean ± SD from 3 independent experiments represented as fold change compared to control (DMSO) with a hypothetical mean of 1. One-sample two-tailed t test; *p = 0.0399. **(D)** Representative images of WT, Mtm1KO#1 and doubleKO C2C12 myoblasts treated for 16h with 10µM PITCOIN3 inhibitor or 0.1% DMSO, and immunostained under non-permeabilizing conditions for active β1-integrin and DAPI for nuclear staining. Scale bar 10µm. **(E)** Surface active β1-integrin intensity per cell in WT, Mtm1KO#1 and doubleKO C2C12 myoblasts treated for 16h with 10µM PITCOIN3 inhibitor or 0.1% DMSO. Mean ± SD from 9 independent experiments represented as fold change compared to control (wild type+DMSO) with a hypothetical mean of 1. One-way analysis of variance (ANOVA; F = 13.97) and Tukey's multiple-comparison test; WT+DMSO vs Mtm1KO#1+DMSO **p = 0.0029, WT+DMSO vs doubleKO+DMSO n.s. p = 0.9325, WT+DMSO vs WT+PITCOIN3 *p = 0.0160, WT+DMSO vs Mtm1KO#1+PITCOIN3 n.s. p = 0.6978, Mtm1KO#1+DMSO vs Mtm1KO#1+PITCOIN3 n.s. p = 0.0760, doubleKO+DMSO vs Mtm1KO#1+PITCOIN3 n.s. p > 0.9999. **(A)** Data obtained by W.T.L. **(B-C)** Data obtained by P.A.K.

4. Discussion

This work described a new function of class II PI3KC2β in the regulation of integrin adhesions, setting a mechanistic background for its role in the rescue of the XLCNM disease phenotype. Furthermore, by establishing cell-based models of XLCNM, we provided insights into cell adhesion defects key to disease pathogenesis, as well as a suitable *in vitro* system for the study of the cellular phenotypes of MTM1 loss and proof-of-principle inhibitor-based therapeutic strategies.

Our data demonstrated that depletion of MTM1 in C2C12 myoblasts results in defective cell adhesion, as shown by decreased FAs and activated β1-integrin at the plasma membrane, and consequently impaired cell spreading, migration and myogenesis. These phenotypes are due to the role of MTM1-mediated PI(3)P turnover in endosomal exocytosis of integrins [83], a recycling pathway for the formation of integrin adhesions. We showed that PI3KC2β depletion in these models rescues adhesion defects and associated functional phenotypes, in accordance with the complete disease rescue in mouse models upon skeletal muscle-specific PI3KC2β ablation [42]. We uncovered the molecular mechanism underlying this rescue by demonstrating a role of PI3KC2β in endocytosis of active β1-integrin, which results in the re-balancing of adhesion capacity in MTM1- and PI3KC2β-depleted C2C12 myoblasts. These data evidence antagonistic roles of MTM1 and PI3KC2β in the regulation of integrin adhesions and open a future perspective for XLCNM therapeutic strategies targeting PI3KC2β. In this context, we provided proof-of-concept evidence using a class II PI3K inhibitor developed in our institute [247].

4.1. Cell-based modelling of XLCNM

Since the firstassociation of MTM1 to XLCNM [9], many studies have focused on deciphering its functions in physiological and pathological conditions, with the main goal of gaining insights into XLCNM pathogenesis in order to develop therapies for this currently incurable disorder [2]. As a result of these studies, MTM1 has been implicated in a variety of cellular functions believed to act synergistically in determining XLCNM pathology, although the precise contribution of each of these mechanisms is still debated [3,6]. A variety of systems ranging from patient muscle biopsies to genetically modified cell lines have been used to model XLCNM in these studies, each with corresponding advantages and limitations but collectively offering comprehensive cellular and histological insights into MTM1 functions [2,3].

Due to the high structural complexity of skeletal muscle, *in vitro* modelling of this tissue presents important limitations for studies aimed at muscle function and histological phenotyping. Whereas some functional readouts, especially related to muscle contractility and Ca^{2+} dynamics, can be assessed using *in vitro* differentiated muscle cells [248], the structural hallmarks of myofibers are not recapitulated in most cell line-based *in vitro* models, implying that elements such as the triad or the contractile machinery, importantly affected in XLCNM, are profoundly different or inexistent compared to organismal tissues [248,249]. Consequently, the availability of mouse models that consistently recapitulate functional and histological hallmarks in physiological and pathological conditions has favored their use in the majority of these studies. In contrast, *in vitro* modelling offers important advantages in terms of availability, maintenance, and experimental manipulation, and is thus

frequently used in cell biological and biochemical studies aiming to investigate the molecular mechanisms of cell processes.

In this study, we selected the murine myoblast cell line C2C12 to generate cell-based models of XLCNM. The fact that the first functional link between MTM1 and PI3KC2β in a mammalian system was established in mouse models [42], as well as reagent availability, favored the selection of this commonly used mouse-derived cell line. Secondly, the C2C12 cell line was originally established because of its proliferative progenitor nature and capacity to differentiate into myotubes [233], thus offering a two-in-one system with migratory, fibroblast-like, and easy-to-manipulate undifferentiated cells, as well as senescent differentiated myoblasts. Additionally, the differentiation capacity of C2C12 cells allows the study of myogenesis *in vitro* [250]. Differential gene expression during myogenesis is exemplified in this thesis by increasing expression of MTM1 during the first four days of differentiation (**Fig. 3-1 A, C**) [237], a phenomenon that was not observed for PI3KC2β.

In C2C12, a complete KO approach was applied via CRISPR-Cas9 genetic engineering technique in order to generate cell lines lacking expression of our proteins of interest MTM1 and PI3KC2β. In contrast to gene silencing via siRNA- or shRNA-mediated KD, complete genetic ablation presents the advantage of facilitating manipulation and decreasing experimental variability intrinsic to KD, yet can give rise to compensatory mechanisms, especially after multiple cell culture passages due to sub-culturing [251]. Additionally, KO cell lines were clonally isolated, implying potential clonal effects might arise [252], as observed for some of the reported phenotypes. To minimize compensatory mechanisms and clonal effects, cell cultures were stocked and maintained at low passage number and more than one clone of each genotype was studied.

Genetic screening of KO cell lines indicated partial KO (< 90% InDel score) in *Mtm1*KO #2 and #3 despite immunoblotting revealing a complete loss of protein expression (**Fig. 3-2 C**; section 2.2.3.5). Even if exclusively genetic data were considered, these clonal cell lines would still be suitable to model XLCNM, as most *MTM1* patient mutations lead to partial loss of function, and female carriers present histological and minor functional hallmarks of XLCNM (see section 1.1.1). Moreover, *Mtm1*KO #2 and #3 displayed the same phenotypes as *Mtm1*KO #1, a clone with complete gene and protein expression loss (**Fig. 3-2 B**; section 2.2.3.5). Similarly, *Mtm1*^{hypo}/*Pik3c2b*KO cell line revealed partial loss of *Pik3c2b* in genetic screening, but complete loss of PI3KC2β by immunoblotting (**Fig. 3-2 D**). Supported by the argument above, we used this clonal cell line to back the results obtained in double KO, even though *Mtm1* gene and protein expression was only partially reduced.

The selection of a cell-based model for this project limits the study of functional and structural alterations in XLCNM such as ECC or triad anomalies (see section 1.3.3.5) due to the reasons discussed above. Although we focused on cell adhesion defects, other cellular phenotypes associated with MTM1 loss and previously described by others were qualitatively observed by immunostaining in *Mtm1*KO C2C12, further supporting the suitability of the model. These included an enlargement of the endolysosomal compartment [82,85], as shown by increased EEA1 and RAB5 signal, corresponding to the early endosomal compartment, and LAMP1 and RAB7 signal, associated with late endosomal compartments. A re-distribution of the recycling compartment, marked by TfR immunostaining and previously shown by Ketel *et al* [83] to be associated with recycling defects, was also observed (**Fig. 3-11 A**). Alterations of the intermediate filament cytoskeleton, reported in myotubes [99,107], were present in

C2C12 myoblasts as a disorganized network upon MTM1 depletion (**Fig. 3-11 C**). Conversely, alterations in ER [253] and mitochondria [34,98,99] were not observed in these cells, and neither were Golgi defects (**Fig. 3-11 B**).

4.2. MTM1 regulates cell adhesions relevant to XLCNM pathogenesis

In this study, we showed that MTM1-depleted cells present major cell adhesion defects and offered a comprehensive overview of this phenotype by investigating cell spreading and FA status, as well as the functional consequences on cell migration and myogenesis. Crucial data defining defective cell adhesion in *Mtm1*KO myoblasts were decreased cell area to cell volume ratio (**Fig. 3-3 D**), which affects the interpretation of immunocytochemical data on adhesion molecules, as explained in section 3.2.1. Although studying cell adhesion dynamics would have been optimal, immunostaining of adhesion molecules on fixed cells provided valuable information using a simpler technique. Analysis of FA number and size reflects cell adhesion status with complementary information on FA formation capacity and maturation [115,116], strengthened by the assessment of molecules corresponding to different functional layers of FAs. A decreased number of FAs per cell, consistent for all proteins analyzed, was either suggestive of an impaired FA assembly process or an enhanced turnover [120]. FA size tended to be decreased in most markers despite lacking statistical significance (**Fig. 3-4**), indicative of minor, if any, defects in maturation by adhesion protein clustering [116]. Even though the study of FA dynamics in live cells would have provided conclusive data on whether FA assembly or disassembly is affected in *Mtm1*KO myoblasts, the known role of MTM1 in β1-integrin exocytosis [83] suggested that the decreased FA number in these cells is due to defective exocytosis of integrins and a subsequent impairment in FA formation.

The involvement of MTM1 in integrin recycling prompted us to investigate integrin molecules complementarily to intracellular FA components. In particular, we focused on the β1-integrin subunit due to its predominance over other β subunits in almost all tissues [254], and the fact that α7β1-integrin dimers are the most abundant in skeletal muscle IACs [156]. Whereas surface activated β1-integrin was studied to assess actively adhesive ECM-bound IACs [254], an intracellular immunostaining of total integrins was performed to identify further impairments in trafficking. In agreement with data from other FA components, *Mtm1*KO myoblasts displayed decreased surface activated β1-integrin, indicative of defective adhesion. The observation of a decreased number of *Mtm1*KO cells compared to WT after immunostaining, likely washed off during the protocol, further suggested low adhesive capacity and a potentially larger effect size of this phenotype than actually reported (**Fig. 3-5 A, B**). The absence of quantitative alterations in intracellular total β1-integrin in MTM1-depleted cells conflicts with the data obtained on surface integrins as well as the observation of intracellular inclusions of β1-integrin by other studies [26, 83,169]. Nevertheless, MTM1-depleted cells displayed important qualitative differences in β1-integrin distribution, as most signal corresponded to intracellular compartments, whereas WT myoblasts presented a typical adhesion-like β1-integrin distribution pattern (**Fig. 3-5 A, C**). Altogether, these data were suggestive of unaltered total β1-integrin levels in *Mtm1*KO myoblasts and argued against differential expression or protein degradation in comparison to WT therefore indicating a putative trafficking alteration leading to altered distribution.

Although we reported comprehensive data on β1-integrin-mediated cell adhesions, certain aspects of integrin biology were not assessed in this project. Firstly, myoblasts were uniquely cultured for cell adhesion evaluation

on a Matrigel-based ECM matrix, implying that, due to the ECM-specificity of integrin dimers [132], the reported adhesive properties of genetically-modified C2C12 may differ on other substrates. However, Matrigel was selected for these experiments due to a mixed composition (collagen IV, laminin, proteoglycans) that mimics myoblast physiological conditions and favors β1-integrin-mediated adhesions [255]. Secondly, integrins other than β1 subunit were not evaluated; this was due to the fact that, as previously discussed, β1-integrin is the most abundant isoform in almost all tissues and plays major roles in skeletal muscle adhesions (see section 1.4.3). Consequently, we considered its study, complemented with FA assessment, sufficient to obtain comprehensive data on adhesion defects. How alternative ECM substrates of different composition and stiffness affect cell adhesions, and how MTM1 and PI3KC2β control the trafficking of α- or β-integrin subunits other than β1, remains to be assessed in future studies. Furthermore, the signaling roles of integrins and some intracellular components of FAs are well described [115,254]. As this study focused on the adhesive roles of these molecules [115], alterations in integrin- and FA-associated signaling and their implications in XLCNM phenotype remain to be assessed in the future.

Regarding the functional implications, the observation of enhanced migration of *Mtm1*KO myoblasts correlates to the described cell adhesion defects either by a decreased FA assembly or increased FA turnover. In both contexts, the inability to form stable, long-lived adhesions facilitates motility due to lack of anchorage points, thus enhancing migration speed [120]. Alterations in FA dynamics also have implications in the process of myogenesis due to the relevance of cell fusion and formation of stable and specialized myoblast adhesions in myogenesis and differentiated cells [157]. This was evidenced in our study by aberrant morphology and impaired usion of MTM1-depleted myotubes at 7 days of differentiation, a phenotype that correlates to the defective skeletal muscle maintenance observed in XLCNM organismal models [169,170].

Data from previous studies shed light on the mechanistic role of MTM1 in endosomal exocytosis [83], additionally establishing an association to adhesion proteins. From this compelling evidence, we hypothesized that MTM1 depletion led to defective cell adhesion due to impaired exocytosis of integrins, which in turn would result in impaired FA formation and endosomal PI(3)P accumulation. In agreement with this hypothesis, we observed increased PI(3)P in *Mtm1*KO myoblasts to similar levels than observed in other cell-based studies (**Fig. 3-9 A, D**; section 1.3.2) [81–84], and showed the adhesion defects to be phosphatase-activity dependent. The latter is supported by the fact that overexpression of wild type but not phosphatase-inactive MTM1 rescued decreased surface integrin levels of *Mtm1*KO myoblasts (**Fig. 3-6**). Decreased expression of VPS34 and PI3KC2α, PI(3)P-synthesizing enzymes [177,198], in *Mtm1*KO myoblasts further supported this observation (**Fig. 3-11 D**), as we expect their downregulation to result from a compensatory mechanism aimed at re-establishing PI homeostasis. Regarding other PI species, assessment of $PI(3,4)P_2$, linked to endocytosis and signaling [50,51], and PI(4)P, intracellularly defining the Golgi compartment [44], revealed no differences in MTM1-depleted cells compared to WT (**Fig. 3-9 B, C, E, F)**. These data are in agreement with observations from other studies, which have mainly reported a PI(3)P accumulation and, in some models, a $PI(3,5)P_2$ accumulation using a variety of techniques [82,83,87].

4.3. Loss of PI3KC2β rescues XLCNM cell adhesion phenotype

In this study, we demonstrated that genetic ablation of PI3KC2β in XLCNM cell-based models rescues cell adhesion defects and subsequent defective migration and myogenesis, a phenomenon mechanistically explained by an involvement of PI3KC2β in the endocytosis of integrins. The reported rescue included a complete normalization of cell spreading, number of FAs and surface activated β1-integrin in MTM1 and PI3KC2β double KO and hypomorphic/KO myoblasts (**Fig 3-12** to **3-15**). Concomitant defective migration and myogenesis were equally normalized in double KO C2C12 (**Fig. 3-17**; **3-18**). Additionally, a rescue of surface activated β1-integrin was also observed upon shRNA-mediated PI3KC2β KD in *Mtm1*KO myoblasts (**Fig. 3-15 J**). Interestingly, double KO and hypomorphic myoblasts displayed decreased levels of total β1-integrin (**Fig. 3-14**; **3-15**), which contrasts to normalized surface active β1-integrin expression. It is plausible to hypothesize that most β1-integrin in these cells constitutes active adhesions, stalled at the plasma membrane due to impaired internalization, yet total decreased levels cannot be explained by our model. Decreased β1-integrin expression or increased degradation associated with a compensatory effect might offer an answer to this unexplained phenotype.

In contrast to the depletion of both enzymes, loss of PI3KC2β alone did not lead to changes in any of the cell adhesion-related phenotypes studied, yet strikingly caused a 25% decrease in myoblast migration distance and speed in *Pik3c2b*KO myoblasts (**Fig. 3-17 B**), an observation consistent with a previously described phenotype [256,257]. Additionally, increased total β1-integrin levels upon PI3KC2β KO (**Fig. 3-14**) may as well associate with an underlying phenotype of enhanced cell adhesion, or a potential involvement of PI3KC2β in integrin degradation. In fact, some of our data (not shown) indicated that PI3KC2β plays a role in endosomal sorting of β1-integrin by promoting lysosomal degradation, which would explain increased total levels in *Pik3c2b*KO. Of note, PI3KC2β depletion led to partially defective myogenic differentiation, potentially due to culture overgrowth as a result of mTORC1 hyperactivation [51], as shown by a mildly decreased differentiation index (**Fig. 3-18 B**). Besides these examples, a surprising lack of phenotypes upon PI3KC2β loss, initially hypothesized to be opposite to those associated to MTM1 depletion, could ultimately be explained by low PI3KC2β expression in C2C12. Interestingly, a similar lack of adhesion-related phenotypes was observed upon depletion of the PI3KC2β homolog in a cell-based *D. melanogaster* study [85]. In contrast to the observations in C2C12, an integrin adhesion phenotype was present in HeLa cells depleted of PI3KC2β via siRNA-mediated KD, whereas MTM1-depletion did not lead to major adhesion defects in these cells (data not shown). This phenomenon is likely due to differential expression of MTM1 and PI3KC2β in C2C12 and HeLa cells, as illustrated in **Fig. 3-1 B**.

In HeLa cells, PI3KC2β depletion led to increased active β1-integrin adhesions (**Fig. 3-24 A, B**), therefore presenting with the opposite phenotype as observed in *Mtm1*KO. Considering the tight association between FA and its transmembrane components integrins, we speculate that loss of PI3KC2β would lead to increased number of FAs in HeLa cells, yet this phenotype was not investigated. Overexpression of wild type but not kinase-inactive PI3KC2β led to normalization of surface active β1-integrin (**Fig. 3-24 A, B**), implying that the PI3KC2β-mediated rescue that we describe is dependent on PI(3)P or PI(3,4)P_2 synthesis. Data on C2C12 showing that overexpression of wild type but not kinase-inactive PI3KC2β in double KO myoblasts mildly decreased active β1-

integrin adhesions (**Fig. 3-16**) further supports an involvement of PI3KC2β catalytic activity. These findings suggest that the kinase-independent scaffolding roles of class II PI3Ks are not involved in the mechanism [204].

4.3.1 Examination of mechanistic hypotheses for a PI3KC2β-mediated rescue of XLCNM

We challenged several hypotheses regarding the normalization of XLCNM phenotypes by PI3KC2β depletion, based on opposed effects of MTM1 and PI3KC2β in the regulation of one or several cellular processes involved in XLCNM pathogenesis. We hypothesized that (i) a control of opposing pathways by kinase-phosphatase protein modules comprising MTM1 and PI3KC2β and/or (ii) a normalization of PI(3)P accumulation via a co-regulation of PI(3)P pools by PI3KC2β could mechanistically explain opposed roles of the two enzymes in (iii) cell adhesion dynamics and/or (iv) mTORC1 signaling.

The scenario of putative (i) MTM1-PI3KC2β complexes would necessitate a co-existence of MTM1 and PI3KC2β at a certain cellular compartment. Previous studies reported kinase-phosphatase modules in PI regulation [86] and evidenced the importance of myotubularins and class II PI3K complexes in membrane remodeling [85,88]. We observed co-immunoprecipitation of phosphatase-inactive myotubularins MTMR5 and MTMR10 with PI3KC2β, yet co-immunoprecipitation with MTM1 occurred neither upon overexpression in HEK293T cells nor endogenously in C2C12 myotubes (**Fig. 3-21**), suggesting that both proteins were unlikely to form a complex. The expression pattern of MTM1 and PI3KC2β during C2C12 myogenesis (**Fig. 3-1 A, C**), increasing for MTM1 and stable for PI3KC2β, further supported this observation. Nevertheless, identification of putative new PI3KC2β interactors with yet undescribed functions opens future research questions as to their physiological relevance and potential involvement in pathology, as MTMR5 has been linked to CMT neuropathy type 4B3 [74]. Their study would provide insights into potentially new regulation mechanisms of PI3KC2β and/or myotubularins, such as those controlling localization or enzymatic activity already described for some inactive myotubularin family members [60].

A second hypothesis that we explored was the (ii) direct rebalancing of PI(3)P levels in *Mtm1*KO cells by removing a potential source of PI(3)P, PI3KC2β. This is assumed to be the main mechanism underlying XLCNM rescue by PI3KC2β loss in most studies since class II PI3K was reported to be involved in this context, and some of them have reported a normalization of PI(3)P in MTM1- and PI3KC2β-depleted skeletal muscle [42] and cells [85,88] by different techniques. Nevertheless, the current discussion on PI3KC2β substrates (see section 1.5.3.2), and the fact that the exact mechanistic role of PI3KC2β in XLCNM rescue remained undescribed until the present study, hindered the acquisition of precise subcellular-level data on PI3KC2β substrates. We challenged the hypothesis above by assessing PI(3)P levels in double KO myoblasts as well as studying the effect of PI(3)P depletion on integrin adhesions. Although a decrease of PI(3)P in *Pik3c2b*KO myoblasts was observed, PI(3)P accumulation was not normalized in double KO cells, which displayed increased levels to a higher extent than MTM1-depleted myoblasts (**Fig. 3-19**). Treatment with a VPS34 inhibitor, well-described to decrease PI(3)P [238], did not restore surface activated β1-integrin adhesions in *Mtm1*KO myoblasts (**Fig. 3-20**). The latter results are in line with organismal-level evidence showing that VPS34 muscle-specific depletion or inhibition did not ameliorate phenotypic XLCNM in *D. melanogaster*, mice, or zebrafish [42,169], but conflicts with a rescue of defective exocytosis and trafficking in XLCNM *D. melanogaster*-derived cells and MTM1-depleted HeLa cells upon VPS34 inhibition

[83,85]. Overall, our data indicated that VPS34 depletion does not rescue the MTM1 loss phenotype, as evidence from animal models suggests, and that the rescue of certain phenotypes on cell-based models might be system-specific. In the context of PI conversion, our data imply that either MTM1 and VPS34 complex II act on different PI(3)P pools or, in case they act on the same pool, its normalization is unrelated to the disease rescue. Considering the existence of MTM1-VPS34 complexes that control PI(3)P pools at endosomes [82,86], the absence of rescue by VPS34 depletion is surprising, as an alternative co-regulation mechanism by PI3KC2β in a complex with MTM1 seems unlikely, as discussed previously. Consequently, it is plausible to hypothesize that the rescue of XLCNM phenotypes by PI3KC2β depletion might occur via an independent pathway without normalization of PI(3)P pools, thus disproving the prevailing model. Even though our PI(3)P immunocytochemical data did not provide subcellular compartment information, implying that an actual normalization of PI(3)P could be occurring at a certain localization, we propose that PI3KC2β rescues XLCNM phenotype via an alternative pathway, functionally opposed to MTM1-mediated exocytosis. Although we show that the rescue mechanism involves PI conversion (**Fig. 3-16; 3-24 A-C**), our data are inconclusive regarding the specific PI species involved, either PI(3)P or $PI(3,4)P_2$. As we propose PI3KC2β to mediate endocytosis of integrins, and considering the relevance of PI3KC2α catalytic activity during CME [50], it is plausible to hypothesize that PI3KC2β synthesizes $PI(3,4)P_2$ in this context. The proposed hypothesis is based on structural and functional similarities among class II PI3Ks, as well as the described role of PI3KC2β in internalization pathways such as pinocytosis [201]. In summary, we propose (iii) MTM1 and PI3KC2β to mediate opposed functions in the regulation of integrin trafficking and, subsequently, in FA dynamics (see section 1.4.2). The fact that CME blockage by dynamin inhibition improved active β1-integrin adhesion phenotype of XLCNM myoblasts (**Fig. 3-23**) suggested this to be the mechanism underlying PI3KC2β-mediated rescue. Similarly, blockage of dynamin-mediated endocytosis has been reported to prevent FA disassembly and impair cell migration in cultured cells [127].

In parallel, an alternative hypothesis was investigated, as a (iv) role of PI3KC2β in the regulation of mTORC1 signaling has recently been described [51,194]. In this context, PI3KC2β depletion triggers peripheral localization of lysosomes [51], whose hydrolytic enzymes have been shown to mediate FA disassembly upon extracellular release during lysosomal exocytosis [130]. Furthermore, MTM1 has been associated with altered mTORC1 signaling in some models [84,97,98]. These evidence prompted to investigate the role of both enzymes in mTORC1 regulation in the context of XLCNM adhesion defects was investigated. *Mtm1*KO C2C12 did not display altered mTORC1 signaling as shown by unchanged phosphorylation status of its downstream effector S6K (**Fig. 3-11 E**). Additionally, mTORC1 inhibition by rapamycin treatment had no effect on integrin adhesions of MTM1-depleted cells (**Fig. 3-22**), altogether suggesting that MTM1 and PI3KC2β were unlikely to co-regulate cell adhesions via modulation of mTORC1 signaling.

The study of further alternative mechanisms underlying XLCNM cell adhesion phenotype rescue by PI3KC2β depletion was beyond the scope of this thesis. Nevertheless, undescribed direct or indirect roles of PI3KC2β in FA disassembly would as well result in a similar rescue upon its loss, due to destabilization of adhesions. An involvement of PI3KC2β in promoting actin cytoskeleton remodeling at membrane protrusions and lamellipodia via RHO GTPases, proposed in studies that linked the kinase to cell migration [214,258], could as well justify the observed rescue in MTM1- and PI3KC2β-depleted cells.

4.4. PI3KC2β mediates endocytosis of active β1-integrin

The absence of PI3KC2β-associated phenotypes in C2C12 KO cells limited the acquisition of mechanistic data from this model, favoring the use of siRNA-mediated KD in HeLa cells. Additionally, genetically modified HEK293T cells expressing endogenously tagged PI3KC2β were used to obtain biochemical data supporting our hypothesis of a PI3KC2β role in integrin CME. These experiments revealed (i) the presence of PI3KC2β at CCPs, and (ii) co-immunoprecipitation with CME components involved in integrin internalization (data not shown). These findings uncover a putative new role of PI3KC2β in CME as well as an interaction with the specific β1-integrin adaptor DAB2 [144,145], whereas interaction with clathrin and ITSN1 had already been reported and linked to β1-integrin internalization [148, 193,259]. Furthermore, we provided functional data supporting the role of these adaptors in integrin endocytosis, showing that their depletion phenocopied PI3KC2β loss by leading to increased surface β1-integrin (data not shown). According to our hypothesis of a cargo-specific role of PI3KC2β in β1-integrin endocytosis, co-localization data evidenced the presence of PI3KC2β at a subpopulation of CCPs, yet not all of them (data not shown), where PI3KC2α-mediated endocytosis of other cargoes may be occurring. Cargo specificity is further supported by the fact that PI3KC2α does not co-immunoprecipitate with β1-integrin adaptors ITSN1 and DAB2 (data not shown). A role of AP-2 in integrin endocytosis is reported for some α-subunits [134], although its involvement in integrin internalization and FA disassembly has been debated [144,145]. Beyond co-immunoprecipitation with the shown CME components, our data are inconclusive regarding an AP-2 role in specific β1-integrin subunit endocytosis, which is also unreported in the literature.

A role of PI3KC2β in integrin CME was eventually confirmed with an internalization assay in which PI3KC2β loss led to impaired active β1-integrin uptake (**Fig. 3-24 C**). In accordance with our previously discussed data, overexpression of wild type but not kinase inactive PI3KC2β constructs rescued the internalization defect of PI3KC2β KD cells, thus confirming an involvement of PI3KC2β catalytic activity in active β1-integrin endocytosis of HeLa cells. Loss of scaffolding protein ITSN1 and adaptor DAB2 phenocopied PI3KC2β depletion by causing a more pronounced defective uptake (data not shown), highlighting the importance and specificity of these adaptors in integrin internalization. The reduction of a 50-70% of internalization ratio upon loss of CME machinery components evidenced the presence of alternative pathways for integrin internalization, potentially clathrin-independent, even though CME is described to account for the majority [132,133].

The hypothesis of antagonistic functions of MTM1 and PI3KC2β in β1-integrin adhesion control, which we showed in double KO C2C12 myoblasts, was consolidated in a HeLa KD system. We showed that co-KD of PI3KC2β and MTM1 ameliorates surface active β1-integrin accumulation in PI3KC2β KD cells (**Fig. 3-24 D**), despite the normalization being incomplete. We hypothesized this to be associated to alternative PI 3-phosphatases, likely from the myotubularin family (see section 1.3.1), mediating β1-integrin recycling upon MTM1 loss in HeLa cells, a phenomenon that could as well explain the lack of a prominent adhesion phenotype in MTM1 KD cells (data not shown). Nevertheless, downregulation of key exocyst components EXOC7 and EXOC1, involved in exocytic machinery downstream of MTM1, led to a complete rescue of increased β1-integrin adhesions of PI3KC2β KD cells, in accordance with previous studies [83].

Altogether, our data indicate that MTM1 and PI3KC2β play antagonistic roles in β1-integrin trafficking, thereby offering a mechanistic explanation for the rescue of XLCNM-associated cell adhesion phenotypes upon PI3KC2β depletion. We propose a model (**Fig. 4-1**) in which loss of MTM1 leads to defective endosomal exocytosis due to its role in PI(3)P turnover in this pathway [83]. This results in impaired plasma membrane delivery of TfR and β1-integrin, likely among other receptors, causing an endosomal accumulation and/or redistribution of these proteins [26,83] and leading to the cell adhesion defects described in this study. Conversely, PI3KC2β depletion causes internalization defects of β1-integrin due to a role in CME of integrins via the specific adaptor DAB2. We hypothesize a subsequently decreased FA turnover associated with defective integrin internalization. In cells depleted of both enzymes, decreased endocytosis stabilizes active β1-integrins at the plasma membrane, which are less effectively internalized, thereby compensating for impaired recycling. This results in a normalization of the number of FAs that impacts cell migration and restores myogenic capacity, both key to the organismal rescue of XLCNM disease phenotype observed in mouse models [42].

Importantly, we reported a new role of PI3KC2β in CME of activated β1-integrin, which adds to its recently described function in mTORC1 signaling regulation [51], both dependent on its catalytic activity. We believe that PI3KC2β acts at two cellular sites modulating the distinct processes of promoting (i) catabolic metabolism by repression of mTORC1, and (ii) FA disassembly via endocytosis of β1-integrins. Related to the regulation of these processes, a recent study shed light on the control of PI3KC2β at the lysosome by upstream plasma membrane mitogen-dependent pathways involving mTORC2 and PKN2 [194]. It was shown that, in nutrient-fed cells, PI3KC2β is sequestered and inactivated at the cytoplasm by 14-3-3 proteins, a mechanism that likely impacts all PI3KC2β-regulated processes in the cell. Thus, it is plausible to hypothesize this upstream regulatory mechanism to be common to the roles of PI3KC2β in CME and mTORC1 signaling. In the context of integrin endocytosis, nutrient-fed cells would maintain an inactive PI3KC2β, resulting in decreased β1-integrin internalization and consequently favoring stable, long-lived FAs and decreased migratory capacity. Conversely, active PI3KC2β in nutrient-depleted cells would promote β1-integrin internalization, increased FA turnover and enhanced migration. This scenario is supported by a study showing that mTORC1 inhibition upon nutrient depletion promotes endocytosis of active β1-integrin [260], and the well-described link between growth factor signaling and cell migration, the main driver of metastatic invasion [261,262]. Overall, we believe that PI3KC2β plays a central role in nutrient-dependent pathways by controlling (i) mTORC1 signaling [51], and (ii) integrin adhesion turnover (this study), thereby emerging as a key regulator of the cellular effects of growth factor signaling. Moreover, an additional link between PI3KC2β-controlled mTORC1 signaling and integrin adhesion turnover may exist, as mTORC1 has been shown to activate by peripheral lysosome positioning in proximity to FAs [263], which occurs upon PI3KC2β depletion [51,92]. This could promote lysosomal exocytosis via an undescribed mechanism, leading to the extracellular degradation of integrin ligands [130] and a consequent induction of integrin endocytosis. Studies to decipher the precise mechanism by which PI3KC2β is regulated in the context of CME of active β1-integrin are required, as well as to investigate further functional links between its roles at lysosomal and plasma membranes. Furthermore, the PI3KC2β cargo specificity and distinct roles from PI3KC2α-mediated endocytosis need to be addressed in the future, together with the involvement of PI3KC2α in cell migration via mechanisms other than CME [221].

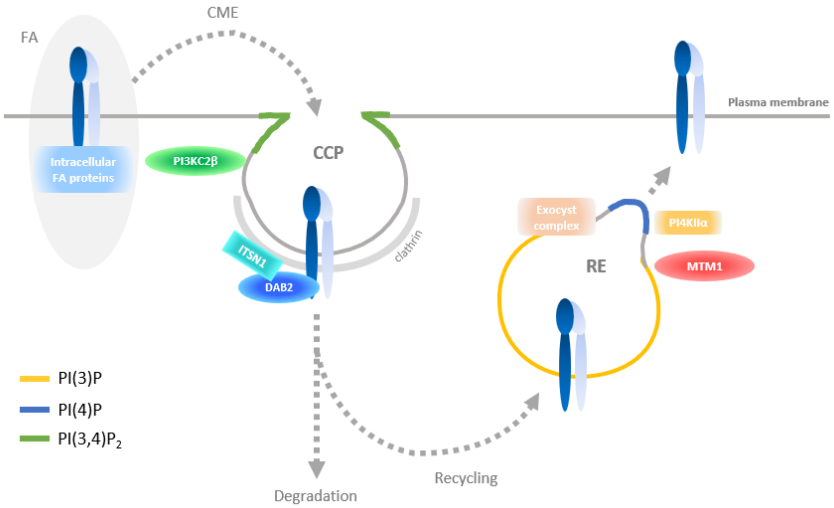

Figure 4-1. Proposed model illustrating the control of active β1-integrin trafficking by MTM1 and PI3KC2β. FA, focal adhesion; CME, clathrin-mediated endocytosis; CCP, clathrin-coated pit; RE, recycling endosome.

4.5. CNM-associated proteins functionally interact in a common pathway defining CNM pathogenesis

In the last two decades, the identification of multiple CNM-associated genes (**Table 1-1**) and their functions has progressively favored the hypothesis of a common molecular pathway leading to CNM [6]. The most extensively described CNM-related proteins, MTM1, DNM2 and BIN1, share membrane dynamics and remodeling roles by respectively participating in endosomal recycling, CCP fission and induction of membrane curvature [14, 19,83]. Direct and functional interactions between these proteins have been reported (see section 1.1.2), the latter mainly elucidated in genetic studies showing that increasing BIN1 expression rescued XLCNM [26] and DNM2-related CNM [264] and decreasing DNM2 expression rescued XLCNM [17] and BIN1-related CNM [20]. These findings, together with the reported direct interaction between BIN1 and MTM1 [22], and the direct interaction and negative regulation of DNM2 by BIN1 [20,21,27] set a background for a mechanistic hypothesis in which MTM1 would activate BIN1, and BIN1 would block DNM2 (**Fig. 4-2**). This hypothesis has been mainly studied in the context of T-tubule biogenesis and maintenance, where DNM2 and BIN1 are hypothesized to induce membrane tubulation without scission by BIN1-mediated inhibition of DNM2 GTPase activity [27,264]. Loss-of-function mutations in RYR1, also associated to CNM, lead to functional impairment of the T-tubule by disrupting ECC [30,31]. Conversely, the mechanism by which MTM1 controls T-tubule organization is unclear. Whereas some studies suggested an indirect role in membrane remodeling by promoting the recruitment of DNM2 and BIN1 via its PI products [114], others hypothesize a direct role in the recycling of T-tubule proteins [81]. The observation of severe T-tubule organization defects in D. *melanogaster* upon loss of the BIN1 homolog, in comparison to milder effects upon MTM1 or DNM2 depletion [169], supports the hypothesis of a central role of BIN1 in T-tubule formation and secondary functions of MTM1 and DNM2. Interestingly, the same study showed in MTM1-depleted *D. melanogaster* models that integrin adhesion formation is independent of T-tubule organization [169], suggesting that MTM1 either acts separately in the two processes or acts at a shared precursor compartment involved in integrin trafficking and also relevant to T-tubule formation.

In the context of β1-integrin adhesion regulation, we hypothesize a scenario in which DNM2 is involved in membrane scission during CME of β1-integrin [14], whereas MTM1 acts in the functionally opposed mechanism of

β1-integrin exocytosis [83]. BIN1 skeletal muscle-specific isoform 8, the isoform involved in CNM [20], would not be involved in CME of integrins as introduced before (see section 1.1.2.2). This process occurs at skeletal muscle adhesions where β1-integrin has been shown to be essential, like costameres and MTJs, participating in their formation and turnover in developing and adult muscle [121,157]. According to our model, PI3KC2β would contribute to β1-integrin endocytosis upstream of DNM2 by generating a pool of PI 3-phosphates involved in CME similarly as described for PI3KC2α [50,137]. Consequently, we hypothesize that gain-of-function mutations in PI3KC2β may lead to CNM phenotypes similarly to DNM2, although the limited expression of PI3KC2β in skeletal muscle would hinder prominent phenotypes.

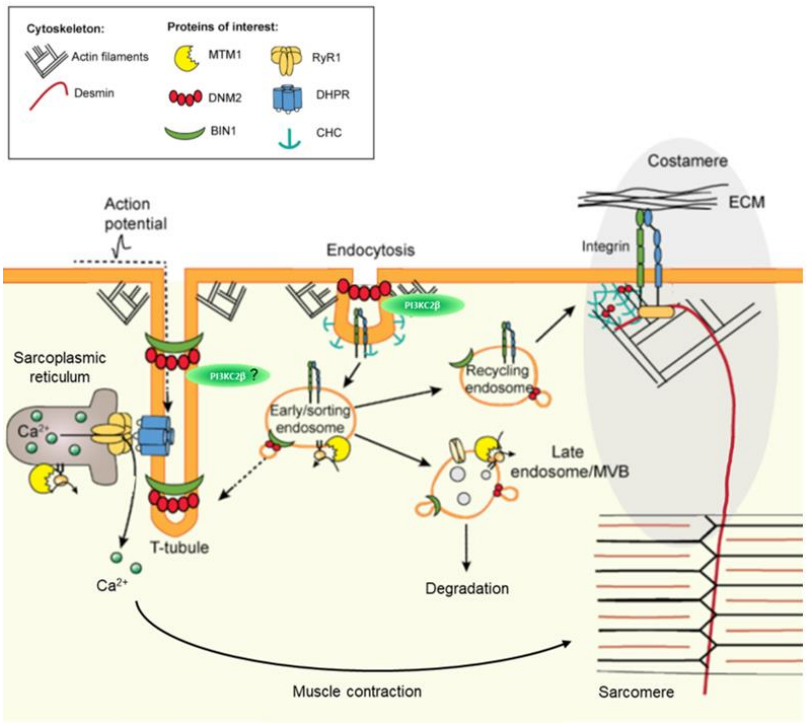

Figure 4-2. Schematic representation of localization and functions of CNM-related proteins MTM1, DNM2, BIN1, RYR1 and PI3KC2β in skeletal muscle. ECM, extracellular matrix; MVB, multivesicular bodies. Adapted figure [6].

4.6. Future perspectives: PI3KC2β as a novel target for XLCNM and other disorders

The results presented in this thesis provide insights into XLCNM cell adhesion-related pathology and its rescue by PI3KC2β depletion. The main future research perspective derived from this study is a therapeutic application for XLCNM treatment targeting PI3KC2β. Additionally, research to further understand the molecular mechanisms that we report, especially those related to the new role of PI3KC2β in CME of β1-integrin, should follow, as suggested in the previous sections.

Providing mechanistic evidence for the rescue of the XLCNM phenotype by PI3KC2β is a crucial advancement for the development of therapeutic strategies targeting PI3KC2β. Moreover, in this thesis we presented proof-of-concept evidence for the first XLCNM inhibitor-based therapy against PI3KC2β using PITCOIN3 (**Fig. 3-25**), a class II PI3KC2α/β-specific inhibitor developed in our institute [247]. PITCOIN3 treatment phenocopied PI3KC2β loss in HeLa cells and rescued active β1-integrin adhesions in *Mtm1*KO C2C12 myoblasts. Despite the need for a PI3KC2β isoform-specific inhibitor, these results suggest that pharmacological inhibition of PI3KC2β could restore adhesion defects in skeletal muscle that are key to XLCNM pathogenesis (see section 1.4.3.1). Although the

differential involvement of class II PI3K isoforms α and β in the context of integrin endocytosis has only partially been addressed in this thesis, the importance of an isoform-specific molecule is illustrated by the potentially prominent effects of PI3KC2α inhibition at organismal level, described to be embryonically lethal in mice [199]. Conversely, we hypothesize that PI3KC2β inhibition would not lead to major undesired on-target effects, as demonstrated by the lack of prominent phenotypes of complete and skeletal muscle-specific *Pik3c2b*KO mouse models [42,171]. This observation further supports differential roles of PI3KC2α and β in endocytosis, suggesting PI3KC2β might be exclusively involved in internalization of integrins and not other cargoes. Speculatively, on-target side effects would derive from PI3KC2β roles in mTORC1 signaling and migration in muscle or at systemic level, depending on the therapeutic approach. In the context of mTORC1 signaling, loss of PI3KC2β would lead to mTORC1 hyperactivation, a potentially beneficial effect in skeletal muscle as it leads to hypertrophy [95], whereas it could be associated to overgrowth phenotypes in other tissues. Highly migratory cells such as immune cells would potentially suffer from decreased migration capacity, which might trigger decreased immune cellular response, acting synergistically with impaired T-cell activation and mast cell degranulation reported to occur upon PI3KC2β loss [209,210]. Besides these, the involvement of PI3KC2β in other mechanisms or pathways such as insulin signaling should be monitored, yet we hypothesize major on-target secondary effects to be unlikely. Overall, evidence suggests that PI3KC2β inhibitors are potentially suitable candidates for drug development with applications in XLCNM therapy, and potentially other diseases such as immune disorders via inhibition of anaphylaxis [211], diabetes via promotion of insulin sensitivity and glucose tolerance [212], or cancer via inhibition of cell migration [171].

As previously discussed, recent studies have taken advantage of the functional interaction between XLCNM-causing genes for the development of CNM therapeutic strategies. Many recent studies have set proof-of-concept evidence for these approaches, some of which are currently undergoing clinical trials (see section 1.1.3). According to our reported role of PI3KC2β in CME, we hypothesize PI3KC2β inhibition to rescue or ameliorate adhesion defects in DNM2-related CNM patients, indicating a potential application for this disorder. Conversely, due to the unknown involvement of PI3KC2β in membrane tubulation and T-tubule biogenesis, we cannot hypothesize which effects PI3KC2β depletion would have in the context of DNM2- or BIN1-CNM. The lack of histological findings such as T-tubule disorganization in PI3KC2β-depleted skeletal muscle [42,171] suggest that PI3KC2β might not play a role in the formation of this structure, in which case we could speculate its loss to not rescue the BIN1-CNM phenotype. Further studies are required to assess the involvement of PI3KC2β in T-tubule formation in order to define the therapeutic adequacy of PI3KC2β inhibition in XLCNM and BIN1-related CNM. Additionally, other forms of CNM directly or indirectly leading to adhesion defects, not discussed in this thesis (**Table 1-1**), might benefit from a PI3KC2β inhibitor treatment as well. Moreover, potential applications of PI3KC2β-specific inhibitors in the treatment of certain myotubularin-related CMT neuropathy subtypes might be identified in the future. This is supported by the fact that β1-integrin plays a role in axon myelination [265], a process that involves extensive membrane remodeling, and the catalytic redundancy among myotubularin family members [60], which could imply similar roles of MTM1 and MTMR2 in skeletal muscle and the peripheral nervous system, respectively, and a corresponding rescue by PI3KC2β loss.

5. Bibliography

1. Spiro, A. J., Shy, G. M., Gonatas, N. K. (1966). Myotubular Myopathy: Persistence of Fetal Muscle in an Adolescent Boy. *Arch. Neurol.* **14**, 1–14.

2. Lawlor, M. W., Dowling, J. J. (2021). X-linked myotubular myopathy. *Neuromuscul. Disord.* **31**, 1004–1012.

3. Jungbluth, H., Wallgren-Pettersson, C., Laporte, J. (2008). Centronuclear (myotubular) myopathy. *Orphanet J. Rare Dis.* **3**, 26.

4. Romero, N. B. (2010). Centronuclear myopathies: a widening concept. *Neuromuscul. Disord.* **20**, 223–228.

5. Vandersmissen, I., Biancalana, V., Servais, L., Dowling, J. J., Vander Stichele, G., Van Rooijen, S., Thielemans, L. (2018). An integrated modelling methodology for estimating the prevalence of centronuclear myopathy. *Neuromuscul. Disord.* **28**, 766–777.

6. Gómez-Oca, R., Cowling, B. S., Laporte, J. (2021). Common pathogenic mechanisms in centronuclear and myotubular myopathies and latest treatment advances. *Int. J. Mol. Sci.* **22**, 11377.

7. Jungbluth, H., Gautel, M., Laporte, J., Denise, F., Cassandrini, A. (2014). AGING NEUROSCIENCE Pathogenic mechanisms in centronuclear myopathies. *Front. Aging Neurosci.* **6**, 339.

8. Agrawal, P. B., Pierson, C. R., Joshi, M., Liu, X., Ravenscroft, G., Moghadaszadeh, B., Talabere, T., Viola, M., Swanson, L. C., Haliloğlu, G., Talim, B., Yau, K. S., Allcock, R. J. N., Laing, N. G., Perrella, M. A., Beggs, A. H. (2014). SPEG Interacts with Myotubularin, and Its Deficiency Causes Centronuclear Myopathy with Dilated Cardiomyopathy. *Am. J. Hum. Genet.* **95**, 218–226.

9. Laporte, J., Guiraud-Chaumeil, C., Vincent, M.-C., Mandel, J.-L., Tanner, S. M., Liechti-Gallati, S., Wallgren-Pettersson, C., Dahl, N., Kress, W., Bolhuis, P. A., Fardeau, M., Samson, F., Bertini, E. (1997) Mutations in the MTM1 gene implicated in X-linked myotubular myopathy and members of the ENMC International Consortium on Myotubular Myopathy. **6**, 1505–1511.

10. Dowling J. J., Lawlor M. W., Das S. (2002; updated 2018). X-Linked Myotubular Myopathy. In: Adam M. P., Everman D. B., Mirzaa G. M., et al., editors. GeneReviews. (University of Washington, Seattle). at <https://www.ncbi.nlm.nih.gov/books/NBK1432/>

11. Savarese, M., Musumeci, O., Giugliano, T., Rubegni, A., Fiorillo, C., Fattori, F., Torella, A., Battini, R., Rodolico, C., Pugliese, A., Piluso, G., Maggi, L., D'Amico, A., Bruno, C., Bertini, E., Santorelli, F. M., Mora, M., Toscano, A., Minetti, C., Nigro, V. (2016). Novel findings associated with MTM1 suggest a higher number of female symptomatic carriers. *Neuromuscul. Disord.* **26**, 292–299.

12. Biancalana, V., Scheidecker, S., Miguet, M., Laquerrière, A., Romero, N. B., Stojkovic, T., Abath Neto, O., Mercier, S., Voermans, N., Tanner, L., Rogers, C., Ollagnon-Roman, E., Roper, H., Boutte, C., Ben-Shachar, S., Lornage, X., Vasli, N., Schaefer, E., Laforet, P., Pouget, J., Moerman, A., Pasquier, L., Marcorelle, P., Magot, A., Küsters, B., Streichenberger, N., Tranchant, C., Dondaine, N., Schneider, R., Gasnier, C., Calmels, N., Kremer, V., Nguyen, K., Perrier, J., Jan Kamsteeg, E., Carlier, P., Carlier, R.-Y., Thompson, J., Boland, A., Deleuze, J.-F., Fardeau, M., Zanoteli, E., Eymard, B., Laporte, J. (2017). Affected female carriers of MTM1 mutations display a wide spectrum of clinical and pathological involvement: delineating diagnostic clues. *Acta Neuropathol.* **134**, 889–904.

13. Cocanougher, B. T., Flynn, L., Yun, P., Jain, M., Waite, M., Vasavada, R., Wittenbach, J. D., de Chastonay, S., Chhibber, S., Micheil Innes, A., MacLaren, L., Mozaffar, T., Arai, A. E., Donkervoort, S., Bönnemann, C. G., Reghan Foley, A. (2019). Neuromuscular and Neurogenetic Disorders of Childhood Section. *Clin. Res. Cent.* **93**, e1535–e1542.

14. Ferguson, S. M., De Camilli, P. (2012). Dynamin, a membrane-remodelling GTPase. *Nat. Rev. Mol.* **13**, 75–88.

15. Bitoun, M., Maugenre, S., Jeannet, P. Y., Lacène, E., Ferrer, X., Laforêt, P., Martin, J. J., Laporte, J., Lochmüller, H., Beggs, A. H., Fardeau, M., Eymard, B., Romero, N. B., Guicheney, P. (2005). Mutations in dynamin 2 cause dominant centronuclear myopathy. *Nat. Genet.* **37**, 1207–1209.

16. Böhm, J., Biancalana, V., DeChene, E. T., Bitoun, M., Pierson, C. R., Schaefer, E., Karasoy, H., Laporte, J., *et al.* (2012). Mutation spectrum in the large gtpase dynamin 2, and genotype-phenotype correlation in autosomal dominant centronuclear myopathy. *Hum. Mutat.* **33**, 949–959.

17. Cowling, B. S., Chevremont, T., Prokic, I., Kretz, C., Ferry, A., Coirault, C., Koutsopoulos, O., Laugel, V., Romero, N. B., Laporte, J. (2014). Reducing dynamin 2 expression rescues X-linked centronuclear myopathy. *J. Clin. Invest.* **124**, 1350–1363.

18. Tasfaout, H., Buono, S., Guo, S., Kretz, C., Messaddeq, N., Booten, S., Greenlee, S., Monia, B. P., Cowling, B. S., Laporte, J. (2017). Antisense oligonucleotide-mediated Dnm2 knockdown prevents and reverts myotubular myopathy in mice. *Nat. Commun.* **8**, 15661.

19. Lee, E., Marcucci, M., Daniell, L., Pypaert, M., Weisz, O. A., Ochoa, G. C., Farsad, K., Wenk, M. R., De Camilli, P. (2002). Amphiphysin 2 (Bin1) and T-tubule biogenesis in muscle. *Science.* **297**, 1193–1196.

20. Cowling, B. S., Prokic, I., Tasfaout, H., Rabai, A., Humbert, F., Rinaldi, B., Nicot, A. S., Kretz, C., Friant, S., Roux, A., Laporte, J. (2017). Amphiphysin (BIN1) negatively regulates dynamin 2 for normal muscle maturation. *J. Clin. Invest.* **127**, 4477–4487.

21. Nicot, A. S., Toussaint, A., Tosch, V., Kretz, C., Wallgren-Pettersson, C., Iwarsson, E., Kingston, H., Garnier, J. M., Biancalana, V., Oldfors, A., Mandel, J. L., Laporte, J. (2007). Mutations in amphiphysin 2 (BIN1) disrupt interaction with dynamin 2 and cause autosomal recessive centronuclear myopathy. *Nat. Genet.* **39**, 1134–1139.

22. Royer, B., Hnia, K., Gavriilidis, C., Tronchère, H., Tosch, V., Laporte, J. (2013). The myotubularin-amphiphysin 2 complex in membrane tubulation and centronuclear myopathies. *EMBO Rep.* **14**, 907–915.

23. Rao, Y., Haucke, V. (2011). Membrane shaping by the Bin/amphiphysin/Rvs (BAR) domain protein superfamily. *Cell. Mol. Life Sci.* **68**, 3983–3993.

24. D'Alessandro, M., Hnia, K., Gache, V., Koch, C., Gavriilidis, C., Rodriguez, D., Nicot, A. S., Romero, N. B., Schwab, Y., Gomes, E., Labouesse, M., Laporte, J. (2015). Amphiphysin 2 Orchestrates Nucleus Positioning and Shape by Linking the Nuclear Envelope to the Actin and Microtubule Cytoskeleton. *Dev. Cell.* **35**, 186–198.

25. Wu, T., Shi, Z., Baumgart, T. (2014). Mutations in BIN1 Associated with Centronuclear Myopathy Disrupt Membrane Remodeling by Affecting Protein Density and Oligomerization. *PLoS One.* **9**, e93060.

26. Lionello, V. M., Nicot, A. S., Sartori, M., Kretz, C., Kessler, P., Buono, S., Djerroud, S., Messaddeq, N., Koebel, P., Prokic, I., Hérault, Y., Romero, N. B., Laporte, J., Cowling, B. S. (2019). Amphiphysin 2 modulation rescues myotubular myopathy and prevents focal adhesion defects in mice. *Sci. Transl. Med.* **11**, eaav1866.

27. Fujise, K., Okubo, M., Abe, T., Yamada, H., Nishino, I., Noguchi, S., Takei, K., Takeda, T. (2020). Mutant BIN1-Dynamin 2 complexes dysregulate membrane remodeling in the pathogenesis of centronuclear myopathy. *J. Biol. Chem.* **296**, 100077.

28. Calderón, J. C., Bolaños, P., Caputo, C. (2014). The excitation-contraction coupling mechanism in skeletal muscle. *Biophys. Rev.* **6**, 133–160.

29. Hernández-Ochoa, E. O., Pratt, S. J. P., Lovering, R. M., Schneider, M. F. (2015). Critical Role of Intracellular RyR1 Calcium Release Channels in Skeletal Muscle Function and Disease. *Front. Physiol.* **6**, 420.

30. Wilmshurst, J. M., Lillis, S., Zhou, H., Pillay, K., Henderson, H., Kress, W., Müller, C. R., Ndondo, A., Cloke, V., Cullup, T., Bertini, E., Boennemann, C., Straub, V., Quinlivan, R., Dowling, J. J., Al-Sarraj, S., Treves, S., Abbs, S., Manzur, A. Y., Sewry, C. A., Muntoni, F., Jungbluth, H. (2010). RYR1 mutations are a common cause of congenital myopathies with central nuclei. *Ann. Neurol.* **68**, 717–726.

31. Jungbluth, H., Zhou, H., Sewry, C. A., Robb, S., Treves, S., Bitoun, M., Guicheney, P., Buj-Bello, A., Bönnemann, C., Muntoni, F. (2007). Centronuclear myopathy due to a de novo dominant mutation in the skeletal muscle ryanodine receptor (RYR1) gene. *Neuromuscul. Disord.* **17**, 338–345.

32. Tasfaout, H., Cowling, B. S., Laporte, J. (2018). Centronuclear myopathies under attack: A plethora of therapeutic targets. *J. Neuromuscul. Dis.* **5**, 387–406.

33. Audentes Therapeutics. (2017) ASPIRO: A Phase 1/2/3, Randomized, Open-Label, Ascending-Dose, Delayed-Treatment Concurrent Control Clinical Study to Evaluate the Safety and Efficacy of AT132, an AAV8-Delivered Gene Therapy in X-Linked Myotubular Myopathy (XLMTM) Patients. at <https://clinicaltrials.gov/ct2/show/NCT03199469>

34. Buj-Bello, A., Fougerousse, F., Schwab, Y., Messaddeq, N., Spehner, D., Pierson, C. R., Durand, M., Kretz, C., Danos, O., Douar, A. M., Beggs, A. H., Schultz, P., Montus, M., Denèfle, P., Mandel, J. L. (2008). AAV-mediated intramuscular delivery of myotubularin corrects the myotubular myopathy phenotype in targeted murine muscle and suggests a function in plasma membrane homeostasis. *Hum. Mol. Genet.* **17**, 2132–2143.

35. Amoasii, L., Bertazzi, D. L., Tronchère, H., Hnia, K., Chicanne, G., Rinaldi, B., Cowling, B. S., Ferry, A., Klaholz, B., Payrastre, B., Laporte, J., Friant, S. (2012). Phosphatase-Dead Myotubularin Ameliorates X-Linked Centronuclear Myopathy Phenotypes in Mice. *PLoS Genet.* **8**, e1002965.

36. Childers, M. K., Joubert, R., Poulard, K., Moal, C., Grange, R. W., Doering, J. A., Lawlor, M. W., Rider, B. E., Jamet, T., Danièle, N., Martin, S., Rivière, C., Soker, T., Hammer, C., Van Wittenberghe, L., Lockard, M., Guan, X., Goddard, M., Mitchell, E., Barber, J., Williams, J. K., Mack, D. L., Furth, M. E., Vignaud, A., Masurier, C., Mavilio, F., Moullier, P., Beggs, A. H., Buj-Bello, A. (2014). Gene therapy prolongs survival and restores function in murine and canine models of myotubular myopathy. *Sci. Transl. Med.* **6**, 220ra10.

37. Dynacure. (2021) A Phase 1/2, Multicenter, Open-label, Dose-confirmation Trial to Evaluate the Safety and

Preliminary Efficacy of DYN101 in Participants 2 to 17 Years of Age With Centronuclear Myopathy Caused by Mutations in MTM1 or DNM2. at <https://clinicaltrials.gov/ct2/show/NCT04743557>

38. Trochet, D., Prudhon, B., Beuvin, M., Peccate, C., Lorain, S., Julien, L., Benkhelifa-Ziyyat, S., Rabai, A., Mamchaoui, K., Ferry, A., Laporte, J., Guicheney, P., Vassilopoulos, S., Bitoun, M. (2018). Allele-specific silencing therapy for Dynamin 2-related dominant centronuclear myopathy. *EMBO Mol. Med.* **10**, 239–253.

39. Raess, M. A., Cowling, B. S., Bertazzi, D. L., Kretz, C., Rinaldi, B., Xuereb, J. M., Kessler, P., Romero, N. B., Payrastre, B., Friant, S., Laporte, J. (2017). Expression of the neuropathy-associated MTMR2 gene rescues MTM1-associated myopathy. *Hum. Mol. Genet.* **26**, 3736–3748.

40. Maani, N., Sabha, N., Rezai, K., Ramani, A., Groom, L., Eltayeb, N., Mavandadnejad, F., Pang, A., Russo, G., Brudno, M., Haucke, V., Dirksen, R. T., Dowling, J. J. (2018). Tamoxifen therapy in a murine model of myotubular myopathy. *Nat. Commun.* **9**, 4849.

41. Gayi, E., Neff, L. A., Massana Muñoz, X., Ismail, H. M., Sierra, M., Mercier, T., Décosterd, L. A., Laporte, J., Cowling, B. S., Dorchies, O. M., Scapozza, L. (2018). Tamoxifen prolongs survival and alleviates symptoms in mice with fatal X-linked myotubular myopathy. *Nat. Commun.* **9**, 4848.

42. Sabha, N., Volpatti, J. R., Gonorazky, H., Reifler, A., Davidson, A. E., Li, X., Eltayeb, N. M., Dall'Armi, C., Di Paolo, G., Brooks, S. V., Buj-Bello, A., Feldman, E. L., Dowling, J. J. (2016). PIK3C2B inhibition improves function and prolongs survival in myotubular myopathy animal models. *J. Clin. Invest.* **126**, 3613–3625.

43. Schink, K. O., Tan, K.-W., Stenmark, H. (2016). Phosphoinositides in Control of Membrane Dynamics. *Annu. Rev. Cell Dev. Biol.* **32**, 143–171.

44. Di Paolo, G., De Camilli, P. (2006). Phosphoinositides in cell regulation and membrane dynamics. *Nature*. **443**, 651–657.

45. De Matteis, M. A., Godi, A. (2004). PI-loting membrane traffic. *Nat. Cell Biol.* **6**, 487–492.

46. Balla, T. (2013). Phosphoinositides: Tiny lipids with giant impact on cell regulation. *Physiol. Rev*. **93**, 1019–1137.

47. Wallroth, A., Haucke, V. (2018). Phosphoinositide conversion in endocytosis and the endolysosomal system. *J. Biol. Chem.* **293**, 1526–1535.

48. Krauß, M., Haucke, V. (2007). Phosphoinositide-metabolizing enzymes at the interface between membrane traffic and cell signalling. *EMBO Rep.* **8**, 241–246.

49. Marat, A. L., Haucke, V. (2016). Phosphatidylinositol 3-phosphates-at the interface between cell signalling and membrane traffic. *EMBO J.* **35**, 561–79.

50. Posor, Y., Eichhorn-Gruenig, M., Puchkov, D., Schöneberg, J., Ullrich, A., Lampe, A., Müller, R., Zarbakhsh, S., Gulluni, F., Hirsch, E., Krauss, M., Schultz, C., Schmoranzer, J., Noé, F., Haucke, V. (2013). Spatiotemporal control of endocytosis by phosphatidylinositol-3,4- bisphosphate. *Nature.* **499**, 233–237.

51. Marat, A. L., Wallroth, A., Lo, W. T., Müller, R., Norata, G. D., Falasca, M., Schultz, C., Haucke, V. (2017). mTORC1 activity repression by late endosomal phosphatidylinositol 3,4-bisphosphate. *Science.* **356**, 968–972.

52. Behnia, R., Munro, S. (2005). Organelle identity and the signposts for membrane traffic. *Nature.* **438**, 597–604.

53. Carlton, J. G., Cullen, P. J. (2005). Coincidence detection in phosphoinositide signaling. *Trends Cell Biol.* **15**, 540–547.

54. Takai, Y., Sasaki, T., Matozaki, T. (2001). Small GTP-binding proteins. *Physiol. Rev.* **81**, 153–208.

55. Laporte, J., Bedez, F., Bolino, A., Mandel, J.-L. (2003). Myotubularins, a large disease-associated family of cooperating catalytically active and inactive phosphoinositides phosphatases. *Hum. Mol. Genet.* **12**, R285–R292.

56. Laporte, J., Blondeau, F., Buj-Bello, A., Mandel, J. L. (2001). The myotubularin family: from genetic disease to phosphoinositide metabolism. *Trends Genet.* **17**, 221–228.

57. Nandurkar, H. H., Huysmans, R. (2002). The myotubularin family: Novel phosphoinositide regulators. *IUBMB Life*. **53**, 37–43.

58. Laporte, J., Bedez, F., Bolino, A., Mandel, J. L. (2003). Myotubularins, a large disease-associated family of cooperating catalytically active and inactive phosphoinositides phosphatases. *Hum. Mol. Genet*. **12**, R285–R292.

59. Tosch, V., Rohde, H. M., Tronchère, H., Zanoteli, E., Monroy, N., Kretz, C., Dondaine, N., Payrastre, B., Mandel, J. L., Laporte, J. (2006). A novel PtdIns3P and PtdIns(3,5)P2 phosphatase with an inactivating variant in centronuclear myopathy. *Hum. Mol. Genet.* **15**, 3098–3106.

60. Raess, M. A., Friant, S., Cowling, B. S., Laporte, J. (2017). WANTED – Dead or alive: Myotubularins, a large disease-

associated protein family. *Adv. Biol. Regul.* **63**, 49–58.

61. Blondeau, F., Laporte, J., Bodin, S., Superti-Furga, G., Payrastre, B., Mandel, J.-L. (2000). Myotubularin, a phosphatase deficient in myotubular myopathy, acts on phosphatidylinositol 3-kinase and phosphatidylinositol 3-phosphate pathway. *Hum. Mol. Genet*. **9**, 2223–2229.

62. Taylor, G. S., Maehama, T., Dixon, J. E. (2000). Myotubularin, a protein tyrosine phosphatase mutated in myotubular myopathy, dephosphorylates the lipid second messenger, phosphatidylinositol 3-phosphate. *Proc. Natl. Acad. Sci.* **97**, 8910–8915.

63. Tronchère, H., Laporte, J., Pendaries, C., Chaussade, C., Liaubet, L., Pirola, L., Mandel, J. L., Payrastre, B. (2004). Production of Phosphatidylinositol 5-Phosphate by the Phosphoinositide 3-Phosphatase Myotubularin in Mammalian Cells. *J. Biol. Chem.* **279**, 7304–7312.

64. Walker, D. M., Urbé, S., Dove, S. K., Tenza, D., Raposo, G., Clague, M. J. (2001). Characterization of MTMR3: An inositol lipid 3-phosphatase with novel substrate specificity. *Curr. Biol.* **11**, 1600–1605.

65. Nandurkar, H. H., Layton, M., Laporte, J., Selan, C., Corcoran, L., Caldwell, K. K., Mochizuki, Y., Majerus, P. W., Mitchell, C. A. (2003). Identification of myotubularin as the lipid phosphatase catalytic subunit associated with the 3-phosphatase adapter protein, 3-PAP. *Proc. Natl. Acad. Sci.* **100**, 8660–8665.

66. Bertazzi, D. L., de Craene, J. O., Friant, S. (2018). Myotubularin MTM1 involved in centronuclear myopathy and its roles in human and yeast cells. *J. Mol. Genet. Med.* **8**.

67. Tsujita, K., Itoh, T., Ijuin, T., Yamamoto, A., Shisheva, A., Laporte, J., Takenawa, T. (2004). Myotubularin regulates the function of the late endosome through the gram domain-phosphatidylinositol 3,5-bisphosphate interaction. *J. Biol. Chem.* **279**, 13817–13824.

68. Marat, A. L., Dokainish, H., McPherson, P. S. (2011). DENN Domain Proteins: Regulators of Rab GTPases. *J. Biol. Chem.* **286**, 13791–13800.

69. Lorenzo, O., Urbe, S., Clague, M. J. (2006). Systematic analysis of myotubularins: heteromeric interactions, subcellular localisation and endosomerelated functions. *J. Cell Sci.* **119**, 2953–2959.

70. Schaletzky, J., Dove, S. K., Short, B., Lorenzo, O., Clague, M. J., Barr, F. A. (2003). Phosphatidylinositol-5-phosphate activation and conserved substrate specificity of the myotubularin Phosphatidylinositol 3-phosphatases. *Curr. Biol.* **13**, 504–509.

71. Gupta, V. A., Hnia, K., Smith, L. L., Gundry, S. R., McIntire, J. E., Shimazu, J., Bass, J. R., Talbot, E. A., Amoasii, L., Goldman, N. E., Laporte, J., Beggs, A. H. (2013). Loss of Catalytically Inactive Lipid Phosphatase Myotubularin-related Protein 12 Impairs Myotubularin Stability and Promotes Centronuclear Myopathy in Zebrafish. *PLoS Genet.* **9**, e1003583.

72. Hnia, K., Tronchère, H., Tomczak, K. K., Amoasii, L., Schultz, P., Beggs, A. H., Payrastre, B., Mandel, J. L., Laporte, J. (2011). Myotubularin controls desmin intermediate filament architecture and mitochondrial dynamics in human and mouse skeletal muscle. *J. Clin. Invest.* **100**, 8660–8665.

73. Bolino, A., Muglia, M., Conforti, F. L., LeGuern, E., Salih, M. A. M., Georgiou, D. M., Christodoulou, K., Hausmanowa-Petrusewicz, I., Mandich, P., Schenone, A., Gambardella, A., Bono, F., Quattrone, A., Devoto, M., Monaco, A. P. (2000). Charcot-Marie-Tooth type 4B is caused by mutations in the gene encoding myotubularin-related protein-2. *Nat. Genet.* **25**, 17–19.

74. Nakhro, K., Park, J. M., Hong, Y. Bin, Park, J. H., Nam, S. H., Yoon, B. R., Yoo, J. H., Koo, H., Jung, S. C., Kim, H. L., Kim, J. Y., Choi, K. G., Choi, B. O., Chung, K. W. (2013). SET binding factor 1 (SBF1) mutation causes Charcot-Marie-Tooth disease type 4B3. *Neurology.* **81**, 165–173.

75. Azzedine, H., Bolino, A., Taïeb, T., Birouk, N., Di Duca, M., Bouhouche, A., Benamou, S., Mrabet, A., Hammadouche, T., Chkili, T., Gouider, R., Ravazzolo, R., Brice, A., Laporte, J., LeGuern, E. (2003). Mutations in MTMR13, a New Pseudophosphatase Homologue of MTMR2 and Sbf1, in Two Families with an Autosomal Recessive Demyelinating Form of Charcot-Marie-Tooth Disease Associated with Early-Onset Glaucoma. *Am. J. Hum. Genet.* **72**, 1141–1153.

76. Berger, P., Tersar, K., Ballmer-Hofer, K., Suter, U. (2011). The CMT4B disease-causing proteins MTMR2 and MTMR13/SBF2 regulate AKT signalling. *J. Cell. Mol. Med.* **15**, 307–315.

77. Sawade, L., Grandi, F., Mignanelli, M., Patiño-López, G., Klinkert, K., Langa-Vives, F., Di Guardo, R., Echard, A., Bolino, A., Haucke, V. (2020). Rab35-regulated lipid turnover by myotubularins represses mTORC1 activity and controls myelin growth. *Nat. Commun.* **11**, 1–18.

78. Mammel, A. E., Delgado, K. C., Chin, A. L., Condon, A. F., Hill, J. Q., Aicher, S. A., Wang, Y., Fedorov, L. M., Robinson, F. L. (2021). Distinct roles for the Charcot-Marie-tooth disease-causing endosomal regulators Mtmr5 and Mtmr13 in axon radial sorting and Schwann cell myelination. *Hum. Mol. Genet.* **31**, 1216–1229.

79. Feltri, M. L., Poitelon, Y., Previtali, S. C. (2016). How Schwann Cells Sort Axons: New Concepts. *Neuroscientist.* **22**, 252–265.

80. Mruk, D. D., Cheng, C. Y. (2011). The myotubularin family of lipid phosphatases in disease and in spermatogenesis. *Biochem. J.* **433**, 253–262.

81. Dowling, J. J., Vreede, A. P., Low, S. E., Gibbs, E. M., Kuwada, J. Y., Bonnemann, C. G., Feldman, E. L. (2009). Loss of myotubularin function results in T-tubule disorganization in zebrafish and human myotubular myopathy. *PLoS Genet.* **5**, e1000372.

82. Cao, C., Backer, J. M., Laporte, J., Bedrick, E. J., Wandinger-Ness, A. (2008). Sequential actions of myotubularin lipid phosphatases regulate endosomal PI(3)P and growth factor receptor trafficking. *Mol. Biol. Cell* **19**, 3334–3346.

83. Ketel, K., Krauss, M., Nicot, A. S., Puchkov, D., Wieffer, M., Müller, R., Subramanian, D., Schultz, C., Laporte, J., Haucke, V. (2016). A phosphoinositide conversion mechanism for exit from endosomes. *Nature*. **529**, 408–412.

84. Razidlo, G. L., Katafiasz, D., Taylor, G. S. (2011). Myotubularin regulates Akt-dependent survival signaling via phosphatidylinositol 3-phosphate. *J. Biol. Chem.* **286**, 20005–20019.

85. Velichkova, M., Juan, J., Kadandale, P., Jean, S., Ribeiro, I., Raman, V., Stefan, C., Kiger, A. A. (2010). Drosophila Mtm and class II PI3K coregulate a PI(3)P pool with cortical and endolysosomal functions. *J. Cell Biol.* **190**, 407-425.

86. Cao, C., Laporte, J., Backer, J. M., Wandinger-Ness, A., Stein, M. P. (2007). Myotubularin lipid phosphatase binds the hVPS15/hVPS34 lipid kinase complex on endosomes. *Traffic*. **8**, 1052–1067.

87. Bachmann, C., Jungbluth, H., Muntoni, F., Manzur, A. Y., Zorzato, F., Treves, S. (2017). Cellular, biochemical and molecular changes in muscles from patients with X-linked myotubular myopathy due to MTM1 mutations. *Hum. Mol. Genet.* **26**, 320–332.

88. Jean, S., Cox, S., Schmidt, E. J., Robinson, F. L., Kiger, A. (2012). Sbf/MTMR13 coordinates PI(3)P and Rab21 regulation in endocytic control of cellular remodeling. *Mol. Biol. Cell.* **23**, 2621–2819.

89. Oda, K., Matsuoka, Y., Funahashi, A., Kitano, H. (2005). A comprehensive pathway map of epidermal growth factor receptor signaling. *Mol. Syst. Biol.* **1**, 2005.0010.

90. Mei, K., Guo, W. (2018). The exocyst complex. *Curr. Biol.* **28**, 922–925.

91. Mayle, K. M., Le, A. M., Kamei, D. T. (2012). The intracellular trafficking pathway of transferrin. *Biochim. Biophys. Acta.* **1820**, 264–281.

92. Korolchuk, V. I., Saiki, S., Lichtenberg, M., Siddiqi, F. H., Roberts, E. A., Imarisio, S., Jahreiss, L., Sarkar, S., Futter, M., Menzies, F. M., O'Kane, C. J., Deretic, V., Rubinsztein, D. C. (2011). Lysosomal positioning coordinates cellular nutrient responses. *Nat. Cell Biol.* **13**, 453–462.

93. Bar-Peled, L., Sabatini, D. M. (2012). SnapShot: mTORC1 Signaling at the Lysosomal Surface. *Cell.* **151**, 1390-1390.e1.

94. Shimobayashi, M., Hall, M. N. (2014). Making new contacts: the mTOR network in metabolism and signalling crosstalk. *Nat. Rev. Mol.* **15**, 155–162.

95. Bodine, S. C., Stitt, T. N., Gonzalez, M., Kline, W. O., Stover, G. L., Bauerlein, R., Zlotchenko, E., Scrimgeour, A., Lawrence, J. C., Glass, D. J., Yancopoulos, G. D. (2001). Akt/mTOR pathway is a crucial regulator of skeletal muscle hypertrophy and can prevent muscle atrophy in vivo. *Nat. Cell Biol.* **3**, 1014–1019.

96. Yoon, M. S. (2017). mTOR as a key regulator in maintaining skeletal muscle mass. *Front. Physiol.* **8**, 788.

97. Al-Qusairi, L., Prokic, I., Amoasii, L., Kretz, C., Messaddeq, N., Mandel, J. L., Laporte, J. (2013). Lack of myotubularin (MTM1) leads to muscle hypotrophy through unbalanced regulation of the autophagy and ubiquitin-proteasome pathways. *FASEB J.* **27**, 3384–3394.

98. Fetalvero, K. M., Yu, Y., Goetschkes, M., Liang, G., Valdez, R. A., Gould, T., Triantafellow, E., Bergling, S., Loureiro, J., Eash, J., Lin, V., Porter, J. A., Finan, P. M., Walsh, K., Yang, Y., Mao, X., Murphy, L. O. (2013). Defective Autophagy and mTORC1 Signaling in Myotubularin Null Mice. *Mol. Cell. Biol.* **33**, 98–110.

99. Hnia, K., Tronchère, H., Tomczak, K. K., Amoasii, L., Schultz, P., Beggs, A. H., Payrastre, B., Mandel, J. L., Laporte, J. (2011). Myotubularin controls desmin intermediate filament architecture and mitochondrial dynamics in human and mouse skeletal muscle. *J. Clin. Invest.* **121**, 70–85.

100. Sandri, M. (2010). Autophagy in skeletal muscle. *FEBS Lett.* **584**, 1411–1416.

101. Xia, Q., Huang, X., Huang, J., Zheng, Y., March, M. E., Li, J., Wei, Y. (2021). The Role of Autophagy in Skeletal Muscle Diseases. *Front. Physiol.* **12**, 638983.

102. Cebollero, E., Van Der Vaart, A., Reggiori, F. (2012). Understanding phosphatidylinositol-3-phosphate dynamics during autophagosome biogenesis. *Autophagy*. **8**, 1868–1870.

103. Kitajima, Y., Yoshioka, K., Suzuki, N. (2020). The ubiquitin-proteasome system in regulation of the skeletal muscle homeostasis and atrophy: From basic science to disorders. *J. Physiol. Sci.* **70**, 1–12.

104. Masiero, E., Agatea, L., Mammucari, C., Blaauw, B., Loro, E., Komatsu, M., Metzger, D., Reggiani, C., Schiaffino, S., Sandri, M. (2009). Autophagy Is Required to Maintain Muscle Mass. *Cell Metab.* **10**, 507–515.

105. Raben, N., Hill, V., Shea, L., Takikita, S., Baum, R., Mizushima, N., Ralston, E., Plotz, P. (2008). Suppression of autophagy in skeletal muscle uncovers the accumulation of ubiquitinated proteins and their potential role in muscle damage in Pompe disease. *Hum. Mol. Genet.* **17**, 3897–3908.

106. Hnia, K., Ramspacher, C., Vermot, J., Laporte, J. (2015). Desmin in muscle and associated diseases: beyond the structural function. *Cell Tissue Res*. **360**, 591–608.

107. Gavriilidis, C., Laredj, L., Solinhac, R., Messaddeq, N., Viaud, J., Laporte, J., Sumara, I., Hnia, K. (2018). The MTM1-UBQLN2-HSP complex mediates degradation of misfolded intermediate filaments in skeletal muscle. *Nat. Cell Biol.* **20**, 198–210.

108. Capetanaki, Y., Papathanasiou, S., Diokmetzidou, A., Vatsellas, G., Tsikitis, M. (2015). Desmin related disease: A matter of cell survival failure. *Curr. Opin. Cell Biol.* **32**, 113–120.

109. Hood, D. A., Memme, J. M., Oliveira, A. N., Triolo, M. (2019). Maintenance of Skeletal Muscle Mitochondria in Health, Exercise, and Aging. *Annu. Rev.* **81**, 19–41.

110. Milner, D. J., Mavroidis, M., Weisleder, N., Capetanaki, Y. (2000). Desmin cytoskeleton linked to muscle mitochondrial distribution and respiratory function. *J. Cell Biol.* **150**, 1283–1297.

111. Kostareva, A., Sjöberg, G., Bruton, J., Zhang, S. J., Balogh, J., Gudkova, A., Hedberg, B., Edström, L., Westerblad, H., Sejersen, T. (2008). Mice expressing L345P mutant desmin exhibit morphological and functional changes of skeletal and cardiac mitochondria. *J. Muscle Res. Cell Motil.* **29**, 25–36.

112. Al-Qusairi, L., Laporte, J. (2011). T-tubule biogenesis and triad formation in skeletal muscle and implication in human diseases. *Skelet. Muscle.* **1**, 1–11.

113. Al-Qusairi, L., Weiss, N., Toussaint, A., Berbey, C., Messaddeq, N., Kretz, C., Sanoudou, D., Beggs, A. H., Allard, B., Mandel, J.-L., Laporte, J., Jacquemond, V., Buj-Bello, A. (2009). T-tubule disorganization and defective excitation-contraction coupling in muscle fibers lacking myotubularin lipid phosphatase. *Proc. Natl. Acad. Sci.* **106**, 18763-18768.

114. Kutchukian, C., Lo, M., Tourneur, Y., Poulard, K., Vignaud, A., Berthier, C. (2016). Phosphatidylinositol 3-kinase inhibition restores Ca2+ release defects and prolongs survival in myotubularin-deficient mice. *Proc. Natl. Acad. Sci.* **113**, 14432–14437.

115. Mishra, Y. G., Manavathi, B. (2021). Focal adhesion dynamics in cellular function and disease. *Cell. Signal.* **85**, 110046.

116. Parsons, J. T., Horwitz, A. R., Schwartz, M. A. (2010). Cell adhesion: integrating cytoskeletal dynamics and cellular tension. *Nat. Rev. Mol.* **11**, 633–643.

117. Kanchanawong, P., Shtengel, G., Pasapera, A. M., Ramko, E. B., Davidson, M. W., Hess, H. F., Waterman, C. M. (2010). Nanoscale architecture of integrin-based cell adhesions. *Nature.* **468**, 580–584.

118. Martino, F., Perestrelo, A. R., Vinarský, V., Pagliari, S., Forte, G. (2018). Cellular mechanotransduction: From tension to function. *Front. Physiol.* **9**, 824.

119. Hirata, H., Tatsumi, H., Sokabe, M. (2008). Mechanical forces facilitate actin polymerization at focal adhesions in a zyxin-dependent manner. *J. Cell Sci.* **121**, 2795–2804.

120. Vicente-Manzanares, M., Horwitz, A. R. (2011). Adhesion dynamics at a glance. *J. Cell Sci.* **124**, 3923–3927.

121. Yuan, L., Fairchild, M. J., Perkins, A. D., Tanentzapf, G. (2010). Analysis of integrin turnover in fly myotendinous junctions. *J. Cell Sci.* **123**, 939–946.

122. Webb, D. J., Donais, K., Whitmore, L. A., Thomas, S. M., Turner, C. E., Parsons, J. T., Horwitz, A. F. (2004). FAK-Src signalling through paxillin, ERK and MLCK regulates adhesion disassembly. *Nat. Cell Biol.* **6**, 154–161.

123. Liu, J., Liu, Z., Chen, K., Chen, W., Fang, X., Li, M., Zhou, X., Ding, N., Lei, H., Guo, C., Qian, T., Wang, Y., Liu, L., Chen, Y., Zhao, H., Sun, Y., Deng, Y., Wu, C. (2021). Kindlin-2 promotes rear focal adhesion disassembly and directional persistence during cell migration. *J. Cell Sci.* **134**, jcs244616.

124. Franco, S. J., Rodgers, M. A., Perrin, B. J., Han, J., Bennin, D. A., Critchley, D. R., Huttenlocher, A. (2004). Calpain-

mediated proteolysis of talin regulates adhesion dynamics. *Nat. Cell Biol.* **6**, 977–983.

125. Flevaris, P., Stojanovic, A., Gong, H., Chishti, A., Welch, E., Du, X. (2007). A molecular switch that controls cell spreading and retraction. *J. Cell Biol.* **179**, 553–565.

126. Chan, K. T., Bennin, D. A., Huttenlocher, A. (2010). Regulation of adhesion dynamics by calpain-mediated proteolysis of focal adhesion kinase (FAK). *J. Biol. Chem.* **285**, 11418–11426.

127. Ezratty, E. J., Partridge, M. A., Gundersen, G. G. (2005). Microtubule-induced focal adhesion disassembly is mediated by dynamin and focal adhesion kinase. *Nat. Cell Biol.* **7**, 581–590.

128. Vasquez, R. J., Howell, B., Yvon, A. M. C., Wadsworth, P., Cassimeris, L. (1997). Nanomolar concentrations of nocodazole alter microtubule dynamic instability in vivo and in vitro. *Mol. Biol. Cell.* **8**, 973–985.

129. Wang, Y., McNiven, M. A. (2012). Invasive matrix degradation at focal adhesions occurs via protease recruitment by a FAK–p130Cas complex. *J. Cell Biol.* **196**, 375–385.

130. Tancini, B., Buratta, S., Delo, F., Sagini, K., Chiaradia, E., Pellegrino, R. M., Emiliani, C., Urbanelli, L. (2020). Lysosomal Exocytosis: The Extracellular Role of an Intracellular Organelle. *Membranes.* **10**, 1–21.

131. Krylyshkina, O., Kaverina, I., Kranewitter, W., Steffen, W., Alonso, M. C., Cross, R. A., Small, J. V. (2002). Modulation of substrate adhesion dynamics via microtubule targeting requires kinesin-1. *J. Cell Biol.* **156**, 349–359.

132. Moreno-Layseca, P., Icha, J., Hamidi, H., Ivaska, J. (2019). Integrin trafficking in cells and tissues. *Nat. Cell Bio*. **21**, 122–132.

133. Paul, N. R., Jacquemet, G., Caswell, P. T. (2015). Endocytic Trafficking of Integrins in Cell Migration. *Curr. Biol.* **25**, 1092–1105.

134. Franceschi, N. De, Hamidi, H., Alanko, J., Sahgal, P., Ivaska, J. (2015). Integrin traffic – the update. *J. Cell Sci.* **128**, 839–852.

135. Byron, A., Askari, J. A., Humphries, J. D., Jacquemet, G., Koper, E. J., Warwood, S., Choi, C. K., Stroud, M. J., Chen, C. S., Knight, D., Humphries, M. J. (2015). A proteomic approach reveals integrin activation state-dependent control of microtubule cortical targeting. *Nat. Commun.* **6**, 1–14.

136. Posor, Y., Eichhorn-Grünig, M., Haucke, V. (2015). Phosphoinositides in endocytosis. *Biochim. Biophys. Acta.* **1851**, 794–804.

137. Kaksonen, M., Roux, A. (2018). Mechanisms of clathrin-mediated endocytosis. *Nat. Rev. Mol.* **19**, 313–326.

138. Edeling, M. A., Smith, C., Owen, D. (2006). Life of a clathrin coat: insights from clathrin and AP structures. *Nat. Rev. Mol.* **7**, 32–44.

139. Traub, L. M. (2009). Tickets to ride: selecting cargo for clathrin-regulated internalization. *Nat. Rev. Mol.* **10**, 583–596.

140. Daumke, O., Roux, A., Haucke, V. (2014). BAR Domain Scaffolds in Dynamin-Mediated Membrane Fission. *Cell.* **156**, 882–892.

141. Perera, R. M., Zoncu, R., Lucast, L., De Camilli, P., Toomre, D. (2006). Two synaptojanin 1 isoforms are recruited to clathrin-coated pits at different stages. *Proc. Natl. Acad. Sci.* **103**, 19332–19337.

142. Massol, R. H., Boll, W., Griffin, A. M., Kirchhausen, T. (2006). A burst of auxilin recruitment determines the onset of clathrin-coated vesicle uncoating. *Proc. Natl. Acad. Sci.* **103**, 10265–10270.

143. Wang, H., Loerke, D., Bruns, C., Müller, R., Koch, P. A., Puchkov, D., Schultz, C., Haucke, V. (2020). Phosphatidylinositol 3,4-bisphosphate synthesis and turnover are spatially segregated in the endocytic pathway. *J. Biol. Chem.* **295**, 1091–1104.

144. Chao, W. T., Kunz, J. (2009). Focal adhesion disassembly requires clathrin-dependent endocytosis of integrins. *FEBS Lett.* **583**, 1337–1343.

145. Ezratty, E. J., Bertaux, C., Marcantonio, E. E., Gundersen, G. G. (2009). Clathrin mediates integrin endocytosis for focal adhesion disassembly in migrating cells. *J. Cell Biol.* **187**, 733–747.

146. Nishimura, T., Kaibuchi, K. (2007). Numb Controls Integrin Endocytosis for Directional Cell Migration with aPKC and PAR-3. *Dev. Cell* **13**, 15–28.

147. Teckchandani, A., Toida, N., Goodchild, J., Henderson, C., Watts, J., Wollscheid, B., Cooper, J. A. (2009). Quantitative proteomics identifies a Dab2/integrin module regulating cell migration. *J. Cell Biol.* **186**, 99–111.

148. Teckchandani, A., Mulkearns, E. E., Randolph, T. W., Toida, N., Cooper, J. A. (2012). The clathrin adaptor Dab2 recruits EH domain scaffold proteins to regulate integrin β1 endocytosis. *Mol. Biol. Cell.* **23**, 2905–2916.

149. De Franceschi, N., Arjonen, A., Elkhatib, N., Denessiouk, K., Wrobel, A. G., Wilson, T. A., Pouwels, J., Montagnac, G., Owen, D. J., Ivaska, J. (2016). Selective integrin endocytosis is driven by interactions between the integrin α-chain and AP2. *Nat. Struct. Mol. Biol.* **23**, 172–179.

150. Arjonen, A., Alanko, J., Veltel, S., Ivaska, J. (2012). Distinct Recycling of Active and Inactive β1 Integrins. *Traffic.* **13**, 610–625.

151. Huet-Calderwood, C., Rivera-Molina, F., Iwamoto, D. V., Kromann, E. B., Toomre, D., Calderwood, D. A. (2017). Novel ecto-tagged integrins reveal their trafficking in live cells. *Nat. Commun.* **8**, 1–13.

152. Steinberg, F., Heesom, K. J., Bass, M. D., Cullen, P. J. (2012). SNX17 protects integrins from degradation by sorting between lysosomal and recycling pathways. *J. Cell Biol.* **197**, 219–230.

153. Bridgewater, R. E., Norman, J. C., Caswell, P. T. (2012). Integrin trafficking at a glance. *J. Cell Sci.* **125**, 3695–3701.

154. Grant, B. D., Donaldson, J. G. (2009). Pathways and mechanisms of endocytic recycling. *Nat. Rev. Mol.* **10**, 597–608.

155. Dozynkiewicz, M. A., Jamieson, N. B., MacPherson, I., Grindlay, J., vandenBerghe, P. V. E., vonThun, A., Morton, J. P., Gourley, C., Timpson, P., Nixon, C., McKay, C. J., Carter, R., Strachan, D., Anderson, K., Sansom, O. J., Caswell, P. T., Norman, J. C. (2012). Rab25 and CLIC3 collaborate to promote integrin recycling from late endosomes/lysosomes and drive cancer progression. *Dev. Cell.* **22**, 131–145.

156. Burkin, D. J., Kaufman, S. J. (1999). The alpha7beta1 integrin in muscle development and disease. *Cell Tissue Res.* **296**, 183–190.

157. Schwander, M., Leu, M., Stumm, M., Dorchies, O. M., Ruegg, U. T., Schittny, J., Müller, U. (2003). Beta1 integrins regulate myoblast fusion and sarcomere assembly. *Dev. Cell.* **4**, 673–685.

158. Roman, W., Martins, J. P., Gomes, E. R. (2018). Local Arrangement of Fibronectin by Myofibroblasts Governs Peripheral Nuclear Positioning in Muscle Cells. *Dev. Cell.* **46**, 102–111.

159. Samarel, A. M. (2005). Costameres, focal adhesions, and cardiomyocyte mechanotransduction. *Am. J. Physiol. Heart Circ. Physiol.* **289**, H2291–2301.

160. Perkins, A. D., Ellis, S. J., Asghari, P., Shamsian, A., Moore, E. D. W., Tanentzapf, G. (2010). Integrin-mediated adhesion maintains sarcomeric integrity. *Dev. Biol.* **338**, 15–27.

161. Sparrow, J. C., Schöck, F. (2009). The initial steps of myofibril assembly: Integrins pave the way. *Nat. Rev. Mol*. **10**, 293–298.

162. Conti, F. J., Felder, A., Monkley, S., Schwander, M., Wood, M. R., Lieber, R., Crithcley, D., Müller, U. (2008). Progressive myopathy and defects in the maintenance of myotendinous junctions in mice that lack talin 1 in skeletal muscle. *Development.* **135**, 2043–2053.

163. Gheyara, A. L., Vallejo-Illarramendi, A., Zang, K., Mei, L., St-Amaud, R., Dedhar, S., Reichardt, L. F. (2007). Deletion of integrin-linked kinase from skeletal muscles of mice resembles muscular dystrophy due to α7β1-integrin deficiency. *Am. J. Pathol.* **171**, 1966–1977.

164. Wang, H. V., Chang, L. W., Brixius, K., Wickström, S. A., Montanez, E., Thievessen, I., Schwander, M., Müller, U., Bloch, W., Mayer, U., Fässler, R. (2008). Integrin-linked kinase stabilizes myotendinous junctions and protects muscle from stress-induced damage. *J. Cell Biol.* **180**, 1037–1049.

165. Mayer, U., Saher, G., Fässler, R., Bornemann, A., Echtermeyer, F., Von Der Mark, H., Miosge, N., Pöschl, E., Von Der Mark, K. (1997). Absence of integrin α7 causes a novel form of muscular dystrophy. *Nat. Genet.* **17**, 318–323.

166. Rozo, M., Li, L., Fan, C. M. (2016). Targeting β1-integrin signaling enhances regeneration in aged and dystrophic muscle in mice. *Nat. Med.* **22**, 889–896.

167. Marino, J. S., Tausch, B. J., Dearth, C. L., Manacci, M. V, Mcloughlin, T. J., Rakyta, S. J., Linsenmayer, M. P., Pizza, F. X. (2008). 2-Integrins contribute to skeletal muscle hypertrophy in mice. *Am J Physiol Cell Physiol.* **295**, 1026–1036.

168. Kaisto, T., Rahkila, P., Marjomäki, V., Parton, R. G., Metsikkö, K. (1999). Endocytosis in skeletal muscle fibers. *Exp. Cell Res.* **253**, 551–560.

169. Ribeiro, I., Yuan, L., Tanentzapf, G., Dowling, J. J., Kiger, A. (2011). Phosphoinositide Regulation of Integrin Trafficking Required for Muscle Attachment and Maintenance. *PLoS Genet.* **7**, e1001295.

170. Buj-Bello, A., Laugel, V., Messaddeq, N., Zahreddine, H., Laporte, J., Pellissier, J. F., Mandel, J. L. (2002). The lipid phosphatase myotubularin is essential for skeletal muscle maintenance but not for myogenesis in mice. *Proc. Natl. Acad. Sci.* **99**, 15060–15065.

171. Bilanges, B., Posor, Y., Vanhaesebroeck, B. (2019). PI3K isoforms in cell signalling and vesicle trafficking. *Nat. Rev.*

Mol. **20**, 515–534.

172. Koch, P. A., Dornan, G. L., Hessenberger, M., Haucke, V. (2021). The molecular mechanisms mediating class II PI 3-kinase function in cell physiology. *FEBS J.* **288**, 7025–7042.

173. Domin, J., Pages, F., Volinia, S., Rittenhouse, S. E., Zvelebil, M. J., Stein, R. C., Waterfield, M. D. (1997). Cloning of a human phosphoinositide 3-kinase with a C2 domain that displays reduced sensitivity to the inhibitor wortmannin. *Biochem. J.* **326**, 139–147.

174. Fruman, D. A., Chiu, H., Hopkins, B. D., Bagrodia, S., Cantley, L. C., Abraham, R. T. (2017). The PI3K Pathway in Human Disease. *Cell.* **170**, 605–635.

175. Vanhaesebroeck, B., Guillermet-Guibert, J., Graupera, M., Bilanges, B. (2010). The emerging mechanisms of isoform-specific PI3K signalling. *Nat. Rev. Mol.* **11**, 329–341.

176. Malek, M., Kielkowska, A., Chessa, T., Anderson, K. E., Barneda, D., Pir, P., Nakanishi, H., Eguchi, S., Koizumi, A., Sasaki, J., Juvin, V., Kiselev, V. Y., Niewczas, I., Gray, A., Valayer, A., Spensberger, D., Imbert, M., Felisbino, S., Habuchi, T., Beinke, S., Cosulich, S., Le Novère, N., Sasaki, T., Clark, J., Hawkins, P. T., Stephens, L. R. (2017). PTEN Regulates PI(3,4)P 2 Signaling Downstream of Class I PI3K. *Mol. Cell.* **68**, 566–580.

177. Pirola, L., Zvelebil, M. J., Bulgarelli-Leva, G., Van Obberghen, E., Waterfield, M. D., Wymann, M. P. (2001). Activation loop sequences confer substrate specificity to phosphoinositide 3-kinase alpha (PI3Kalpha). Functions of lipid kinase-deficient PI3Kalpha in signaling. *J. Biol. Chem.* **276**, 21544–21554.

178. Hirsch, E., Braccini, L., Ciraolo, E., Morello, F., Perino, A. (2009). Twice upon a time: PI3K's secret double life exposed. *Trends Biochem. Sci.* **34**, 244–248.

179. Arafeh, R., Samuels, Y. (2019). PIK3CA in cancer: The past 30 years. *Semin. Cancer Biol.* **59**, 36–49.

180. Janku, F., Yap, T. A., Meric-Bernstam, F. (2018). Targeting the PI3K pathway in cancer: are we making headway? *Nat. Rev. Clin. Oncol.* **15**, 273–291.

181. Devereaux, K., Dall'Armi, C., Alcazar-Roman, A., Ogasawara, Y., Zhou, X., Wang, F., Yamamoto, A., de Camilli, P., Di Paolo, G. (2013). Regulation of mammalian autophagy by class II and III PI 3-kinases through PI3P synthesis. *PLoS One.* **8**, e76405.

182. Backer, J. M. (2016). The intricate regulation and complex functions of the Class III phosphoinositide 3-kinase Vps34. *Biochem. J.* **473**, 2251–2271.

183. Stjepanovic, G., Baskaran, S., Lin, M. G., Hurley, J. H. (2017). Unveiling the role of VPS34 kinase domain dynamics in regulation of the autophagic PI3K complex. *Mol. Cell. Oncol.* **4,** e1367873.

184. Zhou, X., Takatoh, J., Wang, F. (2011). The Mammalian Class 3 PI3K (PIK3C3) Is Required for Early Embryogenesis and Cell Proliferation. *PLoS One.* **6**, e16358.

185. Bago, R., Malik, N., Munson, M. J., Prescott, A. R., Davies, P., Sommer, E., Shpiro, N., Ward, R., Cross, D., Ganley, I. G., Alessi, D. R. (2014). Characterization of VPS34-IN1, a selective inhibitor of Vps34, reveals that the phosphatidylinositol 3-phosphate-binding SGK3 protein kinase is a downstream target of class III phosphoinositide 3-kinase. *Biochem. J.* **463**, 413–427.

186. Falasca, M., Hamilton, J. R., Selvadurai, M., Sundaram, K., Adamska, A., Thompson, P. E. (2017). Class II Phosphoinositide 3-Kinases as Novel Drug Targets. *J. Med. Chem.* **60**, 47–65.

187. Wang, H., Lo, W. T., Vujičić Žagar, A., Gulluni, F., Lehmann, M., Scapozza, L., Haucke, V., Vadas, O. (2018). Autoregulation of Class II Alpha PI3K Activity by Its Lipid-Binding PX-C2 Domain Module. *Mol. Cell.* **71**, 343-351.

188. Lo, W.-T., Zhang, Y., Vadas, O., Roske, Y., Gulluni, F., De Santis, M. C., Zagar, A. V., Stephanowitz, H., Hirsch, E., Liu, F., Daumke, O., Kudryashev, M., Haucke, V. (2022). Structural basis of phosphatidylinositol 3-kinase C2α function. *Nat. Struct. Mol. Biol.* **29**, 218–228.

189. Chen, K. E., Tillu, V. A., Chandra, M., Collins, B. M. (2018). Molecular Basis for Membrane Recruitment by the PX and C2 Domains of Class II Phosphoinositide 3-Kinase-C2α. *Structure.* **26**, 1612–1625.

190. Wheeler, M., Domin, J. (2006). The N-terminus of phosphoinositide 3-kinase-C2β regulates lipid kinase activity and binding to clathrin. *J. Cell. Physiol.* **206**, 586–593.

191. Gaidarov, I., Smith, M. E. K., Domin, J., Keen, J. H. (2001). The class II phosphoinositide 3-kinase C2alpha is activated by clathrin and regulates clathrin-mediated membrane trafficking. *Mol. Cell.* **7**, 443–449.

192. Wheeler, M., Domin, J. (2001). Recruitment of the Class II Phosphoinositide 3-Kinase C2β to the Epidermal Growth Factor Receptor: Role of Grb2. *Mol. Cell. Biol.* **21**, 6660–6667.

193. Das, M., Scappini, E., Martin, N. P., Wong, K. A., Dunn, S., Chen, Y.-J., Miller, S. L. H., Domin, J., O'Bryan, J. P. (2007). Regulation of Neuron Survival through an Intersectin-Phosphoinositide 3'-Kinase C2β-AKT Pathway. *Mol. Cell. Biol.* **27**, 7906–7917.

194. Wallroth, A., Koch, P. A., Marat, A. L., Krause, E., Haucke, V. (2019). Protein kinase N controls a lysosomal lipid switch to facilitate nutrient signalling via mTORC1. *Nat. Cell Biol.*. **21**, 1093–1101.

195. Braccini, L., Ciraolo, E., Campa, C. C., Perino, A., Longo, D. L., Tibolla, G., Pregnolato, M., Cao, Y., Tassone, B., Damilano, F., Laffargue, M., Calautti, E., Falasca, M., Norata, G. D., Backer, J. M., Hirsch, E. (2015). PI3K-C2γ is a Rab5 effector selectively controlling endosomal Akt2 activation downstream of insulin signalling. *Nat. Commun.* **6**, 1–15.

196. Burke, J. E. (2018). Structural Basis for Regulation of Phosphoinositide Kinases and Their Involvement in Human Disease. *Mol. Cell.* **71**, 653–673.

197. Campa, C. C., Franco, I., Hirsch, E. (2015). PI3K-C2α: One enzyme for two products coupling vesicle trafficking and signal transduction. *FEBS Lett*. **589**, 1552–1558.

198. Campa, C. C., Margaria, J. P., Derle, A., Del Giudice, M., De Santis, M. C., Gozzelino, L., Copperi, F., Bosia, C., Hirsch, E. (2018). Rab11 activity and PtdIns(3)P turnover removes recycling cargo from endosomes. *Nat. Chem. Biol.* **14**, 801–810.

199. Yoshioka, K., Yoshida, K., Cui, H., Wakayama, T., Takuwa, N., Okamoto, Y., Du, W., Qi, X., Asanuma, K., Sugihara, K., Aki, S., Miyazawa, H., Biswas, K., Nagakura, C., Ueno, M., Iseki, S., Schwartz, R. J., Okamoto, H., Sasaki, T., Matsui, O., Asano, M., Adams, R. H., Takakura, N., Takuwa, Y. (2012). Endothelial PI3K-C2α, a class II PI3K, has an essential role in angiogenesis and vascular barrier function. *Nat. Med.* **18**, 1560–1569.

200. Krag, C., Malmberg, E. K., Salcini, A. E. (2010). PI3KC2α, a class II PI3K, is required for dynamin-independent internalization pathways. *J. Cell Sci.* **123**, 4240–4250.

201. Aung, K. T., Yoshioka, K., Aki, S., Ishimaru, K., Takuwa, N., Takuwa, Y. (2018). The class II phosphoinositide 3-kinases PI3K-C2α and PI3K-C2β differentially regulate clathrin-dependent pinocytosis in human vascular endothelial cells. *J. Physiol. Sci.* **69**, 263–280.

202. Franco, I., Gulluni, F., Campa, C. C., Costa, C., Margaria, J. P., Ciraolo, E., Martini, M., Monteyne, D., De Luca, E., Germena, G., Posor, Y., Maffucci, T., Marengo, S., Haucke, V., Falasca, M., Perez-Morga, D., Boletta, A., Merlo, G. R., Hirsch, E. (2014). PI3K class II α controls spatially restricted endosomal PtdIns3P and Rab11 activation to promote primary cilium function. *Dev. Cell.* **28**, 647–658.

203. Falasca, M., Hughes, W. E., Dominguez, V., Sala, G., Fostira, F., Fang, M. Q., Cazzolli, R., Shepherd, P. R., James, D. E., Maffucci, T. (2007). The role of phosphoinositide 3-kinase C2α in insulin signaling. *J. Biol. Chem.* **282**, 28226–28236.

204. Gulluni, F., Martini, M., De Santis, M. C., Campa, C. C., Ghigo, A., Margaria, J. P., Ciraolo, E., Franco, I., Ala, U., Annaratone, L., Disalvatore, D., Bertalot, G., Viale, G., Noatynska, A., Compagno, M., Sigismund, S., Montemurro, F., Thelen, M., Fan, F., Meraldi, P., Marchiò, C., Pece, S., Sapino, A., Chiarle, R., Di Fiore, P. P., Hirsch, E. (2017). Mitotic Spindle Assembly and Genomic Stability in Breast Cancer Require PI3K-C2α Scaffolding Function. *Cancer Cell.* **32**, 444–459.

205. Gulluni, F., Prever, L., Li, H., Krafcikova, P., Corrado, I., Lo, W. T., Margaria, J. P., Chen, A., de Santis, M. C., Cnudde, S. J., Fogerty, J., Yuan, A., Massarotti, A., Sarijalo, N. T., Vadas, O., Williams, R. L., Thelen, M., Powell, D. R., Schueler, M., Wiesener, M. S., Balla, T., Baris, H. N., Tiosano, D., McDermott, B. M., Perkins, B. D., Ghigo, A., Martini, M., Haucke, V., Boura, E., Merlo, G. R., Buchner, D. A., Hirsch, E. (2021). PI(3,4)P2-mediated cytokinetic abscission prevents early senescence and cataract formation. *Science.* **374**, eabk0410.

206. Tiosano, D., Baris, H. N., Chen, A., Hitzert, M. M., Schueler, M., Gulluni, F., Wiesener, A., Bergua, A., Mory, A., Copeland, B., Gleeson, J. G., Rump, P., van Meer, H., Sival, D. A., Haucke, V., Kriwinsky, J., Knaup, K. X., Reis, A., Hauer, N. N., Hirsch, E., Roepman, R., Pfundt, R., Thiel, C. T., Wiesener, M. S., Aslanyan, M. G., Buchner, D. A. (2019). Mutations in PIK3C2A cause syndromic short stature, skeletal abnormalities, and cataracts associated with ciliary dysfunction. *PLoS Genet.* **15**, e1008088.

207. Dong, J., Du, X., Wang, H., Wang, J., Lu, C., Chen, X., Zhu, Z., Luo, Z., Yu, L., Brown, A. J., Yang, H., Wu, J. W. (2019). Allosteric enhancement of ORP1-mediated cholesterol transport by PI(4,5)P2/PI(3,4)P2. *Nat. Commun.* **10**, 1–16.

208. Castellano, B. M., Thelen, A. M., Moldavski, O., Feltes, M., Van Der Welle, R. E. N., Mydock-McGrane, L., Jiang, X., Van Eijkeren, R. J., Davis, O. B., Louie, S. M., Perera, R. M., Covey, D. F., Nomura, D. K., Ory, D. S., Zoncu, R. (2017). Lysosomal cholesterol activates mTORC1 via an SLC38A9-Niemann-Pick C1 signaling complex. *Science.* **355**, 1306–1311.

209. Srivastava, S., Di, L., Zhdanova, O., Li, Z., Vardhana, S., Wan, Q., Yan, Y., Varma, R., Backer, J., Wulff, H., Dustin, M. L., Skolnik, E. Y. (2009). The class II phosphatidylinositol 3 kinase C2beta is required for the activation of the K+ channel KCa3.1 and CD4 T-cells. *Mol. Biol. Cell.* **20**, 3783–3791.

210. Srivastava, S., Cai, X., Li, Z., Sun, Y., Skolnik, E. Y. (2012). Phosphatidylinositol-3-Kinase C2β and TRIM27 Function To Positively and Negatively Regulate IgE Receptor Activation of Mast Cells. *Mol. Cell. Biol.* **32**, 3132–3139.

211. Srivastava, S., Li, Z., Skolnik, E. Y. (2017). Phosphatidlyinositol-3-kinase C2 beta (PI3KC2β) is a potential new target to treat IgE mediated disease. *PLoS One.* **12**, e0183474.

212. Alliouachene, S., Bilanges, B., Chicanne, G., Anderson, K. E., Pearce, W., Ali, K., Valet, C., Posor, Y., Low, P. C., Chaussade, C., Scudamore, C. L., Salamon, R. S., Backer, J. M., Stephens, L., Hawkins, P. T., Payrastre, B., Vanhaesebroeck, B. (2015). Inactivation of the Class II PI3K-C2β Potentiates Insulin Signaling and Sensitivity. *Cell Rep.* **13**, 1881–1894.

213. Hanahan, D., Weinberg, R. A. (2011). Hallmarks of cancer: The next generation. *Cell.* **144**, 646–674.

214. Domin, J., Harper, L., Aubyn, D., Wheeler, M., Florey, O., Haskard, D., Yuan, M., Zicha, D. (2005). The class II phosphoinositide 3-kinase PI3K-C2β regulates cell migration by a PtdIns(3)P dependent mechanism. *J. Cell. Physiol.* **205**, 452–462.

215. Katso, R. M., Pardo, O. E., Palamidessi, A., Franz, C. M., Marinov, M., De Laurentiis, A., Downward, J., Scita, G., Ridley, A. J., Waterfield, M. D., Arcaro, A. (2006). Phosphoinositide 3-Kinase C2β Regulates Cytoskeletal Organization and Cell Migration via Rac-dependent Mechanisms. *Mol. Biol. Cell.* **17**, 3729–3744.

216. Maffucci, T., Cooke, F. T., Foster, F. M., Traer, C. J., Fry, M. J., Falasca, M. (2005). Class II phosphoinositide 3-kinase defines a novel signaling pathway in cell migration. *J. Cell Biol.* **169**, 789–799.

217. Mavrommati, I., Cisse, O., Falasca, M., Maffucci, T. (2016). Novel roles for class II Phosphoinositide 3-Kinase C2β in signalling pathways involved in prostate cancer cell invasion. *Sci. Rep.* **6**, 23277.

218. Kitatani, K., Usui, T., Sriraman, S. K., Toyoshima, M., Ishibashi, M., Shigeta, S., Nagase, S., Sakamoto, M., Ogiso, H., Okazaki, T., Hannun, Y. A., Torchilin, V. P., Yaegashi, N. (2016). Ceramide limits phosphatidylinositol-3-kinase C2β-controlled cell motility in ovarian cancer: potential of ceramide as a metastasis-suppressor lipid. *Oncogene.* **35**, 2801–2812.

219. Wu, K., Yang, L., Chen, J., Zhao, H., Wang, J., Xu, S., Huang, Z. (2015). miR-362-5p inhibits proliferation and migration of neuroblastoma cells by targeting phosphatidylinositol 3-kinase-C2β. *FEBS Lett.* **589**, 1911–1919.

220. Chikh, A., Ferro, R., Abbott, J. J., Piñeiro, R., Buus, R., Iezzi, M., Ricci, F., Bergamaschi, D., Ostano, P., Chiorino, G., Lattanzio, R., Broggini, M., Piantelli, M., Maffucci, T., Falasca, M. (2016). Class II phosphoinositide 3-kinase C2β regulates a novel signaling pathway involved in breast cancer progression. *Oncotarget.* **7**, 18325–18345.

221. Li, H., Prever, L., Hsu, M. Y., Lo, W. T., Margaria, J. P., De Santis, M. C., Zanini, C., Forni, M., Novelli, F., Pece, S., Di Fiore, P. P., Porporato, P. E., Martini, M., Belabed, H., Nazare, M., Haucke, V., Gulluni, F., Hirsch, E. (2022). Phosphoinositide Conversion Inactivates R-RAS and Drives Metastases in Breast Cancer. *Adv. Sci.* **9**, e2103249.

222. Islam, S., Yoshioka, K., Aki, S., Ishimaru, K., Yamada, H., Takuwa, N., Takuwa, Y. (2020). Class II phosphatidylinositol 3-kinase α and β isoforms are required for vascular smooth muscle Rho activation, contraction and blood pressure regulation in mice. *J. Physiol. Sci.* **70**, 1–17.

223. Gulluni, F., De Santis, M. C., Margaria, J. P., Martini, M., Hirsch, E. (2019). Class II PI3K Functions in Cell Biology and Disease. *Trends Cell Biol*. **29**, 339–359.

224. Margaria, J. P., Ratto, E., Gozzelino, L., Li, H., Hirsch, E. (2019). Class II PI3Ks at the intersection between signal transduction and membrane trafficking. *Biomolecules*. **9**, 104.

225. Gillooly, D. J., Raiborg, C., Stenmark, H. (2003). Phosphatidylinositol 3-phosphate is found in microdomains of early endosomes. *Histochem. Cell Biol.* **120**, 445–453.

226. Saiki, R. K., Gelfand, D. H., Stoffel, S., Scharf, S. J., Higuchi, R., Horn, G. T., Mullis, K. B., Erlich, H. A. (1988). Primer-directed enzymatic amplification of DNA with a thermostable DNA polymerase. *Science.* **239**, 487–491.

227. Spandidos, A., Wang, X., Wang, H., Seed, B. (2010). PrimerBank: a resource of human and mouse PCR primer pairs for gene expression detection and quantification. *Nucleic Acids Res.* **38**, 792–799.

228. Laemmli, U. K. (1970). Cleavage of structural proteins during the assembly of the head of bacteriophage T4. *Nature.* **227**, 680–685.

229. Doudna, J. A., Charpentier, E. (2014). Genome editing. The new frontier of genome engineering with CRISPR-Cas9. *Science.* **346**, 1258096.

230. Kiernan, J. A. (2000). Formaldehyde, Formalin, Paraformaldehyde And Glutaraldehyde: What They Are And What They Do. *Micros. Today*. **8**, 8–13.

231. Hammond, G. R. V., Schiavo, G., Irvine, R. F. (2009). Immunocytochemical techniques reveal multiple, distinct cellular

pools of PtdIns4P and PtdIns(4,5)P(2). *Biochem. J.* **422**, 23–35.

232. Tinevez, J. Y., Perry, N., Schindelin, J., Hoopes, G. M., Reynolds, G. D., Laplantine, E., Bednarek, S. Y., Shorte, S. L., Eliceiri, K. W. (2017). TrackMate: An open and extensible platform for single-particle tracking. *Methods.* **115**, 80–90.

233. Blau, H. M., Chiu, C. P., Webster, C. (1983). Cytoplasmic activation of human nuclear genes in stable heterocaryons. *Cell.* **32**, 1171–1180.

234. Yaffe, D., Saxel, O. (1977). Serial passaging and differentiation of myogenic cells isolated from dystrophic mouse muscle. *Nature.* **270**, 725–727.

235. Casas-Delucchi, C. S., Brero, A., Rahn, H.-P., Solovei, I., Wutz, A., Cremer, T., Leonhardt, H., Cristina Cardoso, M. (2011). Histone acetylation controls the inactive X chromosome replication dynamics. *Nat. Commun.* **2**, 222.

236. Mukund, K., Subramaniam, S. (2020). Skeletal muscle: A review of molecular structure and function, in health and disease. *Wiley Interdiscip. Rev. Syst. Biol. Med.* **12**, e1462.

237. Kim, S. A., Taylor, G. S., Torgersen, K. M., Dixon, J. E. (2002). Myotubularin and MTMR2, phosphatidylinositol 3-phosphatases mutated in myotubular myopathy and type 4B Charcot-Marie-Tooth disease. *J. Biol. Chem.* **277**, 4526–4531.

238. Bago, R., Malik, N., Munson, M. J., Prescott, A. R., Davies, P., Sommer, E., Shpiro, N., Ward, R., Cross, D., Ganley, I. G., Alessi, D. R. (2014). Characterization of VPS34-IN1, a selective inhibitor of Vps34, reveals that the phosphatidylinositol 3-phosphate-binding SGK3 protein kinase is a downstream target of class III phosphoinositide 3-kinase. *Biochem. J.* **463**, 413–427.

239. Schmid, M. C., Franco, I., Kang, S. W., Hirsch, E., Quilliam, L. A., Varner, J. A. (2013). PI3-Kinase γ Promotes Rap1a-Mediated Activation of Myeloid Cell Integrin α4β1, Leading to Tumor Inflammation and Growth. *PLoS One.* **8**, e60226.

240. Chavakis, E., Carmona, G., Chavakis, T., Andreas M Zeiher, I., Dimmeler, S. (2007). Abstract 1130: Role Of PI3Kγ For Integrin-dependent Adhesive And Migratory Functions Of Progenitor Cells In Vitro And In Vivo. *Circulation.* **116**, II_227.

241. Guillermet-Guibert, J., Bjorklof, K., Salpekar, A., Gonella, C., Ramadani, F., Bilancio, A., Meek, S., Smith, A. J. H., Okkenhaug, K., Vanhaesebroeck, B. (2008). The p110β isoform of phosphoinositide 3-kinase signals downstream of G protein-coupled receptors and is functionally redundant with p110γ. *Proc. Natl. Acad. Sci.* **105**, 8292–8297.

242. Burgett, A. W. G., Poulsen, T. B., Wangkanont, K., Anderson, D. R., Kikuchi, C., Shimada, K., Okubo, S., Fortner, K. C., Mimaki, Y., Kuroda, M., Murphy, J. P., Schwalb, D. J., Petrella, E. C., Cornella-Taracido, I., Schirle, M., Tallarico, J. A., Shair, M. D. (2011). Natural products reveal cancer cell dependence on oxysterol-binding proteins. *Nat. Chem. Biol.* **7**, 639–647.

243. Mesmin, B., Bigay, J., Moser Von Filseck, J., Lacas-Gervais, S., Drin, G., Antonny, B. (2013). A Four-Step Cycle Driven by PI(4)P Hydrolysis Directs Sterol/PI(4)P Exchange by the ER-Golgi Tether OSBP. *Cell.* **155**, 830–843.

244. Heitman, J., Movva, N. R., Hall, M. N. (1991). Targets for cell cycle arrest by the immunosuppressant rapamycin in yeast. *Science.* **253**, 905–909.

245. Macia, E., Ehrlich, M., Massol, R., Boucrot, E., Brunner, C., Kirchhausen, T. (2006). Dynasore, a cell-permeable inhibitor of dynamin. *Dev. Cell.* **10**, 839–850.

246. Fish, K. N. (2009). Total Internal Reflection Fluorescence (TIRF) Microscopy. *Curr. Protoc. Cytom.* **50**, 12.18.1-12.18.13.

247. Lo, WT., Belabed, H., Kücükdisli, M., Metag, J., Roske, Y., Prokofeva, P., Ohashi, Y., Horatscheck, A., Cirillo, D., Krauss, M., Schmied, C., Neuenschwander, M., von Kries, J.P., Médard, G., Kuster, B., Perisic, O., Williams, R.L., Daumke, O., Payrastre, B., Severin, S., Nazaré, M., Haucke, V. (2023). Development of selective inhibitors of phosphatidylinositol 3-kinase C2α. *Nat. Chem. Biol.* **19**, 18–27.

248. Khodabukus, A. (2021). Tissue-Engineered Skeletal Muscle Models to Study Muscle Function, Plasticity, and Disease. *Front. Physiol.* **12**, 619710.

249. Wang, J., Khodabukus, A., Rao, L., Vandusen, K., Abutaleb, N., Bursac, N. (2019). Engineered skeletal muscles for disease modeling and drug discovery. *Biomaterials.* **221**, 119416.

250. Falcieri, E., Burattini, S., Ferri, P., Battistelli, M., Curci, R., Luchetti, F., Falcieri, E. (2009). C2C12 murine myoblasts as a model of skeletal muscle development: morpho-functional characterization. *Eur. J. Histochem.* **48**, 223–234.

251. Hughes, P., Marshall, D., Reid, Y., Parkes, H., Gelber, C. (2007). The costs of using unauthenticated, over-passaged cell lines: How much more data do we need? *Biotechniques.* **43**, 575–586.

252. Giuliano, C. J., Lin, A., Girish, V., Sheltzer, J. M. (2019). Generating Single Cell–Derived Knockout Clones in Mammalian Cells with CRISPR/Cas9. *Curr. Protoc. Mol. Biol.* **128**, e100.

253. Amoasii, L., Hnia, K., Chicanne, G., Brech, A., Cowling, B. S., Muller, M. M., Schwab, Y., Koebel, P., Ferry, A., Payrastre, B., Laporte, J. (2013). Myotubularin and PtdIns3P remodel the sarcoplasmic reticulum in muscle in vivo. *J. Cell Sci.* **126**, 1806–1819.

254. Bachmann, M., Kukkurainen, S., Hytönen, V. P., Wehrle-Haller, B. (2019). Cell adhesion by integrins. *Physiol. Rev.* **99**, 1655–1699.

255. Anguiano, M., Morales, X., Castilla, C., Pena, A. R., Ederra, C., Martínez, M., Ariz, M., Esparza, M., Amaveda, H., Mora, M., Movilla, N., García Aznar, J. M., Cortés-Domínguez, I., Ortiz-De-Solorzano, C. (2020). The use of mixed collagen-Matrigel matrices of increasing complexity recapitulates the biphasic role of cell adhesion in cancer cell migration: ECM sensing, remodeling and forces at the leading edge of cancer invasion. *PLoS One.* **15**, e0220019.

256. Mavrommati, I., Cisse, O., Falasca, M., Maffucci, T. (2016). Novel roles for class II Phosphoinositide 3-Kinase C2β in signalling pathways involved in prostate cancer cell invasion. *Sci. Rep.* **6**, 23277.

257. Maffucci, T., Cooke, F. T., Foster, F. M., Traer, C. J., Fry, M. J., Falasca, M. (2005). Class II phosphoinositide 3-kinase defines a novel signaling pathway in cell migration. *J. Cell Biol.* **169**, 789–799.

258. Katso, R. M., Pardo, O. E., Palamidessi, A., Franz, C. M., Marinov, M., De Laurentiis, A., Downward, J., Scita, G., Ridley, A. J., Waterfield, M. D., Arcaro, A. (2006). Phosphoinositide 3-kinase C2β regulates cytoskeletal organization and cell migration via Rac-dependent mechanisms. *Mol. Biol. Cell.* **17**, 3729–3744.

259. Gaidarov, I., Smith, M. E. K., Domin, J., Keen, J. H. (2001). The Class II Phosphoinositide 3-Kinase C2α Is Activated by Clathrin and Regulates Clathrin-Mediated Membrane Trafficking. *Mol. Cell.* **7**, 443–449.

260. Rainero, E., Howe, J. D., Caswell, P. T., Jamieson, N. B., Anderson, K., Critchley, D. R., Machesky, L., Norman, J. C. (2015). Ligand-Occupied Integrin Internalization Links Nutrient Signaling to Invasive Migration. *Cell Rep.* **10**, 398–413.

261. Huang, S., Zhou, H. (2011). Role of mTOR signaling in tumor cell motility, invasion and metastasis. *Curr. Protein Pept. Sci.* **12**, 30–42.

262. Ata, R., Antonescu, C. N. (2017). Integrins and Cell Metabolism: An Intimate Relationship Impacting Cancer. *Int. J. Mol. Sci.* **18**, 189.

263. Rabanal-Ruiz, Y., Byron, A., Wirth, A., Madsen, R., Sedlackova, L., Hewitt, G., Nelson, G., Stingele, J., Wills, J. C., Zhang, T., Zeug, A., Fässler, R., Vanhaesebroeck, B., Maddocks, O. D. K., Ponimaskin, E., Carroll, B., Korolchuk, V. I. (2021). mTORC1 activity is supported by spatial association with focal adhesions. *J. Cell Biol.* **220**, e202004010.

264. Lionello, V. M., Kretz, C., Edelweiss, E., Crucifix, C., Gómez-Oca, R., Messaddeq, N., Buono, S., Koebel, P., Massana Muñoz, X., Diedhiou, N., Cowling, B. S., Bitoun, M., Laporte, J. (2022). BIN1 modulation in vivo rescues dynamin-related myopathy. *Proc. Natl. Acad. Sci.* **119**, e2109576119.

265. Barros, C. S., Nguyen, T., Spencer, K. S. R., Nishiyama, A., Colognato, H., Müller, U. (2009). Beta1 integrins are required for normal CNS myelination and promote AKT-dependent myelin outgrowth. *Development.* **136**, 2717–2724.

266. MBInfo. (2018). How do Focal Adhesions Facilitate Mechanosensing? at <https://www.mechanobio.info/what-is-mechanobiology/how-do-focal-adhesions-facilitate-mechanosensing/>

267. Latomanski, E. A., Newton, H. J. (2019). Taming the Triskelion: Bacterial Manipulation of Clathrin. *Microbiol. Mol. Biol. Rev.* **83**, e00058–e00018.

268. Durrant, T. N., Hers, I. (2020). PI3K inhibitors in thrombosis and cardiovascular disease. *Clin. Transl. Med.* **9**, 8.

6. Appendix

6.1. List of abbreviations

Abbreviation	Meaning
AF	Alexa Fluor
ANOVA	Analysis of variance
AP-2	Adaptor protein complex 2
ATCC	American type culture collection
ATG	Autophagy-related protein
BAR	Bin, Amphyphysin, Rvs
BIN 1	Bridging integrator 1
BSA	Bovine serum albumin
Ca^{2+}	Calcium ion
Cas9	CRISPR-associated protein 9
CC	Coiled-coiled
CCDC78	Coiled-coiled domain-containing protein 78
CCP	Clathrin-coated pit
CCV	Clathrin-coated vesicle
CHC	Clathin heavy chain
CLIC	Chloride intracellular channel
CME	Clathrin-mediated endocytosis
CMT	Charcot-Marie-Tooth
CNM	Centronuclear myopathy
CRISPR	Clustered regularly interspaced short palindromic repeats
CTL	Control
CytC	Cytochrome C
DAPI	4',6-diamidino-2-phenylindole
DENN	Differentially expressed in normal and neoplastic cells
DEPC	Diethyl pyrocarbonate
Des	Desmin gene (*M. musculus*)
DHPR	Dihydropyridine receptor
DM	Differentiation media
DMEM	Dulbecco's Modified Eagle Medium
DNA	Deoxyribonucleic acid
DNM2	Dynamin 2
ECC	Excitation-contraction coupling
ECM	Extracellular matrix
EDTA	Ethylenediaminetetra-acetic acid
EEA1	Early endosome antigen 1
eGFP	Enhanced green fluorescent protein
EGFR	Epidermal growth factor receptor
ER	Endoplasmic reticulum
EXOC	Exocyst complex protein
FA	Focal adhesion
FACS	Fluorescence-activated cell sorting
FAK	Focal adhesion kinase
FBS	Fetal bovine serum
FMP	Leibniz-Forschungsinstitut für Molekulare Pharmakologie
FYVE	Fab 1, YOTB, Vac 1, EEA1
gDNA	Genomic DNA
GEF	Guanine nucleotide exchange factor
GFP	Green fluorescent protein
GM	Growth media
GM130	Golgi matrix protein 130
GRAM	Glucosyltransferases, RAB-like GTPase activators and myotubularins
h	Hour(s)
HA	Human influenza hemagglutinin
HCl	Hydrochloric acid
HEK293T	Human embryonic kidney 293T
HEPES	4-(2-hydroxyethyl)-1-piperazineethanesulfonic acid
HRP	Horseradish peroxidase

Hrs	Hepatocyte growth factor receptor tyrosine kinase substrate
HS	Horse serum
IAC	Integrin adhesion complex
ICC	immunocytochemistry
IgG/M	Immunoglobulin G/M
ILK	Integrin-linked protein kinase
IP	Immunoprecipitation
ITSN1	Intersectin 1
KCl	Potassium chloride
KD	Knockdown
KH2PO4	Monopotassium phosphate
KI	Kinase inactive
KO	Knockout
LAMP1	Lysosomal-associated membrane protein 1
LB	Lysogeny broth
LSM	Laser scanning microscope
MgCl2	Magnesium chloride
MHC	Myosin heavy chain
min	Minute(s)
MTJ	Myotendinous junction
Mtm	Homolog of MTM1/MTMR2 protein (*D. melanogaster*)
MTM1	Myotubularin 1 gene (*H. sapiens*)
MTM1	Myotubularin 1 protein (*H. sapiens* and *M. musculus*)
Mtm1	Myotubularin 1 gene (*M. musculus*)
MTMR	Myotubularin-related protein
mTORC1	Mechanistic target of rapamycin complex 1
$Na_2HPO_4*2H_2O$	Sodium phosphate dibasic dihydrate
NaCl	Sodium chloride
NaF	Sodium fluoride
NaN3	Sodium azide
NaOH	Sodium hydroxide
NFL	Neurofilament light chain
NGS	Normal goat serum
NH4Cl	Ammonium chloride
NHEJ	Non-homologous end joining
NLS	Nuclear localization signal
nRFP	Nuclear RFP
PBB	PIPES-based buffer
PBS	Phosphate buffer saline
PCR	Polymerase chain reaction
PDZ	PDS95-Dlg1-Zo1
PFA	Paraformaldehyde
PH	Plekstrin homology
pH	Potential of hydrogen
PI	Phosphatidylinositol
PI(3)P	Phosphatidylinositol 3-phosphate
$PI(3,4)P_2$	Phosphatidylinositol 3,4-bisphosphate
$PI(3,4,5)P_3$	Phosphatidylinositol 3,4,5-trisphosphate
$PI(3,5)P_2$	Phosphatidylinositol 3,5-bisphosphate
PI(4)P	Phosphatidylinositol 3-phosphate
$PI(4,5)P_2$	Phosphatidylinositol 4,5-bisphosphate
PI(5)P	Phosphatidylinositol 5-phosphate
PI3K	Phosphatidylinositol 3-kinase
Pi3k68d	Homolog of class II PI3K protein (*D. melanogaster*)
PIC	Protease inhibitor cocktail
Pik3c2b	PI3KC2β gene (*M. musculus*)
PIPES	Piperazine-N,N'-bis(2-ethanesulfonic acid)
PKN2	Protein kinase N 2
PMSF	Phenylmethylsulphonyl fluoride
PTP	Protein tyrosine phosphatase
PX	Phox homology
qPCR	Quantitative PCR

RAB	Ras-associated binding
raptor	Regulatory-associated protein of mTOR
RBD	Ras binding domain
RFP	Red fluorescent protein
RHO	Ras homologous
RNA	Ribonucleic acid
rpm	Revolutions per minute
RTK	Receptor tyrosine kinase
RYR1	Ryanodine receptor 1
s	Second(s)
S6K	p70 S6 Kinase 1
SCR	Scrambled (non-targeting [negative control] si/shRNA)
SDC	Spinning disk confocal
SDS(-PAGE)	Sodium dodecyl sulfate (-polyacrylamide gel electrophoresis)
sgRNA	Single guide RNA
shRNA	Short hairpin RNA
siRNA	Small interfering RNA
SM	Starting material
SNX	Sorting nexin
SPEG	Striated muscle preferentially expressed protein kinase
TBS	Tris -buffered saline
TFEB	Transcription factor EB
TIRF	Total internal reflection fluorescence
T-PBS	Tween-phosphate saline buffer
Tris	Tris(hydroxymethyl)aminomethane
TfR	Transferrin receptor
TSC	Tuberous sclerosis complex
T-TBS	Tween-Tris-buffered saline
TTN	Titin
ULK	Unc-51-like autophagy-activating kinase
UP H_2O	Ultra-purified water
UPS	Ubiquitin-proteasome system
VPS34	Vacuolar protein sorting 34
WB	Western blot
WT	Wild type
XLCNM	X-linked centronuclear myopathy

6.2. List of tables and figures

6.2.1. List of tables

6.2.2. List of figures

6.3. Publications

Samsó, P.[#], Koch, P.A.[#], Posor, Y., Lo, W. T., Belabed, H., Nazare, M., Laporte, J., & Haucke, V. (2022). Antagonistic control of active surface integrins by myotubularin and phosphatidylinositol 3-kinase C2β in a myotubular myopathy model. *Proc. Natl. Acad. Sci.* **119**, e2202236119. doi: 10.1073/pnas.2202236119
([#] equal contribution)

Jang, W., Puchkov, D., Samsó, P., Liang, Y. T., Nadler-Holly, M., Sigrist, S. J., Kintscher, U., Liu, F., Mamchaoui, K., Mouly, V., & Haucke, V. (2022). Endosomal lipid signaling reshapes the endoplasmic reticulum to control mitochondrial function. *Science* **378**, eabq5209. doi: 10.1126/science.abq5209

Schmied, C., Ebner, M., Samsó, P., Haucke, V., Lehmann, M. OrgaMapper: A robust and easy-to-use workflow for anlaysing organelle postioning. (In preparation).